



Graphene **N**anoplatelet (GNP) **R**einforced **T**antalum **C**arbide (TaC)

Benjamin Boesl
FLORIDA INTERNATIONAL UNIVERSITY

08/27/2015
Final Report

DISTRIBUTION A: Distribution approved for public release.

Air Force Research Laboratory
AF Office Of Scientific Research (AFOSR)/ RTB1
Arlington, Virginia 22203
Air Force Materiel Command

REPORT DOCUMENTATION PAGE					Form Approved OMB No. 0704-0188	
<small>The public reporting burden for this collection of information is estimated to average 1 hour per response, including the time for reviewing instructions, searching existing data sources, gathering and maintaining the data needed, and completing and reviewing the collection of information. Send comments regarding this burden estimate or any other aspect of this collection of information, including suggestions for reducing the burden, to the Department of Defense, Executive Service Directorate (0704-0188). Respondents should be aware that notwithstanding any other provision of law, no person shall be subject to any penalty for failing to comply with a collection of information if it does not display a currently valid OMB control number.</small>						
PLEASE DO NOT RETURN YOUR FORM TO THE ABOVE ORGANIZATION.						
1. REPORT DATE (DD-MM-YYYY) 08/19/2015		2. REPORT TYPE Final Report			3. DATES COVERED (From - To) 31 May 2012 to 30 May 2015	
4. TITLE AND SUBTITLE Graphene Nanoplatelet Reinforced Tantalum Carbide				5a. CONTRACT NUMBER		
				5b. GRANT NUMBER FA9550-12-1-0263		
				5c. PROGRAM ELEMENT NUMBER		
6. AUTHOR(S) Dr. Arvind Agarwal and Dr. Benjamin Boesl				5d. PROJECT NUMBER		
				5e. TASK NUMBER		
				5f. WORK UNIT NUMBER		
7. PERFORMING ORGANIZATION NAME(S) AND ADDRESS(ES) Florida International University 10555 W Flagler St. Miami, FL 33174					8. PERFORMING ORGANIZATION REPORT NUMBER	
9. SPONSORING/MONITORING AGENCY NAME(S) AND ADDRESS(ES) Dr. Ali Sayir Program Manager - Materials for Extreme Environments Air Force Office of Scientific Research					10. SPONSOR/MONITOR'S ACRONYM(S) AFOSR	
					11. SPONSOR/MONITOR'S REPORT NUMBER(S)	
12. DISTRIBUTION/AVAILABILITY STATEMENT Distribution A: Available for Public Distribution						
13. SUPPLEMENTARY NOTES						
14. ABSTRACT In this study, Graphene nanoplatelet (GNP) reinforced tantalum carbide (TaC) composites were studied for their mechanical and thermal properties as they relate to usage as ultra high temperature materials. Samples were fabricated using Spark Plasma Sintering (SPS) and ultrahigh-pressure consolidation. The results of mechanical property testing showed GNP reinforced composites have improved modulus, hardness, damping, and damage resistance over unreinforced TaC. Results of thermal analysis during plasma oxidation testing showed an increase in thermal conductivity in GNP reinforced composites resulting in a reduction of peak sample surface temperature. This study resulted in the publications listed below and attached to this document for additional detail (the support from this grant was acknowledged in each). This award also supported the research of three graduate students (A. Nieto, C. Zhang, S. Rengifo : 1 female, 2 of Hispanic decent) and one undergraduate student (S. Thomas).						
15. SUBJECT TERMS Ultrahigh Temperature Ceramics, Nanocomposites, In situ Testing, Plasma Oxidation Testing, Graphene Nanoplatelets						
16. SECURITY CLASSIFICATION OF:			17. LIMITATION OF ABSTRACT UU	18. NUMBER OF PAGES 105	19a. NAME OF RESPONSIBLE PERSON Benjamin Boesl	
a. REPORT U	b. ABSTRACT U	c. THIS PAGE U			19b. TELEPHONE NUMBER (Include area code) (305) 348-3028	

Reset

INSTRUCTIONS FOR COMPLETING SF 298

1. REPORT DATE. Full publication date, including day, month, if available. Must cite at least the year and be Year 2000 compliant, e.g. 30-06-1998; xx-06-1998; xx-xx-1998.

2. REPORT TYPE. State the type of report, such as final, technical, interim, memorandum, master's thesis, progress, quarterly, research, special, group study, etc.

3. DATES COVERED. Indicate the time during which the work was performed and the report was written, e.g., Jun 1997 - Jun 1998; 1-10 Jun 1996; May - Nov 1998; Nov 1998.

4. TITLE. Enter title and subtitle with volume number and part number, if applicable. On classified documents, enter the title classification in parentheses.

5a. CONTRACT NUMBER. Enter all contract numbers as they appear in the report, e.g. F33615-86-C-5169.

5b. GRANT NUMBER. Enter all grant numbers as they appear in the report, e.g. AFOSR-82-1234.

5c. PROGRAM ELEMENT NUMBER. Enter all program element numbers as they appear in the report, e.g. 61101A.

5d. PROJECT NUMBER. Enter all project numbers as they appear in the report, e.g. 1F665702D1257; ILIR.

5e. TASK NUMBER. Enter all task numbers as they appear in the report, e.g. 05; RF0330201; T4112.

5f. WORK UNIT NUMBER. Enter all work unit numbers as they appear in the report, e.g. 001; AFAPL30480105.

6. AUTHOR(S). Enter name(s) of person(s) responsible for writing the report, performing the research, or credited with the content of the report. The form of entry is the last name, first name, middle initial, and additional qualifiers separated by commas, e.g. Smith, Richard, J, Jr.

7. PERFORMING ORGANIZATION NAME(S) AND ADDRESS(ES). Self-explanatory.

8. PERFORMING ORGANIZATION REPORT NUMBER.

Enter all unique alphanumeric report numbers assigned by the performing organization, e.g. BRL-1234; AFWL-TR-85-4017-Vol-21-PT-2.

9. SPONSORING/MONITORING AGENCY NAME(S) AND ADDRESS(ES). Enter the name and address of the organization(s) financially responsible for and monitoring the work.

10. SPONSOR/MONITOR'S ACRONYM(S). Enter, if available, e.g. BRL, ARDEC, NADC.

11. SPONSOR/MONITOR'S REPORT NUMBER(S). Enter report number as assigned by the sponsoring/monitoring agency, if available, e.g. BRL-TR-829; -215.

12. DISTRIBUTION/AVAILABILITY STATEMENT. Use agency-mandated availability statements to indicate the public availability or distribution limitations of the report. If additional limitations/ restrictions or special markings are indicated, follow agency authorization procedures, e.g. RD/FRD, PROPIN, ITAR, etc. Include copyright information.

13. SUPPLEMENTARY NOTES. Enter information not included elsewhere such as: prepared in cooperation with; translation of; report supersedes; old edition number, etc.

14. ABSTRACT. A brief (approximately 200 words) factual summary of the most significant information.

15. SUBJECT TERMS. Key words or phrases identifying major concepts in the report.

16. SECURITY CLASSIFICATION. Enter security classification in accordance with security classification regulations, e.g. U, C, S, etc. If this form contains classified information, stamp classification level on the top and bottom of this page.

17. LIMITATION OF ABSTRACT. This block must be completed to assign a distribution limitation to the abstract. Enter UU (Unclassified Unlimited) or SAR (Same as Report). An entry in this block is necessary if the abstract is to be limited.

Thursday, August 20, 15

Dr. Ali Sayir
Program Manager - Materials for Extreme Environments
Air Force Office of Scientific Research

Dear Dr. Sayir,

Herein, please find the final report for AFOSR Grant FA9550-12-1-0263 entitled "Graphene Nanoplatelet Reinforced Tantalum Carbide," ended 31 MAY 2015. The award was originally granted to PI: Dr. Arvind Agarwal with a transfer of PI to Dr. Benjamin Boesl in January of 2014.

Executive Summary

In this study, Graphene nanoplatelet (GNP) reinforced tantalum carbide (TaC) composites were studied for their mechanical and thermal properties as they relate to usage as ultra high temperature materials. Samples were fabricated using Spark Plasma Sintering (SPS) and ultrahigh-pressure consolidation. The results of mechanical property testing showed GNP reinforced composites have improved modulus, hardness, damping, and damage resistance over unreinforced TaC. Results of thermal analysis during plasma oxidation testing showed an increase in thermal conductivity in GNP reinforced composites resulting in a reduction of peak sample surface temperature. This study resulted in the publications listed below and attached to this document for additional detail (the support from this grant was acknowledged in each). This award also supported the research of three graduate students (A. Nieto, C. Zhang, S. Rengifo : 1 female, 2 of Hispanic decent) and one undergraduate student (S. Thomas).

1. C Rudolf, et al. *In Situ Indentation Behavior of Bulk Graphene Nanoplatelets with Respect to Orientation*, **Carbon** 94 (2015) 872-878
2. Nieto, A. et al. *Three Dimensional Graphene Foam - Polymer Hybrid as a High Strength Biocompatible Scaffold*, **Advanced Functional Materials** Volume 25, Issue 25 (2015), pages 3916–3924
3. A Nieto, et al. *Multi-scale intrinsic deformation mechanisms of 3D graphene foam*, **Carbon** 85 (2015) 299-308
4. B Boesl, et al. *Direct observation of carbon nanotube induced strengthening in aluminum composite via in situ tensile tests*, **Carbon** 69 (2014) 79-85
5. A Nieto, et al. *Oxidation behavior of graphene nanoplatelet reinforced tantalum carbide composites in high temperature plasma flow*, **Carbon** 67 (2014) 398-408

DEPARTMENT OF MECHANICAL & MATERIALS ENGINEERING
COLLEGE OF ENGINEERING AND COMPUTING

6. A Nieto, et. al., *Nanodynamic mechanical behavior of graphene nanoplatelet-reinforced tantalum carbide*. **Scripta Materialia** 69-9 (2013) 678-681
7. A Nieto, et. al. *Graphene NanoPlatelets reinforced tantalum carbide consolidated by spark plasma sintering*. **Materials Science and Engineering: A** 582 (2013) 338-346
8. D Lahiri, et. al., *Boron nitride nanotubes reinforced aluminum composites prepared by spark plasma sintering: Microstructure, mechanical properties and deformation behavior*. **Materials Science and Engineering: A** 574 (2013) 149-156
9. D Lahiri, et. al. *Ultrahigh-pressure consolidation and deformation of tantalum carbide at ambient and high temperatures*. **Acta Materialia** 61-11 (2013) 4001-4009
10. C Zhang, et. al. *Photocatalytic Activity of Spark Plasma Sintered TiO₂-Graphene Nanoplatelet Composite*, **Scripta Materialia** 68 (2013) 719-722
11. D Lahiri, et. al. *Unfolding the Damping Behavior of Multilayer Graphene Membrane in the Low-Frequency Regime*. **ACS Nano** 6-5 (2013), 3992-4000
12. A Nieto, et. al. *Synthesis and properties of bulk graphene nanoplatelets consolidated by spark plasma sintering*. **Carbon** 50-11 (2012), 4068-4077
13. D. Lahiri, et al. *Graphene-induced strengthening in spark plasma sintered tantalum carbide-nanotube composite*. **Scripta Materialia** 68 (2013) 285-288

Sincerely,



Dr. Benjamin Boesl
Assistant Professor
Florida International University
Mechanical and Materials Engineering Department
10555 W Flagler St. EC 3465, Miami, FL 33174
(305) 348-3028
email: bboesl@fiu.edu

DEPARTMENT OF MECHANICAL & MATERIALS ENGINEERING
COLLEGE OF ENGINEERING AND COMPUTING



In situ indentation behavior of bulk multi-layer graphene flakes with respect to orientation



Chris Rudolf, Benjamin Boesl, Arvind Agarwal*

Plasma Forming Laboratory, Composites Laboratory, Department of Mechanical and Materials Engineering, Florida International University, 10555 West Flagler Street, Miami, FL 33174, United States

ARTICLE INFO

Article history:

Received 23 February 2015

Received in revised form 21 July 2015

Accepted 22 July 2015

Available online 23 July 2015

ABSTRACT

In situ indentation is performed on bulk multi-layer graphene flakes (MLG) consolidated by spark plasma sintering to study the effect of orientation on the deformation behavior and associated energy dissipation capabilities of MLG. Spark plasma sintering of MLG aligns them into a uniformly oriented, densely packed pellet. With respect to the 2D surface of consolidated MLG, indentation is carried out on the surface (out-of-plane MLG orientation) and in the orthogonal direction (in-plane MLG orientation). The combination of instrumented indentation and imaging provided evidence of deformation and failure mechanisms in real-time, as well as a quantitative comparison of energy dissipation. Indentation performed in the orthogonal direction resulted in a work of indentation 270% greater than indentation performed on the surface. The prevalent energy dissipation mechanisms observed when indenting in the orthogonal direction are compressive reinforcement, bending, push-out, and pop-out while the prevalent mechanisms observed in the surface indent are sliding, bending, kinking, and MLG pull-out.

© 2015 Elsevier Ltd. All rights reserved.

1. Introduction

Graphene is a single layer of sp^2 bonded carbon that is known for its excellent thermal, mechanical, and electrical properties. The functional properties of graphene include having a high Young's modulus (0.5–1 TPa) [1] and high tensile strength (130 GPa) [2], which has gained it considerable attention for use as reinforcement in polymer, metallic, and ceramic composite matrices [3–5]. Rafiee et al. [3] found that compared to other carbon-based nanostructures, such as single- and multi-walled carbon nanotubes, a low content of graphene addition offered better improvement in mechanical properties in a reinforced epoxy nanocomposite. While offering great reinforcement properties, the use of graphene was slow until the development of multi-layer graphene flakes (MLG) which are also called graphene nanosheets [6]. Multi-layer graphene flakes are particles consisting of multiple layers of stacked graphene [7]. MLG are becoming more widely used because they are easier and less expensive to form compared to single layer graphene while retaining much of the desirable properties [8,9]. Typically, MLG are made up of 10–30 sheets of graphene held together by weak van der Waals forces and have a thickness of 3–10 nm and a width of 1–25 μm , providing large surface areas.

* Corresponding author.

E-mail address: agarwala@fiu.edu (A. Agarwal).

The mechanical properties of graphene have been previously reported by Lee et al. [2] who performed atomic force microscopy on a suspended graphene flake and found that the bending rigidity is higher in the principal (in-plane) direction. Golkarian et al. [10] reported on the effect of the van der Waals forces when increasing the number of layers in graphite flakes and found by theoretical modeling that the Young's modulus decreased about 13% with increasing the number of layers fourfold. Nanoindentation, previously performed on fully dense samples of MLG consolidated by spark plasma sintering (SPS), showed a correlation of mechanical properties as a function of loading direction [11]. Energy dissipation mechanisms were observed post-fracture with a goal of evaluating future use of MLG in ceramic composites. Subsequent published reports on MLG-reinforced composites detail the various deformation or energy dissipation mechanisms. Nieto et al. [12] prepared a 5 vol.% graphene platelet reinforced tantalum carbide composite by spark plasma sintering and reported a fracture toughness increase of 99% over the monolith. Additionally, post fracture analysis of the graphene platelet fracture surfaces has shown evidence of energy dissipation mechanisms [6]. Hypotheses for increased toughness in composites reinforced with MLG can be attributed to three different regimes; (i) property changes during processing, (ii) increased load capacity prior to initial crack propagation, and (iii) crack propagation suppression mechanisms, examples of toughening mechanisms occurring in regime (i) include increased densification and grain wrapping

which can inhibit grain growth during sintering [13,14]. Examples of toughening mechanisms in regime (ii) include stress shielding, sheet pull-out, bending, kinking, and sliding all of which dissipate energy that would otherwise lead to crack initiation [15–17,12]. Examples of toughening mechanisms in regime (iii) include crack bridging and crack deflection after initial propagation leading to mixed mode fracture [18,19]. While the toughening mechanisms of these regimes have been proposed and observed, a quantifiable understanding of the influence of each individual regime on bulk MLG reinforced composite properties remains unclear.

The motive behind this study is to gain a fundamental understanding of the effect of MLG orientation on toughening through the combination of depth sensing indentation and *in situ* imaging using an electron microscope. Bulk MLG compacts were consolidated and tested in two different orientations to study the deformation mechanisms defined above, as a function of MLG anisotropy. Using this combination of experimentation and high magnification imaging, an understanding of which deformation mechanisms occur in each orientation and the associated work of indentation that is required to initiate and propagate each mechanism can be determined. Information related to work and energy can be used to predict both bulk MLG response, as well as improve the mechanistic understanding of MLG reinforced composites, and can be used to engineer new materials that take advantage of this fundamental information for improved response.

2. Experimental

2.1. Sample preparation

Multi-layer graphene flakes (xGNP-M-5) were purchased from XG Sciences, Lansing, MI, USA. The grade M-5 MLG have a thickness of 6–8 nm, an average diameter of 5 μm , and a typical surface area of 120–150 m^2/g [20].

Consolidation was carried out by spark plasma sintering (SPS) (Thermal Technologies model 10–4, Santa Rosa, CA, USA) which uses fast heating and hold times as well as high pressure that reduces the chance of structural damage to the MLG. The retention of the MLG structure after spark plasma sintering has been previously shown by Raman spectroscopy [11,21]. SPS was carried out at 80 MPa and 1850 $^{\circ}\text{C}$ for 10 min and utilized a heating rate of 200 $^{\circ}\text{C}/\text{min}$. The consolidated specimen was a 3 mm thick disk with a diameter of 20 mm. Density measurements carried out using a Helium pycnometer revealed a density of 2.01 g/cm^3 which is higher than the measured MLG powder of 1.82 g/cm^3 . This increase has been previously seen [11] and is attributed to the consolidation of the powder.

Fig. 1a shows an SEM image of the fracture surface of the SPS consolidated MLG. As can be seen, the MLG are aligned in an orientation normal to the pressing axis of the SPS machine. This alignment, as a result of consolidation by SPS, matches what has been previously published [11,21,22]. Fig. 1b shows an SEM image of

the top surface of the consolidated pellet which shows that the MLG are layered but still retain their platelet shape. The consolidation of overlapping MLG at the edges tends to form a grain boundary-like structure as shown in Fig. 1b. Fig. 1c illustrates the two loading directions identified as *surface* and *orthogonal* throughout the manuscript.

2.2. In situ indentation

In situ indentation was carried out inside a dual beam Focused Ion Beam/SEM (JEOL JIB-4500). A linear, screw driven micro-load frame (MTI Instruments SEMtester 1000) instrumented with an approximately 1 μm , 120 $^{\circ}$ conospherical diamond tip loaded across from the prepared sample was used for the indentation experiments. The micro-load frame has a load capacity of 4500 N with an accuracy of 0.2% and a linear movement resolution of 20 nm. The consolidated bulk MLG specimen was prepared by cutting the 20 mm diameter, 3 mm thick cylindrical sample in half and polishing the surface and cross section to a metallographic finish with a surface roughness of 0.25 μm . Indentation was carried out in a vacuum atmosphere at a rate of 0.05 mm/min to 0.5 mm and then unloaded at the same rate. Real time video of the indentations as well as the load–displacement curve outputs, shown in Figs. 2 and 3, enable characterization of deformation mechanisms and energy dissipation.

3. Results and discussion

From the load–displacement curves, it is evident that the orientation of the MLG with respect to the loading direction has a dramatic effect on the mechanical properties. Indentation of the specimen in the orthogonal direction required a maximum load of 42.89 N (Fig. 3) to reach a displacement of 0.48 mm whereas indentation performed on the surface required a maximum load of only 20.40 N (Fig. 2) in order to reach a displacement of 0.46 mm. Loading was carried out in displacement control and started with the indenter tip slightly offset from the sample which is the reason the final displacements differ by 0.02 mm. Loading in the orthogonal direction (in-plane MLG orientation) is expected to be much higher since the high Young's modulus of MLG (1 TPa) [20] is reported for this direction.

The work of indentation versus displacement curves in Figs. 2 and 3 were calculated from the area under the loading curves. It is seen that the work required to achieve the same displacement is much higher when indentation occurs orthogonal to the MLG surface. The total work of indentation in the orthogonal direction was 10.02 mJ or about 270% more than the total work of indentation on the surface which was 3.71 mJ.

When looking at the load–displacement data from the surface indent (Fig. 2) there are five distinct changes in the slope. This change in slope can be correlated to the deformation mechanisms at that stage and amount of normalized associated energy being

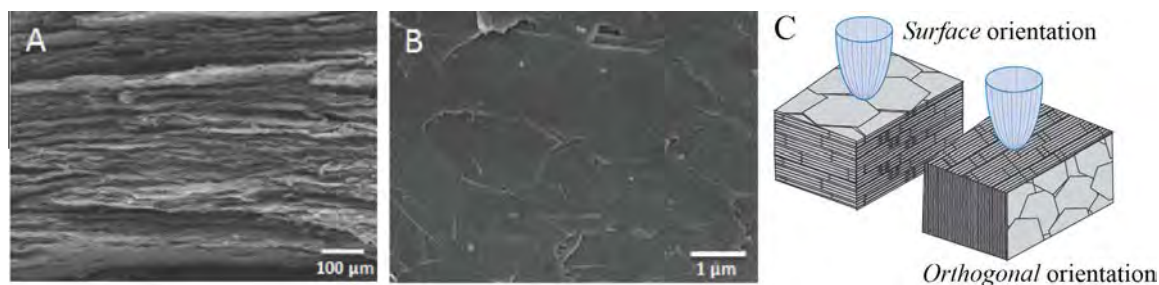


Fig. 1. SEM images of (A) fracture surface and (B) top surface of spark plasma sintered MLG pellet. (C) Schematic of surface and orthogonal indentation orientations.

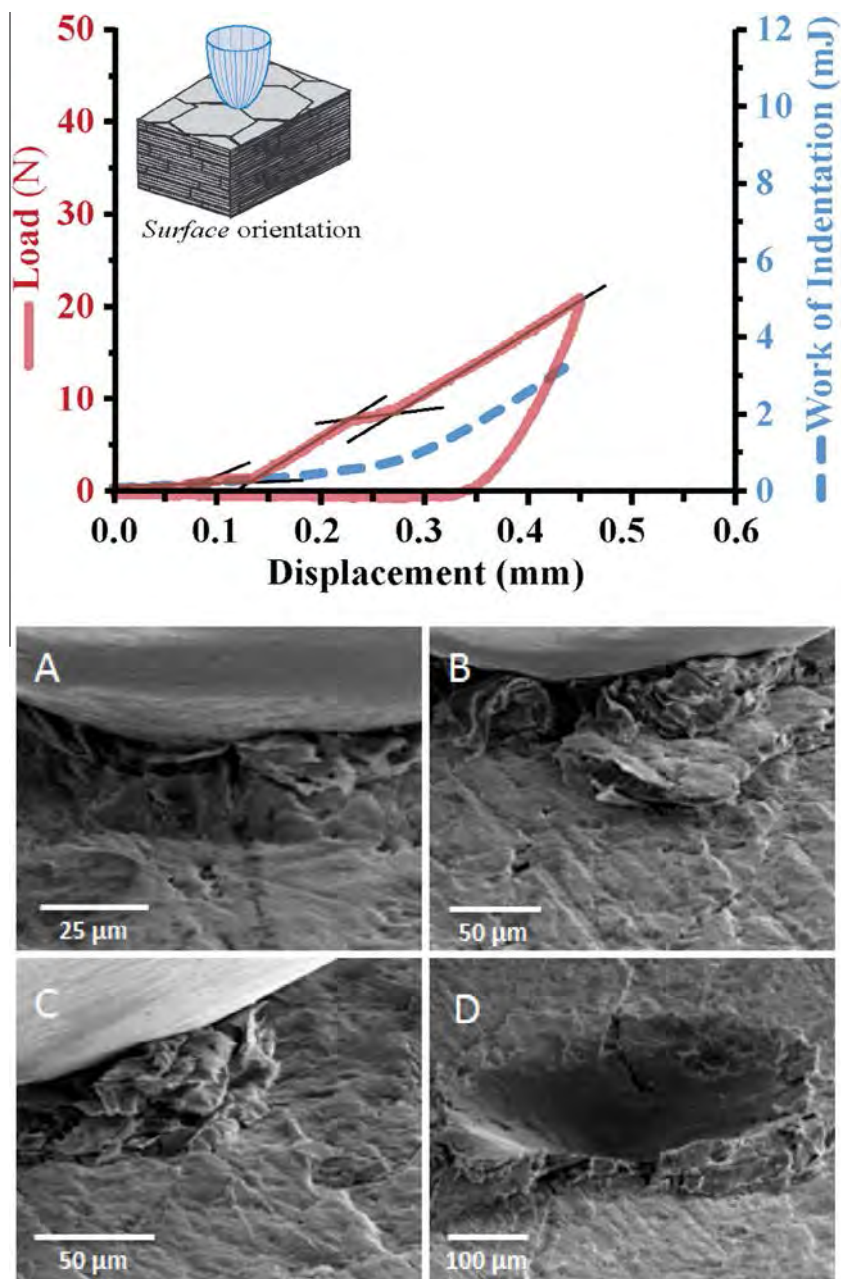


Fig. 2. Surface indent load–displacement and work–displacement curves and images of deformation occurrences.

dissipated in the sample. Normalized energy is found by taking the slope at the various listed displacement ranges and extrapolating that slope over a displacement range from 0 mm to 0.45 mm. This normalized energy is the work of indentation energy that would result if the slope stayed constant over the entire displacement range of 0.45 mm and allows for a comparison to be made between the dissipating energies with what deformation mechanisms are occurring.

Table 1 lists the displacement range (indentation depth), the time ranges on the indentation video (see Video V1 in Supplementary materials), and the normalized associated energy for each distinct slope regime in the load–displacement curve of the surface indent. During slope regime 1, a small amount of sheet delamination occurred in the form of MLG sliding followed by bending over of the pileup of delaminated MLG (Fig. 2A). The energy dissipation associated with this regime is small because

the indentation is mainly occurring on MLG aligned in an out-of-plane orientation. The mechanisms associated with this small energy are the sliding and bending of the MLG, which do not dissipate much energy due to the weak van der Waals forces between MLG layers. This sliding mechanism is evident in the post-indentation SEM image Fig. 4B where it can be seen that the MLG are separating at the indent site and sliding in a direction perpendicular to the indentation load. The wrinkling in the MLG that is seen on the right hand side of the figure (marked with arrows) is further evidence of the lateral MLG movement by the sliding mechanism. In the displacement range corresponding to slope 2 we saw the pileup from regime 1 easily folding over with very little new sheet delamination. At the end of this regime, a large area of slide-out occurs as shown in Fig. 2B. The results of this regime exemplify what was expected, that the MLG sliding mechanism dissipates the least amount of energy. During the slope 3 regime

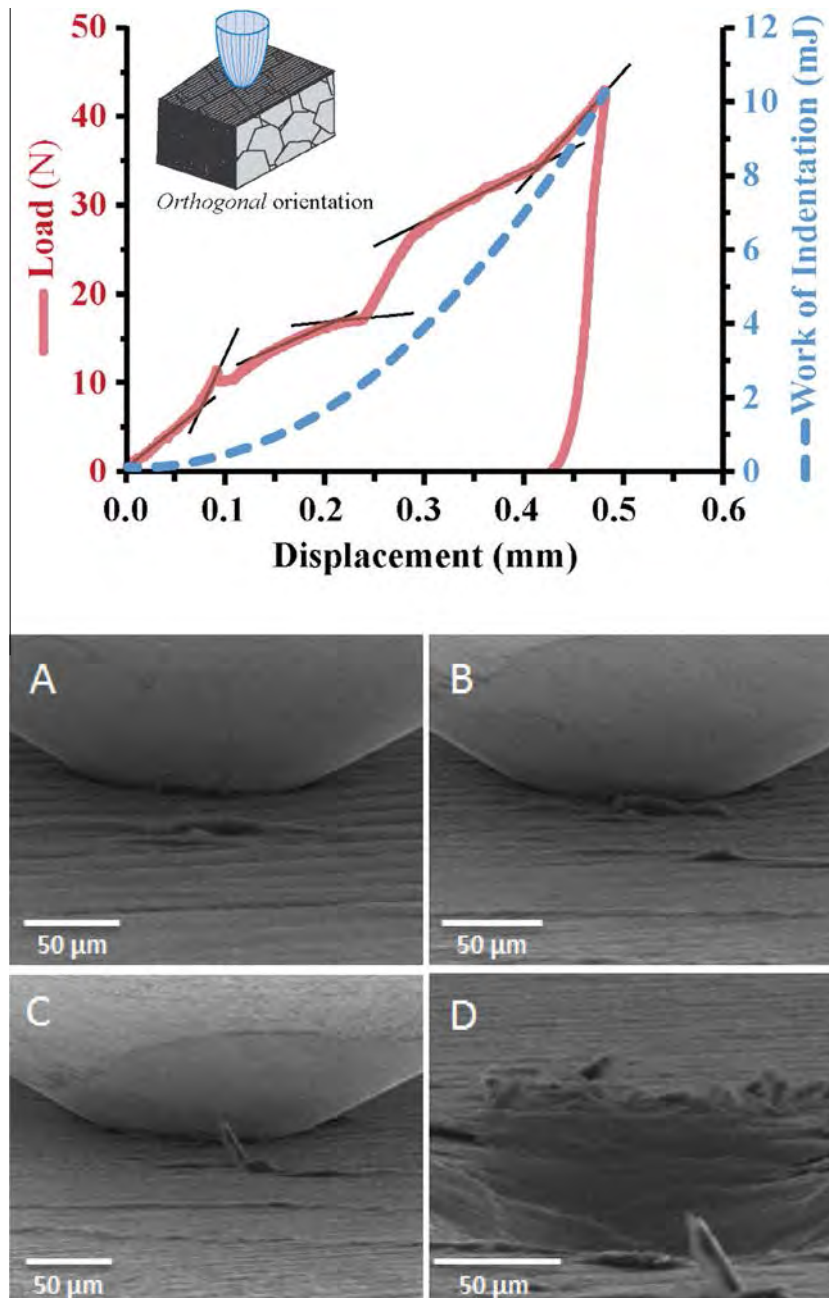


Fig. 3. Orthogonal indent load–displacement and work–displacement curves and images of deformation occurrences.

Table 1
Surface indent energy dissipation.

Slope	Displacement range (mm)	Time range in video (min)	Normalized associated energy (mJ)
1	0.010–0.075	0:12–0:51	1.30
2	0.083–0.100	0:56–1:06	0.01
3	0.108–0.200	1:12–2:06	5.96
4	0.216–0.233	2:16–2:27	1.85
5	0.258–0.455	2:42–4:39	6.06

there is significant new sheet delamination in the form of bending and kinking occurring all around the indentation tip. The large increase in the associated energy occurs as a result of the onset of MLG kinking. A change of orientation is observed from out-of-plane to in-plane MLG alignment to give a mixed-plane

loading. These bending and kinking mechanism occur in the areas surrounding the indenter tip causing pileup, shown in Fig. 4C. The mechanisms that are observed in regime 4 are very similar to what was seen in regime 1. The areas of kinking and pileup are pushed away from the indentation tip by sheet delamination and slide-out as seen in Fig. 2C. Therefore the benefits of the kinked MLG are no longer in contact with the indenter and the associated dissipation energy is again the result of the weak van der Waals forces between sliding MLG layers. Another mechanism that occurred as a result of the sheet sliding is MLG pull-out (Fig. 4D) which occurred when the overlapping MLG that were connected at the grain boundaries separate causing a crack. In regime 5, similar deformation mechanisms as regime 3, bending and kinking, are occurring. This again creates the mixed-plane loading that dissipates a greater energy.

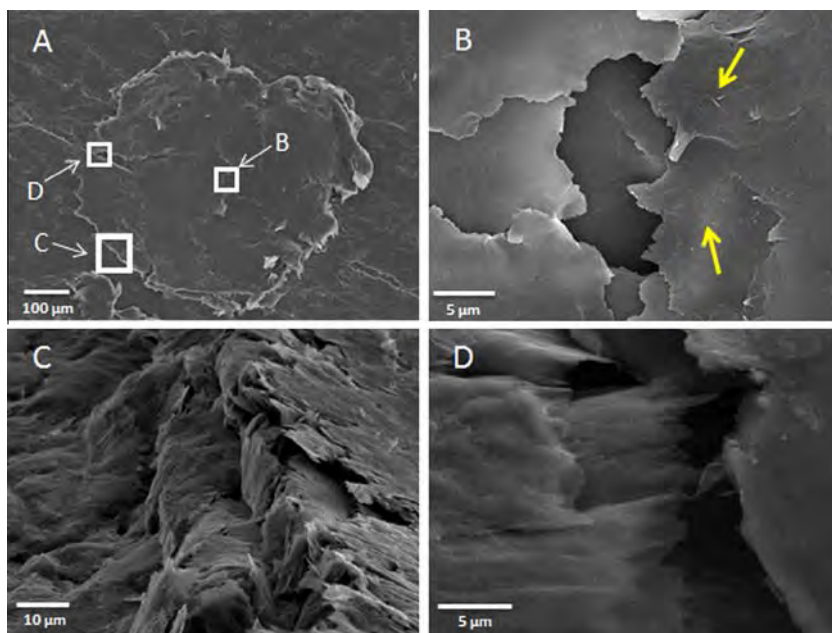


Fig. 4. SEM images of (A) overall residual indentation and magnified images of deformation mechanisms corresponding to the locations marked in image A as a result of the surface indentation: (B) sheet sliding with arrows marking wrinkling, (C) bending and kinking, (D) sheet pull-out.

Table 2 lists the displacement range, the time ranges on the indentation video (see [Video V2 in Supplementary materials](#)), and the normalized associated energy for each distinct slope regime in the load–displacement curve of the indent in the orthogonal direction. During the displacement range of regime 1, the indenter begins compressing the MLG oriented in the in-plane direction and bending starts to occur around the indenter tip ([Fig. 5D](#)). In the displacement range corresponding to regime 2, compression occurs perpendicular or outwards from the indenter tip. This is evident by what appears to be buckling, or MLG push-out, that occur because the outward pressure begins compressing MLG away from the indenter tip. At the end of this regime at a displacement of about 0.09 mm, a large push-out occurs ([Fig. 3A](#)) that relieves the pressure that is reinforcing the MLG at the indent site to remain in the high energy dissipating in-plane direction. This push-out deformation coincides with the drop in load seen in [Fig. 3](#). This is where regime 3 begins. After the compression pressure is relieved, the normalized energy dissipation returns to a value closer to what was seen in regime 1 and more bending occurs around the indenter tip. As the displacement continues deeper, smaller, more frequent push-out formations are seen further out from the indenter tip. This again reduces the compression reinforcing the indenter tip location, which is evident in the lower normalized associated energy in this regime. Another possible occurrence is that when the compression is relieved, the

MLG that were being held in the in-plane orientation by the compressive pressure are now able to bend to give a mixed-plane loading of both in-plane and out-of-plane MLG orientations. At the end of regime 3 and start of regime 4, a large MLG pop-out occurs ([Fig. 3C](#)) which is evidence that the outward compression is again occurring. This gives larger reinforcement to in-plane alignment of the MLG at the indent site that again requires increased work of indentation. In regimes 5 and 6, there is no visible evidence to link the energy dissipation values to any specific MLG deformation mechanisms. A possible reason for this is that the deformation mechanisms occur on the back side of the indenter tip.

[Figs. 4A and 5A](#) show SEM images of the residual damage left after indenting on the surface and orthogonal directions, respectively. Indentation performed on the surface resulted in greater pileup. This is expected because of the slide-out that occurred outward from the indentation site. The indentation performed in the orthogonal direction showed almost no pileup. It is evident from [Fig. 5D](#) that the MLG in contact with the indentation tip experienced bending that reconfigured the MLG alignment to the out-of-plane orientation. In contrast to the cracking that occurred as a result of MLG sheet separation during the surface indent, the cracks that formed during the orthogonal indent propagated outward from the bending locations around the tip as shown in [Fig. 5B and C](#). This occurrence follows what was previously seen by Zhang et al. [16] in a graphene platelet agglomeration of graphene platelet-HA composites under a bending load.

Based on the observed deformation mechanisms and the quantified normalized energy associated with each slope regime, it is possible to arrange the MLG deformation mechanisms in order of energy dissipation capabilities ([Table 3](#)).

When indentation is performed on the surface, the deformation mechanism that dissipates the greatest energy is kinking of the MLG. This is followed by bending of the MLG, MLG pull-out, and sliding. When indentation is performed in the orthogonal direction, the greatest energy is dissipated when compression occurs outward from the indentation site which in turn reinforces the in-plane alignment of the MLG that are in contact with the indenter tip. This is followed by MLG pop-out, push-out, and bending.

Table 2
Orthogonal indent energy dissipation.

Slope	Displacement range (mm)	Time range in video (min)	Normalized associated energy (mJ)
1	0.000–0.060	0:03–0:38	9.08
2	0.080–0.090	0:50–0:56	23.49
3	0.120–0.230	1:13–2:20	4.92
4	0.231–0.280	2:21–2:40	17.48
5	0.320–0.400	3:14–4:02	5.75
6	0.420–0.480	4:14–4:49	12.62

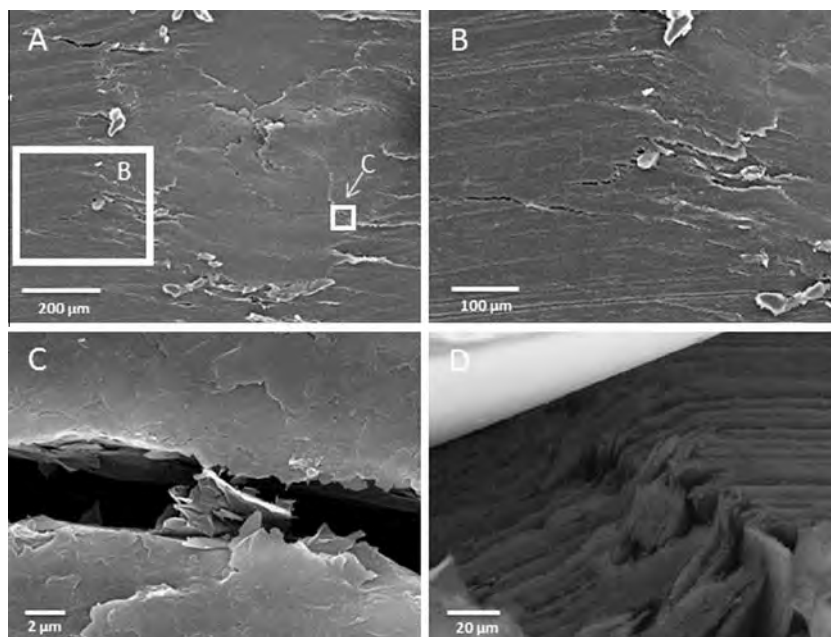


Fig. 5. SEM images of (A) overall residual indentation and magnified images of deformation mechanisms corresponding to the locations marked in image A as a result of orthogonal indentation: (B) separation and cracking, (C) crack propagation, and (D) bending during indentation.

Table 3
MLG deformation mechanisms in order of energy dissipation capabilities.

Deformation mechanism	Associated indent/ regime	Normalized associated energy of regime (mJ)
Reinforcing compression	Orthogonal (2), (4)	23.49, 17.48
MLG push-out, pop-out	Orthogonal (2), (3), (4)	23.49, 4.92, 17.48
Kinking	Surface (3), (5)	5.96, 6.06
Bending	Orthogonal (1), (3)	9.08, 4.92
	Surface (3), (5)	5.96, 6.06
MLG pull-out	Surface (4)	1.85
Sliding	Surface (1), (2), (4)	1.3, 0.01, 1.85

4. Conclusions

The toughening benefits of MLG as a result of deformation mechanisms are highly orientation driven. When indentation is performed on the surface, the energy dissipating deformation mechanism that most readily occurs is MLG sliding followed by bending, kinking, and MLG pull-out. When indentation is performed in the orthogonal direction, the total energy that is dissipated is up to 270% greater than when indentation is performed on the surface. This is attributed to the fact that the deformation mechanism that occurs most readily during the surface indent, MLG sliding, is also recognized as providing the least amount of energy dissipation. The deformation mechanisms that are observed during the orthogonal indentation are bending, push-out, and MLG pop-out as a result of outward compression. The understanding of the fundamental deformation mechanisms and anisotropy of bulk multi-layer graphene flakes in this study will enable the engineering of MLG reinforced composites that can be tailored to desired toughening properties.

Acknowledgements

The authors would like to acknowledge Dr. Ali Sayir, Program Manager of High Temperature Aerospace Materials at the Air Force Office of Scientific Research FA9550-12-1-0263 grant.

Authors also acknowledge the support of the Advanced Materials Engineering Research Institute (AMERI) at FIU.

Appendix A. Supplementary data

Supplementary data associated with this article can be found, in the online version, at <http://dx.doi.org/10.1016/j.carbon.2015.07.070>.

References

- [1] I.W. Frank, D.M. Tanenbaum, A.M. Van der Zande, P.L. McEuen, Mechanical properties of suspended graphene sheets, *J. Vac. Sci. Technol.*, B 25 (6) (2007) 2558–2561.
- [2] C. Lee, X. Wei, J.W. Kysar, J. Hone, Measurement of the elastic properties and intrinsic strength of monolayer graphene, *Science* 321 (5887) (2008) 385–388.
- [3] M.A. Rafiee, Z. Wang, H. Song, Z.Z. Yu, N. Koratkar, Enhanced mechanical properties of nanocomposites at low graphene content, *ACS Nano* 3 (2009) 3884–3890.
- [4] S. Yang, G. Cui, S. Pang, Q. Cao, U. Kolb, X. Feng, et al., Fabrication of cobalt and cobalt oxide/graphene composites: towards high-performance anode materials for lithium ion batteries, *ChemSusChem* 3 (2010) 236–239.
- [5] H. Seiner, P. Sedláček, M. Koller, M. Landa, C. Ramírez, M.I. Osendi, et al., Anisotropic elastic moduli and internal friction of graphene nanoplatelets/silicon nitride composites, *Compos. Sci. Technol.* 75 (2013) 93–97.
- [6] L. Kvetková, A. Duszová, P. Hvizdoš, J. Dusz, P. Kun, C. Balázs, Fracture toughness and toughening mechanisms in graphite platelet reinforced Si₃N₄ composites, *Scripta Mater.* 66 (2012) 793–796.
- [7] XG Sciences, Overview of XG Sciences and Our Materials, XG Sciences Documentation, 2012.
- [8] W. Choi, I. Lahiri, R. Seelaboyina, Y.S. Kang, Synthesis of graphene and its applications: a review, *Crit. Rev. Solid State Mater. Sci.* 35 (2010) 52–71.
- [9] N.A. Kotov, Carbon sheet solutions, *Nature* 442 (2006) 254–255.
- [10] A.R. Golkarian, M. Jabbarzadeh, The density effect of van der Waals forces on the elastic modules in graphite layers, *Comput. Mater. Sci.* 74 (2013) 138–142.
- [11] A. Nieto, D. Lahiri, A. Agarwal, Synthesis and properties of bulk graphene nanoplatelets consolidated by spark plasma sintering, *Carbon* 50 (11) (2012) 4068–4077.
- [12] A. Nieto, D. Lahiri, A. Agarwal, Graphene nanoplatelets reinforced tantalum carbide consolidated by spark plasma sintering, *Mater. Sci. Eng., A* 582 (2013) 338–346.
- [13] J. Liu, H. Yan, M.J. Reece, K. Jiang, Toughening of zirconia/alumina composites by the addition of graphene platelets, *J. Eur. Ceram. Soc.* 32 (16) (2012) 4185–4193.
- [14] T. He, J. Li, L. Wang, J. Zhu, W. Jiang, Preparation and consolidation of alumina/graphene composite powders, *Mater. Trans., JIM* 50 (4) (2009) 749–751.

- [15] J. Liu, H. Yan, K. Jiang, Mechanical properties of graphene platelet-reinforced alumina ceramic composites, *Ceram. Int.* 39 (2013) 6215–6221.
- [16] L. Zhang, X. Zhang, Y. Chen, J.N. Su, W.W. Liu, T.H. Zhang, et al., Interfacial stress transfer in a graphene nanosheet toughened hydroxyapatite composite, *Appl. Phys. Lett.* 105 (2014) 161908.
- [17] A. Nieto, D. Lahiri, A. Agarwal, Nanodynamic mechanical behavior of graphene nanoplatelet-reinforced tantalum carbide, *Scripta Mater.* 69 (2013) 678–681.
- [18] J. Dusza, J. Morgiel, A. Duszová, L. Kvetková, M. Nosko, P. Kun, et al., Microstructure and fracture toughness of Si_3N_4 + graphene platelet composites, *J. Eur. Ceram. Soc.* 32 (2012) 3389–3397.
- [19] G.B. Yadhukulakrishnan, S. Karumuri, A. Rahman, R.P. Singh, A.K. Kalkan, S.P. Harimkar, Spark plasma sintering of graphene reinforced zirconium diboride ultra-high temperature ceramic composites, *Ceram. Int.* 39 (2013) 6637–6646.
- [20] XG Sciences, xGnP® Graphene Nanoplatelets, A Unique Carbon Nanomaterial with Multifunctional Properties, XG Sciences Documentation, 2013.
- [21] L.S. Walker, V.R. Marotto, M.A. Rafiee, N. Koratkar, E.L. Corral, Toughening in graphene ceramic composites, *ACS Nano* 5 (4) (2010) 3182–3190.
- [22] H. Porwal, P. Tatarko, S. Grasso, J. Khaliq, I. Dlouhý, M.J. Reece, Graphene reinforced alumina nano-composites, *Carbon* 64 (2013) 359–369.

Three Dimensional Graphene Foam/Polymer Hybrid as a High Strength Biocompatible Scaffold

Andy Nieto, Rupak Dua, Cheng Zhang, Benjamin Boesl, Sharan Ramaswamy, and Arvind Agarwal*

Graphene foam (GrF)/polylactic acid–poly- ϵ -caprolactone copolymer (PLC) hybrid (GrF-PLC) scaffold is synthesized in order to utilize both the desirable properties of graphene and that of foams such as excellent structural characteristics and a networked 3-D structure for cells to proliferate in. The hybrid scaffold is synthesized by a dip-coating method that enables retention of the porous 3D structure. The excellent wettability of PLC with graphene foam along with the formation of PLC bridges leads to a $\approx 3700\%$ enhancement in strength and a $\approx 3100\%$ increase in ductility in the GrF-PLC scaffold. Biocompatibility of both graphene foam and GrF-PLC scaffold is demonstrated by culturing of human mesenchymal stem cells (hMSCs) for 28 days, a period over which cell proliferation is robust. The hMSCs are differentiated in chondrogenic media and supported chondrogenesis in both scaffolds. The demand for aggrecan extracellular matrix protein synthesis is reduced in hybrids due to improved bearing of cell-induced loads, this may be critical for ensuring adequate cellular distribution and layering of extracellular matrix. Hence, the unique mechanical and biotolerant properties of the GrF-PLC scaffold are suited for musculoskeletal tissue engineering applications, such as the growth of de novo cartilage to replace cartilage lost due to injury or osteoarthritis.

such as high elastic modulus (1 TPa^[7]) and yield strength (≈ 130 GPa^[6]) which have been utilized in polymer, metal, and ceramic matrix composites in order to enhance their mechanical performance. One of the critical challenges for effective graphene-based composites is the uniform distribution of graphene in the composite matrix. The effective dispersion of graphene has been the subject of significant research, with the most effective methods being limited by material systems or cost. The recent development of 3-D graphene foams (GrF)^[10–29] represents a solution for providing uniform distributions of graphene in composites. 3-D graphene foams form an interconnected continuous network of graphene thus eliminating the need for expensive and/or ineffective dispersion methods.

In this study we propose the use of a 3-D graphene foam/polymer composite as a flexible high strength biocompatible scaffolding material for tissue engineering purposes. Graphene has been shown to be a biocompatible material in recent

studies.^[30–32] Human stem cells (neural and mesenchymal) survive and experience accelerated differentiation on a graphene surface. While several studies^[11–16,23,27,28] have utilized the high surface area and macroporous structure of 3-D graphene foam-based composites for energy storage applications, only a few studies to date^[25,33] have exploited the inherent advantages of this unique structure for cell support, proliferation, and extracellular matrix (ECM) deposition. Studies on the biocompatibility of 3-D graphene foams have found that neural stem cells (NSCs) successfully proliferated and differentiated on the 3-D graphene structure. The porous 3-D graphene structure provides a microenvironment for the cells to grow within a 3-D biomimetic framework, while simultaneously enhancing the functionality of the electro-active neural cells by providing highly conductive pathways for charge transport.^[33] Furthermore, 3-D graphene foams cultured with microglial cells exhibited anti-inflammatory behavior not seen in 2-D graphene foams.^[25] A few recent studies have also investigated the mechanical properties of graphene foam reinforced polymer composites.^[34–37] Graphene foam/polymer composites exhibit superb flexibility as evidenced by their recovery after compressive strains of up to 80%^[36,37] and cyclic bending tests of nearly 180°.^[34] The

1. Introduction

Graphene is a 2-D layer of sp^2 bonded carbon atoms that has attracted interest in nearly all fields of materials science because of its excellent electrical,^[1–4] thermal,^[1,5] and mechanical properties.^[1,3,6–9] Graphene has extraordinary mechanical properties

A. Nieto, C. Zhang, Prof. B. Boesl, Prof. A. Agarwal
Nanomechanics and Nanotribology Laboratory
Mechanical and Materials Engineering
Florida International University
Miami, FL 33174, USA
E-mail: agarwala@fiu.edu



A. Nieto
Department of Chemical Engineering and Materials Science
One Shields Avenue
University of California Davis
Davis, CA 95616, USA
Dr. R. Dua, Prof. S. Ramaswamy
Biomedical Engineering
Florida International University
10555 West Flagler Street, EC 3464, USA

DOI: 10.1002/adfm.201500876

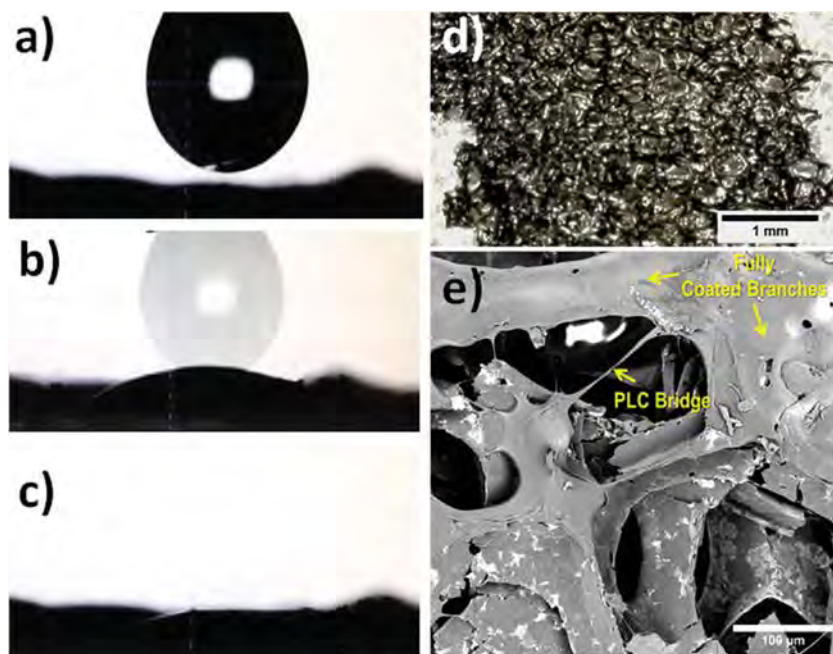


Figure 1. a) Image sequence of contact angle test before droplet contacts the surface. b) Single frame captures both the droplet as it approaches the foam and then rapidly spreads throughout the foam surface. c) Droplet forms near zero contact angle hence demonstrating near perfect wetting. d) Optical image of GrF-PLC hybrid scaffold. e) SEM image of GrF-PLC structure, thin strands of PLC can be seen to form bridges throughout the sample. Retention of 3D porous structure can be seen in both optical and SEM images.

enhancement of toughness, ductility, and tensile strength^[35] in graphene foam/polymer composites is especially noteworthy as their ultra-low density ($\approx 0.005 \text{ g cm}^{-3}$) yield exceptional specific properties.

We focus specifically on the need for high strength biocompatible scaffolding materials for musculoskeletal regenerative applications related to cartilage loss and/or deterioration. Graphene provides many of the properties desirable in a scaffold for de novo cartilage growth. The scaffold must be able to effectively transfer loads to the surrounding joints and bone;^[38] the high surface area of graphene foam enables effective transfer of loads in composites.^[39–42] Viscoelasticity is needed in cartilage scaffolding in order to provide flexibility and damping of loads; graphene has been shown to have excellent damping properties^[43] that can be effectively utilized in a composite material.^[44] A lubricated surface is also desirable as the wear of cartilage ultimately causes osteoarthritis and the associated pain; graphene is a solid state lubricant and can effectively enhance tribological properties of composites.^[40,45] Finally, a cartilage scaffold must be biocompatible in order to prevent infection or rejection by the native tissue; graphene has been shown to be biocompatible^[25,30–32] and it is used in the present work in conjunction with the biodegradable polymer PLC (a copolymer of polylactic acid and poly- ϵ -caprolactone).^[46] Several current works in cartilage tissue engineering make use of hydrogel-based scaffolds.^[47–50] Notably, while hydrogels promote cell proliferation and tissue repair, they do not provide the structure to enable systematic distribution of cellular and ECM components. While graphene itself is not degradable within the composite, we

hypothesized that the sustained presence of graphene after degradation of PLC will continue to support layered ECM deposition in a controlled manner, if interpenetrating networks present within the original composite material can guide initial tissue framework. These tissue remodeling events are crucial for long-term success of the procedure.

In this work, we synthesize a 3D graphene foam/PLC hybrid (GrF-PLC). The foam structure intrinsically facilitates interpenetrating networks between graphene and PLC, in order to promote cell distribution and ECM layering within the construct. We utilize a simple dip coating method for the GrF-PLC fabrication; the coating time is optimized to ensure retention of a porous foam structure. Wetting angle measurements are conducted to demonstrate the effectiveness of the PLC coating. Mechanical properties of the GrF-PLC hybrid are evaluated in tension and compression at multiple length scales using nanoindentation and in situ tensile testing inside scanning electron microscope. Cell seeding in the GrF-PLC scaffold environment is evaluated using human mesenchymal stem cells (hMSCs) on the scaffold, which has shown to be a promising cell source for cartilage tissue engineering in several studies.^[47,51] Specifically, the suitability of the GrF-PLC scaffold for musculoskeletal tissue engineering applications, specifically for cartilage, is evaluated by culturing the hMSCs in a chondrogenic media, while phenotype is evaluated by immunostaining after 28 days.

2. Results and Discussion

2.1. Synthesis

The 3-D graphene foam (Graphene Laboratories, Calverton, NY, USA) used in this study was synthesized by chemical vapor deposition (CVD) growth of graphene on a Ni foam template, followed by an etching step to dissolve the Ni structure. The graphene foam has an ultralow density of 0.005 g cm^{-3} (0.002 relative density) and consists of large macroscale open pores typically 100–200 μm in diameter and 50–80 μm thick foam walls.^[52] It was desired for the scaffold composite to retain this porous, high surface area structure and hence only a thin layer of PLC reinforcement was permissible. Graphene foams are known to be hydrophobic,^[24] as verified by water wetting angles measurements (Supporting Information, Figure S1); such poor wettability is detrimental to obtaining a thin coating. By contrast, wetting angle measurements shown in **Figure 1a–c** revealed that PLC has near perfect wetting with the graphene foam. The drops of PLC instantaneously spread out over the graphene foam, indicating a wetting angle of $\approx 0^\circ$. This excellent wetting allows the PLC to cover the graphene foam with only a very thin layer. The PLC layer will therefore not aggregate and

Table 1. Summary of Graphene Foam/PLC scaffold mechanical properties in compression and tension.

Compression				
Experimental method	Elastic modulus [MPa]	Strain to failure [%]	Hardness [kPa]	Bulk foam elastic modulus (calculated by Equation (1)) [Pa]
Nanoindentation	3.6 ± 0.3	–	69.8 ± 5.7	17.6 ± 1.2
Tension				
Experimental method	Elastic modulus [kPa]	Strain to failure [%]	Ultimate tensile strength (UTS) [kPa]	Foam wall elastic modulus (calculated by Equation (1)) [GPa]
Tensile testing	254.0 ± 43.7	276.3 ± 65.3	184 ± 48.1	52.35 ± 9.0

increase in thickness until the graphene foam surface is fully saturated; this allows the macroporous high surface area structure to be retained.

The graphene foam/PLC (GrF-PLC) hybrids were prepared by a simple dip coating method where the PLC polymer is synthesized in a solution of acetone in which the graphene foam is then dipped for a controlled period of time. The PLC polymer coated on the graphene foam undergoes the final steps of polymerization (i.e., solidification), while in contact with the graphene foam and hence a high strength bond is formed between the graphene foam and PLC in the resulting hybrid structure. The dipping time was optimized to prevent oversaturation of the graphene foam and hence retain the macroporous structure. The evaluation of graphene foam saturation was done using scanning electron microscopy (SEM). SEM images for dipping times of 30 and 120 s are provided in Supporting Information, Figure S2. These times were excessive and resulted in the foam becoming fully embedded in the PLC matrix which results in the loss of the macroporous structure desired for cell proliferation.

The optimum dipping time was found to be 5 s and resulted in the GrF-PLC hybrid structure shown in Figure 1d,e. The dipping time of 5 s resulted in a thin PLC layer over the majority of the interpenetrating networks of foam branches as seen in Figure 1e. The large graphene foam pores are not filled with PLC as with the previous cases, instead strands of PLC can be seen forming interconnected structures between branches of graphene foam. The thickness of the coating is not homogeneous as seen in Figure 1e; however strands of PLC that span some of the macropores in the graphene foam have diameters of ≈10 μm. These strands form as the PLC coating extends beyond branches and across the macropores and thereby provides an estimate of the length scale of the coating thickness. The amount of PLC added was not sufficient to obtain a measureable change in the density of 3D graphene foam which was measured using a helium pycnometer.

2.2. Strengthening Mechanisms

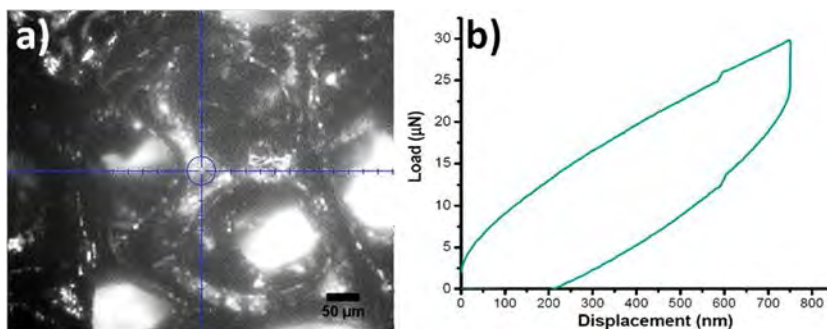
In our recently published work, we reported on the mechanical behavior and deformation mechanisms of freestanding 3-D graphene foam.^[52] The results of that study indicated that due to defects very few graphene branches actually bear any load, thereby indicating the potential was there for increased

strengthening with the reduction of defects. The results of that study serve as a baseline for comparison with the results obtained in the present study for GrF-PLC hybrid. Nanoindentation was performed on the GrF-PLC hybrid in order to investigate the mechanical properties in compression, results are presented in Table 1. A 100 μm conospherical tip was used to indent the material to a depth of 750 nm. A typical indentation location is shown in the optical micrograph in Figure 2a. As previously stated, the thin layer of PLC allows the graphene foam to maintain its porous structure; hence indents were performed on both branches and nodes. The localized nature of nanoindentation yields information on the walls of the GrF-PLC hybrid, the properties of the bulk foam structure can be determined using a simple volume based relation first established by Gibson and Ashby given below as Equation (1),^[53]

$$\frac{E^*}{E_s} = C_1 \left(\frac{\rho^*}{\rho_s} \right)^2; C_1 = 1 \quad (1)$$

where the subscript “s” denotes the solid wall property, and the superscript “*” denotes the foam property.

The load-displacement curve in Figure 2b reveals that the GrF-PLC hybrid has similar behavior to the previously reported pure graphene foam. The branch-node structure of the foam causes deformation to occur by both indentation of the foam wall as well by bending at the branch-node junctions. The load increases steadily under a mixed mode deformation process, where the branch bending is the primary mechanism, until about a depth of 600 nm. The slope then increases substantially as the deformation mechanism changes from branch bending to foam wall indentation.^[52] After a critical depth, branch bending returns as the primary mechanism. This behavior is

**Figure 2.** a) Optical image representative of typical nanoindentation test location. b) Characteristic nanoindentation curve for GrF-PLC hybrid.

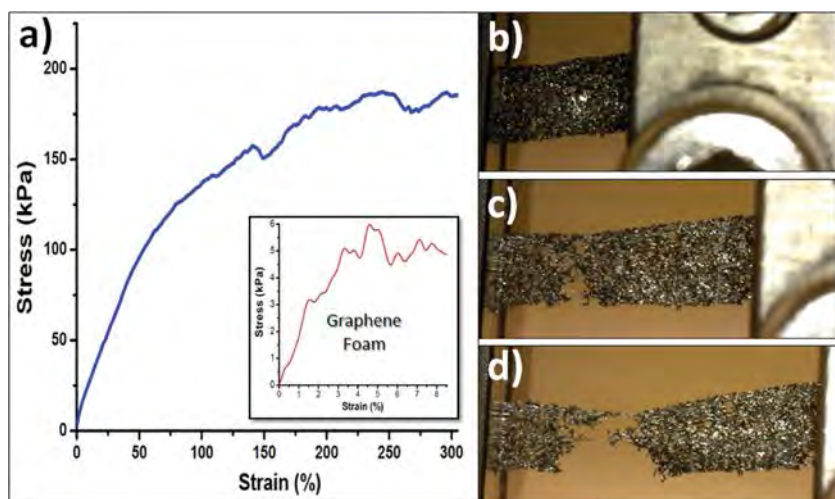


Figure 3. a) Characteristic stress–strain curve of GrF-PLC. Inset: Characteristic curve of pure graphene foam. b) GrF-PLC sample in tensile test setup. c) GrF-PLC sample in tension showing signs of necking. d) GrF-PLC after tensile failure, load prior to failure can be seen to be borne by a few high strength strands.

mirrored during the unloading portion of the curve. While the deformation mechanisms are similar, the compression strength of the GrF-PLC walls and hence the foam structure, are significantly higher than that of the pure graphene foam. The primary reason for strengthening in compression is due to the “healing” effect the PLC coating has on the graphene foam. The high wettability of PLC with the graphene foam allows it to fill preexisting microvoids and microcracks thereby providing increased resistance to elastic and plastic deformation.

The mechanical properties in tension were evaluated by macroscale tensile testing, these properties can be used to determine the foam wall properties by employing Equation (1). Results of macroscale tensile testing, shown in **Figure 3**, indicate that the addition of PLC dramatically increases the ductility and tensile strength of the GrF-PLC hybrid. Graphene foams typically fail at strains of about $\approx 8.5\%$, while the GrF-PLC hybrids typically reach values of $\approx 276\%$ as shown in **Figure 3a**, an increase of about 3100%. Unlike the brittle failure response exhibited by the graphene foam, the GrF-PLC hybrid undergoes necking as seen in **Figure 3c**. During necking branches of GrF-PLC become aligned as is common in foam structures,^[53] this is followed by the failure of individual low strength branches which correspond to the valleys in the stress–strain curves prior to failure. A few high strength branches continue to bear the load prior to failure as can be seen in **Figure 3d**. This results in the GrF-PLC hybrid scaffold having an ultimate tensile strength of ≈ 184 kPa, an increase of $\approx 3700\%$ relative to the pure graphene foam scaffold. Using Equation (1) the elastic modulus of the GrF-PLC hybrid is calculated to be ≈ 52 GPa, a value substantially higher than that of PLC (≈ 81 MPa).^[54] This exceptional high strength enables the utilization of a very porous structure, which is favorable for cell proliferation, without compromising the scaffold’s mechanical performance. The substantially higher mechanical properties in tension relative to those in compression are expected as it was shown in our previous work that the high in-plane

strength of graphene is only utilized in the foam structure during tension after branches become aligned with the loading direction.^[52]

In order to further investigate the deformation mechanisms of GrF-PLC in situ tensile testing was conducted inside an SEM. The reinforcing effect of PLC can be clearly seen during tensile testing (Videos S3 and S4 in the Supporting Information show in situ tensile tests). An individual bridge of PLC can be seen under tension in **Figure 4a**, the same bridge in seen after being strained for 18 s in **Figure 4b**. The PLC bridges along with the excellent bonding with the graphene foam allows for branches to be elongated substantially before fracturing. PLC may also form high strength branches composed of multiple bridges as shown in **Figure 4c**, after 25 s of straining the branch has still not failed as each individual PLC bridge fails one by one as seen in **Figure 4d**.

To summarize, the addition of PLC can hence be seen to provide strength to the GrF-PLC scaffold in both compression and

tension. The PLC provides dual strengthening mechanisms through i) defect healing and ii) PLC bridge formation. The excellent reinforcement effects originate from the excellent wettability between PLC and graphene foam. This high wettability enables the PLC to heal defects in the graphene foam by filling in branch discontinuities, microcracks, and microvoids. These cracks and discontinuities otherwise serve as stress concentrators which result in early branch failure and result in very few branches bearing loads. The filling of these voids with PLC enables more branches to participate in load bearing, thereby greatly enhancing strength. In addition to healing defects, the PLC serves as a fiber reinforcement due to the formation of PLC bridges that provide additional strength and ductility to the

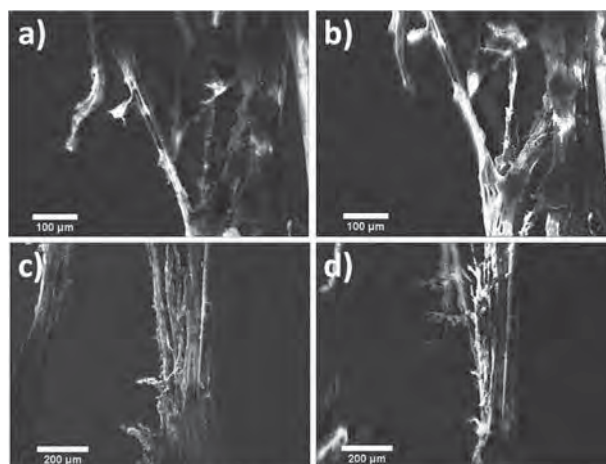


Figure 4. PLC reinforcing effect observed during in situ tensile testing. a) PLC bridge becomes stretched during tensile test. b) After 18 s, PLC bridge becomes stretched, enables foam branches to elongate without fracture. c) Branch composed of multiple PLC bridges under tension. d) After 25 s, PLC bridges become elongated and snap one by one, graphene foam branch at left has fractured.

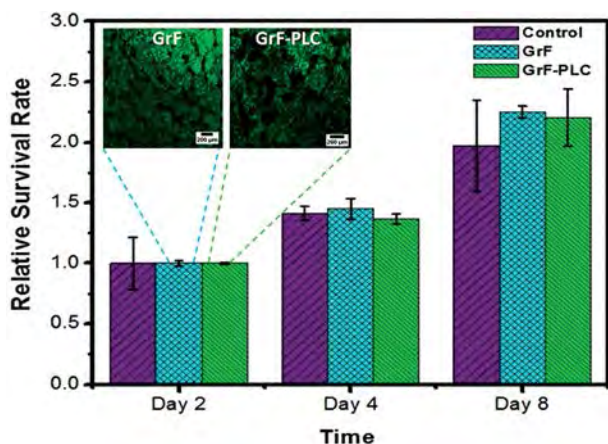


Figure 5. Relative survival of hMSCs in GrF and GrF-PLC scaffolds in comparison to hMSCs grown in a monolayer within a cell culture flask. Proliferation of hMSCs in the two scaffold environments was comparable to standard cell culture methods after 8 days of assessment. Insets show live-dead staining of hMSCs seeded on GrF and GrF-PLC scaffolds after 2 days, green indicates live cells, hardly any red dye (dead cells) is observed on either sample. One way ANOVA tests indicate no significant differences ($p > 0.05$) in survival rate among the GrF and GrF-PLC scaffolds or the control environment.

hybrid structure. The excellent wettability leads to the formation of a high strength interface with the foam which allows loads to be effectively transferred to the PLC bridges.

2.3. Cellular Studies

In order to validate the efficacy of the GrF-PLC for cartilage tissue engineering purposes, cellular studies are conducted using hMSCs. Previous efforts have demonstrated suitability of 3-D graphene foam for the culture of NSCs.^[25,33] Here we first evaluate the survivability of hMSCs on the pure graphene foam and then assess the effect of adding the biocompatible copolymer PLC. Results of survivability of the hMSCs over a period of 8 days are shown in **Figure 5**. The results are normalized relative to the second day, where a value of 1.0 indicates that all cells have successfully survived in their new environment – either the graphene foam or the GrF-PLC scaffold. The results indicate that hMSCs survive on both the graphene foam and GrF-PLC scaffold just as they would in a controlled cell culture environment. The insets of **Figure 5** show the “live-dead” staining of the cells (mitochondrial imaging is provided in Supporting Information, **Figure S5**), where the green dye indicates cells are alive, no red stains are observed as all cells have survived in both the graphene foam and GrF-PLC scaffold. Survival rate values for days 4 and 8 are above 1.0, this indicates that the cells not only survive but they have proliferated—i.e., they have grown and reproduced. It can be seen that for all days cells survive and proliferate to statistically equivalent ($F = 1$, $p > 0.05$) levels in both the GrF/GrF-PLC scaffold environments and the cell culture.

Imaging of the hMSCs in the graphene foam and GrF-PLC hybrid was conducted using SEM and fluorescence microscopy in order to assess any differences in cell growth due to

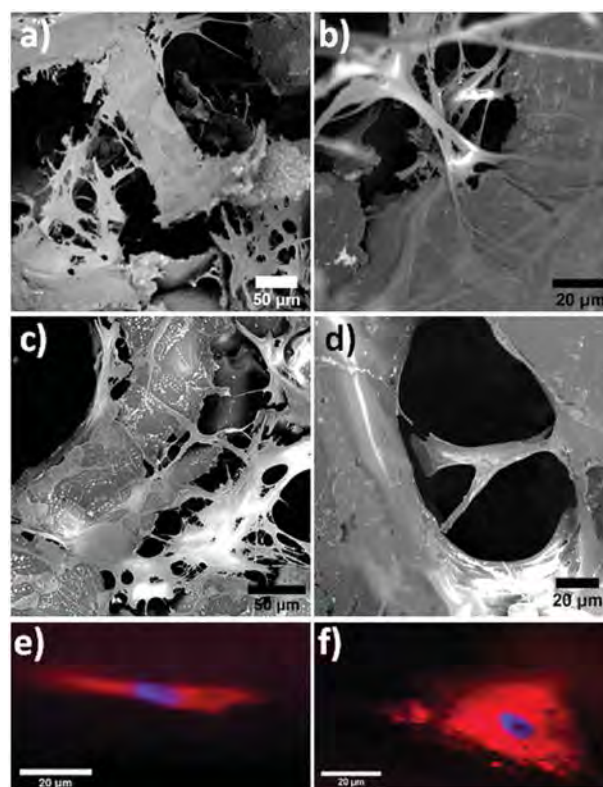


Figure 6. a,b) SEM images of graphene foam scaffold with human mesenchymal stem cells (hMSCs). c,d) SEM images of graphene foam-PLC hybrid scaffold with human mesenchymal stem cells (hMSCs). e) Fluorescence microscopy image of stem cells on graphene foam, cells appear severely stretched and thinned due to the graphene foam yielding under the cell induced stresses. f) Fluorescence microscopy images of stem cells on graphene foam-PLC scaffold, cells have a larger and more rounded morphology indicating normal growth.

the variations in scaffold composition and mechanical strength. **Figure 6** presents SEM and fluorescence images of the hMSCs in the graphene foam and GrF-PLC scaffolds after 28 days of growth in the stem cell media. The SEM images of hMSCs are comparable to those observed growing on high surface area micro-objects by Leferink et al.^[55] The long strands seen in the images in **Figure 6** are the hMSC cells; it can be seen that hMSCs grow in all directions, forming bridges across pores in the GrF and GrF-PLC structures. The porous networked structure is desirable for providing the cells an environment closer to that experienced *in vivo*, hence it is critical that cells do indeed grow through pores and form 3-D networks of cells during growth. Smaller spherical objects observed in the SEM images, also seen by Leferink et al.,^[55] are believed to be products of the formation of ECM material; the presence of ECM indicates that the stem cells are metabolically active.

Fluorescence images in **Figure 6d,e** highlight the nucleus of individual stem cells in blue, and the surrounding cell plasma membrane in red. It can be seen that the nucleus and plasma membrane of the stem cells grown on GrF exhibit a highly elongated morphology as compared to those grown in the GrF-PLC scaffold. The hMSCs on the graphene foam become stretched and thinned likely because the foam is mechanically yielding.

As the cells adhere and grow onto the foam they induce strains on the foam, much the same way as substrates are strained during deposition of thin films and thermal spray coatings. The foam walls are not constrained as a substrate would be and the adhesion between cells and the foam is strong so that rather than debonding, the cell-induced tensile strains cause the graphene foam to become deformed. This causes the cells to be stretched and grow along the deformed foam. Signs of damage in the graphene foam can be seen in Figure 6a,b, the graphene foam has many jagged edges caused by mechanical deformation. The GrF-PLC scaffold in contrast was shown to have superior mechanical strength and hence it is able to support the cells without undergoing deformation, SEM images in Figure 6c,d show that the GrF-PLC scaffold retains a smooth morphology in the scaffold walls. The high strength GrF-PLC scaffold therefore provides a suitable structure for hMSCs to undergo normal growth.

2.4. Differentiation

Stem cells are pluripotent; hence the demonstration of feasibility of effective cell seeding and subsequent differentiation of hMSCs makes the GrF-PLC scaffold a potential candidate for many tissue engineering applications. As stated before, the GrF-PLC scaffold has several advantageous properties in particular, for musculoskeletal tissue engineering applications such as a lubricating surface, high surface area, and efficient energy dissipation. The hMSCs on the GrF and GrF-PLC scaffolds were cultured in a chondrogenic media for 28 days in order to induce differentiation into chondrocytes—the building blocks of cartilage tissue. Cartilage tissue can be characterized by the expression of type II collagen and aggrecan ECM protein. Analysis of the relative amounts of collagen and aggrecan in the samples after 28 days of culturing are done using immunostaining and subsequent quantification of the resulting stain intensities (Figure 7).

The presence of both aggrecan and type II collagen positive staining is seen throughout the graphene foam and GrF-PLC

scaffold, thus indicating the successful differentiation of hMSCs into chondrocytes. Of particular importance, are the relative ratios of aggrecan to collagen present in the samples. Aggrecan is known to be a primary load-bearing component of cartilage ECM, hence making its presence critical for load bearing systems such as the human knee.^[56–58] In healthy adult cartilage, the synthesis and degradation of aggrecan and other components of the cartilage ECM is self-regulated to ensure the proper balance needed for functionality.^[57] Figure 7e shows that the ratio of aggrecan to collagen is higher in the pure graphene foam as compared to the GrF-PLC scaffold. It was seen that the pure graphene foam had less mechanical strength than the GrF-PLC scaffold. This results in the graphene foam undergoing deformation as *de novo* tissue grows, that initiates relatively larger transfer of loads onto the hMSCs. This constrains the cells into a compressed state which alters their shape by stretching and thinning (Figure 6e). The altered morphology subsequently initiates a cascade of cell signaling events to promote overproduction of Aggrecan ECM protein by hMSCs. It is important to note here that a major function of aggrecan is indeed to resist loads in compression.^[59]

On the other hand, the GrF-PLC foam retains a more dilated hMSC structure (Figure 6f) which serves to reduce hMSC-derived aggrecan synthesis. At 28 day post-culture, the engineered tissues are primarily supported by the GrF-PLC scaffold with minimal loads transferred onto the cells. Thus, in contrast to the graphene foam alone, in the GrF-PLC hybrids, resistance to loading via overproduction of hMSC-derived aggrecan is not necessary since the scaffold bears the bulk of the loading. We note however that despite lower levels of aggrecan, cells within the GrF-PLC-seeded samples were found to be healthy (Figure 5) and exhibited relatively robust expression of type II collagen and negligible expression of type I collagen (Figure 7e) demonstrating support for the articular cartilage phenotype.

Evidence of positive collagen type II staining was evident in both the hMSC-seeded graphene-only foam (Figure 7b) and hMSC-seeded graphene foam-PLC composite scaffolds (Figure 7d). The intensity of staining was found to be slightly higher in the graphene foam-PLC hybrid as compared to the

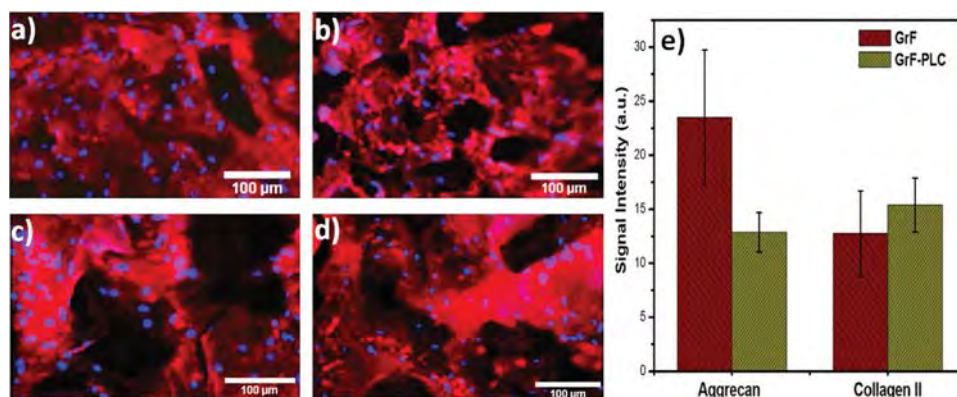


Figure 7. a) Aggrecan immunostaining on graphene foam scaffold. b) Type II collagen immunostaining on graphene foam scaffold. c) Aggrecan immunostaining on graphene foam-PLC hybrid scaffold. d) Type II collagen immunostaining on graphene foam-PLC hybrid scaffold. e) Signal intensities of aggrecan and type II collagen taken from various sample sites on graphene foam and graphene foam-PLC hybrid scaffolds. HMSCs can be seen to have successfully differentiated in the chondrogenic media. T-tests indicate statistically significant differences in aggrecan ($p < 0.05$) but not in type II collagen ($p > 0.05$). Type I collagen expression was found to be negligible in both groups.

graphene foam counterpart but the difference was not significant ($p > 0.05$). Nonetheless, the robust positive staining of collagen II in combination with the demonstrated aggrecan synthesis by the samples (Figure 7a,c) provides evidence that both scaffold groups (hMSC-seeded graphene-only foam and hMSC-seeded graphene foam-PLC composite) continue to support hMSC differentiation along a healthy chondrogenic signaling pathway. Specifically, the chondrogenic media that was utilized while proprietary, is likely to have contained sufficient concentration of the critical cytokine, transforming growth factor-beta 1 (TGF- β 1), for inducing differentiation of hMSCs to chondrocytes within the in vitro cultured, graphene-based scaffold environments.^[60] This being the case, we believe that the signaling pathway for hMSC differentiation is TGF- β 1-mediated. It is well-known that the TGF- β 1 pathway initiates via its receptor linkage with the activin-like kinase 1 (ALK 1) transmembrane protein; following this, activation of the intracellular Smad 2–3 signaling molecule occurs, which in turn leads to the promotion of the articular cartilage phenotype.^[61]

3. Conclusions

A high strength biocompatible scaffold is synthesized by dipping a graphene foam into a liquid solution of the copolymer PLC. The excellent wettability of PLC on graphene foam enables the PLC to form a thin uniform coating over the graphene foam. The high wettability allows the PLC to fill voids and defects present in the graphene foam. The healing of defects in conjunction with the formation of PLC bridges leads to enhanced strength and ductility in the GrF-PLC scaffold. Nanoindentation and macroscale tensile testing shows the increase in strength in both compression and tension at multiple scales. The effectiveness of PLC bridges bearing load is observed directly via in situ tensile testing in an SEM.

Cellular studies conducted on both graphene foam and GrF-PLC scaffolds demonstrate the ability of hMSCs to survive and proliferate throughout both scaffolds. The higher strength of the GrF-PLC scaffold enables the hMSCs to grow normally without undergoing large deformations. The pure graphene foam does not have sufficient strength to withstand cell-induced strains and leads to hMSCs growing with a highly elongated morphology (Figure 6e). The change in cell shape causes aggrecan ECM protein overproduction. By contrast, the cells within the GrF-PLC specimens retain their unconstrained shape (Figure 6f). Subsequently significantly lower ($p < 0.05$) aggrecan content in the GrF-PLC specimens is found compared to its graphene foam-alone counterparts. However, cells within the hybrid material are still able to express slightly higher levels of type II collagen and negligible levels of type I collagen, thereby indicating that GrF-PLC scaffolds permit chondrogenesis of hMSCs (Figure 7e). Since cartilage is load bearing and its ECM constituents are self-regulated, it may be important for the scaffold material to bear the bulk of the loads from the de novo tissues. This is so that in situ cellular proliferation and migration as well as ECM deposition can occur in timescales mimicking normal developmental processes, while cellular overproduction of matrix components is avoided. As mentioned earlier, adequate cell distribution and ECM layering

within the treatment space is critical to long-term success. We demonstrate here that GrF-PLC has the ability to serve as a principal support structure for hMSC-derived engineered tissues resulting in minimal imposition of loads onto the cells thereby reducing their burden to secrete aggrecan, a primary component of articular cartilage ECM. Thus we conclude that the superior mechanical properties of GrF-PLC scaffolds such as augmented strength and ductility and the ability to support stem cell viability and differentiation make it a suitable candidate for musculoskeletal tissue engineering applications, such as the growth of cartilage ECM.

4. Experimental Section

Materials: The graphene foam used in this study was procured from Graphene Laboratories (Calverton, NY, USA). The graphene foam is synthesized by growing graphene on a nickel foam template. The nickel template is then etched away, leaving behind only a free standing 3D graphene foam structure. The starting copolymer of polylactic acid and poly- ϵ -caprolactone (PLC) in 70:30 molar ratio was procured from Purac Biomaterials (Lincoln, IL, USA). The PLC solution was prepared by mixing 1 g of PLC with 20 mL of acetone in a 50 mL beaker; the mixture was stirred for 20 min using a magnetic stirring. Wetting angles measurements between the graphene foam and either PLC or water were conducted using a DM-CEI Contact Angle Meter (Kyowa Interface Science Co., JAPAN). Each droplet of PLC or water had a volume of approximately 2 μ L. Contact angles were calculated with the aid of Kyowa FAMAS software. Pure graphene foam was then dipped in the PLC solution for a set amount of time; the GrF-PLC scaffold found to have the optimal PLC coating was dipped in PLC of 5 s. The morphology of the GrF-PLC scaffolds was characterized using a FEI PHENOM scanning electron microscope with an operating voltage of 5 kV.

Mechanical Characterization: A TI-900 Triboindenter (Hysitron, Minneapolis, MN, USA) was used to conduct nanoindentation experiments. A 100 μ m radius conospherical tip was used to perform displacement-controlled indentations with a depth of 750 nm. The load cycle consisted of a 10 s ramp to 750 nm, following by a 3 s hold at 750 nm, and finally a 10 s unloading. The elastic modulus of the graphene foam and GrF-PLC scaffold were evaluated using the Oliver–Pharr method.^[62] Tensile testing was performed using an Electroforce 3200 tensile tester (BOSE, Eden Prairie, MN, USA) equipped with a 10 N load cell. The crosshead speed was 0.05 mm s⁻¹ and the maximum displacement was 12 mm. The tensile specimens had dimensions of approximately 16 mm gauge length, 5 mm width, and 200 μ m thickness. In situ tensile testing was performed inside a JEOL JIB-4500 MultiBeam SEM-FIB using an MTI SEM tester1000 microload frame. The crosshead speed used during in situ tests was also 0.05 mm s⁻¹. In situ testing was used for the sole purpose of observing deformation mechanisms under tensile loading.

hMSC Growth and Characterization: Human bone marrow derived mesenchymal stem cells (ScienCell, Carlsbad, CA, USA) were seeded onto Poly D-lysine coated T-75 flasks (Fisher Scientific, Pittsburg, PA, USA). The cells were cultured in the AdvanceSTEM Mesenchymal Stem Cell Expansion Kit (Thermo Scientific, Waltham, WA) until passage three. Cell proliferation on the scaffold samples was determined using the sulforhodamine B (SRB) Viability/Cytotoxicity Assay Kit (Vitro Vivo Biotechnology, Rockville, MD) which is based on the measurement of viable cellular protein colorimetrically. hMSCs were seeded on GrF and GrF-PLC scaffolds of size 5 mm² with a cell density of 105 cells mL⁻¹. They were kept in rotisserie for 24 h and then the samples were transferred in 24 well plates in the fresh stem cell media to allow the cells to expand. SRB assay was performed for day 2, day 4, and day 8 on three samples for each day each time period and results were analyzed. To perform the SRB assay, first the cells were fixed to the bottom of the sample using trichloroacetic acid which acted as the fixative. Then the cells were stained using the SRB dye. The unbounded

dye was removed using 1% acetic acid. The dye bounded to the cellular protein was extracted using 10×10^{-3} M Trizma base and the absorbance was measured at a wavelength of 565 nm in BioTek Plate Reader (Biotek Instruments, Inc., Winooski, Vermont). A Live-Dead assay using Calcein AM/Ethidium homodimer (Life Technologies) staining was applied in order to assess the viability of cells on the scaffolds. In brief, samples from these two groups were stained with Calcein AM and Ethidium homodimer in phosphate buffer saline (PBS) solution and incubated for 30 min. Next, they were washed three times with PBS solution to remove the background fluorescence and subsequently visualized under the fluorescent microscope (Olympus IX81, Olympus IX81, Olympus America Inc., Miami FL) at excitation and emission wavelengths of 468 and 568 nm, respectively. Cell viability was subsequently computed for day 2 by counting cells on the three images of each group (ImageJ software, NIH, Bethesda, MD) and calculating the ratio of live cells (green dots) to the sum of live and dead cells (red dots), results of subsequent days were normalized with respect to day 2 measurements. To study the morphology of HMSC seeded on GrF and GrF-PLC scaffolds, live mitochondrial and nuclear imaging of cells was performed using the Live Mitochondrial and Nuclear Labeling Kit (Invitrogen). The GrF and GrF-PLC scaffold samples seeded with hMSCs were incubated with 200×10^{-9} M MitoTracker Red and 5×10^{-6} M Hoechst dye in media for 15 min at 37 °C. When labeling was completed the excess labeling solution was removed by washing with PBS twice. The samples were observed under fluorescence microscope (Olympus IX 81). Samples with cells were also observed with SEM, cells were fixed with chilled ethanol prior to SEM analysis.

Immunohistochemical Studies: HMSC seeded on GrF and GrF-PLC was allowed to differentiate into chondrocytes by culturing them in chondrogenic media (HyClone AdvanceSTEM Chondrogenic Differentiation Medium, Catalog No. SH3088902, Fisher Scientific, Pittsburgh, PA) for 28 d. After 28 d of culture, the graphene and PLC coated graphene were subjected to immunohistochemical studies to test for the presence of collagen types I and II and aggrecan. Briefly, the samples were removed from the well plate in which they were cultured, washed with PBS, fixed with 10% formalin for 2 h at room temperature, and washed again three times with PBS. All sections were subjected to a 2 mg mL⁻¹ hyaluronidase (Fisher Scientific) treatment for 30 min at 37 °C to enhance the binding of the primary antibodies. Samples were then subjected to antigen retrieval process using sodium citrate buffer (10×10^{-3} M sodium citrate, 0.05% tween 20, pH 6.0) at 950–1000 °C for 3 min. For the samples testing for aggrecan, the sections were reduced with 10×10^{-3} M dithiothreitol in 50×10^{-3} M tris HCl, 200×10^{-3} M sodium chloride, pH 7.4, for 2 h at 37 °C. Then the samples were further alkylated by placing them in 40×10^{-3} M iodoacetic acid in PBS for 1 h at 37 °C. After the alkylation was done, samples were washed in PBS for 5 min. After this, all samples were blocked using 2.5% goat serum (Vector Laboratories) for 1 h at room temperature. Excessive blocking buffer was rinsed with a gentle stream of wash buffer solution (1000 mL of PBS and 0.5 mL of tween 20). After serum blocking, primary antibodies mouse anti-pro-collagen I (SP1.D8), anti-collagen II (CIIC1), and anti-aggrecan link protein (9/30/8-A-4) purchased from the Developmental Studies Hybridoma Bank (University of Iowa, Iowa City, IA) were diluted in 1% goat serum to a concentration of 5 µg mL⁻¹ and were added to the sections and incubated overnight at 4 °C. Sections were then incubated with Goat polyclonal Secondary Antibody to Mouse IgG – H&L Cy3-conjugated (Abcam, Cambridge, MA) diluted to 1/50 to the original concentration of 500 µg at 0.5 mg mL⁻¹ for 45 min at 37 °C. Sections were counter stained with Mounting Media with DAPI (Vector Laboratories, Burlingame, CA) and observed under the fluorescence microscope ((Olympus America, Melville, NY). In order to quantify the level of aggrecan and type II collagen gene expression, images were selected ($n = 4/\text{group}$) and signal intensity measured (ImageJ).

Statistics: Statistical analyses were conducted on cell viability and immunohistochemical studies to assess whether significant trends were present. One way analysis of variance (ANOVA) tests were conducted on the cell survival rates for each time period to access whether there was a statistically significant survival rate between the

GrF scaffold, GrF-PLC scaffold, or control environment for a given time period. F values near 1.0 and $p > 0.05$ indicated differences in survival rate were not significant. T-tests were conducted to access whether there was a statistically significant difference of either aggrecan or type II collagen in the GrF and GrF-PLC scaffolds. A value of $p < 0.05$ was taken to indicate a statistically significant difference in value.

Supporting Information

Supporting Information is available from the Wiley Online Library or from the author.

Acknowledgements

The authors would like to thank Dr. Norman Munroe for extending the use of Contact Angle Meter equipment. The assistance of Mr. Vishal Musaramthota in performing wetting angle experiments is greatly appreciated. The authors acknowledge support from the Advanced Materials Engineering Research Institute (AMERI) at FIU for providing and maintaining electron microscopy facilities.

Received: March 4, 2015

Revised: April 21, 2015

Published online:

- [1] W. Wei, X. Qu, *Small* **2012**, *8*, 2131.
- [2] C. N. R. Rao, A. K. Sood, R. Voggu, K. S. Subrahmanyam, *J. Phys. Chem. Lett.* **2010**, *1*, 572.
- [3] C. Soldano, A. Mahmood, E. Dujardin, *Carbon* **2010**, *48*, 2127.
- [4] W. Choi, I. Lahiri, R. Seelaboyina, Y. S. Kang, *CRC Cr. Rev. Sol. State* **2010**, *35*, 52.
- [5] A. A. Balandin, S. Ghosh, W. Bao, I. Calizo, D. Teweldebrhan, F. Miao, C. N. Lau, *Nano Lett.* **2008**, *8*, 902.
- [6] C. Lee, X. Wei, J. W. Kysar, J. Hone, *Science* **2008**, *321*, 385.
- [7] I. W. Frank, D. M. Tanenbaum, A. M. Van der Zande, P. L. McEuen, *J. Vac. Sci. Technol.* **2007**, *B25*, 2558.
- [8] L. Gong, I. A. Kinloch, R. J. Young, I. Riaz, R. Jalil, K. S. Novoselov, *Adv. Mater.* **2010**, *22*, 2694.
- [9] Q. Lu, M. Arroyo, R. Huang, *J. Phys. D Appl. Phys.* **2009**, *42*, 102002.
- [10] C. Liu, J. Yang, Y. Tang, L. Yin, H. Tang, C. Li, *Colloid Surf. A* **2015**, *468*, 10.
- [11] Y. A. Samad, Y. Li, A. Schiffer, S. M. Alhassan, K. Liao, *Small* **2015**, DOI: 10.1002/sml.201403532.
- [12] Y. S. Moon, D. Kim, G. Lee, S. Y. Hong, K. K. Kim, S. M. Park, J. S. Ha, *Carbon* **2015**, *81*, 29.
- [13] A. Bello, F. Barzegar, D. Momodu, J. Dangbegnon, F. Taghizadeh, M. Fabiane, N. Manyala, *J. Power Sources* **2015**, *273*, 305.
- [14] G. Zhou, L. Li, C. Ma, S. Wang, Y. Shi, N. Koratkar, W. Ren, F. Li, H.-M. Cheng, *Nano Energy* **2015**, *11*, 356.
- [15] X. Zhou, Z. Bai, M. Wu, J. Qiao, Z. Chen, *J. Mater. Chem. A* **2015**, *3*, 3343.
- [16] S. Chabi, C. Peng, Z. Yang, Y. Xia, Y. Zhu, *RSC Adv.* **2015**, *5*, 3999.
- [17] J. Liu, J. Wang, D. Li, F. Xi, J. Wang, E. Wang, *Bio Sens. Bioelectron.* **2015**, *65*, 281.
- [18] R. Xu, Y. Lu, C. Jiang, J. Chen, P. Mao, G. Gao, L. Zhang, S. Wu, *ACS Appl. Mater. Inter.* **2014**, *6*, 13455.
- [19] J. Jia, X. Sun, X. Lin, X. Shen, Y.-W. Mai, J.-K. Kim, *ACS Nano* **2014**, *8*, 5774.
- [20] S.-H. Lee, J.-H. Jung, I.-K. Oh, *Small* **2014**, *10*, 3880.
- [21] Y. Li, J. Chen, L. Huang, C. Li, J.-D. Hong, G. Shi, *Adv. Mater.* **2014**, *26*, 4789.

- [22] Z. Chen, C. Xu, C. Ma, W. Ren, H.-M. Cheng, *Adv. Mater.* **2013**, *25*, 1296.
- [23] W. Chen, Z. Fan, G. Zeng, Z. Lai, *J. Power Sources* **2013**, 225, 251.
- [24] E. Singh, Z. Chen, F. Houshmand, W. Ren, Y. Peles, H.-M. Cheng, N. Koratkar, *Small* **2013**, *9*, 75.
- [25] N. Li, Q. Zhang, S. Gao, Q. Song, R. Huang, L. Wang, L. Liu, J. Dai, M. Tang, G. Cheng, *Sci. Rep.* **2013**, *3*, 1604.
- [26] M. Zhou, T. Lin, F. Huang, Y. Zhong, Z. Wang, Y. Tang, H. Bi, D. Wan, J. Lin, *Adv. Funct. Mater.* **2013**, *23*, 2263.
- [27] X. Dong, X. Wang, L. Wang, H. Song, H. Zhang, W. Huang, P. Chen, *ACS Appl. Mater. Inter.* **2012**, *4*, 3129.
- [28] X. Cao, Y. Shi, W. Shi, G. Lu, X. Huang, Q. Yan, Q. Zhang, H. Zhang, *Small* **2011**, *7*, 3163.
- [29] F. Yavari, Z. Chen, A. V. Thomas, W. Ren, H.-M. Cheng, N. Koratkar, *Sci. Rep.* **2011**, *1*, 166.
- [30] T. R. Nayak, H. Andersen, V. S. Makam, C. Khaw, S. Bae, X. Xiangfan, P.-L. R. Ee, J.-H. Ahn, B. H. Hong, G. Pastorin, B. Ozyilmaz, *ACS Nano* **2011**, *5*, 4670.
- [31] S. Y. Park, J. Park, S. H. Sim, M. G. Sung, K. S. Kim, B. H. Hong, S. Hong, *Adv. Mater.* **2011**, *23*, H263.
- [32] Y. Wang, W. C. Lee, K. K. Manga, P. K. Ang, J. Lu, Y. P. Liu, C. T. Lim, K. P. Loh, *Adv. Mater.* **2012**, *24*, 4285.
- [33] Q. Song, Z. Jiang, N. Li, P. Liu, L. Liu, M. Tang, G. Cheng, *Biomaterials* **2014**, *35*, 6930.
- [34] Z. Chen, W. Ren, L. Gao, B. Liu, S. Pei, H.-M. Cheng, *Nat. Mater.* **2011**, *10*, 424.
- [35] H.-B. Zhang, Q. Yan, W.-G. Zheng, H. Zhixian, Z.-Z. Yu, *ACS Appl. Mater. Inter.* **2011**, *3*, 918.
- [36] Y. Zhao, J. Liu, Y. Hu, H. Cheng, C. Hu, C. Jiang, L. Jiang, A. Cao, L. Qu, *Adv. Mater.* **2013**, *25*, 591.
- [37] C. Wu, X. Huang, X. Wu, R. Qian, P. Jiang, *Adv. Mater.* **2013**, *25*, 5658.
- [38] I.-C. Liao, F. T. Moutos, B. T. Estes, X. Zhao, F. Guilak, *Adv. Funct. Mater.* **2013**, *23*, 5833.
- [39] A. Nieto, D. Lahiri, A. Agarwal, *Mater. Sci. Eng. A-Struct.* **2013**, 582, 338.
- [40] Z. Xu, X. Shi, W. Zhai, J. Yao, S. Song, Q. Zhang, *Carbon* **2014**, *67*, 168.
- [41] T. Ramanathan, A. A. Abdala, S. Stankovich, D. A. Dikin, M. Herrera-Alonso, R. D. Piner, D. H. Adamson, H. C. Schniepp, X. Chen, R. S. Ruoff, S. T. Nguyen, I. A. Aksay, R. K. Prud'Homme, L. C. Brinson, *Nat. Nanotechnol.* **2008**, *3*, 327.
- [42] M. A. Rafiee, J. Rafiee, Z. Wang, H. Song, Z. Z. Yu, N. Koratkar, *ACS Nano* **2009**, *3*, 3884.
- [43] D. Lahiri, S. Das, W. Choi, A. Agarwal, *ACS Nano* **2012**, *6*, 3992.
- [44] A. Nieto, D. Lahiri, A. Agarwal, *Scr. Mater.* **2013**, *69*, 678.
- [45] M. Belmonte, C. Ramirez, J. Gonzalez-Julian, J. Schneider, P. Miranzo, M. I. Osendi, *Carbon* **2013**, *61*, 431.
- [46] L. Wang, W. Ma, R. A. Gross, S. P. McCarthy, *Polym. Degrad. Stabil.* **1998**, *59*, 161.
- [47] R. Dua, J. Centeno, S. Ramaswamy, *J. Biomed. Mater. Res. B* **2014**, *102*, 922.
- [48] N. T. Khanarian, J. Jiang, L. Q. Wan, V. C. Mow, H. H. Lu, *Tissue Eng. Pt. A* **2012**, *18*, 533.
- [49] S. Ramaswamy, M. C. Uluer, S. Leen, P. Bajaj, K. W. Fishbein, R. G. Spencer, *Tissue Eng. Pt. C-Meth* **2008**, *14*, 243.
- [50] D. A. Wang, C. G. Williams, Q. Li, B. Sharma, J. H. Elisseeff, *Biomaterials* **2003**, *24*, 3969.
- [51] C. G. Williams, T. K. Kim, A. Taboas, A. Malik, P. Manson, J. Elisseeff, *Tissue Eng.* **2003**, *9*, 679.
- [52] A. Nieto, B. Boesl, A. Agarwal, *Carbon* **2015**, *85*, 299.
- [53] L. J. Gibson, M. F. Ashby, in *Cellular Solids – Structures and Properties* (Eds. D. R. Clark, S. Suresh, I. M. Ward), Cambridge University Press, Cambridge, UK **1997**, pp 175–281.
- [54] D. Lahiri, F. Rouzaud, T. Richard, A. K. Keshri, S. R. Bakshi, L. Kos, A. Agarwal, *Acta Biomater.* **2010**, *6*, 3524.
- [55] A. Leferink, D. Schipper, E. Arts, E. Vrij, N. Rivron, M. Karperien, K. Mittmann, C. Van Blitterswijk, L. Moloni, R. Truckenmuller, *Adv. Mater.* **2014**, *26*, 2562.
- [56] C. Kiani, L. Chen, Y. J. Wu, A. J. Yee, B. B. Yang, *Cell Res.* **2002**, *12*, 19.
- [57] J. R. Matyas, P. F. Ehlers, D. Huang, M. E. Adams, *Arthritis Rheum.* **1999**, *42*, 993.
- [58] S. Roberts, J. Menage, L. J. Sandell, E. H. Evans, J. B. Richardson, *Knee* **2009**, *16*, 398.
- [59] P. Roughley, D. Martens, J. Rantakokko, M. Alini, F. Mwale, J. Antoniou, *Eur. Cell. Mater.* **2006**, *11*, 1.
- [60] L. A. Solchaga, K. J. Penick, J. F. Welter, *Mol. Bio.* **2011**, *698*, 253.
- [61] E. Mariani, L. Pulsatelli, A. Facchini, *Int. J. Mol. Sci.* **2014**, *15*, 8667.
- [62] W. C. Oliver, G. M. Pharr, *J. Mater. Res.* **1992**, *7*, 1564.

Available at www.sciencedirect.com

ScienceDirect

journal homepage: www.elsevier.com/locate/carbon

Multi-scale intrinsic deformation mechanisms of 3D graphene foam

Andy Nieto ^{a,b}, Benjamin Boesl ^a, Arvind Agarwal ^{a,*}

^a Nanomechanics and Nanotribology Laboratory, Department of Mechanical and Materials Engineering, Florida International University, 10555 West Flagler Street, EC 3464, Miami, FL 33174, USA

^b Department of Chemical Engineering and Materials Science, University of California Davis, One Shields Ave, Davis, CA 95616, USA

ARTICLE INFO

Article history:

Received 22 October 2014

Accepted 3 January 2015

Available online 9 January 2015

ABSTRACT

The mechanical properties and multi-scale deformation mechanisms of a freestanding 3D graphene foam are evaluated for the first time. Nanoindentation is used to evaluate the nanoscale properties in compression whereas *in situ* tensile testing inside scanning electron microscope (SEM) is used to evaluate the tensile properties of the bulk foam. Nano-compression results show that the hardness (19.9–26.1 kPa) and elastic modulus (1.2–1.5 MPa) of the foam are relatively low. The deformation mechanisms in compression are graphene branch bending and branch wall elastic depression, which do not utilize the exceptionally high in-plane mechanical properties of graphene. The elastic modulus (69.9 GPa) during tensile loading is found to be four orders of magnitude higher owing to graphene branch alignment which enables branches to bear load along the high strength in-plane direction of graphene. *In situ* SEM tensile testing of free standing 3D graphene foam supports the proposed mechanisms and reveals that the ductile graphene branches gradually become aligned by rotating at rates of $\sim 0.59^\circ/\text{s}$, while the brittle node junctions become aligned abruptly at rates of $\sim 3.08^\circ/\text{s}$. It is observed that due to defects such as cracked branches and discontinuous graphene sheets, only a fraction of graphene branches bear significant loads.

© 2015 Elsevier Ltd. All rights reserved.

1. Introduction

Graphene is a single layer of sp^2 bonded carbon atoms which has been found to have excellent thermal [1,2], electrical [1,3,4], and mechanical properties [1,4,5–8]. This combination of properties has led to graphene being incorporated into nearly every major area of materials science with potential applications in the electronics [1,3,4,9], aerospace [10–14], automotive [14–16], and biomedical industries [17,18]. While many electronics applications can utilize graphene as a free-standing layer or coating, several other applications utilize graphene as a filler or reinforcement for a composite material.

Graphene has been utilized as reinforcement for polymer, metal, and ceramic based composites in order to yield improvements in electrical [19,20] and thermal conductivity [21,22], fracture strength [23,24], toughness [10–12,25], and wear resistance [15,16,26]. One of the most significant impediments to graphene-based composites is the effective dispersion of graphene in the matrix. Homogeneous dispersion is a prerequisite to having a composite material with excellent properties and consistency.

The recent advent of graphene based 3D foam structure [27–36] provides a potential solution for the effective and uniform dispersion of graphene, especially in polymer matrices.

* Corresponding author. Fax: +1 305 348 1932.

E-mail address: agarwala@fiu.edu (A. Agarwal).

<http://dx.doi.org/10.1016/j.carbon.2015.01.003>

0008-6223/© 2015 Elsevier Ltd. All rights reserved.

The foam structure provides an interconnected 3D structure of graphene thus eliminating the need for more expensive and/or ineffective dispersion methods. The porous and interconnected nature of 3D graphene foams also opens up opportunities in applications such as biomedical scaffolds [30], electromagnetic (EMI) shielding [27,37,38], lightweight flexible supercapacitors [39–42] and thermal energy storage [31]. Applications such as EMI shielding require a high enough content of carbon nano-fillers to reach percolation for electrical conductivity however this often leads to agglomerates which deteriorate mechanical properties [27]. An interconnected graphene foam could provide the needed improvement in electrical conductivity without introducing agglomeration. The high thermal conductivity and porous structure also would allow it to serve as a heat sink for electronic devices or as a conductive reservoir for materials used to store thermal energy [31].

The effective use and implementation of graphene foams as either free standing structures or as composite material fillers requires knowledge of their intrinsic mechanical properties at multiple scale lengths. Few studies have evaluated the mechanical properties of polymer based graphene foam composites [37,43–48], however, to date no work has been published on the mechanical properties and intrinsic deformation mechanisms of graphene foams. Graphene is known to have very high elastic moduli (~ 1 TPa) [6] and yield strength (~ 130 GPa) [5], however its 2D sheet-like nature makes the utilization of these properties challenging. The properties of foam structures are heavily dependent on the foam wall properties and will vary in tension and compression. In this study we evaluate the mechanical properties in both tension and compression of 3D graphene foam at nano and macro scales. Nano-indentation is used to evaluate compression properties of the graphene branches and nodes which make up the foam walls. Uniaxial tensile testing is used to evaluate the macro scale properties of the foam. *In situ* SEM observations of the tensile tests are used to elucidate the deformation mechanisms of the 3D graphene foam in real time.

2. Materials and methods

The 3D graphene foam used in this study was procured from Graphene Laboratories (Calverton, NY, USA). The graphene foam is made by first preparing a nickel foam structure on which graphene is grown onto by chemical vapor deposition (CVD). The nickel foam substrate is then dissolved away leaving behind only a freestanding graphene foam structure.

2.1. Structural characterization

A helium gas pycnometer (Accupyc 1340, Micrometrics Instrument Corporation, Norcross, GA, USA) was used to measure the true density of the graphene foam walls. The bulk graphene foam density was calculated geometrically. The microstructure of the 3D graphene foam is characterized using a JEOL-JIB 4500 MultiBeam scanning electron microscope – focused ion beam (SEM-FIB) using an operating voltage of 30 keV. Image J software is used to analyze the SEM micrographs and measure the pore sizes and wall thickness

of the graphene foams. Micro-Raman spectroscopy analysis was conducted using a Spectra Physics (Model 3900S, California, USA) with Ti-sapphire crystal as the target (514 nm), a laser power of 18 mW and a detector with 4 cm^{-1} spectral resolution from Kaiser Optical Systems, Inc. (Michigan, USA).

2.2. Nano-indentation

Nano-indentation experiments were performed using a TI-900 Triboindenter (Hysitron Inc., Minneapolis, MN, USA) using either a $100\text{ }\mu\text{m}$ radius conospherical tip or a $10\text{ }\mu\text{m}$ diameter flat punch tip. The triboindenter was used in quasi-static indentation mode with a displacement controlled load function. When using the conospherical tip, the loading cycle consisted of a 10 s ramp to a displacement of 750 nm, a 3 s hold at 750 nm, and a 10 s unloading. The flat punch loading cycle was the same except the maximum displacement being held at 500 nm, the lower value was necessary as the drift rate when using the flat punch tip was higher. The elastic modulus was calculated from the indentation unloading curves using the Oliver–Pharr method [49].

2.3. Tensile testing

Tensile testing on the graphene foam was performed using an Electroforce 3200 tensile tester (BOSE Corporation, Eden Prairie, Minnesota, USA) equipped with a 10 N load cell. The crosshead speed was 0.005 mm/s and the maximum crosshead displacement was 12 mm. The nine samples tested had approximate dimensions of 16 mm gauge length, 5 mm width, and a thickness of $200\text{ }\mu\text{m}$. *In situ* SEM tensile testing was performed inside a JEOL JIB 4500 MultiBeam SEM-FIB using a MTI Instruments SEM 1000 micro-tensile stage. Specimens were prepared using a razorblade and cut to a size of 40 mm by 8 mm and were secured using stainless steel flat wedges. Testing was performed at an approximate pressure of $8.0 \times 10^{-4}\text{ Pa}$. Samples were loaded at a constant rate of $10\text{ }\mu\text{m/min}$ during testing and displacement was measured at the crosshead using a glass extensometer. An accelerating voltage of 30 kV was used during imaging at a scanning rate of 0.15/s. Videos were recorded at a frame rate of 30 frames/s, with still images captured from the video recording.

3. Results and discussion

3.1. Microstructural characterization

The 3D graphene foam investigated in this study, obtained commercially (Graphene Laboratories, Calverton, NY, USA), is shown in Fig. 1. Fig. 1a shows how the graphene foam consists of interconnected graphene branches which form macro-scale pores. Interconnected graphene branches are made up of several layers of graphene with an open porosity between the branches. This allowed for the true density (ρ_s) of the foam walls to be measured using a helium pycnometer. The wall density was found to be 2.27 g/cm^3 and the bulk density (ρ_f) of the foam was calculated geometrically to be 0.005 g/cm^3 . The relative density (ρ_f/ρ_s) of the graphene foam is calculated to be 0.002. High magnification SEM micrographs in

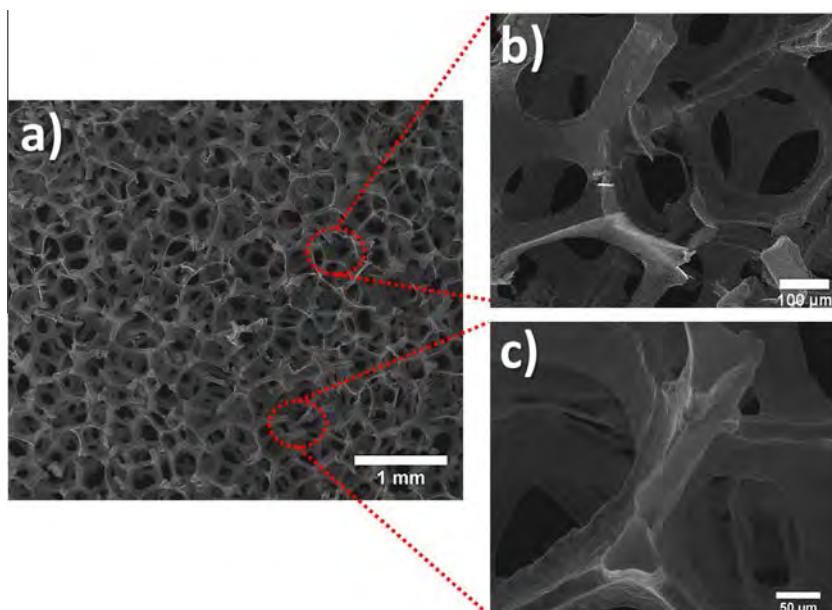


Fig. 1 – (a) Low mag SEM image showing interconnected 3D graphene networks, (b) higher mag SEM image showing typical pore size and (c) SEM image showing cross section of graphene foam walls. (A color version of this figure can be viewed online.)

Fig. 1b and c allow for quantification of the basic foam characteristics. The typical sizes of the foam pores are found to be 100–200 μm in diameter. The thickness of the graphene walls is typically 50–80 μm . The walls thicken significantly when several graphene branches meet as shown in Fig. 1c; throughout this paper the junctions between branches will be referred to as nodes. Fig. 1c provides a cross section of the graphene nodes and it can be seen that the walls are indeed dense. The cross section view also confirms that branches can be in-plane or out-of-plane in any given node, this enables the foam to have a 3D interconnected structure and not merely a collection of 2D graphene films.

Micro Raman spectroscopy was performed on the graphene foam in order to access the level of defects and the number of graphene layers present in the graphene sheets. The micro-Raman spectrum of the graphene foam is presented in Fig. 2. The defects in a graphene structure can be gauged by the I_D/I_G ratio of the Raman spectrum. A high intensity D peak relative to the G peak indicates a high presence of defects and is therefore reflected by a high I_D/I_G ratio [50–52]. Raman spectrum of the graphene foam shows a very low I_D/I_G ratio (~ 0.07) which indicates that the graphene sheets that make up the foam branches are largely defect free. The I_{2D}/I_G and the location of the 2D peak can be used to estimate the number of graphene layers in the graphene sheets. The I_{2D}/I_G of the graphene foam is 1.01, a ratio below one is typically indicative of a graphite-like structure [50–52]. Several recent studies [30–32,45,53,54] however report graphene foam structures consisting of few layer (~ 3 –10) graphene layers with I_{2D}/I_G ratios of ~ 1 or lower.

Studies by Chen et al. [45] and Zhou et al. [31] confirm the number of layers by HRTEM. The 2D peak position of single layer graphene is typically 2700 cm^{-1} [50], this peak shifts in the positive direction with an increasing amount of graphene

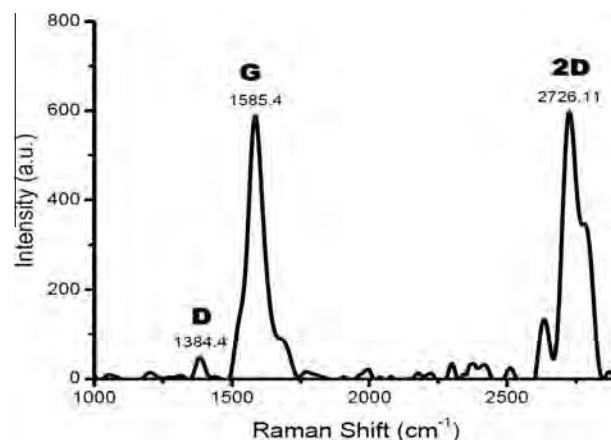


Fig. 2 – Raman spectrum of graphene foam showing peaks characteristic of graphene. Low I_D/I_G ratio suggests as received graphene foam has only minimal defects.

layers [50–52]. The 2D peak of the graphene foam in this study is 2726.1 cm^{-1} , this is comparable to the peak position of the graphene foam used by Chae et al. [53] which consisted of ~ 8 –10 graphene layers. These results indicate that the foam used in this study also consists of multi-layer graphene. It is emphasized that the number of graphene layers in a foam structure refers to the individual graphene sheets or platelets that make up the foam walls – branches could be made up of several hundred graphene sheets or platelets.

3.2. Nanoscale compression properties

Nanoscale compression properties of the foam are evaluated through nanoindentation in order to obtain the intrinsic properties of the foam walls which constitute the foam

structure. Nanoindentation is performed using a 10 μm flat punch tip and a 100 μm radius conospherical tip. Indentation using low stress concentration factor tips approximates compression in the regions being indented; with the conospherical tip providing a slightly higher stress concentration factor. The indentation depth using the flat punch and conospherical tips was 500 nm and 750 nm, respectively. This variation was due to a higher drift rate when using the flat punch tip which results in a lower range of indenter movement. The indentations are performed on both nodes and branches of the graphene foam; a typical indent location is shown in Fig. 3a. No significant property change was observed from branches to nodes.

Characteristic indentations done using the 10 μm flat punch and 100 μm conospherical tip are provided in Fig. 3b and c, respectively. The spikes in loading at the onset of indentation are due to adhesion of out of plane graphene sheets with the indenter prior to the indenter reaching the in-focus branch or node. Out of plane graphene sheets are the result of defect sites where graphene sheets peel off from the graphene branches/nodes. As the indenter continues, these out of plane graphene sheets yield and the load decreases until contact is made with the foam wall. These spikes are more prominent when using the larger 100 μm conospherical tip as it provides a larger area for adhesive forces. The elastic moduli and nanohardness obtained from the load–displacement curves is provided in Table 1. It can be seen that the indentations using the 100 μm conospherical tip yield higher values than indentations done with the 10 μm flat punch for both elastic modulus and nanohardness.

The mechanisms behind this deviation in properties are deduced from the load–displacement curves and presented

schematically in Fig. 4. Indentation using both the flat punch tip and conospherical tip proceed through stage 1; the only variation in behavior at this stage consists of an increased interaction of out of plane graphene sheets with the conospherical tip because of the larger size of the tip. The 3D structure of the graphene foams makes pure compression of a graphene wall impossible without constricting the foam branches – a condition that can't hold through in freestanding graphene foams. The second stage of indentation instead consists of the branches bending as the load is increased; deformation of the actual walls at this stage is minimal or negligible. Once a critical stress is reached, stage 3 is initiated and deformation occurs primarily through indentation and depression of the foam walls, the bending of the branches becomes secondary here. The initiation of stage 3 can be identified in the load displacement curve when using the conospherical tip as the loading slope rises dramatically at an indentation depth of ~ 650 nm. After the tip has indented the graphene wall for ~ 30 –40 nm, the stress required for continued depression of the branch wall increases and the indentation reaches stage 4 where branch bending returns as the primary deformation mechanism. The change in loading slope is absent when using the flat punch tip because the lower stress concentration factor tip doesn't provide a sufficient stress to initiate significant foam wall depression and instead the load continues to be transferred to the supporting branches.

Properties of the foam and the walls can be related by the simple volume-fraction relation given in Eq. (1), where E denotes the property of the foam structure and the constant C_1 is obtained by fitting data on polymer, metal, and ceramic foam structures [55].

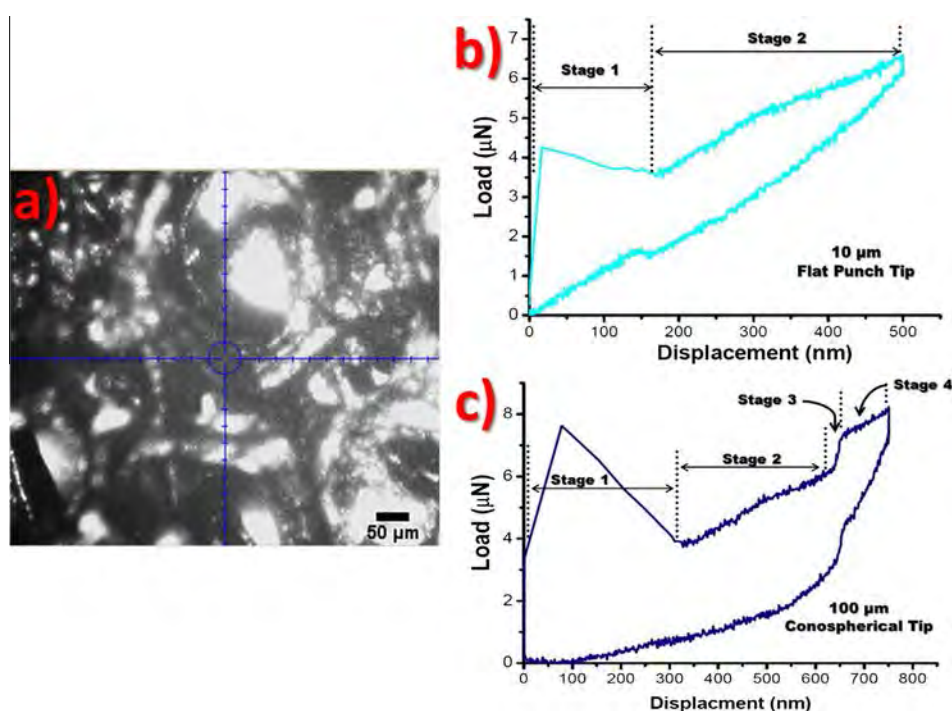


Fig. 3 – (a) Location of indent location is indicated by crosshairs, indents were typically done on solid nodes or branches, (b) typical nanoindentation curves obtained from tests using the 10 μm flat punch and (c) typical nanoindentation curved obtained from curved using the 100 μm conospherical tip. (A color version of this figure can be viewed online.)

Table 1 – Summary of graphene foam mechanical properties in compression and tension.

Experimental method	Elastic modulus (MPa)	Hardness (kPa)	Bulk foam properties (calculated by Eq. (1)) (Pa)
Compression			
Nanoindentation using 10 μm flat punch	1.2 + 0.3	19.9 + 2.0	6.0 + 1.4
Nanoindentation using 100 μm conospherical	1.5 + 0.3	26.1 + 4.6	7.3 + 1.6
Experimental method	Elastic modulus (kPa)	Ultimate tensile strength (UTS) (kPa)	Foam wall properties (calculated by Eq. (1)) (GPa)
Tension			
Tensile testing	339.0 + 81.9	4.8 + 1.7	69.9 + 16.9

$$\frac{E_w}{E_s} = C_1 \left(\frac{\rho_w}{\rho_s} \right)^2; C_1 = 1 \quad (1)$$

This relation is valid in compression and tension and therefore information of the wall property can be related to that of the foam and vice versa. The relative density (ρ_w/ρ_s) was measured previously to be .002 and the elastic moduli of the wall in compression (E_s) are known from nanoindentation, thereby enabling the calculation of the compression elastic modulus of the bulk freestanding graphene foam. These values are provided in Table 1 using values obtained with both the flat punch and the conospherical tip. These values are very low but are to be expected in a freestanding graphene foam structure where the primary deformation mechanism in compression consists of branch bending. Graphene sheets and platelets are very flexible due to the weak van der waal forces between layers that enable graphene layers to slide easily. The indentation of graphene platelets/sheets provides slightly higher resistant to deformation, however neither branch bending or platelet indentation utilizes the excellent in-plane strength of graphene thus resulting in low mechanical properties of the graphene foam in compression.

3.3. Macro-scale tensile properties

Measurement of tensile properties of the 3D graphene foam is done at the macroscale using conventional tensile testing. Information on the graphene foam walls can be extracted from bulk foam properties using Eq. (1). A typical graphene foam sample used for tensile testing is shown in Fig. 5a during the final stages of failure. A typical stress–strain curve obtained during tensile testing is provided in Fig. 5b, elastic modulus and ultimate tensile strength (UTS) are extracted from these curves and are provided in Table 1. Several peaks and valleys are seen in the stress–strain curve and these unique features can begin to be understood from the image of the foam during failure in Fig. 5a. It can be seen that the fracture occurs at the 45° plane where maximum stress, in the form of shear stress, is experienced. This confirms that the freestanding graphene foam has the required structural integrity to transfer forces throughout the foam and act as a bulk networked reinforcement structure for matrices.

The bulk graphene foam however has unique deformation mechanisms, as can be seen in the final stages of fracture in

Fig. 5a. Several strands of graphene foam can be seen where the tensile sample has fractured and the remaining unfractured section appears to be held together by only 2–3 foam branches. *In situ* SEM tensile testing is utilized to investigate the deformation mechanisms of the graphene foam during tension in real time. As is common in foam structures [55], during the early stages of deformation the graphene foam walls tend to become aligned toward the direction of the tensile force as shown in Fig. 6 and Supplementary video file V1. Fig. 6a and b provide snapshots of *in situ* SEM tensile testing showing a graphene branch bending in order to become more aligned with the tensile force. *In situ* SEM snapshots in Fig. 6c and d show a similar alignment occurring at the base of the branch at the node. The alignment at the node, is much more rapid (3.08 °/s) as compared to at the branch (0.58 °/s). This more sudden change in alignment at the node occurs because the nodes consist of several intersecting branches making them more rigid and brittle. A single branch in contrast is as flexible as the graphene platelets it is made of.

The peaks and valleys in the stress–strain curve indicate that not all graphene foam branches become aligned at the same time as in conventional foam structures. Instead, when one foam branch becomes fully taut it bears a significantly higher portion of the load. Such a branch is seen in Fig. 7 as the surrounding structure has either fractured or appears to be undergoing minimal deformation. Fig. 7b shows that the center of the branch is fully aligned with the tensile load and in Fig. 7c signs of necking are seen. The full sequence of the branch undergoing necking and fracture are provided in Supplementary video file V2. When branches undergo necking, the stress plateaus and the dips seen in the stress–strain curve are the result of the aligned branch failing. The stress then begins to rise again as more branches become aligned; as aligned branches fail the dips in stress continue. The high in-plane strength of graphene gives aligned branches incredible strength thus allowing them to bear significant load even as more portions of the foam fail. This allows individual foam branches to bear significant stress even after the majority of branches have succumbed to the maximum stress. This is directly seen in Fig. 5a as just 2–3 branches of graphene are bearing the loading during the final stages of failure.

From the bulk foam tensile properties, the intrinsic tensile properties of the foam walls are calculated using Eq. (1) and it

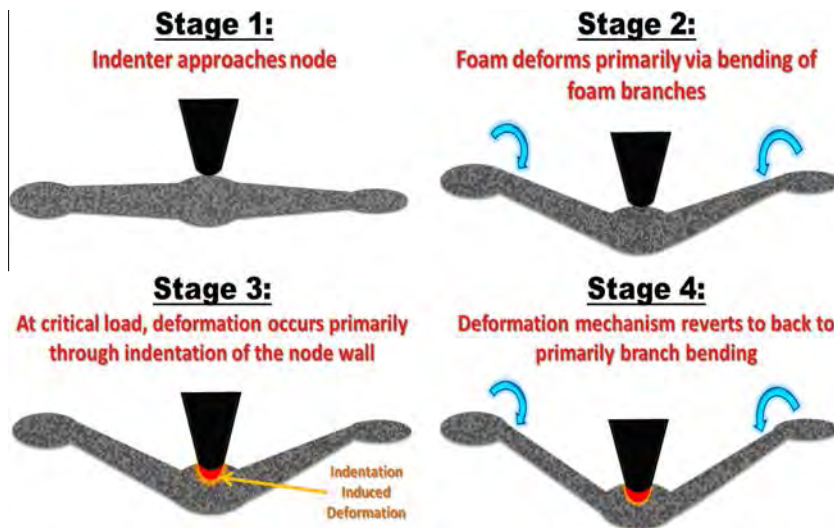


Fig. 4 – Schematic illustrating deformation mechanisms during nanoscale compression of graphene foam via nanoindentation. Indenter approaches during Stage 1, spikes in load may be induced by branch strands. During Stage 2 the foam deforms via bending of foam branches. At Stage 3, a critical stress is reached where the indentation of the node wall becomes more favorable. At Stage 4, bending resumes as the primary deformation mechanism. During indentation with a flat punch, the low stress intensity factor of the tip does not allow for initiation of Stage 3. (A color version of this figure can be viewed online.)

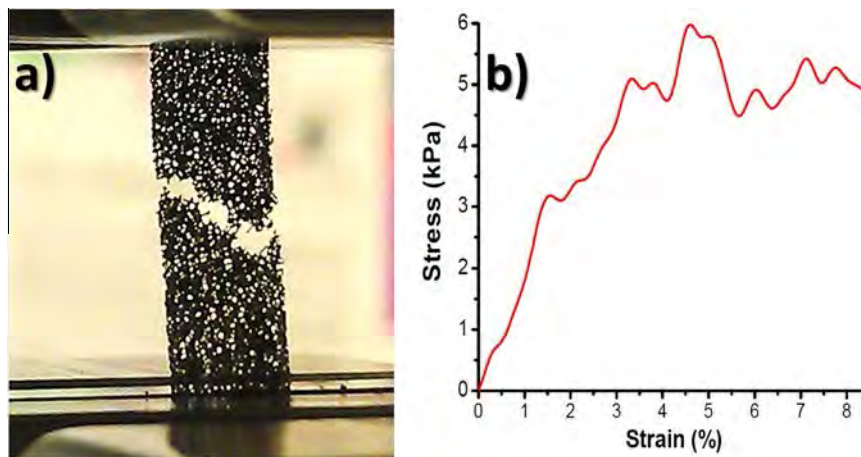


Fig. 5 – (a) Fractured Gr foam during tensile testing. Foam is fracturing near the 45° plane, it can be seen that high strength branches align and bear the load and (b) typical stress–strain curve showing peaks and valleys induced by alignment and fracturing of graphene foam branches. (A color version of this figure can be viewed online.)

can be seen from Table 1 that the graphene foam's strength is four orders of magnitude higher in tension. This is due to the utilization of the high in-plane mechanical properties of graphene that are utilized during tension but not compression. The graphene foam wall is found to have an elastic modulus of 69.9 ± 16.9 GPa which is this significantly lower than the value for a single graphene layer. This value reflects that while the tensile strength of the graphene foam is substantially higher than the compression strength, the foam walls strength is far weaker than that of a graphene layer. The foam wall properties however are derived from the macro-scale properties and those properties are influenced by defects in the structure.

It is observed during *in situ* SEM tensile testing that the presence of defects greatly reduces the capacity of branches

to bear to load. Fig. 8 presents a sequence of deformation events during an *in situ* SEM tensile test of graphene branches with intrinsic defects. Fig. 8a shows that one branch has a large crack and another branch consists of discontinuous graphene sheets. As the tensile force is applied, the cracked branch fractures and bends at nearly 90° as shown in Fig. 8b, the high in-plane strength of graphene prevents the complete failure. The load is therefore increasingly transferred to the uppermost branch in the chain and the branch with the discontinuous graphene sheets. The uppermost branch is held together by two smaller branches and as the tensile force increases one of the branches fails as shown in Fig. 8c. The load is now born primarily by the second upper branch, once it fails, the entire segment no longer bears any

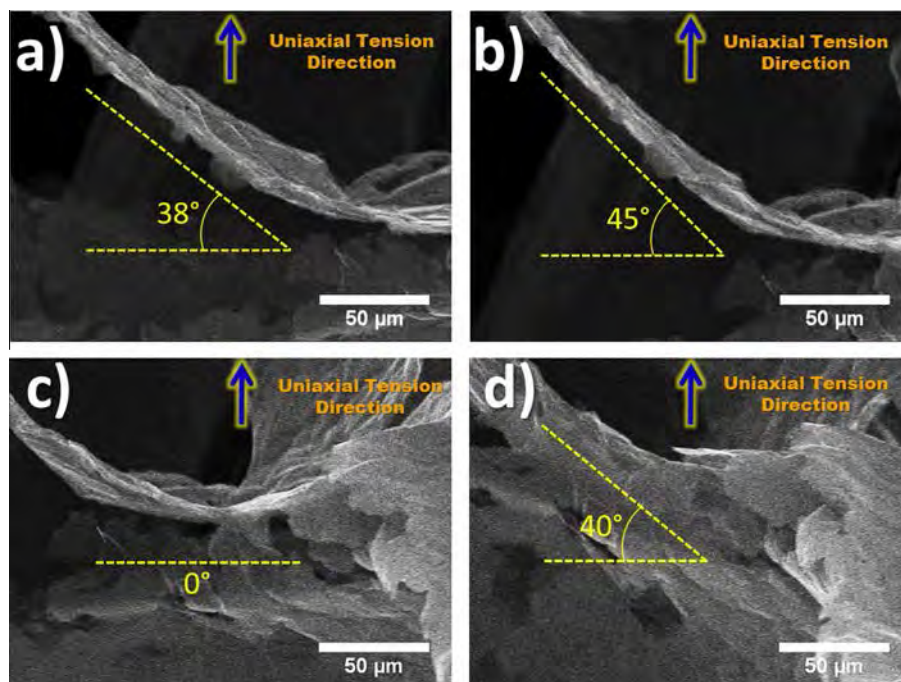


Fig. 6 – (a) Graphene foam branch during in situ SEM tensile tests – tensile force is applied in the vertical direction, (b) graphene branch is gradually bending and becoming aligned in direction of tensile force. From image (a) to (b) branch rotates about 7° in 12 s, (c) graphene branch at the base of the node and (d) branch base shifts severely near the node – rotating from nearly 0° to 40° in 13 s. (A color version of this figure can be viewed online.)

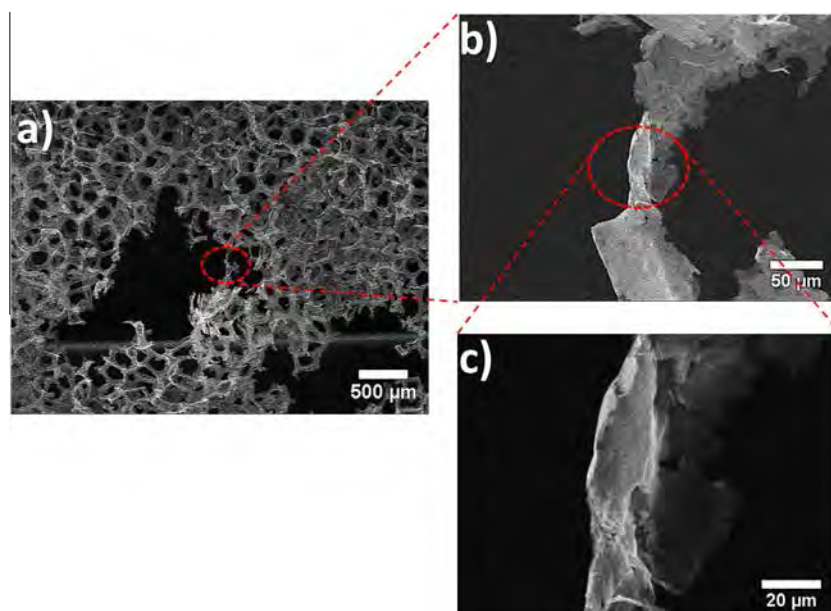


Fig. 7 – (a) SEM micrograph of aligned graphene foam branch under tension, (b) intermediate mag image shows variation in branch girth and (c) high mag of thinnest section of branch which bears highest stress. Middle of section appears to be undergoing some degree of necking. (A color version of this figure can be viewed online.)

load as shown in Fig. 8d. The branch with the discontinuous graphene likely does not fracture because of a sheet sliding mechanism. The volume based relation of Eq. (1) is based

on the entire foam bearing load, therefore the foam wall properties in tension are underestimated as it can be seen that minor defects cause large segments of the foam to remain

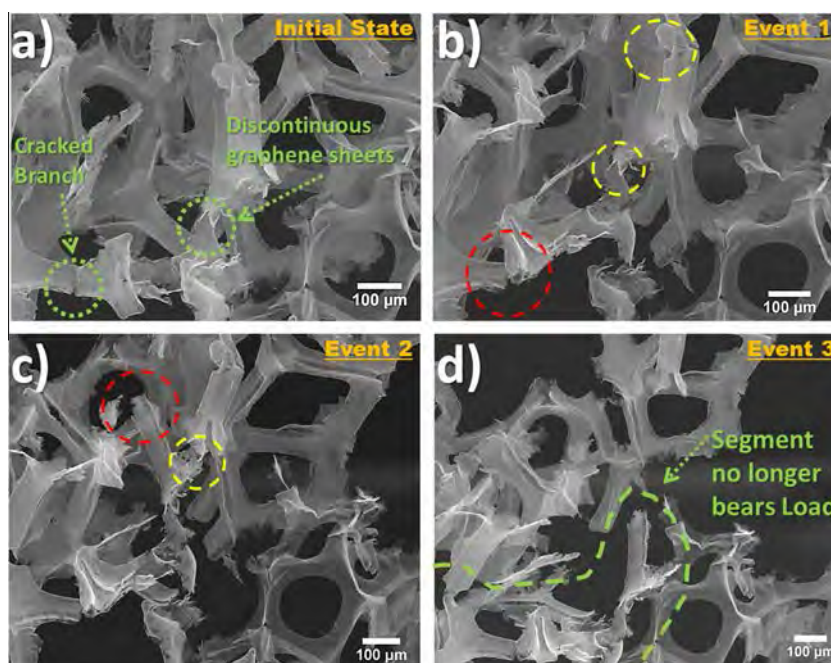


Fig. 8 – Sequence of SEM micrographs of fracture at branch defect sites. (a) Initial state: two significant defects on graphene foam branch are indicated by dotted circles, (b) Event 1: as tension is applied, the crack on the bottom-most branch (red dashed circle) propagates causing branch to fracture to near failure. More load is now bore by regions in dashed circles – the branch with discontinuous graphene layers and the upper branches, (c) Event 2: failure occurs at branch denoted with red dashed circle, thereby transferring more load to branch denoted with yellow dashed circle and (d) Event 3: second of interconnected branches fails and load is no longer bore by any region of the outlined segment. (A color version of this figure can be viewed online.)

unused and intact. A more defect-free 3D structure could allow load to be transferred to a higher number of graphene branches and result in significant strengthening of the foam.

4. Conclusions

The mechanical properties and intrinsic deformation mechanisms of a freestanding 3D graphene foam are evaluated in tension and compression using macroscale tensile testing and nanoscale compression testing, respectively. A volume based relation is used to correlate bulk foam properties to foam wall properties and vice-versa. It is found that the elastic modulus in tension of the graphene foam is four orders of magnitude higher than the elastic modulus in compression. *In situ* SEM observations reveal that the high strength in tension is due to graphene branch alignment that enables branches to utilize the high in-plane mechanical properties of graphene. In contrast, during compression the primary deformation mechanisms are branch bending and branch indentation, neither of which utilizes the high in-plane mechanical properties of graphene. It is observed that due to defects in the graphene foam structure, such as cracked graphene branches and discontinuous graphene sheets, only a small fraction of graphene branches bear the loads.

The fabrication of a more defect free graphene foam structure would lead to more branches bearing load and hence significantly enhance the mechanical performance of 3D graphene foams. The current findings also serve to guide future works on 3D graphene foam reinforced polymer matrix composites.

Knowledge of the differential deformation mechanisms in tension and compression can be used to design polymer matrix composites in ways that take advantage of the high tensile strength and minimize the shortcomings in compression.

Acknowledgements

Authors would like to acknowledge Dr. Ali Sayir, Program Manager of High Temperature Aerospace Materials at the Air Force Office of Scientific Research and FA9550-12-1-0263 grant. Authors would like to thank Dr. Sharan Ramaswamy and Dr. Rupak Dua for extending the use of their tensile testing equipment and for providing assistance during the graphene foam tensile tests. Authors also acknowledge support from the Advanced Materials Engineering Research Institute (AMERI) at FIU.

Appendix A. Supplementary data

Supplementary data associated with this article can be found, in the online version, at <http://dx.doi.org/10.1016/j.carbon.2015.01.003>.

REFERENCES

- [1] Wei W, Qu X. Extraordinary physical properties of functionalized graphene. *Small* 2012;8:2131–7.

- [2] Balandin AA, Ghosh S, Bao W, Calizo I, Teweldebrhan D, Miao F, et al. Superior thermal conductivity of single-layer graphene. *Nano Lett* 2008;8(3):902–7.
- [3] Rao CNR, Sood AK, Voggu R, Subrahmanyam KS. Some novel attributes of graphene. *J Phys Chem Lett* 2010;1:572–80.
- [4] Soldano C, Mahmood A, Dujardin E. Production, properties, and potential of graphene. *Carbon* 2010;48:2127–50.
- [5] Lee C, Wei X, Kysar JW, Hone J. Measurement of the elastic properties and intrinsic strength of monolayer graphene. *Science* 2008;321(5887):385.
- [6] Frank IW, Tanenbaum DM, Van der Zande AM, McEuen PL. Mechanical properties of suspended graphene sheets. *J Vac Sci Technol* 2007.
- [7] Gong L, Kinloch IA, Young RJ, Riaz I, Jalil R, Novoselov KS. Interfacial shear stress transfer in a graphene monolayer nanocomposite. *Adv Mater* 2010;22:2694–7.
- [8] Lu Q, Arroyo M, Huang R. Elastic bending modulus of monolayer graphene. *J Phys D Appl Phys* 2009;42.
- [9] Coskun E, Zaragoza-Contreras EA, Salavagione HJ. Synthesis of sulfonated graphene/polyaniline composites with improved electroactivity. *Carbon* 2012;50:2235–43.
- [10] Walker LS, Marotto VR, Rafiee MA, Koratkar N, Corral EL. Toughening in graphene ceramic composites. *ACS Nano* 2011;5(4):3182–90.
- [11] Yadhukulakrishnan GB, Karamuri S, Rahman A, Singh RP, Kalkan AK, Harimkar SP. Spark plasma sintering of graphene reinforced zirconium diboride ultra-high temperature ceramic composites. *Ceram Int* 2013;39(6):6637–46.
- [12] Nieto A, Lahiri D, Agarwal A. Graphene nanoplatelets reinforced tantalum carbide consolidated by spark plasma sintering. *Mater Sci Eng, A* 2013;582:338–46.
- [13] Nieto A, Lahiri D, Agarwal A. Nano dynamic mechanical behavior of graphene nanoplatelets reinforced tantalum carbide. *Scripta Mater* 2013;69:678–81.
- [14] Nieto A, Kumar A, Lahiri D, Zhang C, Seal S, Agarwal A. Oxidation behavior of graphene nanoplatelet reinforced tantalum carbide composites in high temperature plasma flow. *Carbon* 2014;67:398–408.
- [15] Berman D, Erdemir A, Sumant AV. Few layer graphene to reduce wear and friction on sliding steel surfaces. *Carbon* 2013;54:454–9.
- [16] Belmonte M, Ramirez C, Gonzalez-Julian J, Schneider J, Miranzo P, Osendi MI. The beneficial effect of graphene nanofillers on the tribological performance of ceramics. *Carbon* 2013;61:431–5.
- [17] Chung C, Kim Y-K, Shin D, Ryoo S-R, Hong BH, Min D-H. Biomedical applications of graphene and graphene oxide. *Acc Chem Res* 2013;46:2211–44.
- [18] Zhang L, Liu W, Yue C, Zhang T, Li P, Xing Z, et al. A tough graphene nanosheet/hydroxyapatite composite with improved in vitro biocompatibility. *Carbon* 2013;61:105–15.
- [19] Ramirez C, Figueiredo FM, Miranzo P, Poza P, Osendi MI. Graphene nanoplatelet/silicon nitride composites with high electrical conductivity. *Carbon* 2012:3607–15.
- [20] Miranzo P, Ramirez C, Roman-Manso B, Garzon L, Gutierrez HR, Terrones M, et al. In situ processing of electrically conducting graphene/SiC composites. *J Eur Ceram Soc* 2013;33:1665–74.
- [21] Song SH, Park KH, Kim BH, Choi YW, Jun GH, Lee DJ, et al. Enhanced thermal conductivity of epoxy-graphene composites by using non-oxidized graphene flakes w non-covalent functionalization. *Adv Mater* 2013;25:732–7.
- [22] Wu H, Drzal LT. Graphene nanoplatelet paper as a light-weight composite with excellent electrical and thermal conductivity and good gas barrier properties. *Carbon* 2012;50:1135–45.
- [23] Cai D, Jin J, Yusoh K, Rafiq R, Song M. High performance polyurethane/functionalized graphene nanocomposites with improved mechanical and thermal properties. *Compos Sci Technol* 2012;2012:72.
- [24] Lahiri D, Dua R, Zhang C, Socarras-Novoa ID, Bhat A, Ramaswamy S, et al. Graphene nanoplatelet-induced strengthening of ultra high molecular weight polyethylene and biocompatibility in vitro. *ACS Appl Mater Interface* 2012;4:2234–41.
- [25] Liu J, Yan H, Reece MJ, Jiang K. Toughening of zirconia/alumina composites by the addition of graphene platelets. *J Eur Ceram Soc* 2012;32:4185–93.
- [26] Kandanur SS, Rafiee MA, Yavari F, Schrameyer M, Yu Z-Z, Blanchet TA, et al. Suppression of wear in graphene polymer composites. *Carbon* 2012;50:3178–83.
- [27] Chen Z, Xu C, Ma C, Ren W, Cheng H-M. Lightweight and flexible graphene foam composites for high-performance electromagnetic interference shielding. *Adv Mater* 2013;25:1296–300.
- [28] Cheng W, Fan Z, Zeng G, Lai Z. Layer-dependent supercapacitance of graphene films grown by chemical vapor deposition on nickel foam. *J Power Sources* 2013;225:251–6.
- [29] Singh E, Chen Z, Houshmand F, Ren W, Peles Y, Cheng H-M, et al. Superhydrophobic graphene foams. *Small* 2013;9:75–80.
- [30] Li N, Zhang Q, Gao S, Song Q, Huang R, Wang L, et al. Three-dimensional graphene foam as a biocompatible and conductive scaffold for neural stem cells. *Sci Rep* 2013;3:1604.
- [31] Zhou M, Lin T, Huang F, Zhong Y, Wang Z, Tang Y, et al. Highly conductive porous graphene/ceramic composites for heat transfer and thermal energy storage. *Adv Funct Mater* 2013;23:2263–9.
- [32] Dong X, Wang X, Wang, Song H, Zhang H, Huang W, Chen P. 3D graphene foam as a monolithic and macroporous carbon electrode for electrochemical sensing. *ACS Appl Mater Interface* 2012;4:3129–33.
- [33] Cao X, Shi Y, Shi W, Lu G, Huang X, Yan Q, et al. Preparation of novel 3D graphene networks for supercapacitor applications. *Small* 2011;7:3163–9.
- [34] Yavari F, Chen Z, Thomas AV, Ren W, Cheng H-M, Koratkar N. High sensitivity gas detection using a macroscopic three-dimensional graphene foam network. *Sci Rep* 2011;1:166.
- [35] Jiang L, Fan Z. Design of advanced porous graphene materials: from graphene nanomesh to 3D architectures. *Nanoscale* 2014;6:1922–45.
- [36] Li Y, Chen J, Huang L, Li C, Hong J-D, Shi G. Highly compressible macroporous graphene monoliths via an improved hydrothermal process. *Adv Mater* 2014;26:4789–93.
- [37] Zhang H-B, Yan Q, Zheng W-G, He Z, Yu Z-Z. Tough graphene-polymer microcellular foams for electromagnetic interference shielding. *ACS Appl Mater Interface* 2011;3:918–24.
- [38] Eswaraiah V, Sankaranarayanan V, Ramaprabhu S. Functionalized graphene-PVDF foam composites for EMI shielding. *Macromol Mater Eng* 2011;296:894–8.
- [39] Xia X, Chao D, Fan Z, Guan C, Cao X, Hua Z, et al. A new type of porous graphite foams and their integrated composites with oxide/polymer core/shell nanowires for supercapacitors: structural design, fabrication, and full supercapacitor demonstrations. *Nano Lett* 2014;14:1651–8.
- [40] Zhang Z, Xiao F, Qian L, Xiao J, Wang S, Liu Y. Facile synthesis of 3D MnO₂-graphene and carbon nanotube-graphene composite networks for high performance, flexible, all-solid-state asymmetric supercapacitors. *Adv Energy Mater* 2014;4:140064.
- [41] Yu P, Zhao X, Huang Z, Li Y, Zhang Q. Free-standing three-dimensional graphene and polyaniline nanowire arrays hybrid foams for high-performance flexible and lightweight supercapacitors. *J Mater Chem A* 2014;2:14413–20.

- [42] Liu L, Zhiqiang N, Zhang L, Weiya Z, Chen X, Xie S. Nanostructured graphene composite papers for highly flexible and foldable supercapacitors. *Adv Mater* 2014;26:4855–62.
- [43] Wu C, Huang X, Wu X, Qian R, Pingkai J. Mechanically flexible and multifunctional polymer-based graphene foams for elastic conductors and oil-water separators. *Adv Mater* 2013;25:5658–62.
- [44] Zhao Y, Liu J, Hu Y, Cheng H, Hu C, Jiang C, et al. Highly compressible-tolerant supercapacitor based on polypyrrole-mediated graphene foam electrodes. *Adv Mater* 2013;25:591–5.
- [45] Chen Z, Ren W, Gao L, Liu B, Pei S, Cheng H-M. Three-dimensional flexible and conductive interconnected graphene networks grown by chemical vapour deposition. *Nat Mater Lett* 2011;10:424–8.
- [46] Lee S-H, Jung J-H, Oh I-K. 3D networked graphene-ferromagnetic hybrids for fast shape memory polymers with enhanced mechanical stiffness and thermal conductivity. *Small* 2014;10:3880–6.
- [47] Jia J, Sun X, Lin X, Shen X, Mai Y-W, Kim J-K. Exceptional electrical conductivity and fracture resistance of 3D interconnected graphene foam/epoxy composites. *ACS Nano* 2014;8:5774–83.
- [48] Xu R, Lu Y, Jiang C, Chen J, Mao P, Gao G, et al. Facile fabrication of three-dimensional graphene foam/poly(dimethylsiloxane) composites and their potential application as strain sensor. *ACS Appl Mater Interface* 2014;6:13455–60.
- [49] Oliver WC, Pharr GM. An improved technique for determining hardness and elastic modulus using load and displacement sensing indentation experiments. *J Mater Res* 1992;7:1564–83.
- [50] Ferrari AC, Meyer JC, Scardaci V, Casiraghi C, Lazzeri M, Piscanec S, et al. Raman spectrum of graphene and graphene layers. *Phys Rev Lett* 2006;97:187401.
- [51] Dresselhaus MS, Jorio A, Hofmann M, Dresselhaus G, Saito R. Perspectives on carbon nanotubes and graphene Raman spectroscopy. *Nano Lett* 2010;10:751–8.
- [52] Graf D, Molitor F, Ensslin K, Stampfer C, Jungen A, Hierold C, et al. Spatially resolved Raman spectroscopy of single- and few-layer graphene. *Nano Lett* 2007;7:238–42.
- [53] Chae SK, Gunes F, Kim KK, Kim ES, Han GH, Kim SM, et al. Synthesis of large-area graphene layers on poly-nickel substrate by chemical vapor deposition: wrinkle formation. *Adv Mater* 2009;21:2328–33.
- [54] Chen W, Fan Z, Zeng G, Lai Z. Layer-dependent supercapacitance of graphene films grown by chemical vapor deposition in nickel foam. *J Power Sources* 2013;225:251–6.
- [55] Gibson LJ, Ashby MF. The mechanics of foams: basic results. In: Clarke DR, Suresh S, Ward IM, editors. *Cellular solids – structures and properties*. Cambridge, UK: Cambridge University Press; 1997. p. 175–281.

Available at www.sciencedirect.com

ScienceDirect

journal homepage: www.elsevier.com/locate/carbon

Direct observation of carbon nanotube induced strengthening in aluminum composite via *in situ* tensile tests

Benjamin Boesl^a, Debrupa Lahiri^{a,b}, Sadegeh Behdad^a, Arvind Agarwal^{a,*}

^a Department of Mechanical and Materials Engineering, Florida International University, Miami, FL 33174, USA

^b Department of Metallurgical and Materials Engineering, Indian Institute of Technology, Roorkee, Roorkee 247667 Uttarakhand, INDIA

ARTICLE INFO

Article history:

Received 27 August 2013

Accepted 25 November 2013

Available online 1 December 2013

ABSTRACT

In situ tensile tests inside a scanning electron microscope chamber are conducted on spark plasma sintered Al and Al-1 vol.% CNT composites to understand the strengthening and deformation mechanisms due to long (25–30 μm) CNT reinforcement addition. Al-CNT composite shows 40% higher tensile strength, and 65% higher stiffness for mere 1 vol.% CNT addition. The failure occurs by CNT pullout from the matrix, which is directly imaged during the tensile testing. Telescopic sliding of CNT walls is also observed which aids to strengthening.

© 2013 Elsevier Ltd. All rights reserved.

1. Introduction

Carbon nanotube (CNT) has been explored as reinforcement for developing high strength aluminum based composites, due to its high surface/volume ratio, elastic modulus (0.6–1.1 TPa) and tensile strength (35–110 GPa) [1,2]. Fabrication of Al-CNT composites has largely been done through powder metallurgy techniques. The dispersion of CNT in Al has been done by ball milling [3–7], wet chemistry [8], blending [9], chemical vapor deposition [10], spray drying [11] and nano-scale dispersion [12]. The consolidation has been carried out through compaction and sintering [13–15], cold and hot isostatic pressing [3,16], hot rolling [4], spark plasma sintering [17,18] and thermal spray techniques [9,11,19–21]. These processes are often followed by hot extrusion and/or heat treatment to provide enhanced densification to the consolidated structure [5,6,17,22].

The major challenges in fabricating Al-CNT composites are twofold: (i) the dispersion of CNT in Al matrix and (ii) nature of bonding at Al/CNT interface. The high surface energy of CNTs leads to agglomeration, which is deleterious to

strengthening of the composite. The favorable thermodynamics and fast kinetics of aluminum carbide (Al₄C₃) formation makes its existence inevitable at Al/CNT interface, even in rapid processes like SPS and plasma spraying [11,17,20]. Thick layer of brittle Al₄C₃ at Al/CNT interface is deleterious for the mechanical properties. Although it has been reported a thin (2–10 nm) layer of the Al₄C₃ enhance the anchoring and pinning of CNT with the Al matrix resulting in higher strength [23]. The strengthening in Al-CNT composites has been attributed to multiple mechanisms: (i) fiber strengthening by load transfer through the interface [3,24], (ii) dislocation pile-up or strain hardening [3,21,25] and, (iii) grain boundary pinning and fine sub-grain formation [21]. These findings do not lead to an obvious inference regarding which mechanism dominates the strengthening. However, among all the proposed mechanisms, fiber strengthening is the most agreed one, due to one dimensional fiber like structure of CNT with a very large aspect ratio. This is augmented by the fact that post consolidation extrusion leads to CNT alignment resulting in enhanced strengthening [6,7]. The fracture strength of metal-CNT composites has been explained using shear lag

* Corresponding author.

E-mail address: agarwala@fiu.edu (A. Agarwal).

0008-6223/\$ - see front matter © 2013 Elsevier Ltd. All rights reserved.

<http://dx.doi.org/10.1016/j.carbon.2013.11.061>

model, for discontinuous fiber reinforcement [26]. The critical length of 50 nm diameter CNT for strengthening in Al–CNT system is estimated as 10–15 μm [7]. The present study utilizes long (25–30 μm) and slender (10–30 nm diameter) CNT reinforcement to provide a direct evidence of CNT induced strengthening in aluminum based composite using *in situ* tensile tests inside a SEM chamber.

Previous experimental studies including direct observation of the interaction of matrix and CNTs (or other nano-reinforcements) have tended to focus on one of two methods; (i) the deformation of an individual reinforcement or (ii) the interfacial strength between reinforcement and the matrix at the scale of the reinforcement. Lourie et al. [27] and Wagner et al. [28] observed fracture and buckling in individual CNTs in reinforced polymers using an *in situ* TEM experiment in which the sample was thermally loaded using the electron beam and qualitative analysis of damage was completed. Filleter et al. [29] measured tensile strength and observed deformation mechanisms of irradiated double-walled CNTs with a thermally actuated *in situ* TEM load frame. Qian et al. [30] investigated the interfacial strength of CNT reinforced polymer composites using thermal loading within the chamber of a TEM. Deng et al. [31] used a micro-load frame inside a high resolution TEM to investigate the deformation mechanisms in electron transparent CNT–PEEK composites. Boesl et al. [32] used a focused ion beam to mill 10 μm long ZnO reinforced polymer μ -cantilevers and an omniprobe micromanipulator to investigate fracture mechanisms in polymer nanocomposites. *In situ* SEM/AFM pullout experiments have also been used to investigate the interfacial properties and damage initiation of individual nanotube reinforcements [33,34]. *In situ* SEM/nanindentation has also been used to quantify and image deformation in various nanoparticle reinforced systems [35,36]. While each of these techniques investigated important phenomenon, the scale of each experiment is on the order of the individual reinforcement, and therefore it is uncertain if the mechanisms that are being observed have any relationship to the deformation mechanisms present in bulk samples. Moreover, most of those *in situ* studies have been performed on polymer and ceramic matrix composites. The fiber strengthening mechanism in bulk Al–CNT or other composite systems has always been inferred indirectly based on the *post deformation fracture surface observation*. Signs of fiber strengthening are deduced from the pull-out/protruded CNTs, alignment of CNTs along the loading direction, dislocation pile-up around CNTs, and crack bridging [5,11,17,19,21]. However, no direct *in situ* observation of CNT strengthening in bulk samples has been observed or reported in the literature.

The prime novelty of this study is the shift from testing sample sizes on the order of the constituent to the use of an *in situ* load frame that can quantify bulk properties, while directly imaging strengthening mechanisms of nano-reinforcements using a SEM. Load and displacement are measured on the bulk scale while imaging remains on the constituent scale. Elongation, crack initiation and propagation, and CNT pull-out are observed in *real time* inside the SEM, providing insight on the role of CNT in strengthening of the bulk composite.

2. Experimental procedure

Thin and long multiwall CNTs with diameter ranging 10–30 nm and length 25–30 μm were obtained from C-Nano Technologies (Beijing, China). Aluminum powder (H3, Valimet Inc., USA) of spherical shape with 90% particles having diameter <10.5 μm and purity $\geq 99.7\%$ was used as the matrix. Al-1 vol.% CNT composite powder was prepared by wet-mixing method using acetone as the medium. Nanotubes were ultrasonicated in acetone for 2 h to disperse in liquid medium. Once dispersion was achieved, Al powder was introduced gradually in the suspension and further ultrasonicated for one hour. Composite powder was dried in a vacuum oven at 60 $^{\circ}\text{C}$ for 2 h. Fig. 1a shows a SEM image of the Al–CNT powder mixture after vacuum drying. The powder was consolidated by spark plasma sintering (SPS) in vacuum. A heating rate of 50–60 $^{\circ}\text{C}/\text{min}$ was applied to reach a maximum temperature of 500 $^{\circ}\text{C}$, with a hold time of 1 h at 80 MPa pressure. The powders were consolidated into 40 mm diameter and 5 mm thick pellets (Fig. 1b). Pure Al powder was also consolidated under similar conditions, as a reference sample. Flat dog bone shaped samples were fabricated from the SPS disks using wire EDM (Fig. 1c). Surface of the machined tensile samples was gently ground to remove machining effects. The overall length of each sample was 27.82 mm with a gage length of 6.60 mm and thickness 2.28 mm. Density of the sintered Al and Al–CNT composite was measured using a Helium pycnometer (Accupyc II 1340: Micro-metrics Instrument Corporation, Norcross, GA, USA). The density of Al and Al-1 vol.% CNT was measured to be 99.9% of theoretical density computed using rule of mixtures.

An MTI SEMtester 1000 micro load frame was used to load the samples inside the electron microscope vacuum chamber (JEOL, JIB 4500 Dual-Beam FIB–SEM). Concurrent loading and imaging of the sample occurred during each test. The samples were loaded in displacement control at a rate of 0.2 mm/min and SEM imaging was conducted at 20 keV over the duration of the test in which the typical chamber pressure was 7.0×10^{-4} Pa. Samples were imaged at a scanning rate of 0.15 full-scan/s and was captured at a resolution of 640×480 and 30 fps during loading. Post-test imaging was completed using a higher-resolution FESEM (JEOL 7000F). A minimum of 3 tensile tests were conducted for each composition.

3. Results and discussion

Fig. 2 shows the experimental results for the unreinforced SPS aluminum sample. A video (V1) of the crack propagation during *in situ* tensile testing in aluminum sample is included in the online submission. Individual still images were obtained from the video (V1) capture during the tensile test and are presented in Fig. 2a–d. The corresponding stress–strain behavior during tensile test for aluminum without CNTs is also shown. The yield strength of the aluminum sample was measured to be 68.1 MPa. Post yield, microscale analysis reveals the presence of microcracking and the propagation of major cracks with an increase in load. Continued loading leads to the coalescence of microcracks and ultimately, results in failure.

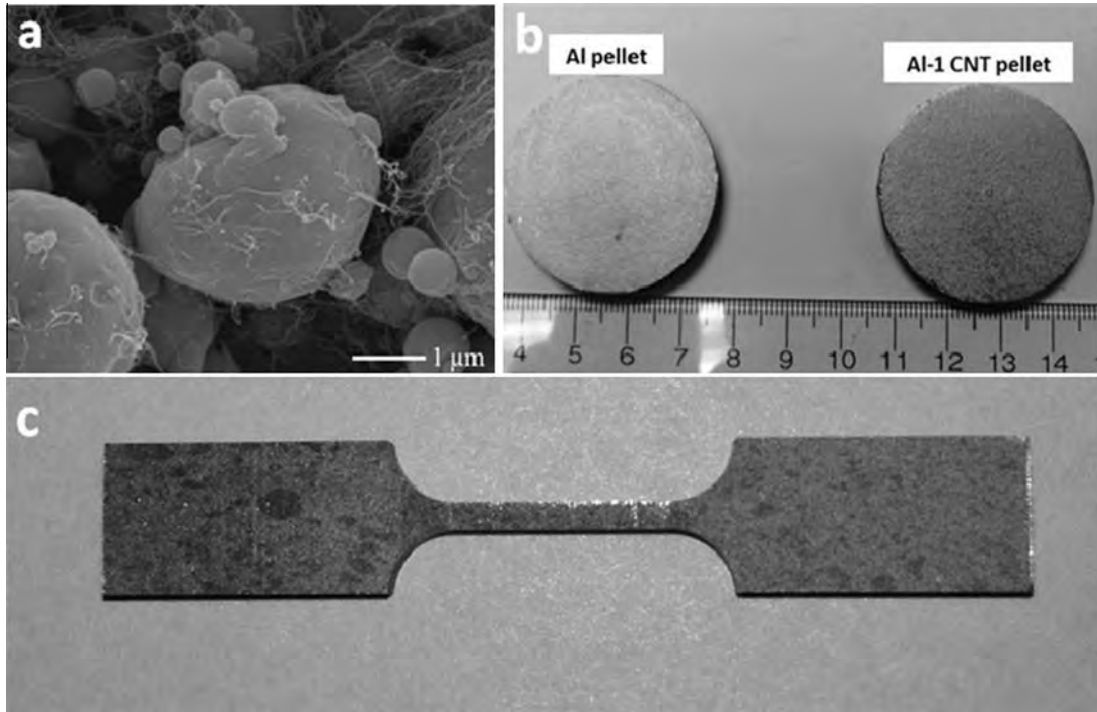


Fig. 1 – (a) SEM micrograph of Al powder and CNT after mixing. (b) Spark plasma sintered pellets (Al and Al-1 wt.% CNT) of 40 mm diameter and 5 mm thickness. (c) Dog bone shape tensile sample machined from sintered pellets using wire EDM. The total length of the tensile sample is 27.82 mm.

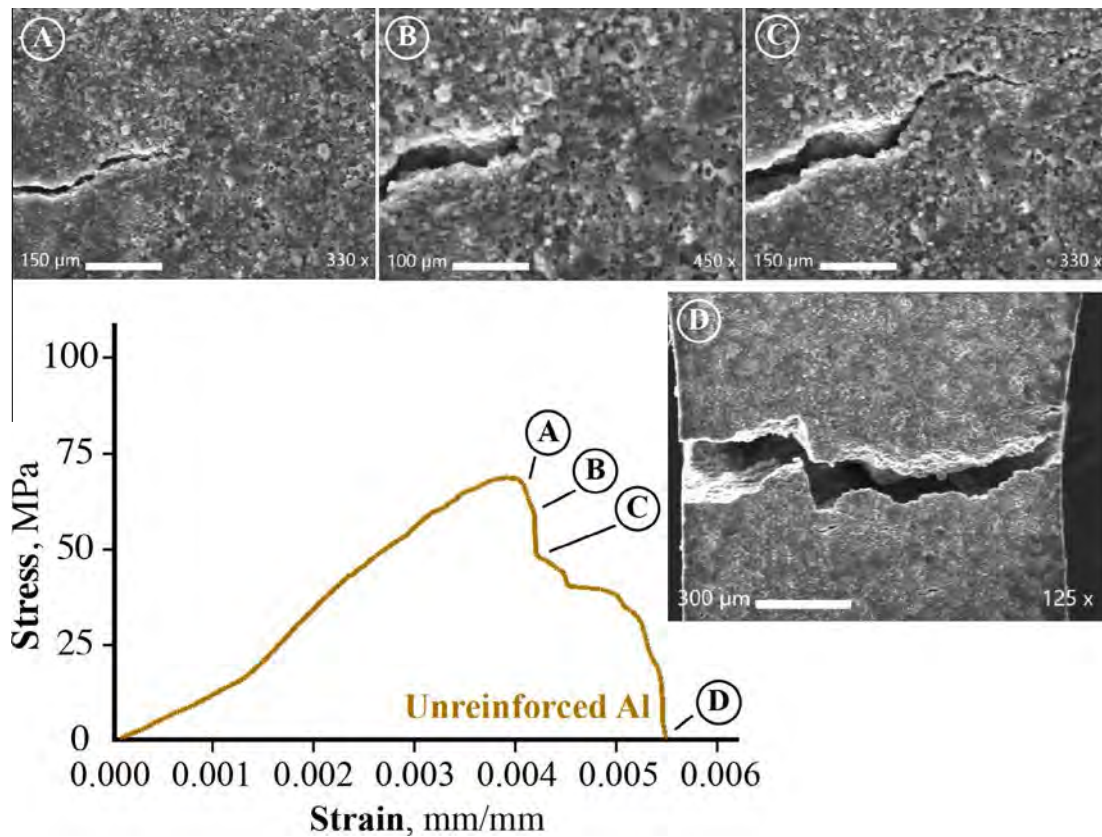


Fig. 2 – Results from in situ testing of the spark plasma sintered (SPS) aluminum sample. A propagating crack in the material is shown from (A) to (D) with the corollary load shown on the stress strain diagram. (A color version of this figure can be viewed online.)

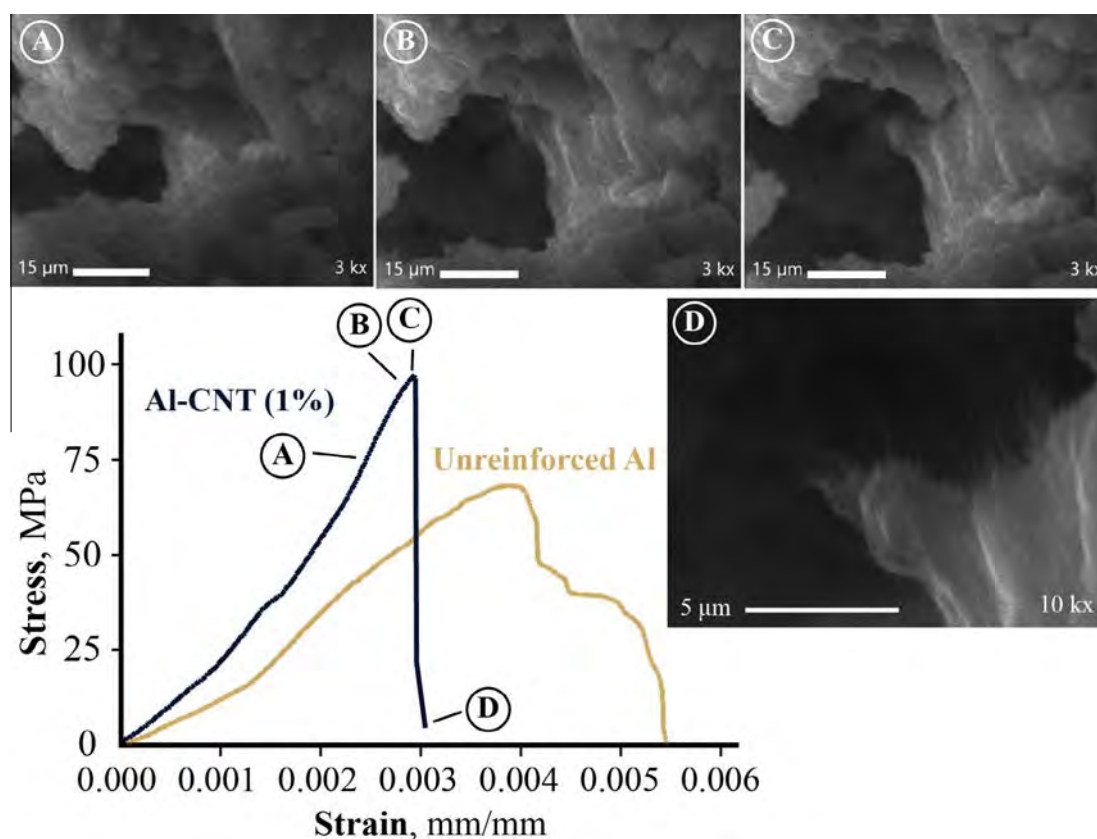


Fig. 3 – In situ testing of the spark plasma sintered (SPS) CNT reinforced aluminum. Due to the brittle failure of the CNT nanocomposite, the propagation of the major crack was not imaged, but subsequent imaging of failure in the material reveals the mechanisms of deformation in the sample. Image (A) shows the major crack seconds after propagation and figures (B) through (D) show the evolution of damage during subsequent loading within the major crack including CNT elongation, pullout and breakage. (A color version of this figure can be viewed online.)

The change in stress–strain response due to the addition of 1 vol.% CNT is shown in Fig. 3 along with corollary images captured from the video (V2) during loading. The yield strength of the reinforced sample was 95.5 MPa, exhibiting a significant 40% increase over the Al for mere 1 vol.% CNT addition. The increase in elastic modulus (E) of Al–CNT composite is visible from the higher slope in Fig. 3. The ratio of $E_{\text{Al-CNT}}/E_{\text{Al}}$ is 1.65, which indicates elastic modulus of Al–CNT composite is 65% higher than Al without reinforcement. However, the nature of the fracture is largely brittle without much yielding. It has been consistently observed in Al–CNT composites that CNT addition results in improved tensile strength and stiffness but at the expense of ductility [1,2,12]. A similar behavior is observed here, where strain to failure in Al–1 vol.% CNT composite is 0.003 as compared to 0.0055 for unreinforced aluminum. The strain in each sample was estimated from the extensometer readings of the cross-head displacement with a correction for compliance of the machine based on a known standard. The testing conditions did not allow for the use of standard gauge length extension measurements such as a strain gage or an LVDT due to both the environment (within the SEM chamber) and the small sample size. Hence, we have not reported the absolute value of elastic modulus “ E ” due to the uncertainty of the strain

measurement. However, the ratio of “ E ” of Al–CNT/Al for the same loading, and analysis conditions shows that elastic modulus of Al–CNT composite is higher than Al by 65%.

A video (V2) of the CNT pull out in Al–1 vol.% CNT sample is also provided online. Due to the less plastic flow in Al–1 vol.% CNT and the restrictions in the field of view in the microscope, the propagation of the major crack was not imaged. The imaging was focused to capture CNT pull out instead of crack propagation. The gentle pullout of several CNTs is clearly visible in video (V2) after 20 s, which provides a direct evidence of CNT induced strengthening. CNTs are slowly pulled out from the matrix with a cheese like flow pattern and deformation. Fig. 3a shows the major crack seconds after failure. As loading continued, subsequent images shown in Fig. 3b–d were captured within the major crack region at higher magnification. Imaging of deformation and subsequent failure within the region verifies occurrences of CNT loading, extension and subsequent CNT pullout upon maximum loading.

Post fracture analysis of Al–1 vol.% CNT sample is presented in Fig. 4. Representative images are shown to illustrate the presence of CNT extension and pullout failure across the fracture region. Evidence of CNT induced strengthening and pulled out protrusion measuring up to 6–7 μm is shown in

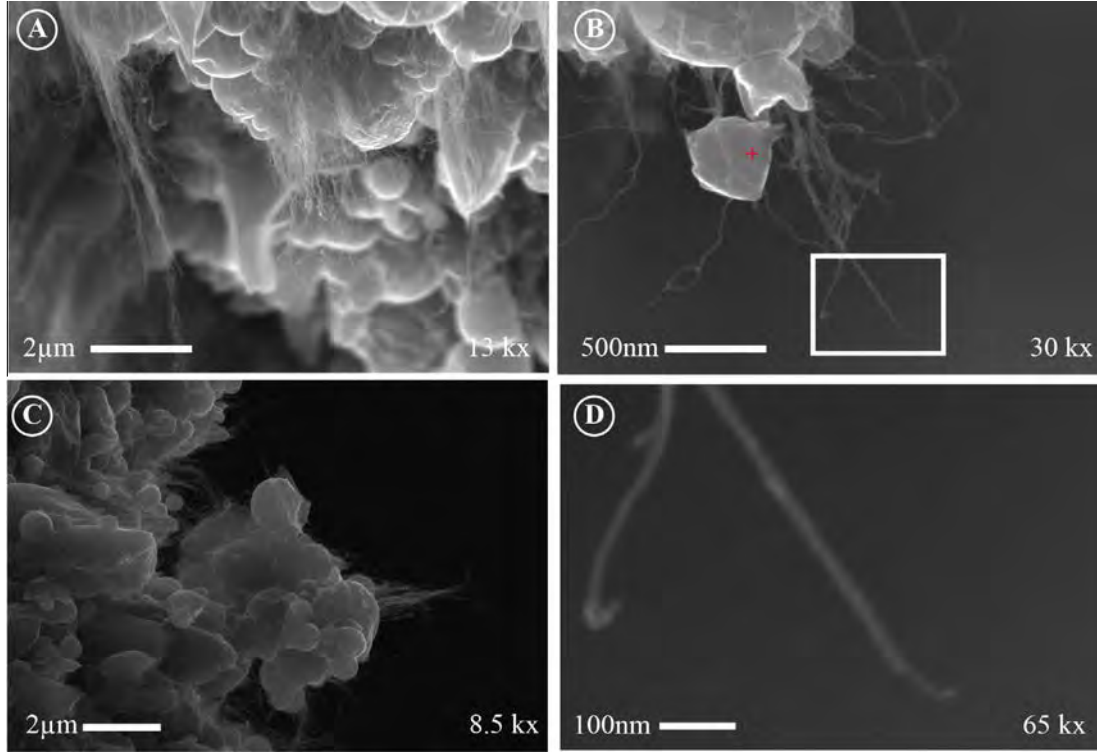


Fig. 4 – Post failure SEM images of fracture surfaces: (A) Wide field view shows fiber pullout of close to 10 μm. (B) Region of nanotube deformation. (C) Evidence of bridging of nanotubes between Al constituents. (D) Increased magnification image from highlighted region in Fig. 4(B), image shows evidence of telescopic failure of individual nanotubes.

Fig. 4a and c. Fig. 4b and d shows the presence of telescopic fracture behavior at the ends of the MWCNT within a region of approximately 100 nm. The telescopic structure is formed due to transfer of load from the matrix to reinforcement and then gradual failure of outer layers of the multiwall CNT. Fig. 4b also shows evidence of CNT bridging and adhesion to individual aluminum particles.

Fig. 4a and c also show finer aluminum particles with incomplete sintering. It must be noted that aluminum powder size used for this study had 10% powder as fines (500 nm–1 μm diameter) which is more prone to thin layer of surface oxide (Al_2O_3) formation due to higher surface area. Thin oxide layer on fine particles hinders sintering. Fig. 5 shows fracture surface of unreinforced aluminum sample. Larger aluminum particles are fully sintered and display a classical ductile failure by coalescence of voids. The fine and partially sintered aluminum particles are trapped between fully sintered large particles (Fig. 5). EDS analysis (not shown here) of the individual fine Al particle did not show presence of carbon peak suggesting lack of formation of Al_4C_3 [37].

Kelly and Tyson has proposed a shear lag model for estimating strengthening in short fiber composites where applied stress is transferred to the fibers through an interfacial shear stress [26]. The fracture strength of the composite for fiber longer than critical length l_c is given by Eq. (1):

$$\sigma_C = \sigma_{\text{CNT}} V_{\text{CNT}} \left(1 - \frac{l_c}{2l}\right) + \sigma_M (1 - V_{\text{CNT}}) \text{ for } l > l_c \quad (1)$$

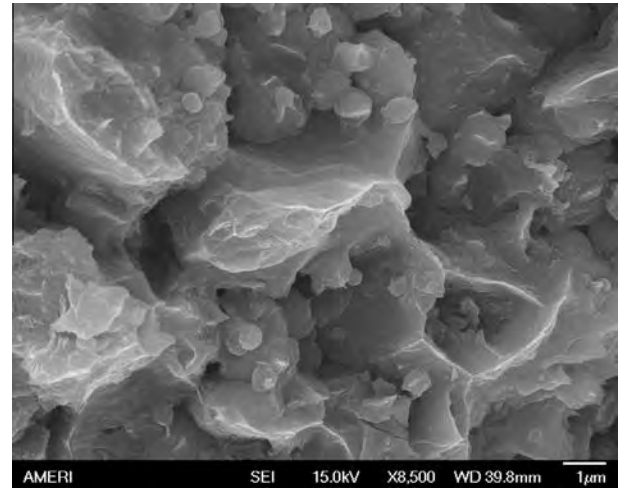


Fig. 5 – Post failure SEM image of fracture surface of unreinforced aluminum sample. Larger aluminum articles are fully sintered and show ductile failure whereas finer aluminum particles are not fully sintered and trapped between voids.

where $l_c = \frac{\sigma_{\text{CNT}} D}{2\tau_m}$ is the critical length of the fiber, V_{CNT} is the CNT volume fraction, l is the average CNT length, D is the CNT diameter, τ_m is the matrix shear strength ($=\sigma_M/2$), and σ_{CNT} is the tensile strength of CNT. Assuming the following values for these variables ($l = 20\text{--}30 \mu\text{m}$, $D = 20\text{--}30 \text{ nm}$,

$\sigma_M = 68$ MPa, $l_c = 2\text{--}4$ μm , $V_{\text{CNT}} = 0.01$, $\sigma_{\text{CNT}} = 6\text{--}8$ GPa [1]), the estimated composite strength σ_C is 90–110 MPa, which is comparable with *in situ* tensile test result (95.5 MPa) for Al–CNT composite and validates fiber strengthening mechanisms and model. In our previous study on strengthening mechanisms in Al–CNT composites, it was concluded that strengthening and stiffening is highest for CNT content less than 2 vol.% due to ease of dispersion [7]. A similar behavior is observed in the present study.

It is concluded that longer CNTs at lower concentration are beneficial for improving the strengthening and stiffening in aluminum composites. Longer CNTs translates the localized stiffening to macroscopic level. Lower CNT concentration would minimize Al_4C_3 content and prevent degradation of CNT/Al interface [37]. *In situ* tensile experiments have clearly demonstrated that fiber strengthening is the dominating mechanism in CNT reinforced composites. In future, metal–CNT composites could be designed using longer and slender CNTs at lower concentration for load bearing and electronic packaging applications due to their high specific strength, high thermal conductivity and low coefficient of thermal expansion.

Acknowledgement

Authors acknowledge the support of the Advanced Materials Engineering Research Institute (AMERI) at FIU for providing the characterization facilities. A.A. would also like to acknowledge High Temperature Aerospace Materials at the Air Force Office of Scientific Research (FA9550-11-1-0334 Grant).

Appendix A. Supplementary data

Supplementary data associated with this article can be found, in the online version, at <http://dx.doi.org/10.1016/j.carbon.2013.11.061>.

REFERENCES

- [1] Yu MF, Lurie O, Dyer MJ, Moloni K, Kelly TF, Rouff RF. Strength and breaking mechanism of multiwalled carbon nanotubes under tensile load. *Science* 2000;287:636.
- [2] Peng B, Locascio M, Zapol P, Li S, Mielke SL, Schatz GC, et al. Measurements of near-ultimate strength for multiwalled carbon nanotubes and irradiation-induced crosslinking improvement. *Nat Nanotechnol* 2008;3:626.
- [3] Stein J, Leczkowski B, Frety N, Anglaret E. Mechanical reinforcement of a high-performance aluminium Mechanical reinforcement of a high-performance aluminium carbon nanotubes. *Carbon* 2012;50:2264.
- [4] Choi HJ, Shin JH, Min BH, Bae DH. Deformation behavior of Al–Si alloy based nanocomposites reinforced with carbon nanotubes. *Compos A* 2010;41:327.
- [5] Pérez-Bustamante R, Gómez-Esparza CD, Estrada-Guel I, Miki-Yoshida M, Licea-Jiménez L, Pérez-García SA, et al. Microstructural and mechanical characterization of Al–MWCNT composites Microstructural and mechanical characterization of Al–MWCNT composites. *Mater Sci Eng A* 2009;502:159.
- [6] Esawi AMK, Morsi K, Sayed A, Abdel Gawad A, Borah P. Fabrication and properties of dispersed carbon nanotube–aluminum composites. *Mater Sci Eng A* 2009;508:167.
- [7] Bakshi SR, Agarwal A. An analysis of the factors affecting strengthening in carbon nanotube reinforced aluminum composites. *Carbon* 2011;49:533.
- [8] Kuzumaki T, Miyazawa K, Ichinose H, Ito K. Processing of carbon nanotube reinforced aluminum composite. *J Mater Sci* 1998;13:2445.
- [9] Laha T, Agarwal A, McKechnie T, Seal S. Synthesis and characterization of plasma spray formed carbon nanotube reinforced aluminum composite. *Mater Sci Eng A* 2004;381:249.
- [10] He C, Zhao N, Shi C, Du X, Li J, Li H, et al. An approach to obtaining homogeneously dispersed carbon nanotubes in Al powders for preparing reinforced Al–matrix composites. *Adv Mater* 2007;19:1128.
- [11] Bakshi SR, Singh V, Seal S, Agarwal A. Aluminum composite reinforced with multiwalled carbon nanotubes from plasma spraying of spray dried powders. *Surf Coat Technol* 2009;203:1544.
- [12] Noguchi T, Magario A, Fukazawa S, Shimizu S, Beppu J, Seki M. Carbon nanotube/aluminum composites with uniform dispersion. *Mater Trans JIM* 2004;45:602.
- [13] George R, Kashyap KT, Rahul R, Yamdagni S. Strengthening in carbon nanotube/aluminium (CNT/Al) composite. *Scr Mater* 2005;53:1159.
- [14] He CN, Zhao NQ, Shi CS, Song SZ. Mechanical properties and microstructures of carbon nanotube-reinforced Al matrix composite fabricated by *in situ* chemical vapor deposition. *J Alloys Compd* 2009;487:258.
- [15] Sridhar I, Narayanan KR. Processing and characterization of MWCNT reinforced aluminum matrix composites. *J Mater Sci* 2009;44:1750.
- [16] Deng C, Zhang X, Wang D, Lin Q, Li A. Preparation and characterization of carbon nanotubes/aluminum matrix composites. *Mater Lett* 2007;61:1725.
- [17] Kwon H, Estili M, Takagi K, Miyazaki T, Kawasaki A. Combination of hot extrusion and spark plasma sintering for producing carbon nanotube reinforced aluminum matrix composites. *Carbon* 2009;47:570.
- [18] Kim I-Y, Leea J-H, Lee Gyu-Sun, Baik S-H, Kim Y-J, Lee Y-Z. Friction and wear characteristics of the carbon nanotube–aluminum composites with different manufacturing conditions. *Wear* 2009;267:593.
- [19] Laha T, Chen Y, Lahiri D, Agarwal A. Tensile properties of carbon nanotube reinforced aluminum nanocomposite fabricated by plasma spray forming. *Compos A* 2009;40:589.
- [20] Kang K, Bae G, Kim B, Lee C. Thermally activated reactions of multi-walled carbon nanotubes reinforced aluminum matrix composite during the thermal spray consolidation. *Mater Chem Phys* 2012;133:495.
- [21] Kang K, Bae G, Won J, Lee C. Mechanical property enhancement of kinetic sprayed Al coatings reinforced by multi-walled carbon nanotubes. *Acta Mater* 2012;60:5031.
- [22] Laha T, Agarwal A. Effect of sintering on thermally sprayed carbon nanotube reinforced aluminum nanocomposites. *Mater Sci Eng A* 2008;480:323.
- [23] Ci L, Ryu Z, Jin-Phillipp NY, Ruhle M. Investigation of the interfacial reaction between multiwalled carbon nanotubes and aluminum. *Acta Mater* 2006;54:5367.
- [24] Agarwal A, Bakshi SR, Lahiri D. Carbon nanotubes: reinforced metal matrix composites. Boca Raton, FL: CRC Press; 2010, ISBN 9781439811498.
- [25] Lahiri D, Bakshi SR, Keshri AK, Liu Y, Agarwal A. Dual strengthening mechanisms induced by carbon nanotubes in roll bonded aluminum composites. *Mater Sci Eng A* 2009;523:263.

- [26] Kelly A, Tyson WR. Tensile properties of fibre-reinforced metals: copper/tungsten and copper/molybdenum. *J Mech Phys Solids* 1965;13:329–50.
- [27] Lourie O, Cox DM, Wagner HD. Buckling and collapse of embedded carbon nanotubes. *Phys Rev Lett* 1998;81:1638.
- [28] Wagner HD, Lourie O, Feldman Y, Tenne R. Stress-induced fragmentation of multiwall carbon nanotubes in a polymer matrix. *Appl Phys Lett* 1998;72:188.
- [29] Filleter T, Bernal R, Li S, Espinosa HD. Ultrahigh strength and stiffness in cross-linked hierarchical carbon nanotube bundles. *Adv Mater* 2011;23:2855.
- [30] Qian D, Dickey EC, Andrews R, Rantell T. Load transfer and deformation mechanisms in carbon nanotube-polystyrene composites. *Appl Phys Lett* 2000;76:2868.
- [31] Deng F, Ogasawara T, Takeda N. Tensile properties at different temperature and observation of micro deformation of carbon nanotubes–poly(ether ether ketone) composites. *Compos Sci Technol* 2007;67:2959.
- [32] Boesl BP, Bourne GR, Sankar BV. Insitu multiscale analysis of fracture mechanisms in nanocomposites. *Compos B* 2011;42:1157.
- [33] Xia Z, Riester L, Curtin W, Li H, Sheldon B, Liang J, et al. Direct observation of toughening mechanisms in carbon nanotube ceramic matrix composites. *Acta Mater* 2004;52:931.
- [34] Yamamoto G, Shirasu K, Hashida T, Takagi T, Suk JW, An J, et al. Nanotube fracture during the failure of carbon nanotube/alumina composites. *Carbon* 2011;49:3709.
- [35] Carlton CE, Ferreira PJ. *In situ* TEM nanoindentation of nanoparticles. *Micron* 2012;43:1134.
- [36] Lockwood AJ, Inkson BJ. *In situ* TEM nanoindentation and deformation of Si-nanoparticle clusters. *J Phys D Appl Phys* 2009;42:035410.
- [37] Bakshi SR, Keshri AK, Singh V, Seal S, Agarwal Arvind. Thermodynamic analysis and experimental verification of interfacial reactions in CNT reinforced Aluminum Silicon composites. *J Alloys Compd* 2009;481:207.

Available at www.sciencedirect.com

ScienceDirect

journal homepage: www.elsevier.com/locate/carbon

Oxidation behavior of graphene nanoplatelet reinforced tantalum carbide composites in high temperature plasma flow

Andy Nieto^a, Amit Kumar^b, Debrupa Lahiri^a, Cheng Zhang^a, Sudipta Seal^b, Arvind Agarwal^{a,*}

^a Plasma Forming Laboratory, Nanomechanics and Nanotribology Laboratory, Mechanical and Materials Engineering, 10555 West Flagler Street, EC 3464, Florida International University, Miami, FL 33174, USA

^b AMPAC and Nanoscience Technology Center, 4000 Central Fl Boulevard, University of Central Florida, Orlando, FL 32816, USA

ARTICLE INFO

Article history:

Received 17 August 2013

Accepted 8 October 2013

Available online 19 October 2013

ABSTRACT

Graphene nanoplatelets (GNP) reinforced tantalum carbide (TaC) composites are exposed to a high temperature plasma flow in order to evaluate the effects of GNP on the oxidation behavior of TaC at conditions approaching those of hypersonic flight environments. The addition of GNP is found to suppress the formation of the oxide layer by up to 60%. The high thermal conductivity of GNPs dissipates heat throughout the sample thereby reducing thermal gradients and reducing the intensity of heating at the surface exposed to plasma. In addition, GNPs enhance oxidation resistance by providing toughening which suppresses crack formation and bursting that accelerates oxidation. Scanning electron microscopy (SEM) and high resolution transmission electron microscopy (HR-TEM) reveal that GNPs have the ability to survive the intense high temperature of the plasma. GNPs are believed to seal oxide grain boundaries and hinder the further influx of oxygen. GNPs also provide nano sized carbon needed to induce the localized reduction of Ta₂O₅ to TaC. Micro computed X-ray tomography (MicroCT) validates that the above mechanisms protect the underlying unoxidized material from the structural damage caused by thermal shocks and high shear forces, by reducing thermal gradients and providing toughening.

© 2013 Elsevier Ltd. All rights reserved.

1. Introduction

Tantalum carbide (TaC) is an ultra high temperature ceramic (UHTC) with potential applications in high temperature aerospace systems such as hypersonic missiles, planetary entry vehicles, and SCRAM jet engines [1–3]. The high melting point (3880 °C) [4] and resistance to chemical attack make TaC an ideal candidate for surviving the extreme conditions of hypersonic flows. TaC oxidizes at temperatures as low as 400 °C (Ta₂O₅), however, both the oxides (1872 °C [5]) and other stoichiometric variants of tantalum carbide (>2500 °C [6]) possess high melting

points. The high density of TaC (14.65 g/cm³) [7] makes it more promising for leading edge components as compared to lower density UHTCs such as ZrB₂ and HfB₂ (6.12 g/cm³ [8] and 11.21 g/cm³ [8] respectively) as it facilitates the shifting of the aerodynamic center forward. The extreme shock waves experienced during hypersonic flight mandate that the candidate material should possess excellent mechanical properties alongside resistance to oxidation and chemical attack. TaC has high hardness (13.5–20 GPa) [9] and high elastic modulus (477–560 GPa) [9], however the low fracture toughness (4–5 MPa m^{1/2}) [10] makes it currently unviable for aerospace applications.

* Corresponding author. Fax: +1 305 348 1932.

E-mail address: agarwala@fiu.edu (A. Agarwal).

0008-6223/\$ - see front matter © 2013 Elsevier Ltd. All rights reserved.

<http://dx.doi.org/10.1016/j.carbon.2013.10.010>

Previous studies in our lab reported the use of carbon nanotubes (CNT) as reinforcement for TaC [7,11]. It was found that short CNTs that transformed into graphene platelets resulted in the largest improvements in toughness and rupture strength. Graphene nanoplatelets are carbon allotropes consisting of few (20–40) layers of graphene with a high aspect ratio [12]. Graphene nanoplatelets have been shown to be promising fillers for improving the fracture toughness of Si_3N_4 [13–17], Al_2O_3 [18–26], and ZrB_2 [27] matrix composites. In our previous work [28,29] Graphene nanoplatelets are used to reinforce TaC in order to improve toughness, damping behavior, and consolidation. Addition of GNP leads to increased densification, reduced grain growth, and enhancements in toughness and damping of up to 99% [28] and 300% [30] respectively. The high electrical and thermal conductivities of GNPs aid in uniformly sintering the composites without inducing phase transformations. GNP wraps the grains and inhibits grain growth. The primary mechanisms responsible for improving the toughness and damping of the TaC–GNP composites are the unique energy dissipating mechanisms of GNP such as sheet bending, sliding, and pull-out.

While improving the mechanical properties of TaC is a crucial step in making it a viable material, it is not sufficient if the oxidation properties are not also improved upon. The improvement of the oxidation behavior is crucial as formation of oxides consume the high strength parent material while the oxides themselves have low structural integrity. When evaluating the oxidation behavior of a UHTC it is necessary to go beyond the conventional isothermal furnace exposure tests and evaluate the materials response in an environment approaching the conditions experienced during hypersonic flight. UHTCs in service will likely fail by a combination of melting, ablation, spalling, sublimation, and oxidation [30]. Several oxidation tests have been carried out on UHTCs under extreme aerothermal conditions using oxyacetylene torches [31–34], plasma arc jets [35–39], subsonic plasma wind tunnels [40], and supersonic plasma wind tunnels [30,41–45]. These tests closely approximate the intense aero-thermal loads experienced during hypersonic flight because of the extreme temperatures and high speeds of the flows. The high speeds of the flow during these tests provide high shear stresses that can influence the microstructural evolution and lead to mechanical failure. The temperatures of the flow also typically exceed 2000 °C which is high enough to melt most UHTC oxides.

While only one aerothermal oxidation study has been done on TaC to date [34], several studies have been conducted on ZrB_2 –SiC composites [32,37,40–42,44] and hafnium based UHTCs [31,38]. Studies comparing oxidation of ZrB_2 –SiC with Si_3N_4 –SiC in a high temperature supersonic plasma flow revealed how the phase transformations and superior thermal conductivity of ZrB_2 –SiC resulted in superior oxidation behavior [40]. The enhanced thermal conductivity leads to less severe thermal gradients while the formation of boride and silicates provides protective glassy phases that inhibit the penetration of oxygen.

In this work, TaC–GNP composites are exposed to a high temperature plasma flow for 60 s. The plasma is generated by a direct current (DC) plasma spray gun and reaches temperatures of ~ 2500 °C. Oxidation behavior is characterized

in terms of oxide layer formation, oxide layer microstructure, and thermal gradients during testing. These high temperature oxidation tests are complimented by steady state isothermal TGA experiments done for 120 min at 1000 °C. It is found that GNPs improve the oxidation behavior by providing structural toughness, enhancing the thermal conductivity, and inducing localized reducing conditions.

2. Materials and methods

2.1. Materials

The TaC powder (1:1 Ta:C ratio) used was obtained from Infra-mat Advanced Materials LLC, CN, USA and had a purity of 99.7% (major impurities were <0.15% free carbon, 0.15–0.30% oxygen, and <0.3% niobium). Graphene nanoplatelets (xGNP-M-5) were obtained from XG Sciences, Lansing, MI, USA. The GNP particles have an average diameter of 15 μm and a thickness of 6–14 nm (20–40 graphene layers). In accordance with the recent editorial on the nomenclature of graphenic materials [46], it is clarified here that the term GNP should indeed refer to graphite nanoplatelets rather than graphene nanoplatelets. The GNPs here consist of over 10 graphene layers and therefore do not merit the term graphene as per the editorial. However, this work retains the term graphene for consistency with our previous works. The GNPs have a relative surface area of 120–150 m^2/g [12] and an aspect ratio of ~ 1500 . The GNPs have functional groups at the edges consisting of approximately 0.075% ether, 0.035% carboxyl, and 0.03% hydroxyl groups [12]. TaC reinforced with 1 vol.% (TaC-1G), 3 vol.% (TaC-3G), and 5 vol.% (TaC-5G) of GNP are synthesized by mixing TaC powder and GNP powder by wet chemistry methods. The composite powders are consolidated to bulk samples by spark plasma sintering (SPS) using a 20 mm graphite die with sintering parameters of 1850 °C, 80–100 MPa, and a holding time of 10 min.

2.2. Oxidation tests

2.2.1. High temperature plasma flow tests

The high temperature plasma jet tests are conducted using a SG 100 DC plasma gun (Praxair, Danbury, CT, USA) operating at a plasma power of 32 kW. Plasma is generated with the primary gas, argon, flowing at 56 slpm and the secondary gas, helium, flowing at 60 slpm. This plasma gun is typically used to deposit thermal sprayed coatings. Plasma spray guns generate plasma at temperatures above 10,000 °C and deposit powders at speeds of 75–300 m/s [47], making them an excellent choice for simulating the extreme conditions experienced during hypersonic flight. The setup for testing the TaC–GNP composites is shown in Fig. 1. The plasma gun is set at a stand-off distance of 50 mm relative to the TaC–GNP sample. This stand-off distance is sufficiently large that it ensures the sample will not be fully immersed in the plasma flow and will therefore be exposed to substantial amount of oxygen from the atmosphere. The TaC–GNP sample is held in position using a tungsten fixture and exposed for 60 s.

The tungsten fixture has a small 1 mm diameter hold drilled into the backside in order to accommodate a

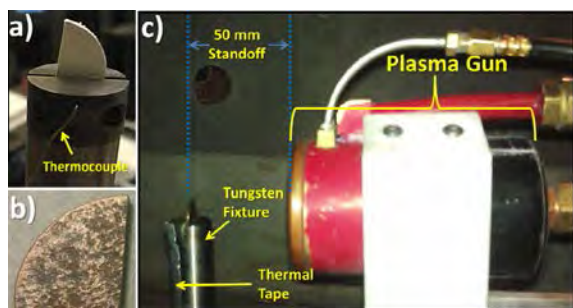


Fig. 1 – Setup for plasma flow oxidation experiments, (a) tungsten fixture for holding samples, small hole in the back allows for insertion of thermocouple to record backside temperature in situ, (b) typical geometry of TaC-GNP samples tested and (c) plasma gun at a standoff distance of 50 mm to sample. (A color version of this figure can be viewed online.)

thermocouple for measuring the backside temperature in situ. A K-type thermocouple (KMQSS-02OU, Omega Engineering Inc., Stamford, CN, USA) is inserted into the hole and bent at an upwards angle in order to ensure proper contact with the sample backside. Thermal tape is used in order to protect the thermocouple from thermal damage. The backside temperatures do not exceed the thermocouple's limit ($\sim 1200^\circ\text{C}$) during the 60 s oxidation test; however the temperatures on the front side are significantly higher and therefore unsuitable for measurement via thermocouple. The front side of the sample is not directly measured in this experimental set-up. Instead, the front side temperature is gauged by using accuraspray in-flight particle diagnostic sensor (Tecnar Automation Ltd, QC, Canada) to estimate the temperature at a distance of 50 mm from the plasma gun. Accuraspray temperature is measured to be $2575 \pm 55^\circ\text{C}$. Assuming a steady state condition is reached after some time at the front surface, $2575 \pm 55^\circ\text{C}$ can be approximated as the front side temperature in order to qualitatively gauge the temperature gradient. The desire to evaluate as large a test sample as possible combined with the limited amount of material available from the TaC-GNP compacts dictates the irregular sample shape shown in Fig. 1c. The samples are quarter-ellipses with major axis lengths of ~ 15 mm and minor axis lengths of ~ 10 mm. The samples have a thickness of ~ 1.0 – 1.5 mm.

2.2.2. Steady state isothermal thermal gravimetric analysis (TGA)

Thermal gravimetric analysis (TGA) was done using an SDT Q600 (TA Instruments, New Castle, DE, USA). The samples were placed in an alumina crucible during the tests. The temperature is rapidly increased (heating rate $>250^\circ\text{C}/\text{min}$) to 1000°C and held at steady state equilibrium. The initial weight is recorded once the steady state equilibrium is reached. Samples used for TGA testing has an initial starting mass of ~ 10.0 – 15.0 g, samples were obtained by fracturing the samples and obtaining small chips. It is emphasized that the TGA study is not the central focus of this work. TGA studies are used to compliment the plasma flow oxidation in order to further strengthen the proposed GNP oxidation mechanisms.

2.3. Structural characterization

Cross sections of the TaC-GNP oxidized samples were prepared by grinding and polishing to a $0.3\ \mu\text{m}$ finish using SiC polishing papers (up to 600 grit size) and diamond slurries. The cross sections were examined in a Buehler Versamet 3 Optical Microscope (Illinois, USA) in order to measure the thickness of the oxide layers. Scanning electron microscopy of the TaC-GNP samples before and after oxidation was done using a JEOL JSM-6330F field emission scanning electron microscope (FE-SEM) with an operating voltage of 15 kV. Energy dispersive spectroscopy (EDS) of the oxidized TaC-GNP cross sections was done in a JEOL JSM 5900LV SEM equipped with an EDAX EDS system. Phase analysis is done by X-ray diffraction (XRD) using a Siemens D-500 X-ray diffractometer operating at a current and voltage of 40 mA and 40 kV respectively. Transmission electron microscopy of the oxidized TaC-GNP samples was done using a Philips/FEI Tecnai high-resolution TEM operating at a voltage of 300 keV. Sample preparation consisted of crushing the brittle oxides to a fine powder and dispersing into an acetone solution via ultrasonication. Forward and inverse fast Fourier transforms (FFT) are done using Gatan Inc. Digital Microscope software in order to accurately measure lattice plane spacings. Micro computed X-ray tomography (MicroCT) was done at XRADIA (Pleasanton, California, USA) using a VersaXRM-500. MicroCT scan was performed with a voxel size of $0.58\ \mu\text{m}$, a field of view of 0.58 mm, and X-ray beam energy of 70 kV. Microhardness testing of the oxide layers was done using a HXD-1000 TMC microhardness tester (Shanghai Taiming Optical Instrument Co. Ltd, Shanghai, China) using a Vickers tip in order to characterize the structural integrity after oxidation. A load of 100 g (~ 1 N) was used with a holding time of 15 s.

3. Results and discussion

3.1. Pre-oxidation microstructural characterization

The synthesis and characterization of TaC-GNP composites is briefly described here, details can be found elsewhere [28]. The resulting TaC-GNP compacts consolidated by spark plasma sintering have high relative densities, ranging from $\sim 94\%$ for pure TaC to $\sim 99\%$ for TaC-5G. The grain sizes of the compacts ranges from $\sim 4.5\ \mu\text{m}$ for TaC to $\sim 1.5\ \mu\text{m}$ for TaC-3G and TaC-5G. The GNPs form networked structures such as that shown in Fig. 2a, in both the TaC-3G and TaC-5G structures. The GNPs wrap and weave around grains as shown in Fig. 2b, grain wrapping inhibits grain growth and promotes more effective sintering because of the high thermal and electrical conductivity of GNPs. The networked GNP structures enable GNP energy dissipating mechanisms to effectively toughen the composite structure.

3.2. Oxide layer formation

Fig. 3 shows TaC and TaC-5G samples post oxidation. It can be seen that TaC and TaC-5G samples survived 60 s exposure to the high temperature plasma flow. No visible structural damage, such as chipping or spallation, has occurred. The

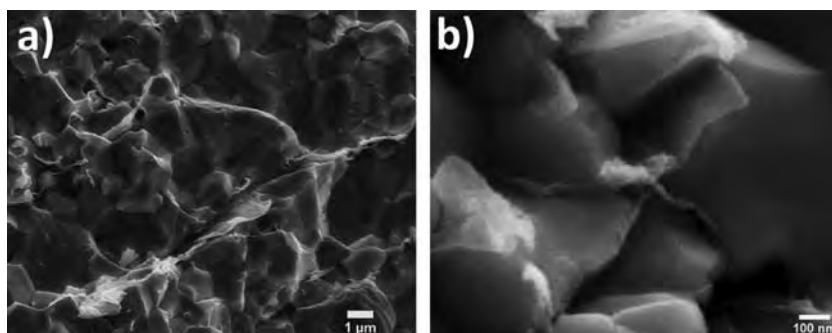


Fig. 2 – SEM micrographs showing distribution of GNPs in TaC–GNP composites, (a) GNPs wrap and weave around TaC grains to form a networked structure in TaC-3G and (b) GNP grain wrapping inhibits grain growth and provides toughness.

samples are fully covered by a rough white oxide layer which is confirmed by XRD, shown in Fig. 4, to be mostly Ta_2O_5 . Ta_2O_5 formation occurs by the simple oxidation reaction given in Eq. (1):



other minor phases present include TaO_3 , Ta_4C_3 , TaC, Ta, and free carbon (graphite). Traces of melting can be seen at the edges of the samples in Fig. 2, as evidenced by the presence of a glassy phase. The glassy phase is the result of the oxide melting and rapidly solidifying once the plasma is turned off. The presence of glassy phases indicates the temperature experienced is in excess of 1872°C , the melting temperature of Ta_2O_5 [5]. The primary quantification of the oxidation performance of the TaC–GNP composites is done by measuring the thickness of the formed oxide layer. The thickness of the front oxide layer is provided in Fig. 5. The front side oxide layer is of interest as it was directly exposed to the $\sim 2500^\circ\text{C}$ plasma flow. It can be seen that the GNP reinforced samples have oxide layers that are significantly thinner than the TaC sample. The insets show optical micrographs of the cross sections of the thickest oxide layer (TaC), and the thinnest oxide layer (TaC-3G). The addition of GNP thus suppresses the formation of the oxide layer by up to 60%. The differences in oxide layer formation with varying GNP content are minor and not a focus of discussion. The addition of GNP is believed to enhance the oxidation resistance and suppress the formation of the oxide layer due to an enhanced thermal conductivity, microstructural interactions, and the formation of

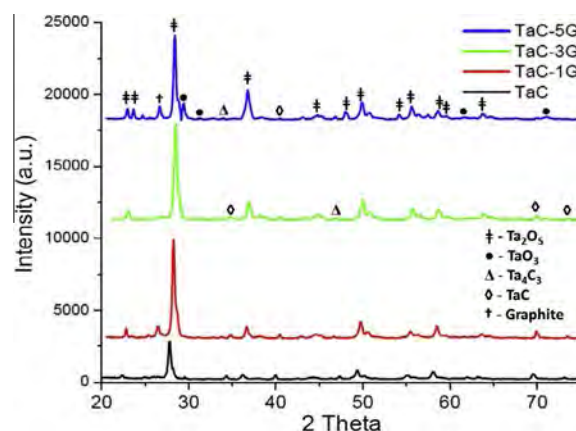


Fig. 4 – X-ray diffractions (XRD) patterns of TaC–GNP samples after exposure to high temperature plasma flow for 60 s. (A color version of this figure can be viewed online.)

localized reducing conditions, which is elucidated in following sections.

3.3. GNP oxidation mechanisms

3.3.1. Enhanced thermal conductivity

GNP has a thermal conductivity ($5.3 \times 10^3 \text{ W/m K}$) [22] that is two orders of magnitude higher than TaC (30 W/m K) [48]. In our previous work [28] it was postulated that GNP increased the thermal conductivity of the composite powder leading

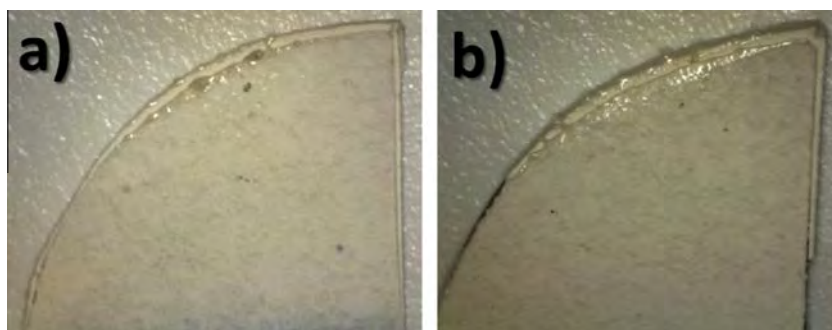


Fig. 3 – TaC–GNP samples after exposure to high temperature plasma flow for 60 s, (a) TaC and (b) typical TaC–GNP samples – TaC-5G. (A color version of this figure can be viewed online.)

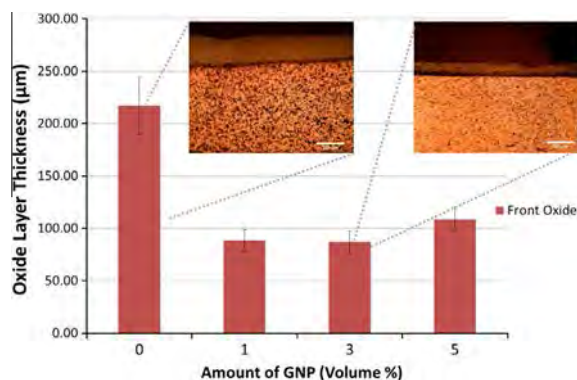


Fig. 5 – Front side and back side oxide layer thickness of TaC–GNP samples. Insets show optical micrographs of thickest oxide (TaC) and thinnest oxide (TaC-3G). The scale bar on insets reads 200 μm. (A color version of this figure can be viewed online.)

to more uniform heating during sintering process. In the present study, the effects of thermal conductivity are directly observed by analyzing the thermal gradients experienced during the exposure to the plasma flow. As explained in Section 2.2.1, the front side temperature was assumed to reach equilibrium with the plasma flame and the backside temperatures were measured *in situ* during exposure to the plasma flow. The thermal gradients of the TaC–GNP samples are presented in Fig. 6a. The time zero is taken once the oxidation tests have begun and hence the starting gradients are not the same. The small oscillations in the thermal gradient at the onset of testing are due to the initial turbulence of the plasma flow. It can be seen that the largest thermal gradient is experienced by the TaC sample while the TaC-3G and TaC-5G samples have the lowest. Given that experimental conditions and sample sizes were similar, the thermal gradient is inversely proportional to the thermal conductivity. The addition of

GNPs can be seen to increase the thermal conductivity, with the effect leveling off at 3 vol.% GNP.

The effect of enhanced thermal conductivity on the oxidation behavior is schematically illustrated in Fig. 6b. Improved thermal conductivity reduces the oxidation of the TaC–GNP by more effectively transferring heat throughout the sample. The transferring of heat is especially effective in the TaC-3G and TaC-5G samples where GNPs were seen to form networked structures [28] as shown in Fig. 2. As illustrated in Fig. 6b, by effectively transferring heat away from the front of the sample, the regions with the most intense heating is greatly reduced. The lower intensity heating provides less energy for the oxidation of TaC to Ta₂O₅. The effective conduction of heat away from the leading edge is essential for the hypersonic flight applications for which the use of TaC is intended [3]. In a hypersonic body, the extreme heating conditions are drastically reduced away from the stagnation point, making it desirable to transfer heat from the high flux stagnation point to the relatively ‘cool’ components downstream of the flow.

3.3.2. GNP microstructural interactions

In order to understand GNP microstructural mechanisms we first compare the microstructures of the oxidized TaC and the TaC–GNP composites. SEM micrographs of the surface directly exposed to the plasma flow are provided in Fig. 7. Fig. 7a and c, show how the morphology of the oxide varies dramatically between TaC and GNP reinforced TaC samples. Multiple chasms, 7–26 μm in span (avg. 10.4 μm), can be seen on the TaC sample. High magnification images in Fig. 7b, show that the material is peeling outwards indicating that the chasm is a result of a bursting phenomenon. The inset in Fig. 7b, shows that the area inside the chasm is heavily oxidized. It is therefore believed that the bursting is caused by an accumulation of CO and CO₂ gases trying to escape the sample. These large chasms accelerate the oxidation process by providing an easier route for oxygen infiltration into the sample.

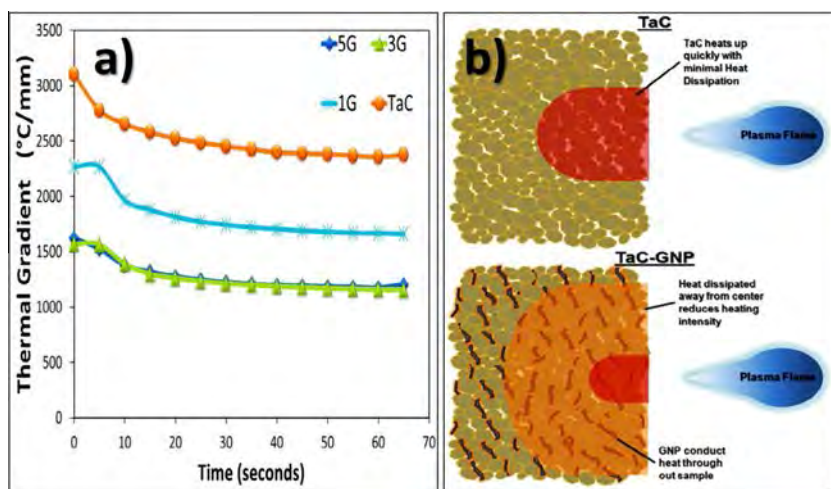


Fig. 6 – (a) Thermal gradients of TaC–GNP samples, backside temperatures were recorded *in situ* while front side temperatures were assumed to reach and remain close to the flame temperature and (b) schematic illustrating the change in heat transfer with higher thermal conductivity. Higher thermal conductivity of GNPs enables higher heat dissipation throughout the sample, thereby decreasing the intensity of heat near the front surface. Decreased heat at the front surface reduces the amount of energy available to drive the oxidation of TaC. (A color version of this figure can be viewed online.)

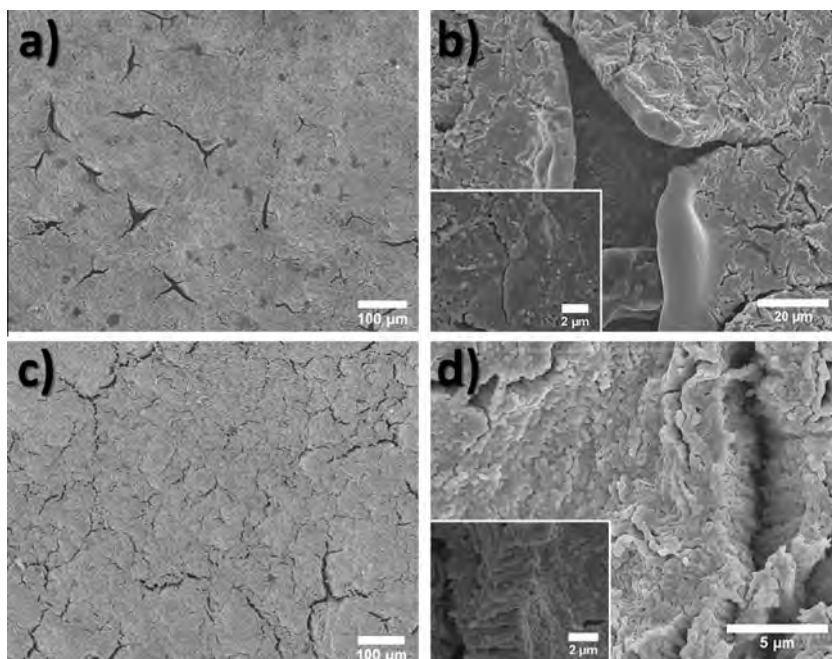


Fig. 7 – Microstructures of TaC–GNP oxidized samples, (a) TaC sample displays large ‘burst out’ regions, (b) area around burst appears to have been in a molten state, inset shows region inside burst is heavily oxidized, (c) TaC–GNP samples display large cracks with some areas bulging out and (d) regions with heavy cracking are peeling but not bursting, inset shows region near bulge maintain crystalline structure.

In contrast, the TaC–GNP samples show no signs of large chasms; cracks ranging in intensity are seen throughout the sample. Fig. 7d, provides a high magnification image of one of the cracks and it can be seen that the area around the crack is bulging out, however it is not severe enough to expose the underlying oxide layer. The largest cracks where bulging occurs have widths of 1–5 μm (avg. 3.9 μm), which are significantly smaller than the deep chasms found in TaC. The structure of the bulged region in the TaC–GNP samples is also vastly different from the edge of the burst regions in the TaC sample. The edge of the TaC bursts shows a smooth glassy structure indicating that partial melting has occurred as a result of the severe temperatures. The TaC–GNP structures however, as can be seen in the inset of Fig. 7d, maintain the crystalline structure of the oxide. As discussed in the previous section, the higher thermal conductivity of the TaC–GNP samples enhances heat flow away from the front surface leading to lower temperatures near the front surface.

In addition to severe heating conditions, the initiation of bursting requires that the pressure of gases accumulating beneath the surface exceeds the strength of the oxide. It is known that the TaC–GNP samples are up to 99% tougher than the TaC samples [28]. It is possible that some of this toughening effect carries over in the formed oxide structure. The porous structure makes it unviable for evaluating the toughness by the Vickers Indentation Method. However, measuring the microhardness of the oxide structures gives a measure of the structural integrity of the formed oxide. The microhardness results of the oxide layers are presented in Fig. 8. The variation is high due to the highly porous nature of the oxide; however the trend clearly indicates that the GNP reinforced samples have a higher hardness and therefore a superior

structural integrity. This enhanced strength allows the GNP reinforced samples to better resist bursting and spallation. The lower hardness of the TaC–5G sample as compared to the other GNP reinforced samples is attributed to the uneven distribution of GNPs which causes some areas to be devoid of GNPs and hence the toughening effect to be absent.

To further understand the role of GNPs in enhancing oxidation resistance, SEM analysis was used to gauge whether GNPs survived the harsh environment due to plasma flow. Fig. 9 provides SEM and TEM micrographs of several carbon structures found in the TaC–GNP oxide layers. Fig. 9a, shows

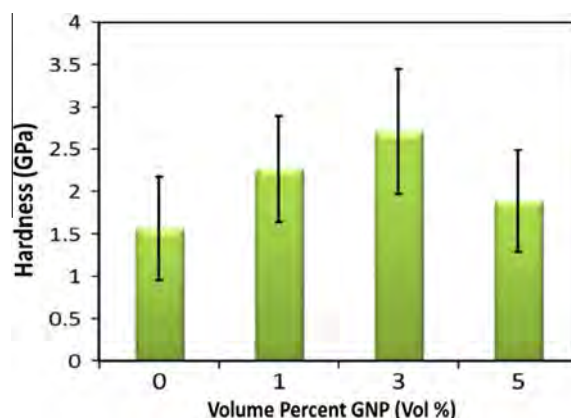


Fig. 8 – Microhardness of TaC–GNP oxide layers. Higher hardness values in GNP reinforced samples indicate higher structural integrity. Less severe cracking was observed in GNP reinforced sample microstructures. (A color version of this figure can be viewed online.)

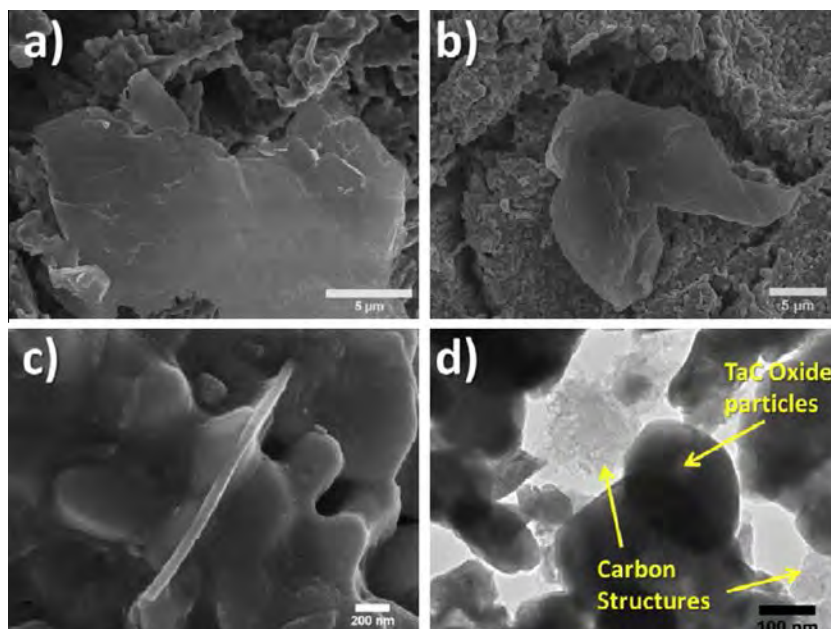


Fig. 9 – SEM and TEM analysis showing survival of GNPs and other carbonaceous structures, (a) SEM of smooth undamaged GNP, (b) SEM of charred and heavily wrinkled GNP, (c) SEM of carbon band embedded in oxide structures and (d) TEM of fine carbon structures among the TaC oxide particles. (A color version of this figure can be viewed online.)

a 15 μm GNP that appears to have undergone little to no damage during the oxidation process. Fig. 9b, shows a GNP that has appeared to become charred and lightly damaged as a result of the plasma flow. Evidence of finer carbon structures originating from the GNP are shown in the form of embedded submicron carbon bands in Fig. 9c, and in the form of 100 nm sized particles in the TEM micrograph in Fig. 9d. These micrographs provide substantial evidence that GNP have the ability to survive to some extent the harsh conditions of the plasma flow. The survival of GNPs can be partially attributed to the insulating effect of the TaC matrix. The survival of GNPs indicates that GNPs may be able to play a more active role in resisting oxidation, which is elucidated below.

It is known that GNPs wrap around grains and form weaving networked structures [13–20,28]. It is postulated here that wrapped GNP can effectively “seal” the grain boundaries and

inhibit the influx of oxygen through grain boundaries. This GNP grain sealing mechanism is most effective if GNP survive the harsh conditions. The mechanism by which grain sealing inhibits the influx of oxygen is schematically presented in Fig. 10. Oxygen encountering a sealed grain boundary may be forced to seek a more arduous path around the sealed grain boundary.

The oxygen may also diffuse through the GNP which requires more energy than diffusing through a high energy

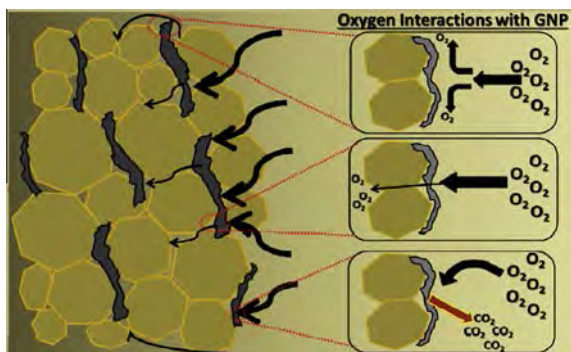


Fig. 10 – Schematic illustrating how grain sealing mechanism hinders diffusion of oxygen into the TaC–GNP structure. (A color version of this figure can be viewed online.)

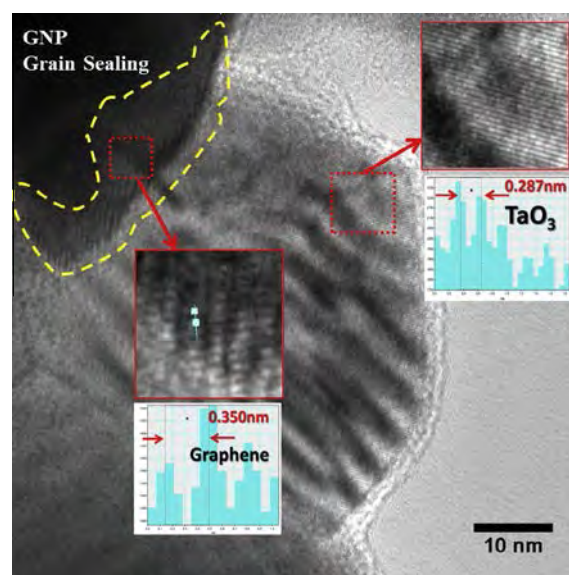


Fig. 11 – TEM micrograph showing carbon structures wrapping and effectively sealing two TaC oxides grains. TaO₃ spacing is that of (040) planes. (A color version of this figure can be viewed online.)

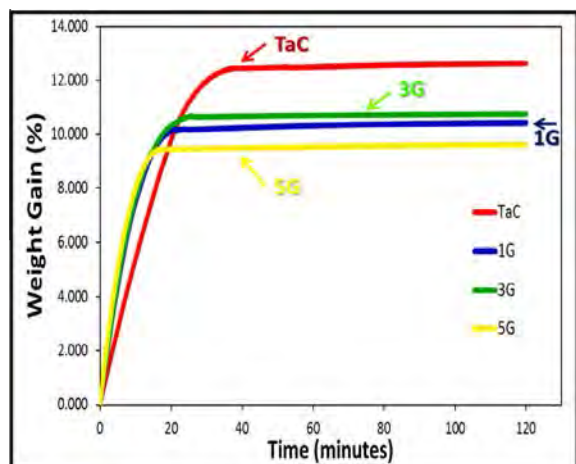


Fig. 12 – Thermal gravimetric analysis (TGA) at 1000 °C shows GNP reinforced samples oxidize to a lower extent. GNP grain sealing is dominant mechanism at this temperature range. (A color version of this figure can be viewed online.)

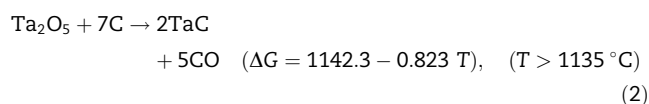
grain boundary. The GNP may also oxidize as well as would be expected, this consumes oxygen, making less oxygen available to penetrate further into TaC. The HR-TEM micrograph of the oxide layer in Fig. 11 provides evidence of GNP sealing a grain boundary and surviving the plasma flow. The GNP structure, identified by its signature ~ 0.35 nm layer spacing, lies on top of a TaO_3 grain and an unidentifiable oxide grain effectively sealing the grain boundary. The survival of the GNP indicates the plausibility of GNP hindering oxygen influx throughout the oxidation process by both physical and chemical means.

The effect of the grain sealing mechanism is further explored by isothermal TGA experiments on TaC and TaC–GNP samples at 1000 °C. The conditions here are not nearly as severe and therefore the effects of bursting and increased structural integrity don't play a role here. Any improvements in the oxidation behavior would be largely due to GNP grain sealing mechanisms. The TGA results are shown in Fig. 12 and it can be seen that all GNP reinforced TaC samples oxidize to a lower extent than the TaC sample. The conditions here are less

severe and therefore more GNPs are expected to survive, this results in the superior oxidation resistance with higher GNP content. The initial increased oxidation rate in the TaC–GNP samples is due to the higher thermal conductivity of the samples which increases heat flow into the sample.

3.3.3. GNP induced reducing environment

The addition of carbon to carbides has been known to suppress the formation of oxides during sintering [49–51]. Similarly the addition of nano-scale carbon can have the effect of suppressing the formation of oxides in TaC by inducing a localized reducing environment. The reduction of Ta_2O_5 to TaC occurs by the equation given in Eq. (2):



The presence of a high temperature plasma flow in air makes reduction reactions unfavorable; however the nano-scale nature of GNPs could allow for localized reducing environments. GNP showed the ability to survive the oxidation process. These GNPs would provide the source of carbon needed to reduce Ta_2O_5 to TaC above 1135 °C; thus suppressing the formation of the oxide layer. Electron dispersive spectroscopy (EDS) is performed along the cross section of the oxides in order to examine the amounts of carbon and oxygen in the oxide layers. The EDS results for TaC shown in Fig. 13a, indicate that throughout the oxide layer the amount of oxygen exceeds that of carbon. In contrast, EDS results for a typical TaC–GNP sample shown in Fig. 13b, indicate that the oxide layer contains more carbon than oxygen. This increase in carbon content is believed to be due to the presence of carbon from GNPs and that found in TaC. The reduction of oxygen is due to the reduction of Ta_2O_5 to TaC and CO gases which escape the sample. Additional evidence of GNP induced localized reduction environments comes from the HR-TEM micrograph presented in Fig. 14. Analysis of plane spacings reveals that adjacent carbon and TaC phases are embedded in the amorphous structure. The amorphous phase is the result of Ta_2O_5 reaching its melting point of 1872 °C and rapidly solidifying upon cessation of the plasma flow exposure. The high temperature needed to melt Ta_2O_5

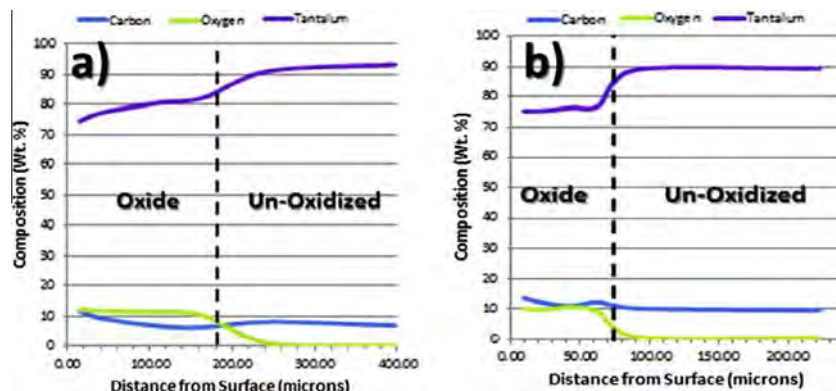


Fig. 13 – Thermal gravimetric analysis (TGA) at 1000 °C shows GNP reinforced samples oxidize to a lower extent. GNP grain sealing is dominant mechanism at this temperature range. (A color version of this figure can be viewed online.)

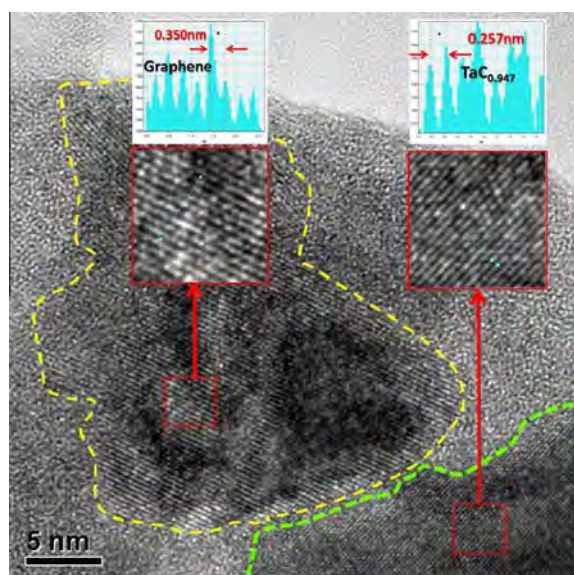


Fig. 14 – TEM micrographs shows presence of TaC near and graphene structure. Both structures are embedded in amorphous structures. Amorphous glassy structures are formed when temperatures exceed $\sim 1100^\circ\text{C}$ and Ta_2O_5 melts. (A color version of this figure can be viewed online.)

also catalyzes the reduction of Ta_2O_5 upon coming across excess carbon provided by the GNP. In a molten state, Ta_2O_5 would provide a protective layer and thus the newly formed TaC would not readily oxidize. The formed CO gases however would be expected to easily escape the molten Ta_2O_5 .

3.3.4. Unoxidized sub layer structural integrity

Aside from the suppression of the formed oxide layer, it is imperative for a UHTC to maintain its structural integrity during exposure to harsh aerothermal conditions. The oxide layer is porous by nature and not expected to provide structural strength; however it is highly desirable for the underlying unoxidized material to maintain its structural integrity. The structure of the TaC and TaC-GNP samples is evaluated at

the interface of the oxide and the unoxidized sub layer by X-ray micro CT. The TaC and TaC-GNP interfaces, shown in Fig. 15 as well as in [Supplementary video files V1 and V2 \(available online\)](#), can be seen to have vastly different morphologies. The TaC interface has large protruding interconnected cracks throughout the surface, while the TaC-GNP sample is largely crack free. The TaC sample experiences severe cracking mostly due to thermal shock. These large cracks further enable the penetration of oxygen thus accelerating the formation of the oxide layer and the consumption of the unoxidized material.

The superior structural integrity of the TaC-GNP interface region is the result of a combination of the mechanisms discussed before. The TaC-GNP samples are inherently tougher and thus less susceptible to cracking because of GNP toughening mechanisms such as grain wrapping. The higher thermal conductivity of TaC-GNP induces small thermal gradients thereby reducing thermal shock which can initiate crack nucleation and propagation. Furthermore, the suppression of cracking at the interface with the oxide layer inhibits the penetration of oxygen deeper into the sample. The addition of GNP therefore not only suppresses the formation of the oxide layer, it protects the underlying unoxidized sub layer from the structural damage.

4. Conclusions

The addition of GNPs is shown to enhance the oxidation resistance of TaC-GNP composites exposed to a high temperature plasma flow. Through several mechanisms unique to GNP, the formation of the oxide layer thickness is suppressed by up to 60%. The high thermal conductivity of GNPs allows heat to flow throughout the sample and away from the front surface which experiences the most extreme conditions. The toughening effect of GNPs enables them to resist cracking due to thermal shock, chemical attack, and the high speed plasma flow. The suppression of cracks is vital to hindering the rate of oxidation as cracks enable the rapid penetration of oxidation. SEM and HR-TEM analysis reveals that GNP survive the extreme oxidizing environment, thereby signaling that GNP may play an active role throughout the oxidation process.

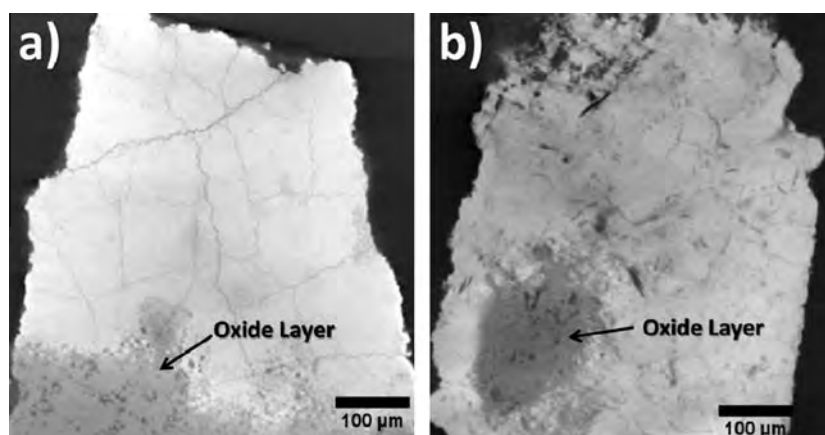


Fig. 15 – Micro computed tomography (MicroCT) results show the interface between formed oxide layer and unoxidized sublayer. The structural integrity of (a) TaC is considerably deteriorated compared to (b) TaC-GNP. Large cracks can be seen at the interface of TaC and the oxide layer in the TaC sample.

A GNP grain sealing mechanism is proposed, in which GNPs seal grain boundaries and inhibit the influx of oxygen. Surviving GNP also induce localized reducing environments by providing excess carbon needed to drive the conversion of the formed oxide, Ta_2O_5 to TaC. X-ray MicroCT analysis reveals that GNP oxidation resistance mechanisms also protect the underlying unoxidized structure from structural damage. The GNP toughening, grain sealing, and thermal conductivity mechanisms are inherent to GNPs and could be extended to other ultrahigh temperature ceramics systems.

Acknowledgements

Authors would like to acknowledge Dr. Ali Sayir, Program Manager of High Temperature Aerospace Materials at the Air Force Office of Scientific Research and FA9550-11-1-0334 and FA9550-12-1-0263 Grants. Dr. Allen Gu and Mr. Bryan Majkrzak at XRADIA are acknowledged for extending the use of their micro computed tomography (Micro CT) facilities. Authors also acknowledge the support of the Advanced Materials Engineering Research Institute (AMERI) at FIU. The authors would like to thank Mr. Thomas Beasley at the Florida Center for Advanced Electron Microscopy (FCAEM) at FIU for his assistance in performing energy dispersive spectroscopy (EDS) analysis.

Appendix A. Supplementary data

Supplementary data associated with this article can be found, in the online version, at <http://dx.doi.org/10.1016/j.carbon.2013.10.010>.

REFERENCES

- [1] Moses PL, Rausch VL, Nguyen LT, Hill JR. NASA hypersonic flight demonstrators – overview, status, and future plans. *Acta Astronaut* 2004;55:619–30.
- [2] Canan JW. Breathing new hope into hypersonics. *Aerosp Am* 2007;11:26–31.
- [3] Squire TH, Marschall J. Material Property requirements for analysis and design of UHTC components in hypersonic applications. *J Eur Ceram Soc* 2010;30:2239–51.
- [4] Chen Y-J, Li J-B, Wei Q-M, Zhai H-Z. Preparation and growth mechanism of TaCx whiskers. *J Crystal Growth* 2001;224:244–50.
- [5] Wuchina E, Opila M, Fahrenholtz W, Talmy I. UHTCs: ultra-high temperature ceramic materials for extreme environment applications. *Electrochem Soc Interface* 2007;30–6.
- [6] Morris RA, Wang B, Thompson GB, Butts D. Variations in tantalum carbide microstructures with changing carbon content. *Int J Appl Ceram Technol* 2013;10.
- [7] Bakshi SR, Musaramthota V, Virzi DA, Keshri AK, Lahiri D, Singh V, et al. Spark plasma sintered tantalum carbide–carbon nanotube composite: effect of pressure, carbon nanotube length and dispersion technique on microstructure and mechanical properties. *Mater Sci Eng A* 2011;528:2538–47.
- [8] Fahrenholtz WG, Hilmas GE, Talmy IG, Zaykoski JA. Refractory diborides of zirconium and hafnium. *J Am Ceram Soc* 2007;90:1347–64.
- [9] Dodd SP, Cankurtaran M, James B. Ultrasonic determination of the elastic and nonlinear acoustic properties of transition-metal carbide ceramics: TiC and TaC. *J Mater Sci* 2003;38:1107–15.
- [10] Kim B-R, Woo K-D, Doh J-M. Mechanical properties and rapid consolidation of binderless nanostructured tantalum carbide. *Ceram Int* 2009;30:3395–400.
- [11] Lahiri D, Khaleghi E, Bakshi SR, Li W, Olevsky EA, Agarwal A. Graphene induced strengthening in spark plasma sintered tantalum carbide-nanotube composite. *Scripta Mater* 2013;68(5):285.
- [12] XG Sciences. xGNP graphene nanoplatelets carbon nanoparticles with multifunctional capability. XG Sciences Documentation; 2009.
- [13] Fan Y, Wang L, Li J, Li J, Sun S, Chen F, et al. Preparation and electrical properties of graphene nanosheet/ Al_2O_3 composites. *Carbon* 2010;48:1743–9.
- [14] He T, Li J, Wang L, Zhu J, Jiang W. Preparation and consolidation of alumina/graphene composite powders. *Mater Trans* 2009;50(4):749–51.
- [15] Wang K, Wang Y, Fan Z, Yan J, Wei T. Preparation of graphene nanosheet/alumina composites by spark plasma sintering. *Mater Res Bull* 2011;46(2):315–8.
- [16] Liu J, Yan H, Reece MJ, Jiang K. Toughening of zirconia/alumina composites by the addition of graphene platelets. *J Eur Ceram Soc* 2012;32:4185–93.
- [17] Liu J, Yan H, Jiang K. Mechanical properties of graphene platelet-reinforced alumina ceramic composites. *Ceram Int* 2013 [in press].
- [18] Walker LS, Marotto VR, Rafiee MA, Koratkar N, Corral EL. Toughening in graphene ceramic composites. *ACS Nano* 2011;5(4):3182–90.
- [19] Ramirez C, Figueiredo FM, Miranzo P, Poza P, Osendi MI. Graphene nanoplatelets/silicon nitride composites with high electrical conductivity. *Carbon* 2012;50:3607–15.
- [20] Dusza J, Morgiel J, Duszova A, Kvetkova L, Nosko M, Kun P, et al. Microstructure and fracture toughness of Si_3Ni_4 +graphene platelet composites. *J Eur Ceram Soc* 2012;32:3389–97.
- [21] Tapasztó O, Tapasztó L, Marko M, Kern F, Gadow R, Balazsi C. Dispersion patterns of graphene and carbon nanotubes in ceramic matrix composites. *Chem Phys Lett* 2011;511:340–3.
- [22] Kun P, Tapasztó O, Weber F, Balazsi C. Determination and mechanical properties of multilayer graphene added silicon nitride-based composites. *Ceram Int* 2012;38:211–6.
- [23] Kvetkova L, Duszova A, Hvizdos P, Dusza J, Kun P, Balazsi C. Fracture toughness and toughening mechanisms in graphene platelet reinforced Si_3N_4 composites. *Scripta Mater* 2012;66:793–6.
- [24] Seiner H, Sedlak P, Koller M, Landa M, Ramirez C, Osendi MI, et al. Anisotropic elastic moduli and internal friction of graphene nanoplatelets/silicon nitride composites. *Compos Sci Technol* 2013;75:93–7.
- [25] Ramirez C, Osendi I. Characterization of graphene nanoplatelets– Si_3N_4 composites by Raman spectroscopy. *J Eur Ceram Soc* 2013;33:471–7.
- [26] Kvetkova L, Duszova A, Kasiarova M, Dorcakova F, Dusza J, Balazsi C. Influence of processing on fracture toughness of Si_3N_4 +graphene platelet composites. *J Eur Ceram Soc* 2013 [in press].
- [27] Yadhukulkrishnan GB, Karamuri S, Rahman A, Singh RP, Kalkan AK, Harimkar SP. Spark plasma sintering of graphene reinforced zirconium diboride ultra-high temperature ceramic composites. *Ceram Int* 2013;39(6):6637–46.
- [28] Nieto A, Lahiri D, Agarwal A. Graphene nanoplatelets reinforced tantalum carbide consolidated by spark plasma sintering. *Mater Sci Eng A* 2013;582:338–46.

- [29] Nieto A, Lahiri D, Agarwal A. Nano dynamic mechanical behavior of graphene nanoplatelets reinforced tantalum carbide. *Scripta Mater* 2013;69:678–81.
- [30] Marshall J, Fletcher DG. High-enthalpy test environments, flow modeling and in situ diagnostics for characterizing ultra-high temperature ceramics. *J Eur Ceram Soc* 2010;30:2323–36.
- [31] Wang YL, Xiong X, Li G-D, Liu H-F, Chen Z-K, Sun W, et al. Ablation behavior of HfC protective coating for carbon/carbon composites in oxyacetylene combustion flame. *Corros Sci* 2012;65:549–55.
- [32] Tang S, Deng J, Wang S, Liu W, Yang K. Ablation behaviors of ultra-high temperature ceramic composites. *Mater Sci Eng A* 2007;465:1–7.
- [33] Paul A, Venugopal S, Binner JGP, Vaidhyanathan B, Heaton ACJ, Brown PM. UHTC-carbon fibre composites: preparation, oxyacetylene torch testing and characterization. *J Eur Ceram Soc* 2013;33:423–32.
- [34] Lashtabeg A, Smart M, Riley D, Gillen A, Drennan J. The effect of extreme temperature in an oxidizing atmosphere on dense tantalum carbide (TaC). *J Mater Sci* 2013;48:258–64.
- [35] Gasch M, Ellerby D, Irby E, Beckman S, Gusman M, Johnson S. Processing, properties and arc jet oxidation of hafnium diboride/silicon carbide ultra high temperature ceramics. *J Mater Sci* 2004;39(19):5925–37.
- [36] Fahrenholtz WG. Thermodynamic analysis of ZrB_2 -SiC oxidation: formation of a SiC-depleted region. *J Am Ceram Soc* 2007;90(1):143–8.
- [37] Zhang X, Hu P, Han J, Meng S. Ablation behavior of ZrB_2 -SiC ultra high temperature ceramics under simulated atmospheric re-entry conditions. *Compos Sci Technol* 2008;68:1718–26.
- [38] Savino R, Fumo MDS, Silvestroni L, Sciti D. Arc-jet testing on HfB_2 and HfC-based ultra-high temperature ceramic materials. *J Eur Ceram Soc* 2008;28:1899–907.
- [39] Savino R, Fumo MDS, Paterna D, Maso AD, Monteverde F. Arc-jet testing of ultra-high-temperature-ceramics. *Aerosp Sci Technol* 2010;14:178–87.
- [40] Alfano S, Scatteia L, Monteverde F, Beche E, Balat-Pichelin M. Microstructural characterization of ZrB_2 -SiC based UHTC tested in the MESOX plasma facility. *J Eur Ceram Soc* 2010;30:2345–55.
- [41] Monteverde F, Savino R, Fumo MDS, Maso AD. Plasma wind tunnel testing of ultra-high temperature ZrB_2 -SiC composites under hypersonic re-entry conditions. *J Eur Ceram Soc* 2010;30:2312–21.
- [42] Sciti D, Savino R, Silvestroni L. Aerothermal behavior of a SiC fiber-reinforced ZrB_2 sharp component in supersonic regime. *J Eur Ceram Soc* 2012;32:1837–45.
- [43] Sciti D, Silvestroni L. Processing, sintering and oxidation behavior of SiC fibers reinforced ZrB_2 composites. *J Eur Ceram Soc* 2012;32:1933–40.
- [44] Monteverde F, Savino R. ZrB_2 -SiC sharp leading edges in high enthalpy supersonic flows. *J Am Ceram Soc* 2012;95(7):2282–9.
- [45] Parthasarathy TA, Petry MD, Cinibulk MK, Mathur T, Gruber MR. Thermal and oxidation response of UHTC leading edge samples exposed to simulated hypersonic flight conditions. *J Am Ceram Soc* 2013:1–9.
- [46] Bianco A, Cheng H-M, Enoki T, Gogotsi Y, Hurt RH, Koratkar N, et al. All in the graphene family – a recommended nomenclature. *Carbon* 2013;65:1–6.
- [47] Fauchais P, Vardelle A, Dussoubs B. Quo vadis thermal spraying? *J Therm Spray Technol* 2001;10(1):44–66.
- [48] Opeka MM, Talmy IG, Wuchina EJ, Zaykoski JA, Causey SJ. Mechanical, thermal and oxidation properties of refractory hafnium and zirconium compounds. *J Eur Ceram Soc* 1999;19:2405–12.
- [49] Sauterau J, Mocellin A. Sintering behavior of ultrafine NbC and TaC powders. *J Mater Sci* 1974;9:761–7.
- [50] Zhang X, Hilmas GE, Fahrenholtz WG, Deason DM. Hot pressing of tantalum carbide with and without sintering additives. *J Am Ceram Soc* 2007;90(2):393–401.
- [51] Gubernat A. Pressureless sintering of single-phase tantalum carbide and niobium carbide. *J Eur Ceram Soc* 2013;33(13–14):2391–8.



This article appeared in a journal published by Elsevier. The attached copy is furnished to the author for internal non-commercial research and education use, including for instruction at the authors institution and sharing with colleagues.

Other uses, including reproduction and distribution, or selling or licensing copies, or posting to personal, institutional or third party websites are prohibited.

In most cases authors are permitted to post their version of the article (e.g. in Word or Tex form) to their personal website or institutional repository. Authors requiring further information regarding Elsevier's archiving and manuscript policies are encouraged to visit:

<http://www.elsevier.com/authorsrights>



Nanodynamic mechanical behavior of graphene nanoplatelet-reinforced tantalum carbide

Andy Nieto,^a Debrupa Lahiri^{a,b} and Arvind Agarwal^{a,*}

^aPlasma Forming Laboratory, Nanomechanics and Nanotribology Laboratory, Mechanical and Materials Engineering, Florida International University, 10555 West Flagler Street, EC 3464, Miami, FL 33174, USA

^bDepartment of Materials and Metallurgical Engineering, Indian Institute of Technology, Roorkee, Uttarakhand 247667, India

Received 6 June 2013; revised 26 July 2013; accepted 27 July 2013

Available online 1 August 2013

Nanodynamic mechanical analysis (nanoDMA) is performed on spark plasma sintered tantalum carbide composites reinforced with graphene nanoplatelets (GNPs). The addition of GNPs enhances damping ($\tan\delta$) at 25–100 Hz frequencies by up to 300%. It also improves damping behavior through energy-dissipating mechanisms, such as GNP bending, kinking and sliding. A model for correlating improvement in the damping behavior with the fracture toughness is presented. GNP energy-dissipating mechanisms are most effective in improving damping behavior when GNPs are dispersed uniformly.

© 2013 Acta Materialia Inc. Published by Elsevier Ltd. All rights reserved.

Keywords: TaC; NanoDMA; Graphene nanoplatelet; Damping; Tan delta

Ultrahigh-temperature ceramics (UHTCs) have attracted much attention because of their excellent refractory properties and high strength. These properties make them ideal candidates for aerospace systems, such as hypersonic missiles, planetary entry vehicles and rocket propulsion systems [1–3]. One of the factors impeding the implementation of these materials is their low fracture toughness. Several studies have been conducted on composite UHTCs designed to improve fracture toughness and flexure strength [4–9]. One crucial property of UHTCs that has received little attention is their poor damping behavior. UHTCs such as tantalum carbide (TaC) will be utilized in hypersonic systems that are subjected to a barrage of shock waves. Shock waves are unsteady phenomena which impart impulse forces onto the surface generating them. Damping of such impulsive forces is critical to preventing accumulative damage. Hypersonic vehicles and spacecraft are also subjected to substantial amounts of vibrations and flutter, which can cause cracking. Improving the dissipation of vibrations can suppress crack nucleation and thus reduce the amount of critical cracks and defects.

Our approach utilizes the addition of graphene nanoplatelets (GNPs) as reinforcement for TaC to enhance both the fracture toughness and the damping behavior.

The details of TaC–GNP composite synthesis, microstructure and fracture toughness can be found elsewhere [10,11]. The motive behind using GNPs as a dampening phase stems from the excellent damping behavior of multi-layer graphene [12]. Lahiri et al. [12] showed that multi-layer graphene membranes improved the damping behavior of a rigid Si/SiO₂ surface by up to 260%. The improvement in damping behavior ($\tan\delta$) was seen at various dynamic loads (0.1–50 μ N) and for a range of frequencies (50–250 Hz). The damping behavior of 10-layer graphene was found to be superior to that of 5-layer graphene, thus raising the prospects that GNPs (20–30 layers) may also exhibit excellent damping properties. Additionally, GNPs have been shown to have intrinsic energy-dissipating mechanisms, such as kinking, bending, sliding and shearing of graphene layers [13].

TaC–GNP composites were prepared with GNP contents of 1 vol.% (TaC-1G), 3 vol.% (TaC-3G) and 5 vol.% (TaC-5G). As-received GNPs (xGNP-M-5, XG Sciences, Lansing, MI, USA) were ultrasonicated in acetone for 90 min in order to alleviate agglomeration. The GNP powder was then mixed with the TaC powder (99.7% purity, $0.36 \pm 0.13 \mu$ m particle size and 1:1 Ta to C ratio; Inframat Advanced Materials LLC, CT, USA) for 60 min. The powders were consolidated by spark plasma sintering using parameters of 100 MPa and 1850 °C [10,11]. The samples achieved high degrees of densification, with relative densities ranging from ~94% to ~99%, as shown in Table 1.

* Corresponding author. Tel.: +1 305 348 1701; fax: +1 305 348 1932; e-mail: agarwala@fiu.edu

Table 1. Summary of TaC–GNP samples used for nanoDMA tests.

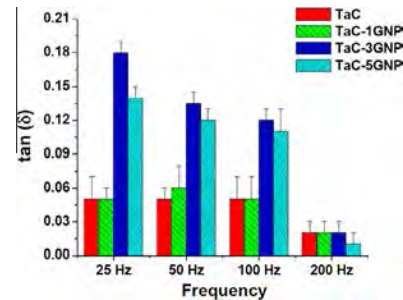
Sample	GNP content (vol.%)	Relative density (%)	Grain size (μm)	DMA sample thickness (μm)
TaC	None	94.4 ± 0.7	4.5 ± 0.9	~ 190
TaC-1G	1	96.9 ± 0.4	3.4 ± 1.6	~ 130
TaC-3G	3	97.5 ± 0.4	1.4 ± 0.6	~ 80
TaC-5G	5	98.8 ± 0.2	1.4 ± 0.7	~ 150

From the bulk consolidated disks, thin slices were prepared for nanodynamic mechanical analysis (nanoDMA) testing. Samples were mounted in epoxy and then ground to a thickness of ~ 0.5 mm and polished to a $0.1 \mu\text{m}$ finish. The sample was then retrieved from the mount and the unpolished surface was ground down further and polished to a $0.1 \mu\text{m}$ finish. The sample was subsequently removed from the mount once again, yielding a thin slice of thickness $< 200 \mu\text{m}$.

Such a thin slice was required as the working principle behind nanoDMA mandates that the sample be placed between two rigid bodies – where one rigid body is the indenter tip. If the sample is too thick, then the role of the non-interacting volume may become significant. As shown in Table 1, the thickness of the samples had some variation; however, these differences are not expected to have an impact, given the high hardness and stiffness of TaC. The thin TaC–GNP sample was placed on an Si/SiO₂ wafer [12] which has very low damping ($\tan\delta \sim 0.06$) and therefore approximates a rigid body. The nanoDMA experiments were carried out using a TriboIndenter TI 900 (Hysitron Inc., Minneapolis, MN, USA) with a 100 nm Berkovich tip. NanoDMA experiments consist of a quasistatic loading and a low-frequency (< 200 Hz) dynamic loading. The nanoDMA tests on TaC–GNP samples were conducted using a 1000 μN quasistatic load with a 7.5% (75 μN) dynamic load. Tests were performed with the dynamic load frequency set at 25, 50, 100 and 200 Hz. $\tan\delta$ is obtained through measurement of the displacement response to the applied force. The angle δ is the phase lag between the force applied and the displacement response – a perfectly elastic material would have zero phase lag. A higher lag indicates a higher ratio of viscoelastic to elastic response in the material and thus $\tan\delta$ serves as a measure of damping.

The values of $\tan\delta$ for the different TaC–GNP composites are presented in Figure 1. It can be seen that the GNP improves the damping behavior of the composite in all cases except at a frequency of 200 Hz. The 200 Hz frequency appears to exceed the recovery time needed for the GNP damping mechanisms to be effective. The effect of the GNPs in the TaC-1G sample is negligible – there are not enough GNPs to make an impact. The TaC-3G and TaC-5G show significant improvement in damping behavior. TaC-3G composite shows the highest $\tan\delta$ especially at the lower frequencies. The TaC-3G sample shows a damping improvement of $\sim 300\%$ over pure TaC at a frequency of 25 Hz. The effect of the GNPs dominates over the potential effects from varying the porosity as the pure TaC sample has the poorest damping despite being the most porous.

To begin to understand the effect of GNPs on the damping behavior of TaC–GNP composites, their effect on the overall microstructure should be understood. The

**Figure 1.** Damping behavior ($\tan\delta$) of TaC–GNP composites at various frequencies.

two principle microstructural features impacted by the GNPs are the grain size and the microstructural homogeneity. Figure 2 presents scanning electron microscopy (SEM) images of the TaC–GNP microstructures as seen from the fracture surfaces. The grain size of the pure TaC sample is the largest, with a slight decrease in the TaC-1G sample, while the TaC-3G and TaC-5G samples experienced substantial grain size reduction (Table 1). GNPs have been shown to inhibit grain growth by grain wrapping and grain pinning [14–16]. Additionally, they increase the electrical and thermal conductivity of the composite powder, and thus more uniform heating is achieved during SPS processing. This leads to a higher and more uniform densification of the sample. It should be noted that GNPs become aligned after consolidation, and thus the enhancement in conductivity may display an anisotropic nature. The distribution of GNPs in the sample is dependent on the amount of GNPs used and the powder processing. It can be seen in Figure 2b that the GNP presence in the TaC-1G sample is scarce. The GNPs are mostly found embedded in grains, as seen in the inset of Figure 2b, or as a few isolated agglomerates. The TaC-3G and TaC-5G samples have a significant perpendicular presence of GNPs. The GNPs are largely oriented perpendicular to the SPS pressing axis [17]. The GNPs in the TaC-3G are widely dispersed and are distributed uniformly throughout the sample, forming a networked structure. The inset of Figure 2c shows GNPs weaving throughout the TaC grains with no signs of agglomeration. The GNPs in the TaC-5G sample are relatively poorly distributed: some areas are saturated with them, while other areas are largely GNP-free (Fig. 2d).

The microstructure of the SPS compacts is reflected in the thin slices used for the nanoDMA testing, as can be seen in SEM micrographs of the TaC and TaC-3G thin slices in Figure 3. The TaC structure shown in Figure 3a shows a compact and rigid ceramic microstructure that is not conducive to viscoelastic behavior. The mere addition of GNPs is not enough to improve the damping behavior if the amount and dispersion of the GNPs is not adequate. The scarcity of GNPs in

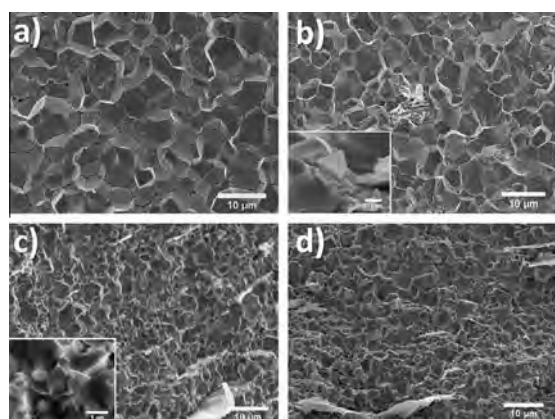


Figure 2. SEM micrographs of TaC–GNP composites. (a) Pure TaC, (b) TaC-1G, with slight grain size reduction (inset: GNP embedded in TaC grains), (c) TaC-3G, with reduced grain size and homogeneous GNP dispersion (inset: well-dispersed and networked GNPs) and (d) TaC-5G, with significant presence of GNPs and some agglomeration.

the TaC-1G structure leads to the lack of improvement in damping behavior. Likewise, the poor dispersion and uniformity of the GNPs in the TaC-5G sample are the cause of the trend reversal in damping behavior as the GNP content is increased from 3 to 5 vol.%. The TaC-3G sample had an adequate amount of GNPs that were effectively disbursed. Figure 3b shows GNPs near the surface of the TaC-3G thin slice where nanoDMA testing was performed. Having established the TaC-3G as the sample with the most effective GNP distribution, the GNP damping mechanisms can now be discussed.

Figure 3b shows that GNPs in the TaC matrix display two general kinds of structure: either they are sandwiched between TaC grains or they display a kinked and corrugated structure. Sandwiched GNPs are expected to behave similarly to multi-layer graphene [12]. Weak van der Waals forces will allow the GNPs to exhibit spring-like behavior and deform in the out-of-plane direction. The compression of sandwiched GNPs will provide some degree of damping to the TaC matrix. Corrugated GNPs display energy-dissipating mechanisms which are unique to GNPs [13]. Figure 4a shows a kinked GNP in the TaC-3G microstructure. The bending and kinking of GNPs requires energy that would otherwise be used in fracture; hence increasing damping. It can be seen from Figure 4a and b that the GNPs bend at angles greater than 90° without fracturing or tearing. The corrugated GNPs also display platelet sliding. Figure 4b shows two GNPs sliding past one another while maintaining their structural integrity and kinked features. Sliding GNPs enable the transfer of shear forces from TaC grains to the GNPs. The sliding of GNPs in addition to bending provides damping to the TaC matrix.

The energy-dissipating mechanisms to improve damping described above can also improve the fracture toughness [10,11]. Table 2 shows the improvement in fracture toughness with varying GNP content. We propose a semi-empirical model here to correlate fracture toughness enhancement with improvement in damping ($\tan\delta$). Improvements in fracture toughness and damping have previously been correlated in plasma-sprayed carbon nanotube-reinforced Al_2O_3 coatings [18].

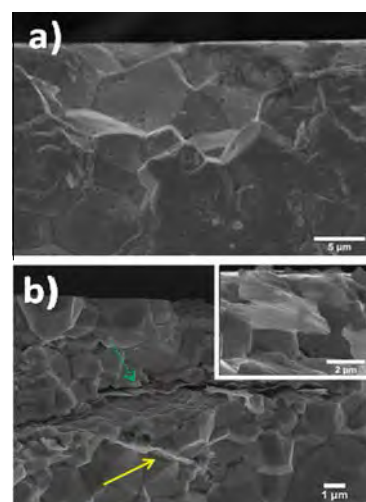


Figure 3. SEM micrographs of (a) TaC and (b) TaC-3G thin slices near surfaces where nanoDMA experiments were performed. Rigidly held TaC grains lead to poor damping behavior. GNPs between TaC grains enhance damping behavior in TaC-3G and TaC-5G. Both sandwiched GNPs (yellow solid arrow) and corrugated GNPs (green dotted arrow) are present in the structure, Inset: GNPs are typically present on the surface of the TaC–GNP samples tested. (For interpretation of the references to colour in this figure legend, the reader is referred to the web version of this article.)

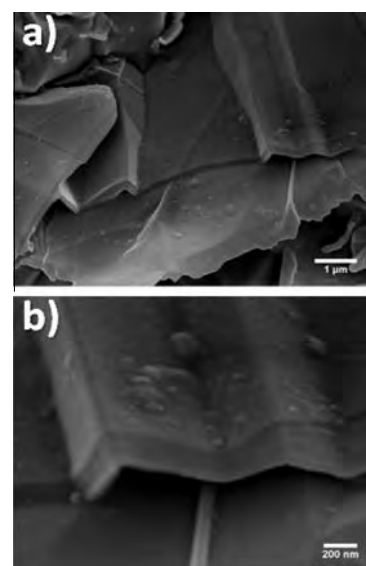


Figure 4. GNP energy-dissipation mechanisms: (a) GNP sliding, kinking and bending; GNPs are seen to bend at high angles without fracturing; and (b) high-magnification image of GNP kinking while GNPs slide and shear past one another.

The present model factors in the grain size reduction, densification and GNP dispersion. The grain size reduction factor is denoted as K_1 and represents the fractional grain size reduction of the TaC–GNP composite as compared to the TaC sample. The reduction in grain size leads to more surfaces that can dissipate energy, thus the factor K_1 is positive. The densification factor is denoted as K_2 and represents the fractional increase in densification of the TaC–GNP over pure TaC. Increased densification leads to a more rigid structure with less

Table 2. Summary of enhancement of fracture toughness and damping: the constants used for the model relating toughness to damping (all constants are dimensionless) Tests at 50 Hz frequency were taken as the baseline.

Sample	ΔK_{IC} (%)	$\Delta(\tan\delta_{50\text{Hz}})$ (%)	K_1	K_2	K_3	$\beta_{25\text{Hz}}$	$\beta_{50\text{Hz}}$	$\beta_{100\text{Hz}}$	$\beta_{200\text{Hz}}$
TaC-1G	49	20	0.26	0.03	0.1	0	1	0	0
TaC-3G	39	170	0.68	0.03	0.9	1.53	1	0.82	0
TaC-5G	99	140	0.69	0.05	0.3	1.29	1	0.86	−0.36

porosity; this would decrease damping and hence K_2 is negative. The GNP dispersion factor K_3 is based solely on qualitative SEM observations of the microstructure. K_3 values range from 0 to 1, with 1 being a high level of dispersion and 0 signifying poor dispersion. A high level of dispersion is essential for the effective use of GNPs and thus K_3 is positive. The determination of this factor could be further improved upon by using more rigorous methods, such as the dispersion parameter quantification developed by Bakshi et al. [19]. Both toughness (ΔK_{IC}) and damping enhancement ($\Delta(\tan\delta)$) are relative to the TaC sample and are presented as percentages.

The baseline calculations were done for the damping behavior at a frequency of 50 Hz. The variation in the damping behavior due to frequency is taken into account with the factor β . The model proposed is presented in Eq. (1):

$$\Delta(\tan\delta) = \beta(aK_1 - bK_2 + cK_3)\Delta(K_{IC}) \quad (1)$$

The constants a , b and c are calculated by fitting the experimental results (these constants are dimensionless). Eq. (2) presents the model with the fitted values; the model correlates the fracture toughness enhancement with the damping enhancement within the experimental margins of error:

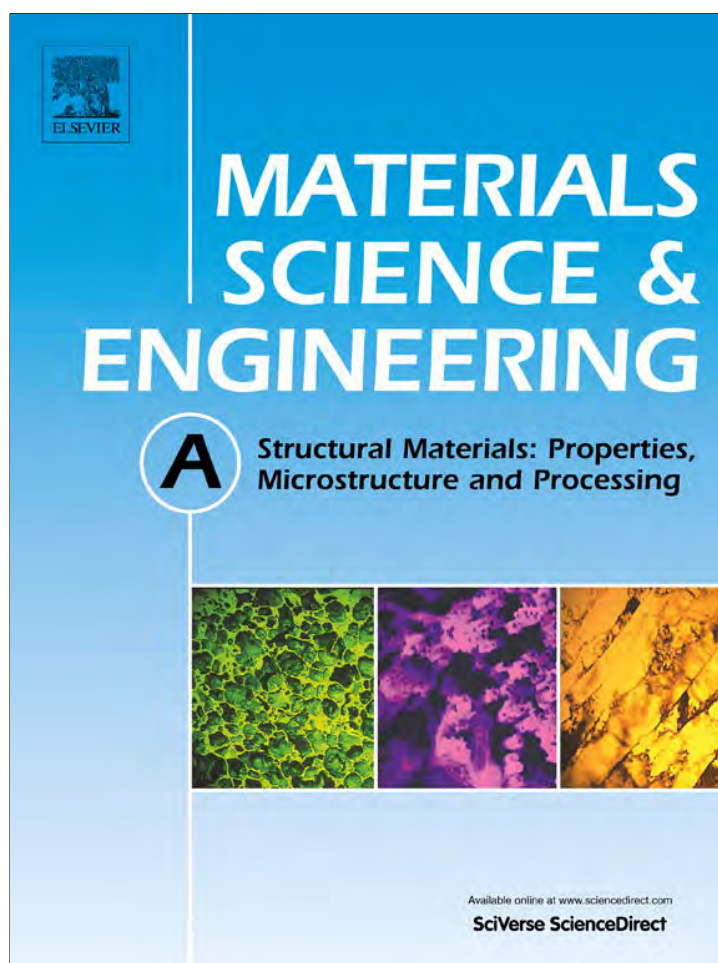
$$\Delta(\tan\delta) = \beta\left(\frac{1}{2}K_1 - 7K_2 + 5K_3\right)\Delta(K_{IC}) \quad (2)$$

The factors and parameters used in the model above are presented in Table 2. The β values are relative to the corresponding value at a frequency of 50 Hz. A value above 1 indicates that the enhancement of damping was greater than in the 50 Hz test; likewise, a value of less than 1 indicates that the damping was less. A value of zero indicates no improvement in damping over the TaC samples and a negative value indicates that the damping behavior decreased relative to the TaC sample. As previously discussed, damping enhancement dies down at 200 Hz and is generally higher at lower frequencies. The role of GNP dispersion is elucidated in the model; wide dispersion is critical to effective damping enhancement. The TaC-3G sample displays such wide dispersion, and this corresponds to the highest improvement in damping. The highest enhancement in fracture toughness is obtained by the TaC-5G, indicating that the toughness is more sensitive to the amount of GNPs than the dispersion. This study demonstrates that the intrinsic energy-dissipating mechanisms of GNPs can

be utilized in a composite material to enhance the fracture toughness and damping behavior of the UHTC TaC.

The authors acknowledge Dr. Ali Sayir, Program Manager of High Temperature Aerospace Materials at the Air Force Office of Scientific Research, and the receipt of Grants FA9550-11-1-0334 and FA9550-12-1-0263. The authors also acknowledge the support from the Advanced Materials Engineering Research Institute (AMERI).

- [1] T.H. Squire, J. Marschall, J. Eur. Ceram. Soc. 30 (2010) 2239–2251.
- [2] P.L. Moses, V.L. Rausch, L.T. Nguyen, J.R. Hill, Acta Astronaut. 55 (2004) 619–630.
- [3] J.W. Canan, Aerosp. Am. 11 (2007) 26–31.
- [4] S. Guicciardi, L. Silvestroni, M. Nygren, D. Sciti, J. Am. Ceram. Soc. 93 (2010) 2384–2391.
- [5] L. Silvestroni, D. Sciti, S. Guicciardi, C. Melandri, J. Eur. Ceram. Soc. 30 (2010) 2155–2164.
- [6] J. Zou, G.-J. Zhang, C.-F. Hu, T. Nishimura, Y. Sakka, H. Tanaka, J. Vleugels, O. Van der Biest, J. Eur. Ceram. Soc. 32 (2012) 2527–2529.
- [7] S.R. Bakshi, V. Musaramthota, D.A. Virzi, A.K. Keshri, D. Lahiri, V. Singh, S. Seal, A. Agarwal, Mater. Sci. Eng., A 528 (2011) 2538–2547.
- [8] D. Lahiri, E. Khaleghi, S.R. Bakshi, W. Li, E. Olevsky, A. Agarwal, Scripta Mater. 68 (2013) 285–288.
- [9] F. Yang, X. Zhang, J. Han, S. Du, J. Alloy. Compd. 472 (2009) 395–399.
- [10] A. Nieto, Thesis and Dissertations, Florida International University, March 2013.
- [11] A. Nieto, D. Lahiri, A. Agarwal, Mater. Sci. Eng., A 582 (2013) 338–346.
- [12] D. Lahiri, S. Das, W. Choi, A. Agarwal, ACS Nano 6 (2012) 3992–4000.
- [13] A. Nieto, D. Lahiri, A. Agarwal, Carbon 50 (2012) 4068–4077.
- [14] K. Wang, Y. Wang, Z. Fan, J. Yan, T. Wei, Mater. Res. Bull. 46 (2011) 315–318.
- [15] L.S. Walker, V.R. Marotto, M.A. Rafiee, N. Koratkar, E.L. Corral, ACS Nano 5 (2011) 3182–3190.
- [16] J. Dusza, J. Morgiel, A. Duszova, L. Kvetkova, M. Nosko, P. Kun, C. Balazsi, J. Eur. Ceram. Soc. 32 (2012) 3389–3397.
- [17] C. Ramirez, F.M. Figueiredo, P. Miranzo, P. Poza, M.I. Osendi, Carbon 50 (2012) 3607–3615.
- [18] K. Balani, A. Agarwal, J. Appl. Phys. 104 (2008) 063517.
- [19] S.R. Bakshi, R.G. Batista, A. Agarwal, Compos. A 40 (2009) 1311–1318.



This article appeared in a journal published by Elsevier. The attached copy is furnished to the author for internal non-commercial research and education use, including for instruction at the authors institution and sharing with colleagues.

Other uses, including reproduction and distribution, or selling or licensing copies, or posting to personal, institutional or third party websites are prohibited.

In most cases authors are permitted to post their version of the article (e.g. in Word or Tex form) to their personal website or institutional repository. Authors requiring further information regarding Elsevier's archiving and manuscript policies are encouraged to visit:

<http://www.elsevier.com/authorsrights>



Contents lists available at SciVerse ScienceDirect

Materials Science & Engineering A

journal homepage: www.elsevier.com/locate/msea

Graphene NanoPlatelets reinforced tantalum carbide consolidated by spark plasma sintering

Andy Nieto, Debrupa Lahiri, Arvind Agarwal*

Plasma Forming Laboratory, Nanomechanics and Nanotribology Laboratory, Mechanical and Materials Engineering, Florida International University, 10555 West Flagler Street, EC 3464, Miami, FL 33174, USA

ARTICLE INFO

Article history:

Received 18 April 2013

Received in revised form

2 June 2013

Accepted 4 June 2013

Available online 19 June 2013

Keywords:

Ceramics

Composites

Sintering

Fracture

Nanoindentation

ABSTRACT

Graphene NanoPlatelets (GNP) reinforced tantalum carbide composites are synthesized by spark plasma sintering (SPS) at processing conditions of 1850 °C and 80–100 MPa. The GNP addition enhances the densification of TaC–GNP composites to 99% theoretical density, while reducing the grain size by over 60% through grain wrapping mechanism. Survival and structure retention of GNP is confirmed through scanning electron microscopy and micro-Raman spectroscopy. Nanoindentation and high load (20–30 N) microindentation are utilized to evaluate elastic modulus and hardness. GNP improves fracture toughness of TaC by up to 99% through toughening mechanisms such as GNP bending, sheet sliding, cracking bridging, and crack deflection.

© 2013 Elsevier B.V. All rights reserved.

1. Introduction

Next generation aerospace systems such as hypersonic aircraft, spaceplanes, and rocket engines have created a demand for high performance refractory materials. Hypersonic flight creates extreme conditions consisting of ionized high temperature flows and continuous high energy shock waves. Such environments dictate the need for materials with both high strength and high resistance to oxidation and chemical attack. Groups IV and V ultrahigh temperature ceramics (UHTC) such as carbides, nitrides, and borides have attracted much attention because of their excellent refractory properties and high strength. These properties make them ideal candidates for next generation aerospace and rocket propulsion systems [1–3]. Tantalum carbide is a UHTC with high Young's Modulus (477–560 GPa) [4], high hardness (13.5–20 GPa) [4], very high melting point (3880 °C) [5] and high resistivity to chemical attack. Low fracture toughness (4–5 MPa m^{1/2}) [6] and bulk consolidation of TaC to high density without sacrificing its structural and mechanical integrity are the major challenges in its application. The high melting point of TaC necessitates long sintering times in conventional sintering methods which leads to substantial grain growth thus deteriorating the mechanical properties. The formation of Ta₂C is also a possibility when sintering TaC for a prolonged time. Ta₂C (3327 °C [7]) has a

lower melting than TaC, however it is comparable to the more widely studied UHTCs ZrB₂ (3245 °C [8]) and HfB₂ (3380 °C [8]). A toughened Ta₂C structure with high flexure strength can be obtained through grain elongation [9]; however the instability of Ta₂C at high temperatures makes it less preferred for aerospace applications. [9].

Hot pressing has been commonly used to consolidate UHTCs where sintering occurs above 2000 °C for several hours in order to reach full densification [10–14]. Another conventional technique, pressure less sintering, has been shown to consolidate TaC to 97.5% of theoretical density at 2300 °C [15]. High frequency induction heating has shown more promise resulting in 96% dense TaC in 3 min, without high levels of grain growth [6]. One of the promising and relatively new sintering methods is spark plasma sintering (SPS). SPS technique employs a pulsing electric current that enables very fast heating rates; thereby reducing grain growth while still maintaining a high level of densification. SPS has a great potential for the consolidation of UHTCs to high densification with rapid sintering times (5–20 min) [9,16–19].

Several studies have been conducted on UHTC composites designed to improve consolidation, fracture toughness, and flexure strength [13,16,18–28]. Previous studies in our lab have investigated the effect of CNT as a sintering aid and reinforcement in TaC. TaC and TaC–CNT composites were sintered by SPS at 1850 °C and pressures of 100 MPa, 255 MPa, and 363 MPa [18,19]. Densification is shown to increase with the pressure for all compositions. The CNTs act as grain growth inhibitors during sintering by pinning grains together. Both short CNTs (1–3 μm) and long CNTs

* Corresponding author. Tel.: +1 305 348 1701; fax: +1 305 348 1932.
E-mail address: agarwala@fiu.edu (A. Agarwal).

(30–40 μm) were used as reinforcement [18,19]. Transverse rupture tests revealed that the CNT reinforcement increased the rupture strength, the specific strength, and the strain at rupture [29]. The short CNT reinforcement yielded the highest rupture strength and specific strength. SEM analysis revealed that the short CNTs had unzipped and transformed into graphene platelets during the SPS processing [29]. The increased surface area of these graphene platelets enhances the bridging and pull-out mechanisms resulting in superior performance over the long CNTs which experience only minimal transformations. The increased surface area of graphene provides a higher surface available for reinforcing composites. The 2D nature of graphene also lends itself to high pressure processing whereas 1D structures such as CNT are more prone to buckle under high pressures.

Graphene has a very high tensile strength (130 GPa) [30] and Young's Modulus (0.5–1 TPa) [31] making it an ideal reinforcement in composite materials. Graphene NanoPlatelets (GNP), consisting of approximately 20–30 graphene sheets and with a thickness of 5–10 nm, [32] exhibit many of graphene's unique properties. The increased thickness of GNP may also make them less prone to agglomeration and entanglement as compared to single layer graphene and CNTs. Due to these properties, Graphene NanoPlatelets (GNP) have been explored as reinforcement of composite materials. Most of the studies have focused on polymer matrix composites. Recently some studies have been done on silicon carbide [33], aluminum oxide [34–38] and silicon nitride [39–47] matrices reinforced with GNP in order to improve mechanical, thermal, and electrical properties of the ceramic. The use of GNP as reinforcement for UHTCs has recently been reported in one study on a ZrB_2 -GNP composite [48]. GNP reinforced Al_2O_3 , Si_3N_4 , and ZrB_2 matrices have shown improvement in the fracture toughness of up to 53% [36], 235% [39], and 83% [48] respectively. GNP hinders grain growth during sintering by pinning grains and impeding diffusion thus resulting in a refined grain structure [34,36,38]. The GNP wrapping mechanism leads to strong interfaces with the matrix allowing stress to be transferred to the GNP. GNP inhibits crack initiation and propagation by bridging and deflecting cracks [37–39,41,47,48]. GNPs have intrinsic energy dissipating mechanisms such as kinking, bending, sliding, and shearing of GNP or graphene layers [49]. Our previous study showed that GNP survives and retains its structure during SPS processing at 1850 $^\circ\text{C}$ and 80 MPa. These extreme processing conditions are similar to those required for consolidating a UHTC. The present study utilizes GNP as reinforcement for TaC to enhance the fracture toughness. Mechanical properties of TaC-GNP composites are evaluated through nanoindentation and high load microindentation. GNP induced toughening mechanisms in TaC are also discussed.

2. Materials and methods

2.1. Materials

The starting tantalum carbide (TaC) powder was obtained from Inframat Advanced Materials LLC, Connecticut, USA. The tantalum carbide has an average particles size of $0.36 \pm 0.13 \mu\text{m}$. The purity of the tantalum carbide powder by weight is 99.7%. The impurities present include free carbon (<0.15%), oxygen (0.15–0.30%), and niobium (<0.3%). The total carbon content is $\geq 6.20\%$ which yields a Ta to C ratio of approximately 1:1. Graphene NanoPlatelets (xGNP-M-5) were obtained from XG Sciences, Lansing, MI, USA. The GNP has an average thickness of 6–14 nm indicating 20–40 sheets of graphene in each GNP [32,50]. GNP particles have an average diameter of 15 μm , giving the platelets a relative surface area of 120–150 m^2/g [32]. GNPs have some functional groups at

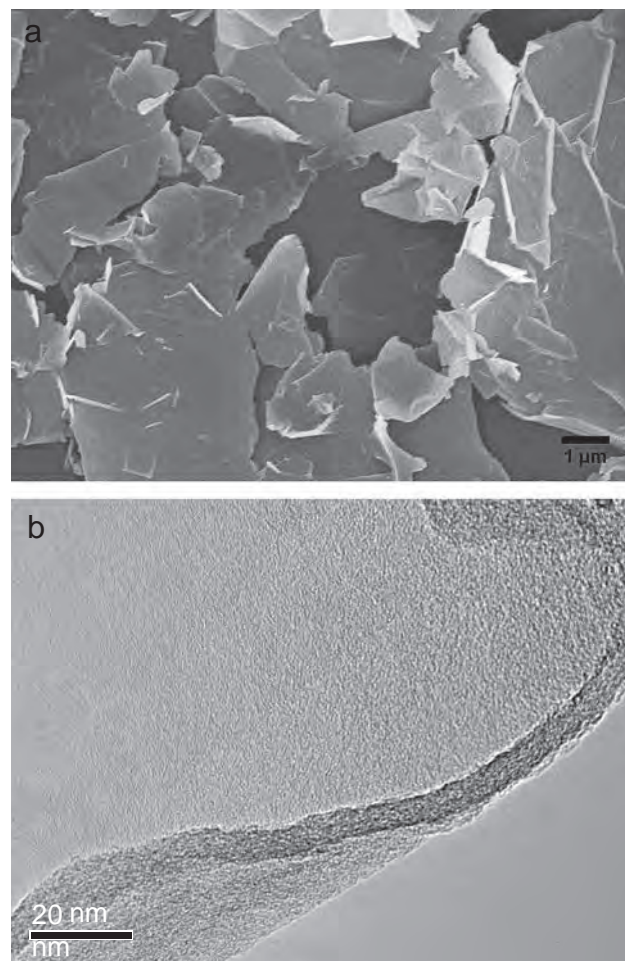


Fig. 1 (a) SEM micrograph of wrinkled top surface of GNPs, (b) TEM of folded GNP showing thickness less than 10 nm.

the edges, consisting of approximately 0.075% ether, 0.035% carboxyl, and 0.03% hydroxyl groups [32]. Fig. 1a shows an SEM micrograph of the as-received GNPs, varying degrees of wrinkles and folds are seen on top surfaces. Fig. 1b shows a TEM image of a single GNP in cross section with a thickness of less than 10 nm.

2.2. Composite powder processing

TaC-GNP composites were prepared with a GNP content consisting of 1 vol% (TaC-1G), 3 vol% (TaC-3G), and 5 vol% (TaC-5G). The wet chemistry method was chosen to mix TaC and GNP powders because of its simplicity and effectiveness. The sonication medium was acetone as no known reactions occur between acetone and either TaC or GNP. The as-received GNP powders were ultrasonicated in acetone for 90 min in order to alleviate agglomeration. The GNP powder was then mixed with the TaC powder and ultrasonicated for 90 min. Pure TaC powder was also ultrasonicated for 90 min as the control sample. After ultrasonication, TaC-GNP-acetone solution was placed inside an oven at 75 $^\circ\text{C}$ for 24 h for drying. The dried powders were subsequently crushed and placed in the oven for an additional 24 h.

2.3. Spark plasma sintering processing

TaC-GNP powders were consolidated at Thermal Technologies LLC (Santa Rosa, California, USA) using a model 10⁻⁴ spark plasma sintering machine. The consolidation was carried out in a 20 mm diameter graphite die using a holding pressure of 80–100 MPa,

a holding temperature of 1850 °C, and a hold time of 10 min. The environment in the die consisted of Argon gas at a pressure of 3–6.5 Pa. TaC–GNP powders were packed and wrapped in a graphite foil for improved current flow and to prevent reactions between the powder and the die. The heating rate used was 200 °C/min.

2.4. Structural characterization

The TaC and TaC–GNP pellets obtained through SPS processing were polished in order to remove thin layer of graphite from the surface, which originates from the graphite foil used during the SPS to keep the powder from contacting the die. A Helium gas pycnometer (Accupyc 1340, Micrometrics Instrument Corporation, Norcross, GA, USA) was used to measure the true density of the bulk pellets and the starting powders. The TaC and TaC–GNP composite compacts were ground progressively using finer silicon carbide papers (up to 600 grit size), and then polished using diamond slurries with 1.0 µm and 0.10 µm particles. X-ray diffraction (XRD) experiments were carried out on the starting powders and the sintered pellets using a Siemens D-500 X-ray diffractometer to identify phase transformation, if any. The operating voltage and current are 40 kV and 40 mA respectively. The radiation used is Cu Kα which has a wavelength of 1.542 Å. The starting powders and the bulk pellets were also characterized using Micro-Raman spectroscopy in order to study the effects of the SPS processing on the GNP structure. The equipment used was a Spectra Physics (Model 3900S, California, USA) with Ti-sapphire crystal as the target (514 nm), a laser power of 18 mW and a detector with 4 cm⁻¹ spectral resolution from Kaiser Optical Systems, Inc. (Michigan, USA). Transmission electron microscopy of the starting GNP was done using a Philips/FEI Tecnai F30 high-resolution TEM operating at a voltage of 300 keV. Sample preparation consisted of dispersing GNP powder in an acetone solution via ultrasonication. Scanning electron microscopy of the powders and the bulk pellets was done using a JEOL JSM-6330F field emission scanning electron microscope (FE-SEM) with an operating voltage of 15 kV. ImageJ software is used to analyze the SEM micrographs of the TaC and TaC-composite samples in order to measure the grain sizes.

2.5. Mechanical properties evaluation

Nano-indentation experiments were carried out using a TI 900 Triboindenter (Hysitron Inc., Minneapolis, MN, USA) with a 100 nm Berkovich tip. The tip-area calibration was done using a standard fused quartz substrate of known modulus (69.6 GPa). The triboindenter was used in quasi-static indentation mode in order to measure the elastic modulus and hardness of the sintered compacts. Indentations were done on the polished cross sections. The indentation process for these hard samples consisted of a 10 s period to reach 4500 µN, with a holding time of 3 s, followed by a 10 s unloading to 0 N. The elastic modulus was calculated from the load–displacement unloading curves using Oliver–Pharr method [51].

TaC, TaC-1G, TaC-3G and TaC-5G samples were also subjected to high load (20 and 30 N) indentation testing using a Vickers tip. The high load indents were subsequently observed using SEM and the lengths of the generated cracks was measured using ImageJ software. The crack length (*c*) was measured from the center of the indent and used to calculate the fracture toughness (*K_{IC}*) through Anstis equation [52].

$$K_{IC} = 0.016 \left(\frac{E}{H} \right)^{1/2} \left(\frac{P}{c^{3/2}} \right) \quad (1)$$

The other parameters needed to use the Anstis equation are the load (*P*) which is either 20 N or 30 N depending on which indent generated the crack being measured. The hardness value (*H*) is known from the hardness tests used to generate the cracks. The elastic modulus (*E*) values used are those calculated from the nanoindentation experiments.

3. Results and discussion

3.1. Synthesis and consolidation

3.1.1. Powder processing

The composite powders were analyzed prior to sintering in order to evaluate the effectiveness of the mixing and processing. The varying degrees of GNP dispersion in the composite powders can be seen from the SEM images shown in Fig. 2. Fig. 2a shows a large transparent GNP found in the TaC-1G sample. The impression of fine TaC particles can be seen through GNP sheet in Fig. 2a. The transparency indicates that thin platelet has a few graphene sheets. Thin transparent GNPs were typically not seen in the starting powder, indicating that ultrasonication was effective in alleviating agglomeration in as-received GNPs. TaC-3G and TaC-5G powders show higher GNP content in Fig. 2b. GNPs are well

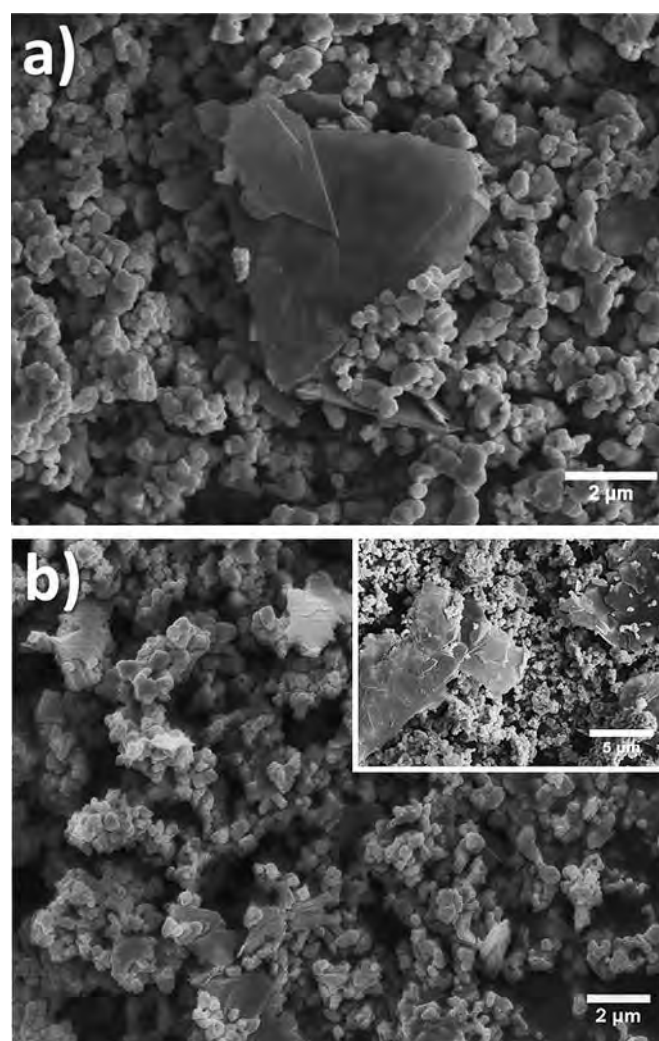


Fig. 2. SEM images of composite powders, (a) Few scattered GNPs such as that shown are found throughout the TaC-1G powder, (b) TaC-3G and TaC-5G powders show substantial presence of GNPs throughout powder, inset: some areas in TaC-5G powder have large agglomerated GNP.

distributed throughout TaC-3G powder and show no signs of agglomeration. The increased GNP volume in the TaC-5G powder however appears to have had an adverse effect on the dispersion of GNP as agglomerates are found in some regions. Large ($> 15 \mu\text{m}$ wide) agglomerated and segregated GNPs in TaC-5G powder can be seen in the inset of Fig. 2b.

3.1.2. Densification

TaC and TaC-GNP powders were consolidated by SPS using the processing cycle shown in Fig. 3. The densification can be seen to occur in two steps based on the punch displacement measurements. The initial and major consolidation begins when the maximum pressure is reached. At this time the temperature is ramped up from 1100°C to 1850°C at a rate of $200^\circ\text{C}/\text{min}$. The final densification step occurs when the sample is being held and sintered at the maximum pressure and temperature for 10 min. The samples achieved high degrees of densification, with relative densities ranging from ~94% to ~99%.

The densification with varying GNP content, relative to theoretical density is plotted in Fig. 4. Density of TaC and GNP is taken as $14.65 \text{ g}/\text{cm}^3$ [19] and $1.82 \text{ g}/\text{cm}^3$ [53] respectively for calculation of theoretical density. XRD analysis (not shown) confirmed that SPS processing did not induce formation of other phases such as Ta_2C . TaC was the major phase in all compositions. The pure TaC sample reached a densification of ~94% whereas GNP containing TaC have a density from 97–99%. GNPs have a much higher electrical

($10^6 \Omega^{-1} \text{ cm}^{-1}$ [54]) and thermal conductivity ($5300 \text{ W}/\text{m K}$ [43]) than TaC ($\sim 10^4 \Omega^{-1} \text{ cm}^{-1}$ [55] and $\sim 30 \text{ W}/\text{m K}$ [56] respectively) which enables the composite powder to have a more uniform distribution of the current and heat during consolidation. Uniform heating of the powders leads to improved sintering and densification. The TaC-5G sample (99%) achieved the highest densification despite it being sintered at a pressure of 80 MPa and not 100 MPa. The effect of GNP content appears to have more influence on the densification than 20 MPa difference in the consolidation pressure. Pure TaC displays a much higher level of consolidation (94%) than TaC processed under similar conditions (89%) by Bakshi et al. [19]. The difference in the densification of pure TaC is attributed to the variations in powder processing conditions. TaC powder was not ultrasonicated prior to sintering by Bakshi et al. [19], which may have not removed the thin surface layer of impurities as well as agglomerates, which could have suppressed the effective surface area and degree of densification.

3.1.3. Grain refinement

Fig. 5 shows the low magnification SEM micrographs of the fracture surface of sintered TaC-GNP composites. Fig. 6 shows the TaC grain size as a function of GNP content obtained from several micrographs similar to that in Fig. 5. Despite the relatively high densification (~94%), some areas of the TaC such as that shown in the inset of Fig. 5a have been poorly sintered. The poorly sintered regions have a highly granulated structure with grain sizes of $1.43 \pm 0.38 \mu\text{m}$. These areas are in sharp contrast to the majority of the dense structure which has a grain size of $4.54 \pm 0.91 \mu\text{m}$. The addition of GNPs result in TaC grain refinement which can be clearly seen from the micrographs of each composition presented in Fig. 5b and c and the grain size measurements plotted in Fig. 6.

TaC-1G experiences limited grain refinement. The amount of GNP in this sample is too small to hinder grain growth throughout the structure. Grain refinement occurred in localized regions leading to the slight decrease in the grain size. The localized nature of the grain refinement leads to a wide range of grain sizes which results in the large error bar for TaC-1G in Fig. 6. The grain refinement in the TaC-3G and TaC-5G samples is significant as the grain sizes are reduced by over 60% relative to the pure TaC. Fig. 5c and d reveals that TaC-3G and TaC-5G consist of $1\text{--}2 \mu\text{m}$ grains with GNPs scattered throughout the structure. The grain refinement has occurred throughout TaC-3G and TaC-5G structures, thus resulting in the lower error bars in Fig. 6. The amount of GNP in these samples is high enough to hinder grain growth throughout the structure. It is noteworthy that TaC-5G does not experience further refinement with increased GNP content. This leveling off may occur because at 5 vol% the effect of GNP in enhancing heat transfer may dominate over the effect of additional GNP available to wrap around and pin grains. This possible inflection point in GNP mechanism effectiveness may be accentuated by the agglomerated GNPs in TaC-5G that may still be effective at increasing thermal and electrical conductivity but not of providing effective grain wrapping and pinning. The ability to hinder grain growth while ensuring high densification is ideal and significant for sintered materials. GNPs wrap around grains and act as diffusion barriers and hinder grain growth. The high surface area and high thermal conductivity of GNP allow for strong interfacial bonding between TaC grains and GNP which minimizes porosity formation. The presence of the grain wrapping mechanisms which are responsible for inhibiting grain growth is shown in the next section where the structure of the GNPs in each sample is elaborated upon.

3.2. Survival and structure of GNP

The structure of the GNP after SPS processing is accessed through SEM and Micro-Raman spectroscopy. High magnifications

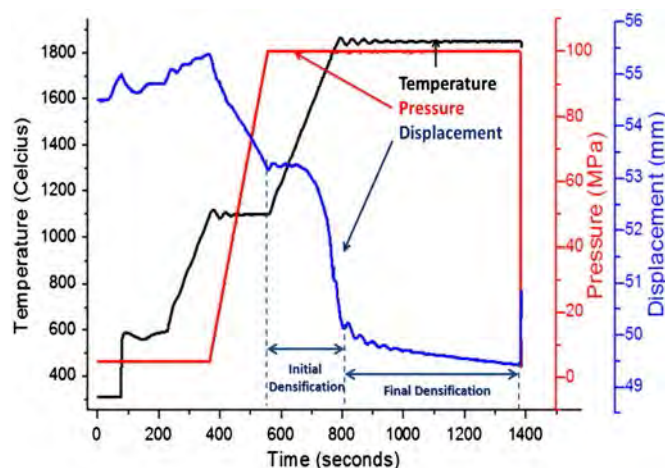


Fig. 3. Typical SPS processing cycle used showing temperature, pressure, and die displacement throughout the sintering process.

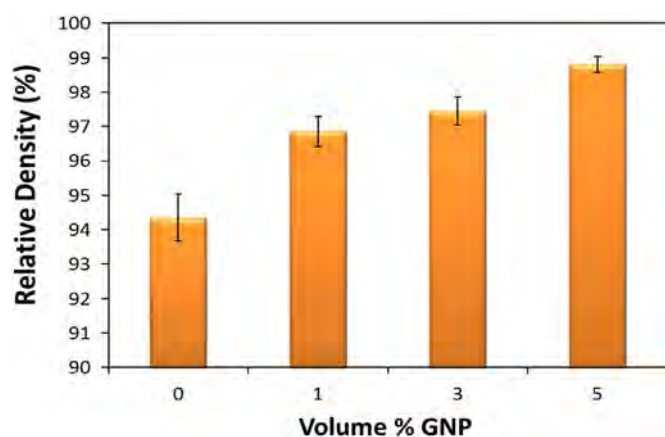


Fig. 4. Densification (relative to theoretical density) vs. GNP content. Densification increases with the increasing GNP content.

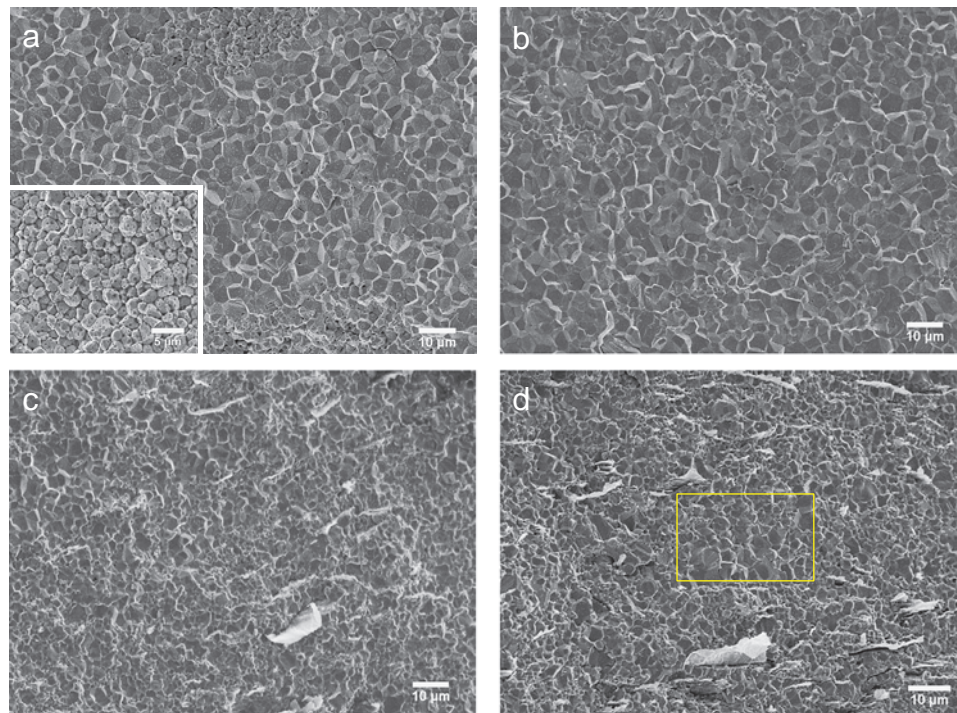


Fig. 5. SEM micrographs of TaC–GNP after SPS consolidation. (a) Pure TaC with inset showing region of poor consolidation, (b) TaC-1G with slight grain size reduction, (c) TaC-3G has reduced grain size and homogenous structure, (d) TaC-5G has significant presence of GNPs, with some agglomeration. Yellow rectangle denotes region devoid of any GNP. (For interpretation of the references to color in this figure legend, the reader is referred to the web version of this article.)

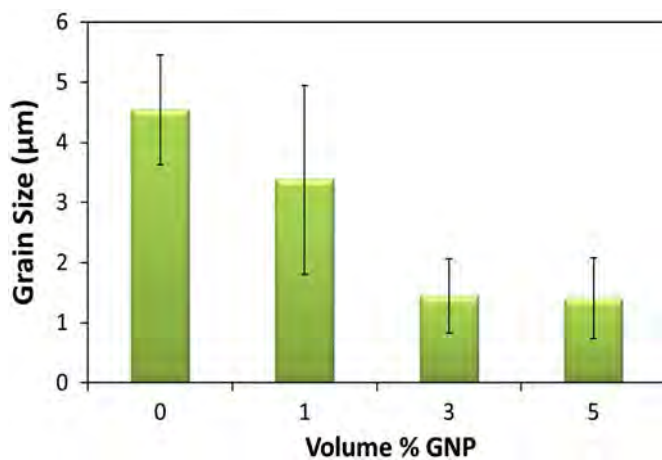


Fig. 6. Grain Size vs. GNP Content. Grain size decreases with increasing GNP content.

image, shown in Fig. 7a reveals that GNPs are embedded in grains throughout the TaC-1G sample. The size of the embedded GNPs varies substantially; the largest GNP in Fig. 7a is about a micron in width, while the smallest are 100–200 nm wide. Most GNPs in the TaC-1G structure have a low aspect ratio. A few GNPs such as that shown in the inset of Fig. 7a display the high aspect ratio typical of GNPs. Lower aspect ratio GNPs likely occur as a result of agglomeration of GNPs that fractured during the high pressure SPS processing. Higher aspect ratio GNPs are due to the ripping and shearing of GNPs. TaC-3G and TaC-5G samples showed substantial presence of GNP in Fig. 5c and d. The GNPs in both these samples are aligned perpendicular to the SPS pressing axis. Such alignment has previously been seen in graphene platelets [40] and other high aspect ratio particles such as graphite [57] and SiC platelets [58]. Chou et al. [58] found that higher platelet aspect ratios lead to a

higher degree of orientation and that higher orientation correlates with higher toughness. The GNPs in our study have a very high aspect ratio and were processed under a uniaxial pressure of 80–100 MPa; these factors induce the alignment of GNP in the TaC–GNP microstructure. Fig. 7b shows that GNPs in the TaC-3G sample weave around grains and form discontinuous “networks”. GNPs tend to form a coherent structure without becoming entangled or agglomerate. These weaving GNPs constitute the GNP wrapping mechanism which suppresses the grain growth. In TaC-5G sample, in addition to weaving GNPs, there are regions with large segregated GNPs. The presence of large GNPs is due to the agglomeration and results in the surrounding area becoming devoid of GNP as shown in Fig. 7c. The inset of Fig. 7c presents a large GNP with a smooth surface and fine wrinkles which are signatures of pristine GNPs. The clustering of GNPs may enable them to better withstand the harsh processing conditions resulting in the presence of undamaged GNPs in the compacts.

Raman spectroscopy was employed to further characterize the structure of GNP in both the TaC–GNP powder and sintered compacts. A typical Raman spectrum of the TaC–GNP compacts is provided in Fig. 8. It can be seen that the SPS compacts tend to have lower I_D/I_G ratios and higher I_{2D}/I_G ratios. The I_D/I_G ratio is a measure of defects, the larger the ratio the more defects present. The I_{2D}/I_G ratio is a measure of graphene structure with increasing amount of graphene layers increasing the ratio; ratio below 1 is indicative of a graphite-like structure. The ultrasonication of TaC–GNP powders leads to strong interactions between GNP and the harder TaC particles. These interactions appear to have adverse effects on the GNP resulting in lower I_{2D}/I_G ratio indicating partial loss of graphene-like structure. TaC-5G powder exhibited highest I_{2D}/I_G ratio of 3.4 (not shown here) showing the presence of graphene-like structure. The presence of large undamaged GNPs is widely seen in the TaC-5G powder in the inset Fig. 2b. The increase in I_{2D}/I_G ratio with increasing GNP content indicates the presence of higher fraction of undamaged GNPs with graphene-like structure.

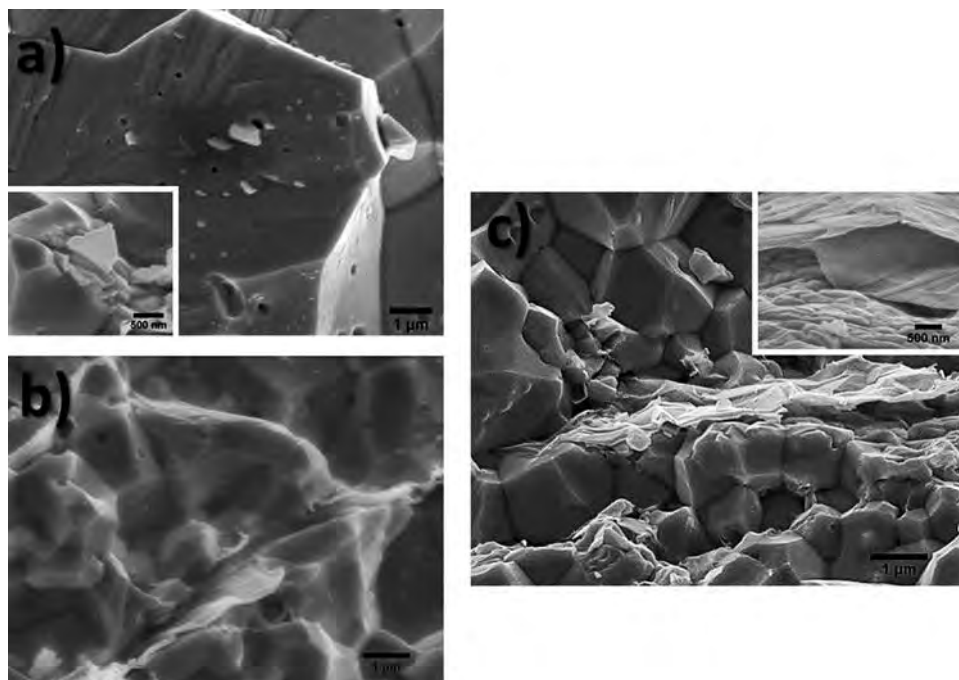


Fig. 7. SEM micrographs of GNP in TaC–GNP composites, (a) GNP in TaC-1G embedded in grains; inset shows embedded GNPs, (b) GNP in TaC-3G form a network structure, (c) TaC-5G structure has both fine and larger GNPs, inset: large GNPs in TaC-5G appear to survive processing with little damage as seen from the fine crinkled structure.

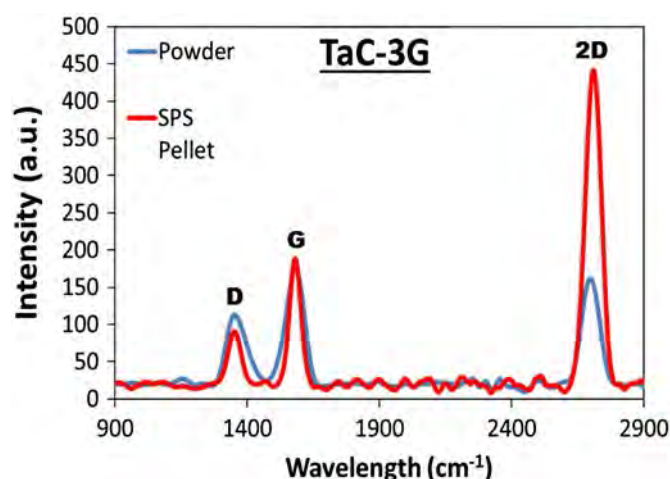


Fig. 8. Raman Spectrum of SPS TaC–GNP (TaC-3G). Powder processing appears to induce defects in GNPs. Graphene appear to survive processing with little to no damage. I_D/I_G ratio is an indication of defects in the graphene structure. I_{2D}/I_G ratio is an indicator of the number of graphene layers present, ratio below one indicates presence of a graphite-like structure.

During SPS processing GNP undergo phenomena such as sliding and shearing off of individual GNP platelets; this increases the amount of few layer GNP thus increasing the signature (I_{2D}/I_G ratio) of a graphene-like structure. GNPs have been observed to bond together and form continuous platelets during SPS processing of a bulk GNP structure [49]. The bonding of platelets in the bulk GNP structure occurred ‘edge to edge’ which reduced the presence of edge defects [49]. The I_{2D}/I_G ratio of the bulk SPS GNP compact was higher than that of the as-received GNP powder; this is consistent with the results for the TaC–GNP composites. GNP bonding may also occur during the SPS of the TaC–GNP compacts; the reduction of edge defects along with an increase in few layer GNP likely induces the reduction in the I_D/I_G ratio and increase in the I_{2D}/I_G .

3.3. Mechanical properties

3.3.1. Elastic modulus

The elastic modulus of TaC–GNP samples is evaluated through nanoindentation. The reduced modulus (E_r) is obtained from nanoindentation and is related to the sample's elastic modulus (E_s) by Eq. (4.1).

$$\frac{1}{E_r} = \frac{1-\nu_i^2}{E_i} + \frac{1-\nu_s^2}{E_s} \quad (2)$$

The elastic modulus (E_i) and Poisson's ratio (ν_i) of the indenter are 1140 GPa and 0.07 respectively. The Poisson ratio of the sample (ν_s) is taken to be 0.24 [59]. The elastic moduli and mechanical properties are summarized in Table 1. The elastic modulus value of TaC (547.7 ± 25.6 GPa) is in the higher end of values reported in the literature [46]. A high value is attained because of the small volume tested during the nanoindentation. The width of indent on TaC was typically ~ 1.0 – 1.5 μm with a depth of 40–50 nm. These dimensions indicate that the indentations are largely being done on a single TaC grain. Thus, values from a single grain represent the intrinsic properties of TaC which is the reason for high elastic modulus value in a structure with 94% theoretical density.

TaC–GNP samples have lower elastic modulus values (Table 1) because GNPs play a role when the TaC grain being indented is surrounded by platelets. In pure TaC, an individual grain is held by other tightly bound TaC grains under and adjacent to it. In the TaC–GNP, however, there can be GNP adjacent and underneath the grain being indented. These GNPs will cause increased displacement of the TaC grain in two modes. Firstly, GNP between TaC grains will act as a lubricating phase and allow slippage of the grain. The bonds between individual graphene sheets in GNP are held by weak Van der Waals forces. Sheets of graphene will shear off from the GNP causing the TaC grain to slip and be further displaced. Secondly, GNP may increase displacement of a TaC grain if it is sitting on top a GNP. The GNP will not support the TaC grain as would another TaC grain, instead the GNP will deform and shear off as shown in Fig. 9a. Fig. 9b clearly shows localized porosity between grains which provides space for the GNP to deform and

Table 1
Microstructure and Mechanical properties of TaC–GNP composites.

Sample	GNP content (vol%)	Relative density (%)	Grain size (μm)	Elastic modulus (GPa)	Micro-hardness (GPa)	Nano-hardness (GPa)	Fracture toughness ($\text{MPa m}^{1/2}$)
TaC	0	94.6 ± 0.7	4.5 ± 0.9	547.7 ± 25.6	18.9 ± 3.4	28.3 ± 2.0	5.6 ± 1.8
TaC-1G	1	96.9 ± 0.4	3.4 ± 1.6	411.9 ± 13.2	16.5 ± 1.8	19.0 ± 1.4	8.3 ± 1.8
TaC-3G	3	97.5 ± 0.4	1.4 ± 0.6	395.3 ± 29.7	14.1 ± 1.6	22.5 ± 2.2	7.7 ± 1.9
TaC-5G	5	98.8 ± 0.2	1.4 ± 0.7	490.4 ± 38.8	12.9 ± 1.4	20.6 ± 1.9	11.1 ± 2.4

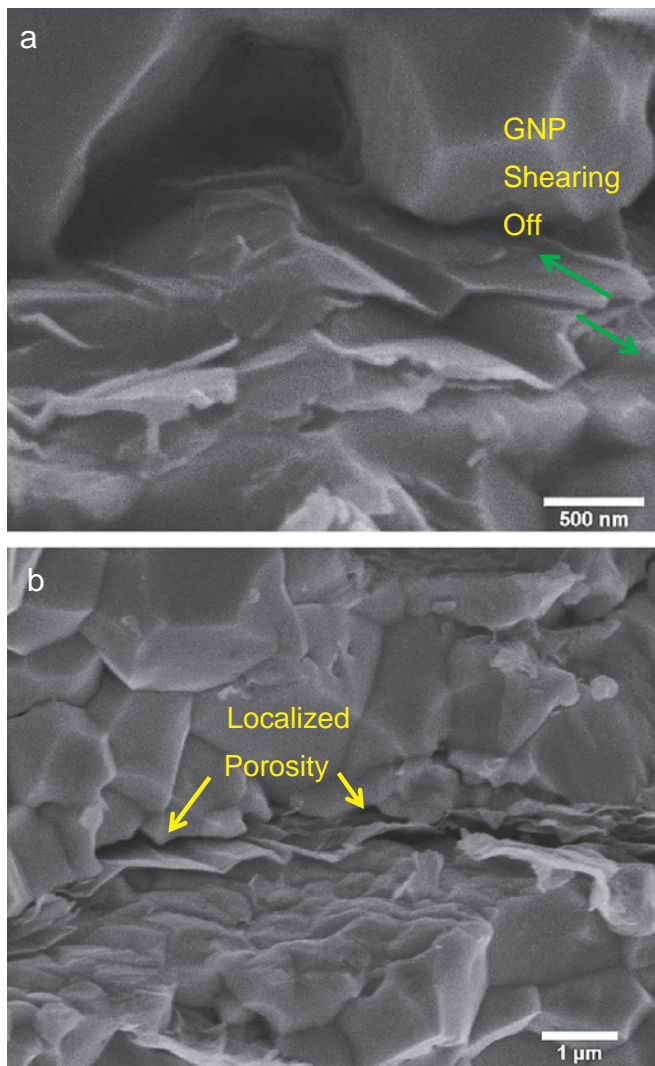


Fig. 9. GNP between TaC grains can induce localized reductions in stiffness and resistance to deformation, (a) GNP deforming and shearing off, (b) GNP causing localized porosity in between TaC grains.

the TaC grain to be displaced. Such interaction between GNP and TaC grains during indentation leads to lower elastic modulus values of TaC–GNP as compared to pure TaC. TaC-1G and TaC-3G samples have elastic moduli values that differ slightly, however it is within the margin of error. The TaC-5G sample has higher elastic modulus than TaC-1G and TaC-3G. Many regions in the TaC-5GNP sample were observed to be devoid of GNP due to agglomeration. These regions would have no effect from the GNP during indentation and behave similar to pure TaC. This variation in the microstructure leads to TaC-5G having the highest error bar of any sample. The TaC-5G sample also had the highest densification, so local porosity effects induced by the GNP would be suppressed, resulting in higher modulus.

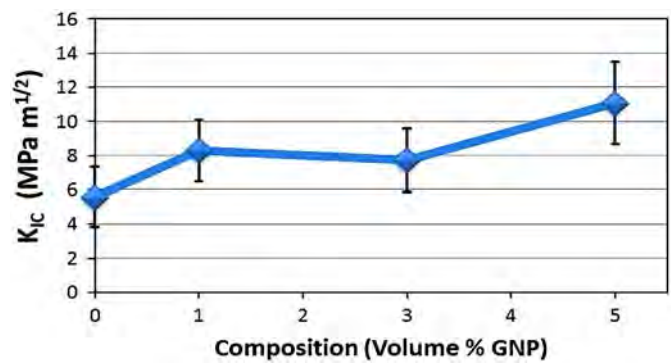


Fig. 10. Fracture toughness vs. GNP content.

3.3.2. Hardness

Hardness is evaluated at both nano and micro scales, and presented in Table 1. The nanohardness largely mirrors the elastic moduli behavior and can be explained by the same mechanisms. A single TaC grain is indented which yields high hardness values (28.3 ± 2.0 GPa). The TaC–GNP samples experience lower values as a result of GNP induced grain yielding and grain slipping. At the high load (20–30 N) indentation, there is a significant difference in TaC–GNP composites with microhardness decreasing steadily with an increasing GNP content. GNP is a soft phase so a decrease in the microhardness is expected. The microhardness is significantly lower than nanoindentation because a much larger volume is being indented. The width of a microindent is typically over $50 \mu\text{m}$ as compared to $1 \mu\text{m}$ in nanoindentation. In the larger volume of microindent, a higher volume fraction of softer GNPs is encountered which results in the lower hardness. The adverse effect of GNP on microhardness are partially mitigated by the increased densification and grain size reduction experienced as the GNP content is increased.

3.3.3. Fracture toughness

The addition of GNP to TaC results in improvement in the indentation fracture toughness as shown in Fig. 10a. The fracture toughness is increased by 99% in the TaC-5G composite. The amount and intensity of cracking is found to be more severe in the TaC sample than in the composites. The increase in toughness correlates with an increasing GNP content however the trend is not clear for TaC-3G where fracture toughness is statistically the same as TaC-1G. This indicates that GNP induced toughening is not continuous with increasing GNP content, rather increases occur at certain quanta. The increased toughening at 5 vol% is likely due to the increased probability of finding closely spaced GNP structures because of the higher GNP content. This leveling off in fracture toughness values is also seen in ZrB_2 reinforced with 2 and 4 vol% GNP [48]. In that work the fracture toughness values increase at 6 vol% similarly to our increase at 5 vol%. The increase in fracture toughness at 5 vol% (99%) in the present study however is higher

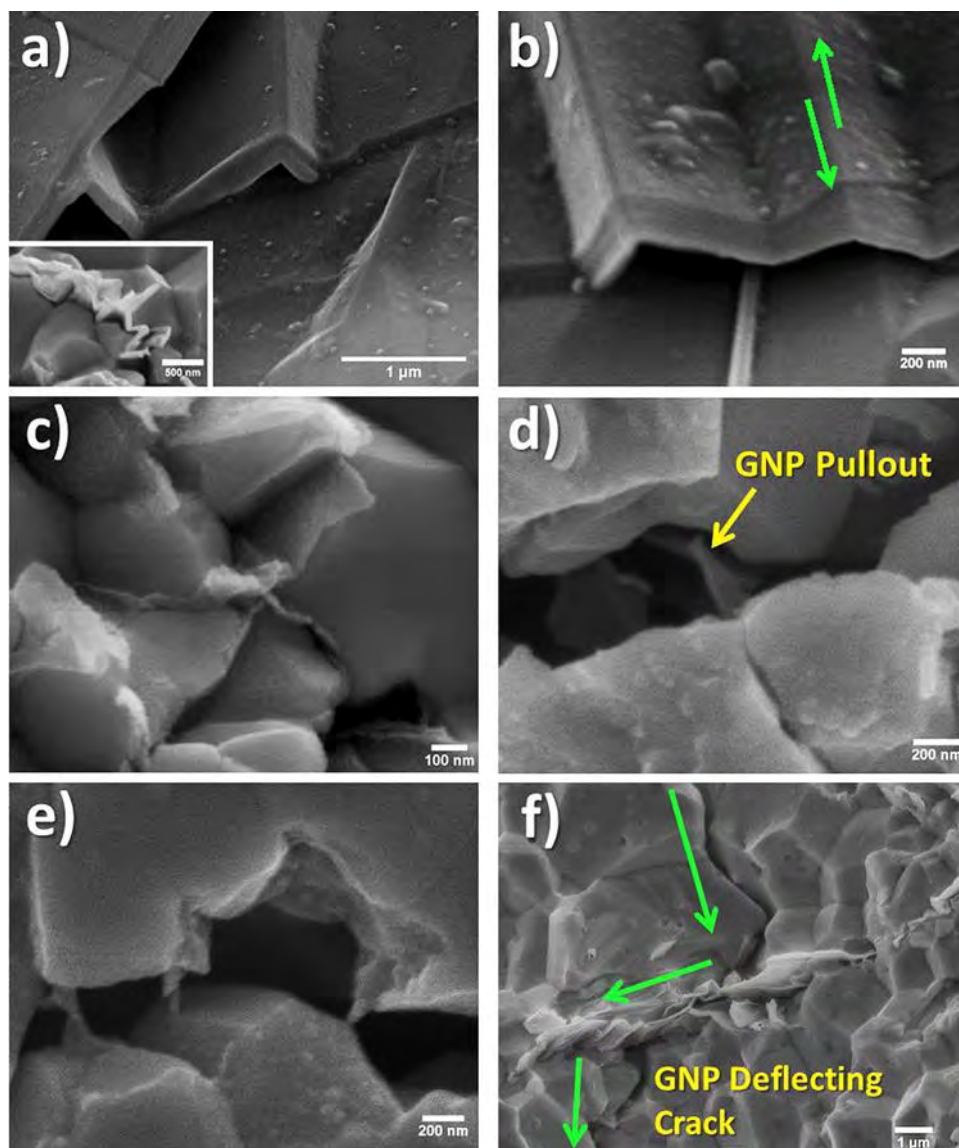


Fig. 11. GNP toughening mechanisms in TaC, (a) GNP bending and kinking, (b) GNP sliding, (c) grain wrapping, (d) sheet pull-out, (e) crack bridging, (f) crack deflection.

than the increase in fracture toughness in the 6 vol% (83%) GNP reinforced ZrB₂ [47] in spite of the lower GNP content.

The fracture toughness in the TaC–GNP composites is enhanced because of the intrinsic energy dissipating mechanisms of GNP. GNP energy dissipating mechanisms such as sheet bending, kinking, and sliding were shown to be inherent to GNP in our previous work [49]. In the present study six distinct GNP toughening mechanisms are observed in the TaC–GNP composites. The first two mechanisms, shown in Fig. 11a and b are the intrinsic GNP bending and sliding mechanisms. The bent GNP can be found in between grains or embedded in grains as shown in the inset of Fig. 11a. While this bending and sliding occurs during the high pressure processing, it is expected that these intrinsic GNP mechanisms would also occur during load bearing. The bending and sliding of GNPs requires strain energy that would otherwise be used for crack formation and propagation. The GNP mechanisms in Fig. 11c and d, grain wrapping and sheet pullout, are the result of GNP interactions with the TaC matrix. The wrapping of GNP not only inhibits grain growth during sintering, it can also help grains resist crack propagation when several grains are wrapped together. Sheet pullout occurs when a GNP is pulled out of a grain as a result of a loading. The energy expended to pull

GNP out of a grain or to displacement wrapped grains is strain energy that would otherwise propagate a crack. Together the intrinsic GNP mechanisms and their interactions with grains leads to crack suppressing mechanisms—crack bridging and crack deflection. Crack bridging occurs when GNP span across a crack as shown in Fig. 11e, these high strength GNP resist the tensile forces induced by a growing crack. The resistance of GNP can be so strong that the crack seeks a lower energy path and deflects as shown in Fig. 11f. The intrinsic GNP energy dissipating mechanisms can thus be translated into toughening mechanisms in TaC–GNP composites.

4. Conclusions

TaC–GNP composites with enhanced fracture toughness were successfully synthesized by SPS. SPS processing conditions of 1850 °C and 80–100 MPa yield dense composites without adversely affecting GNP. The addition of GNP simultaneously improves densification and reduces grain sizes by over 60%. Densification is improved as a result of the high electrical and thermal conductivity of GNP which enables more uniform heat

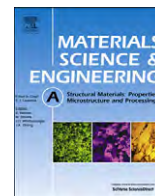
distribution during SPS processing. Grain size is reduced as GNPs tend to wrap around grains and inhibit grain growth. Nanoindentation experiments give intrinsic properties of TaC leading to high values of elastic modulus and hardness. High load microindentations reveal that increasing GNP content causes a steady drop in hardness. GNP improves fracture toughness by up to 99% through toughening mechanisms such as GNP bending, sheet sliding, cracking bridging, and crack deflection.

Acknowledgments

Authors would like to acknowledge Dr. Ali Sayir, Program Manager of High Temperature Aerospace Materials at the Air Force Office of Scientific Research and FA9550-11-1-0334 and FA9550-12-1-0263 grants. Drs. Sudipta Seal and Virendra Singh at the University of Central Florida are acknowledged for extending the use of their TEM facilities for characterization of the starting GNP. Authors also acknowledge the support of the Advanced Materials Engineering Research Institute (AMERI) at FIU. The Center for the Study of Materials in Extreme Conditions (CeSMEC) is acknowledged for extending the use of its Micro-Raman spectroscopy facility for this study.

References

- [1] T.H. Squire, J. Marschall, J. Eur. Ceram. Soc. 30 (2010) 2239–2251.
- [2] P.L. Moses, V.L. Rausch, L.T. Nguyen, J.R. Hill, Acta. Astronaut. 55 (2004) 619–630.
- [3] J.W. Canan, Aerosp. Am. 11 (2007) 2631.
- [4] S.P. Dodd, M. Cankurtaran, B. James, J. Mater. Sci. 38 (2003) 1107–1115.
- [5] Y.J. Chen, J.B. Li, Q.M. Wei, H.Z. Zhai, J. Cryst. Growth 224 (2001) 244–250.
- [6] B.R. Kim, K.D. Woo, J.M. Doh, Ceram. Int. 35 (2009) 3395–3400.
- [7] C.L. Yeh, E.W. Liu, J. Alloys Compd. 415 (2006) 66–72.
- [8] W.G. Fahrenholtz, G.E. Hilmas, I.G. Talmy, J.A. Zaykoski, J. Am. Ceram. Soc. 90 (2007) 1347–1364.
- [9] L. Liu, H. Liu, F. Ye, Z. Zhang, Y. Zhou, Ceram. Int. 38 (2012) 4707–4713.
- [10] K. Hackett, S. Verhoef, R.A. Cutler, D.K. Shetty, J. Am. Ceram. Soc. 92 (2009) 2404–2407.
- [11] C.M. Carney, J. Mater. Sci. 44 (2009) 5673–5678.
- [12] X. Zhang, G.E. Hilmas, W.G. Fahrenholtz, Mater. Sci. Eng. A 501 (2009) 37–43.
- [13] D. Sciti, L. Silvestroni, S. Guicciardi, D.D. Fabrice, A. Bellosi, J. Mater. Res. Soc. 24 (6) (2009) 2056–2065.
- [14] X. Zhang, G.E. Hilmas, W.G. Fahrenholtz, J. Am. Ceram. Soc. 90 (2007) 393–401.
- [15] J.X. Liu, Y.M. Kan, G.L. Zhang, J. Am. Ceram. Soc. 93 (2010) 370–373.
- [16] H. Liu, L. Liu, F. Ye, Z. Zhang, Y. Zhou, J. Eur. Ceram. Soc. 32 (2012) 3617–3625.
- [17] E. Khaleghi, Y.S. Lin, M.A. Meyers, E.A. Olevsky, Scr. Mater. 63 (2010) 577–580.
- [18] S.R. Bakshi, V. Musaramthota, D. Lahiri, V. Singh, S. Seal, A. Agarwal, Mater. Sci. Eng. A 528 (2011) 1287–1295.
- [19] S.R. Bakshi, V. Musaramthota, D.A. Virzi, A.K. Keshri, D. Lahiri, V. Singh, S. Seal, A. Agarwal, Mater. Sci. Eng. A 528 (2011) 2538–2547.
- [20] S. Guicciardi, L. Silvestroni, M. Nygren, D. Sciti, J. Am. Ceram. Soc. 93 (2010) 2384–2391 8.
- [21] L. Silvestroni, D. Sciti, S. Guicciardi, C. Melandri, J. Eur. Ceram. Soc. 30 (2010) 2155–2164.
- [22] J. Zou, G.J. Zhang, C.F. Hu, T. Nishimura, Y. Sakka, H. Tanaka, J. Vleugels, O. Van der Biest, J. Eur. Ceram. Soc. (2012) 2519–2527.
- [23] F. Yang, X. Zhang, J. Han, S. Du, J. Alloys Compd. 472 (2009) 395–399.
- [24] H. Wang, B. Fan, L. Feng, D. Chen, H. Lu, H. Xu, C.A. Wang, R. Zhang, Ceram. Int. 38 (2012) 5015–5022.
- [25] H. Wang, C.A. Wang, X. Yao, D. Fang, J. Am. Ceram. Soc. 90 (2007) 1992–1997.
- [26] D. Sciti, L. Silvestroni, J. Eur. Ceram. Soc. 32 (2012) 1933–1940.
- [27] L.M. Liu, F. Ye, Y. Zhou, Mater. Sci. Eng. A 528 (2011) 4710–4714.
- [28] J. Watts, G.E. Hilmas, W.G. Fahrenholtz, D. Brown, B. Clausen, J. Am. Ceram. Soc. 30 (2010) 2165–2171.
- [29] D. Lahiri, E. Khaleghi, S.R. Bakshi, W. Li, E.A. Olevsky, A. Agarwal, Scr. Mater. 68 (5) (2013) 285–288.
- [30] C. Lee, X. Wei, J.W. Kysar, J. Hone, Science 321 (5887) (2008) 385.
- [31] I.W. Frank, D.M. Tanenbaum, A.M. Van der Zande, P.L. McEuen, J. Vac. Sci. Technol. (2007).
- [32] XG Sciences, XG Sciences Documentation, 2009.
- [33] P. Miranzo, C. Ramirez, B. Roman-Manso, L. Garzon, H.R. Gutierrez, M. Terrones, C. Ocal, M.I. Osendi, M. Belmonte, J. Eur. Ceram. Soc. 33 (10) (2013) 1665–1674.
- [34] Y. Fan, L. Wang, J. Li, J. Li, S. Sun, F. Chen, L. Chen, W. Jiang, Carbon 48 (2010) 1743–1749.
- [35] T. He, J. Li, L. Wang, J. Zhu, W. Jiang, Mater. Trans. 50 (4) (2009) 749–751.
- [36] K. Wang, Y. Wang, Z. Fan, J. Yan, T. Wei, Mater. Res. Bull. 46 (2) (2011) 315–318.
- [37] J. Liu, H. Yan, M.J. Reece, K. Jiang, J. Eur. Ceram. Soc. 32 (2012) 4185–4193.
- [38] J. Liu, H. Yan, K. Jiang, Ceram. Int. 39 (6) (2013) 6215–6221.
- [39] L.S. Walker, V.R. Marotto, M.A. Rafiee, N. Koratkar, E.L. Corral, ACS Nano 5 (4) (2011) 3182–3190.
- [40] C. Ramirez, F.M. Figueiredo, P. Miranzo, P. Poza, M.I. Osendi, Carbon 50 (2012) 3607–3615.
- [41] J. Dusza, J. Morgiel, A. Duszova, L. Kvetkova, M. Nosko, P. Kun, C. Balazsi, J. Eur. Ceram. Soc. 32 (2012) 3389–3397.
- [42] O. Tapasztó, L. Tapasztó, M. Marko, F. Kern, R. Gadow, C. Balazsi, Chem. Phys. Lett. 511 (2011) 340–343.
- [43] P. Kun, O. Tapasztó, F. Weber, C. Balazsi, Ceram. Int. 38 (2012) 211–216.
- [44] L. Kvetkova, A. Duszova, P. Hvizdos, J. Dusza, P. Kun, C. Balazsi, Scr. Mater. 66 (2012) 793–796.
- [45] H. Seiner, P. Sedlak, M. Koller, M. Landa, C. Ramirez, M.I. Osendi, M. Belmonte, Compos. Sci. Technol. 75 (2013) 93–97.
- [46] C. Ramirez, I. Osendi, J. Eur. Ceram. Soc. 33 (2013) 471–477.
- [47] L. Kvetkova, A. Duszova, M. Kasiarova, F. Dorcakova, J. Dusza, C. Balazsi, J. Eur. Ceram. Soc. 33 (12) (2013) 2299–2304.
- [48] G.B. Yadhukulkrishnan, S. Karamuri, A. Rahman, R.P. Singh, A.K. Kalkan, S.P. Harimkar, Ceram. Int. 39 (6), 2013, 6637–6646.
- [49] A. Nieto, D. Lahiri, A. Agarwal, Carbon 50 (2012) 4068–4077.
- [50] W. Choi, I. Lahiri, R. Seelaboyina, Y.S. Kang, Crit. Rev. Solid State Mater. Sci. 35 (2010) 52–71.
- [51] W.C. Oliver, G.M. Pharr, J. Mater. Res. 76 (1992) 1564–1583.
- [52] G.R. Anstis, P. Chantikul, B.R. Lawn, D.B. Marshall, J. Am. Ceram. Soc. 64 (9) (1981) 533–538.
- [53] D. Lahiri, R. Dua, C. Zhang, I.D. Socarras-Novoa, A. Bhat, S. Ramaswamy, A. Agarwal, ACS Appl. Mater. Interfaces (2012) 2234–2241.
- [54] K. Jagannadham, J. Vac. Sci. Technol. B 30 (3) (2012) 03D109 1–9.
- [55] G.V. Samsonov, I.M. Vinitskii, Handbook of Refractory Compounds, Plenum Data Company, New York, 1980.
- [56] M.M. Opeka, I.G. Talmy, E.J. Wuchina, J.A. Zaykoski, S.J. Causey, J. Eur. Ceram. Soc. 19 (1999) 2405–2412.
- [57] B.C. Kellet, D.S. Wilkinson, J. Am. Ceram. Soc. 78 (1995) 1198–1200.
- [58] Y.S. Chou, D.J. Green, J. Am. Ceram. Soc. 75 (1992) 3346–3352.
- [59] L. Lopez-de-la-Torre, B. Winkler, J. Schreuer, K. Knorr, M. Avalos-Borja, Solid State Commun. 134 (2005) 245–250.



Boron nitride nanotubes reinforced aluminum composites prepared by spark plasma sintering: Microstructure, mechanical properties and deformation behavior

Debrupa Lahiri^a, Ali Hadjikhani^a, Cheng Zhang^a, Tan Xing^b, Lu Hua Li^b, Ying Chen^b, Arvind Agarwal^{a,*}

^a Plasma Forming Lab, Advanced Materials Engineering Research Institute (AMERI), Mechanical and Materials Engineering, Florida International University, Miami, FL 33174, USA

^b Institute for Frontier Materials, Deakin University, Geelong Waurn Ponds Campus, VIC 3216, Australia

ARTICLE INFO

Article history:

Received 29 December 2012

Received in revised form

19 February 2013

Accepted 9 March 2013

Available online 16 March 2013

Keywords:

Boron nitride nanotube

Spark plasma sintering

Micro-pillar

Deformability

Aluminum

Composite

ABSTRACT

Boron nitride nanotubes (BNNT) reinforced aluminum based composites are synthesized by spark plasma sintering (SPS). The concentration of BNNT is varied as 0, 2 and 5 vol% in the aluminum matrix. Micro-pillar compression testing revealed that Al–5 vol% BNNT has yield strength and compressive strength as 88 MPa and 216 MPa respectively, which is more than 50% improvement over unreinforced Al. BNNT play an active role in strengthening Al matrix through effective load bearing and transfer by crack bridging and sword in sheath mechanisms. Cold rolling of Al–5 vol% BNNT with 75% thickness reduction in a single pass exhibited high deformability without cracking or disintegration. The deformation is dominated by slip signifying ductile behavior in sintered Al with and without BNNT. BNNT survives the extreme temperature and pressure conditions during SPS processing and heavy deformation during cold rolling.

© 2013 Elsevier B.V. All rights reserved.

1. Introduction

Boron nitride nanotube (BNNT) is of current interest as reinforcement to structural composites. Its potential is projected based on the excellent elastic modulus of > 1 TPa [1,2], tensile strength (up to 61 GPa [3]), high flexibility [4] and high temperature inertness (oxidation starts > 950 °C) [4–6]. Mettle of BNNT as structural reinforcement has been proven by few studies for polymer and ceramic matrices. Polymer matrix composites with randomly or aligned BNNT furnishes improvement in thermal, mechanical and optical properties [7–12]. Studies on ceramic–BNNT composites report improvement in elastic modulus, hardness, fracture toughness, flexural strength and high temperature superplasticity in different ceramics, e.g. Al_2O_3 , SiO_2 , Si_3N_4 and hydroxyapatite [13–19]. However, reinforcing metal matrix composite remains a challenge due to high reactivity of metals at elevated processing temperatures. The problem becomes significant especially for low melting metals, like Al which is most researched among metal matrix composites due to its light weight and high strength characteristics.

Carbon nanotube (CNT), which is a structural analog of BNNT, has been extensively studied as reinforcement for metal matrix

composites, including Al, in last 10 years. However, CNT reacts with the Al matrix to form aluminum carbide (Al_4C_3) at Al–CNT interface which serves as a mechanically weak point [20]. BNNT could be a better choice as compared to CNT due to its much high inertness. BNNT starts oxidizing above 950 °C, as compared to CNT at 500 °C [4–6]. A recent study from the present authors, on Al–BNNT interface reaction mechanism, has experimentally shown minimal reactivity at Al–BNNT interface when exposed to 650 °C for more than an hour [21]. A theoretical comparison based on thermodynamics also shows less volume and reaction product formation at Al–BNNT interface, as compared to Al–CNT [21]. Apart from having comparable elastic modulus and strength and higher inertness to CNTs, the structure of BNNT is more flexible and capable of withstanding heavy deformation without getting damaged [4]. A recent study has shown BNNT possess higher fracture strain than CNT [22]. All these characteristics of BNNT add to the potential of Al–BNNT system as a strong composite structure.

The outcomes from a recent investigation on Al–BNNT nanocomposite were encouraging in establishing the BNNT as an effective reinforcement for Al matrix [27]. The composite was prepared by magnetron sputtering of Al on dispersed BNNT, forming 5–200 nm thick coating on individual BNNT. Nanocrystalline aluminum coated individual BNNT shows tight bonding at the Al/BNNT interface and an impressive nine-times improvement in tensile strength with a recorded value of 360 MPa. *In situ* TEM

* Corresponding author.

E-mail address: agarwala@fiu.edu (A. Agarwal).

tensile strength was measured along the axial direction of Al coated single BNNT, which is supposedly the strongest direction in nanotubes [23]. An impressive improvement in strength indicates that BNNT has the potential to strengthen the bulk composite structures. Singhal et al. have reported synthesis of bulk Al–BNNT composite through conventional sintering route [24]. Al–BNNT displayed higher compressive strength as compared to sintered Al pellets. However, there was significant density difference (~12%) between Al and Al–BNNT samples, with Al being only 83% dense. Hence, improvement in compressive strength could not be attributed solely due to BNNT addition.

In view of the present scenario, the objective of this study is set to evaluate BNNT as a potential reinforcement to the aluminum matrix and evaluate the deformability of the resulting composite.

This study presents the first report on synthesis of macro-scale Al–BNNT composite by spark plasma sintering (SPS). The mechanical properties of the composite are evaluated using micro-pillar compression testing to estimate the effect of BNNT addition on strengthening of Al matrix. The deformability of Al–BNNT composite by cold rolling is also studied to evaluate its formability.

2. Materials and methods

2.1. Powder preparation and consolidation

Boron nitride nanotubes were synthesized by catalyst enhanced ball milling and annealing method. The details of the synthesis

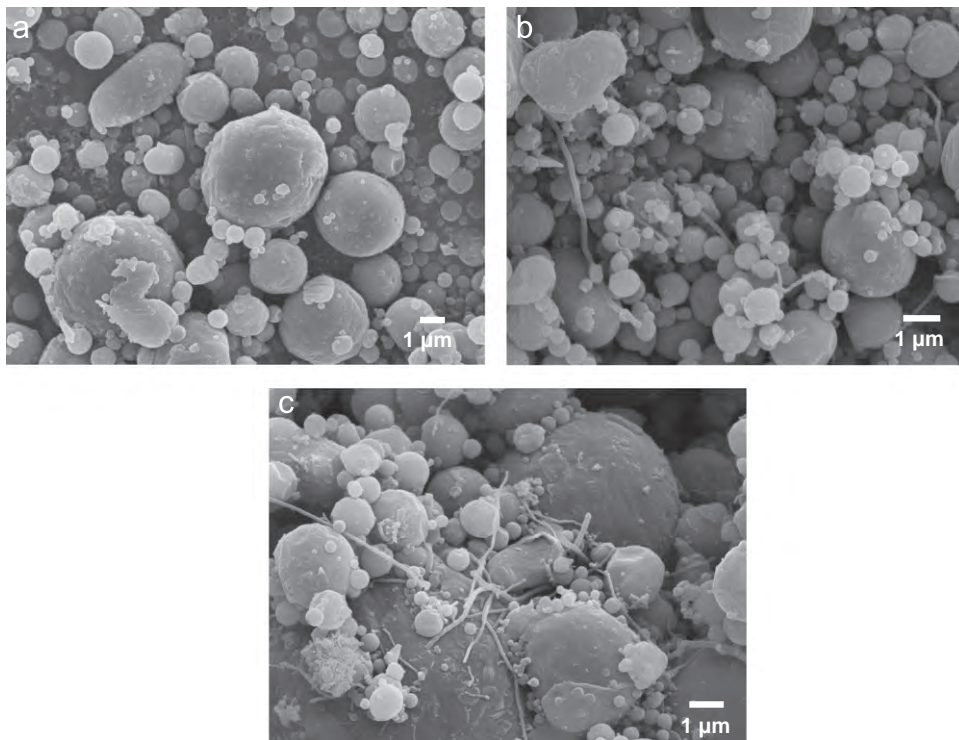


Fig. 1. SEM micrograph of: (a) Al; (b) Al–2BNNT and (c) Al–5BNNT powders prepared by ultrasonication mixing.

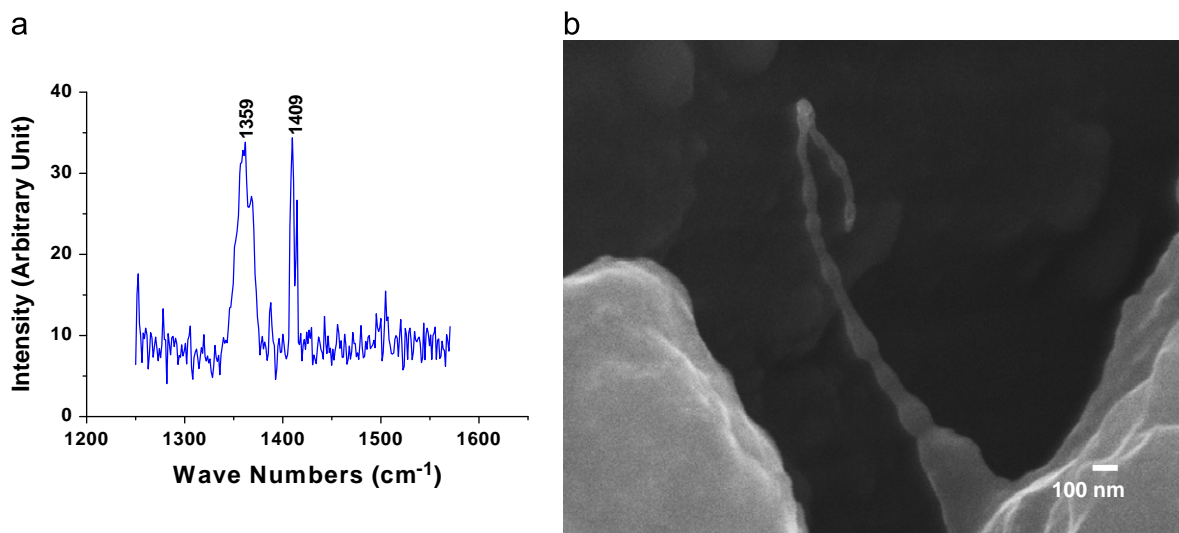


Fig. 2. (a) Raman spectrum from sintered Al–5BNNT pellet showing peaks from h-BN; (b) SEM micrograph of a BNNT covered with molten Al in Al–2BNNT pellet, which was partially melted due to higher sintering temperature.

procedure are presented in an earlier publication [25]. Aluminum powder (H3, Valimet Inc., USA) of spherical shape with 90% particles having diameter $< 10.5 \mu\text{m}$ and purity of $\geq 99.7\%$ were used for this study. Several studies have reported strengthening in Al based composites by using nanosized pre-alloyed Al powder as matrix, followed by cryomilling and sintering [26–29]. Reducing the size of high purity Al powder to nanometer range would make them more reactive and possibly explosive in nature. Hence, we did not use nanosized pure Al powder in the present study. Al–BNNT composite powders, containing 2 and 5 vol% BNNT, were prepared

by wet-mixing method using acetone as medium. Nanotubes were ultrasonicated in acetone for 1 h, followed by mixing of Al powder in the suspension and further ultrasonication for 30 min. Drying of the composite powder was carried out at 60°C for 2 h. Three compositions of pure Al and with 2 and 5 vol% BNNT, would be referred as Al, Al–2BNNT and Al–5BNNT hereafter.

Due to unavailability of literature on Al–BNNT consolidation by spark plasma sintering (SPS), there was a learning curve to optimize the process parameters. In that process, the Al–2BNNT pellet suffered partial melting during sintering at 600°C . Consequently, SPS of Al and Al–5BNNT powders were performed at a maximum temperature of 500°C and 80 MPa pressure (heating rate of $50\text{--}60^\circ\text{C}/\text{min}$) for 1 h in vacuum using the graphite die. The hold time at maximum temperature was 1 h, which is similar to other SPS studies in the literature [30,31]. The powders were consolidated into pellets of 20 mm diameter and 5 mm thickness. Mechanical characterization has been carried out for Al and Al–5BNNT samples only. Al–2BNNT was not used for reporting mechanical properties due to its different microstructure caused by partially melting at 600°C . Semi-molten Al–2BNNT microstructure was used to understand the wetting and reactivity of Al with BNNT.

The density of the sintered pellets was measured using helium gas pycnometry (Accupyc 1340, Micromeritics Instrument Corporation, Norcross, GA, USA) and expressed in terms of relative density, while calculating the true density of the composites by weighted average. The microstructural characterization of the powders and fracture surfaces of the pellets was carried out using JEOL JSM-6330F field emission scanning electron microscope operating at 15 kV. X-ray diffraction (XRD) studies on sintered pellets were carried out in a Siemens D-5000 X-ray diffractometer (Munich, Germany) using $\text{Cu K}\alpha$ ($\lambda = 1.542 \text{ \AA}$) radiation. Raman spectrum of Al–5BNNT pellet was obtained using an argon ion

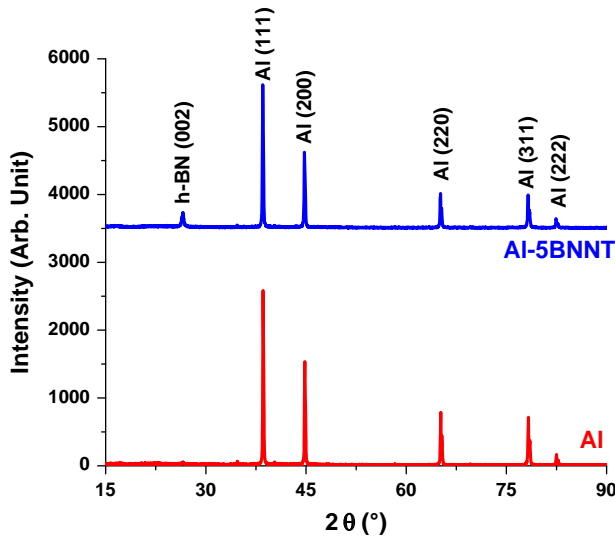


Fig. 3. X-ray diffraction patterns of Al and Al–5BNNT SPS pellet showing aluminum peaks and the highest intensity h-BN peak in the latter.

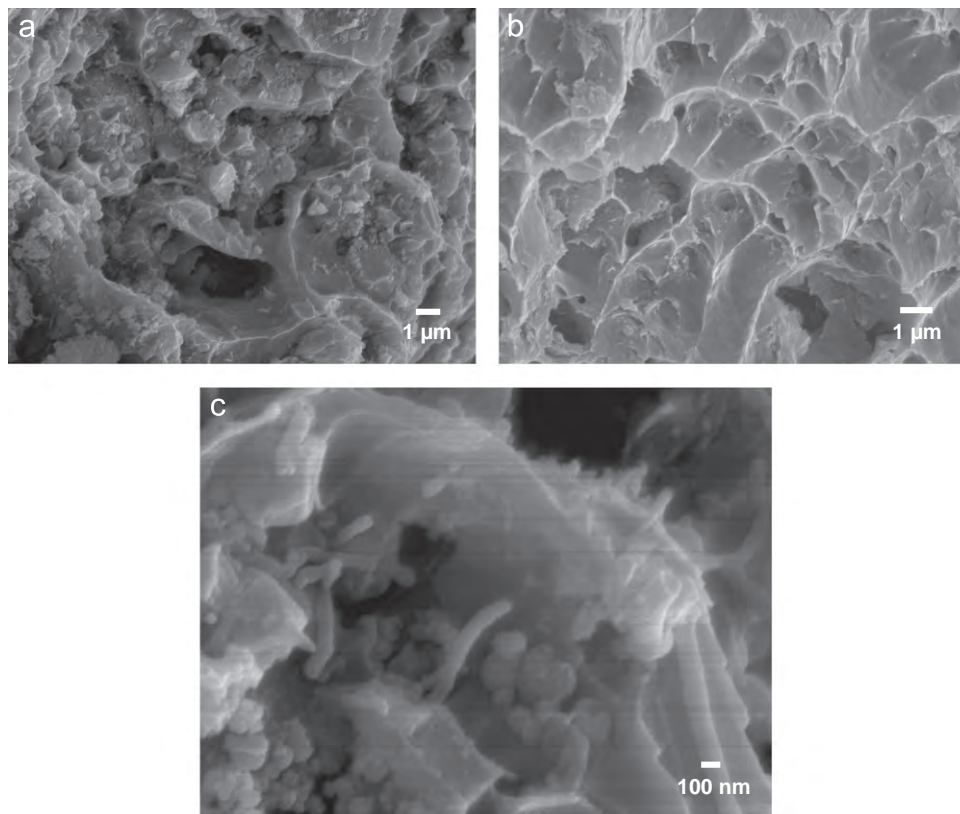


Fig. 4. SEM micrograph of the fracture surfaces of (a) Al and (b) Al–5BNNT pellets indicating ductile type failure. (c) High magnification micrograph of Al–BNNT fracture surface reveals protruding tubular shaped BNNT.

(Ar⁺) laser system (Spectra Physics, model 177G02) of wavelength 514.5 nm. Backscattered spectrum was collected by a high throughput holographic imaging spectrograph (Kaiser Optical Systems, model HoloSpec *f*/1.8i) with a volume transmission grating, holographic notch filter, and charge coupled device detector (Andor Technology). The Raman system has a spectral resolution of 4 cm⁻¹ and the spectrum was collected at an exposure of 300 s.

2.2. Micropillar machining and compression testing

Polished surfaces of Al and Al-5BNNT pellets were used to machine several micro-pillars using JEOL-JIB 4500 focused ion beam (FIB) milling system using Ga⁺ ions. Each micro-pillar was spaced ~100 μm from each other. The optimum milling conditions had an acceleration voltage of 30 kV and 500 pA current which yielded a spot diameter of 0.1 μm. The micro-pillar was machined with an inner diameter of 4 μm in a trench of diameter of 16.5 μm. The height of each pillar was ~15 μm.

The compression testing of micropillars was carried out using Hysitron Triboindenter (TI-900, Hysitron Inc, Minneapolis, MN, USA) in quasistatic mode with a conospherical diamond probe of 1 μm tip radius. Scanning probe microscopy module, in-built in triboindenter, was used to locate the micro-pillar before the compression test. The loading rate was 100 μN/s and the peak load was set to 5000 μN, though all the pillars broke/failed before

reaching the peak load. The stress was calculated by dividing the load with the cross-sectional area of the pillar. The area was calculated at half the height of the pillar in order to minimize over-/under-estimation of the stress value.

2.3. Heavy deformation by cold rolling

SPS pellets were cut into 5 mm wide thin strips of ~0.6 mm thickness and then deformed in a cold rolling machine (International Rolling Machine, RI-02860). Thickness was reduced to ~150 μm in a single pass, indicating 75% thickness reduction. The strips were heated to 80 °C, using a hot air gun, immediately before rolling. Cross-sectional surface of the rolled sheet was observed using SEM. Microhardness of SPS pellets and rolled strips was measured (Shanghai Taiming Optical Instrument Co. Ltd., model HXD-1000 TMC, Shanghai) on polished cross sections with a Vickers probe and application of 200 g load for 15 s of dwell time.

Table 1

Yield and compressive strength of Al and Al-5BNNT from micro-pillar testing.

Composition	Yield strength (MPa)	Compressive strength (MPa)
Al	57 ± 6	142 ± 10
Al-5BNNT	88 ± 7	216 ± 27

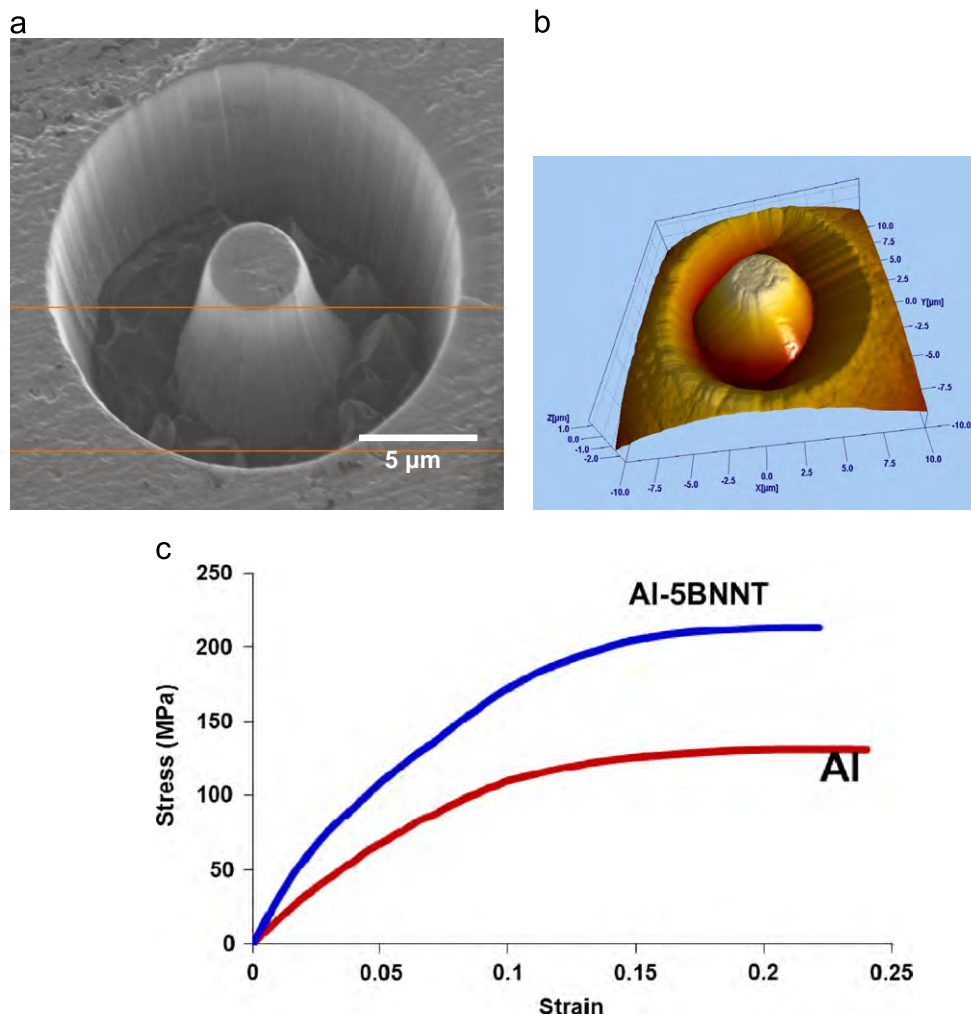


Fig. 5. (a) SEM micrograph of the Al-5BNNT micro-pillar prepared by FIB milling; (b) SPM image of the pillar after centering and prior to compression testing; (c) representative stress-strain curve from micro-pillar compressive tests of Al and Al-5BNNT composites.

3. Results and discussion

3.1. Microstructural and phase characterization

Dispersion of BNNT in the aluminum powder and sintered composite is very important towards its mechanical performance. Fig. 1a, b and c presents the SEM micrographs of Al, Al-2BNNT and Al-5BNNT powders, respectively. Fig. 1b shows well dispersed long BNNT in Al-2BNNT composition. Trace of BNNT agglomeration is observed in Fig. 1c in Al-5BNNT powder due to higher (5 vol%) BNNT content. It is concluded that the overall dispersion of BNNT in Al powder by ultrasonication is effective at lower BNNT concentration.

As mentioned earlier, while developing SPS processing parameters, Al-2BNNT powder was sintered at a maximum hold temperature of 600 °C. Al-2BNNT pellet suffered partial melting during sintering treatment. Thus, this study does not use the mechanical property data from Al-2BNNT to compare it with Al and Al-5BNNT. However, we have reported microstructure of Al-2BNNT sintered pellet as it helps in understanding the effect of molten Al on BNNT. SPS leads to effective consolidation of Al-BNNT composites into macro-scale structures. The Al pellet has achieved an excellent densification with a relative density of 99.4% TD. The density recorded for Al-5BNNT is 97.8% TD. A decrease in density by 1.6% can be explained in terms of partial agglomeration of BNNT in Al-5BNNT (Fig. 1c), leaving some intermediate voids. However, the relative density of Al-5BNNT is high enough to suggest very good densification. The density of Al-2BNNT is not reported as it involved melting.

Micro-Raman analysis was carried out to obtain the signature of h-BN structure in the SPS pellet, to study the survivability of BNNT in harsh processing conditions of SPS for 1 h. Fig. 2a shows

the Raman spectrum for sintered Al-5BNNT pellet, with two peaks at 1359 and 1409 cm^{-1} , characteristic of h-BN structure and often observed for BNNT [32–35]. The h-BN peak existing at 1363–1368 cm^{-1} is E_{2g} mode peak for h-BN, which shifts to a lower angle due to buckling of the BNNT [35], also observed in the present study. Fig. 2b shows a SEM micrograph of a dangling BNNT from the fracture surface of Al-2BNNT pellet. It must be recalled that Al-2BNNT undergone partial melting due to high temperature (600 °C) exposure during SPS. The tubular structure of BNNT is undamaged and fully wrapped with a thin layer of resolidified Al, indicating excellent wetting of Al on BNNT. A thicker Al layer is observed on the knotty region of the bamboo shaped BNNT. The intact BNNT in partially melted aluminum widens the scope of synthesizing Al-BNNT composite via melting and solidification route. Boron nitride nanotubes were also intact in Al-5BNNT pellet, which is discussed in Section 3.2 of this study.

X-ray diffraction analysis on the surface of sintered pellets (Fig. 3) provides insight into the possibility of chemical reaction between BNNT and Al. The diffraction pattern from SPS Al pellet shows the peaks related to FCC Al structure. X-ray diffraction pattern for SPS Al-5BNNT shows peaks from FCC-Al and basal plane of h-BN. The presence of h-BN peak is another evidence of survival of BNNT structure after SPS processing. Absence of any diffraction peak corresponding to reaction products of Al and C refutes the chance of significant reaction between graphite die and Al. Further, absence of peaks corresponding to reaction products such as AlN and AlB_2 indicates, minimal reaction occurring in sintered Al-5BNNT pellet. Our previous study found insignificant amount of reaction product formation at Al/BNNT interface at temperature near the melting point of Al for 1 h [21]. This is

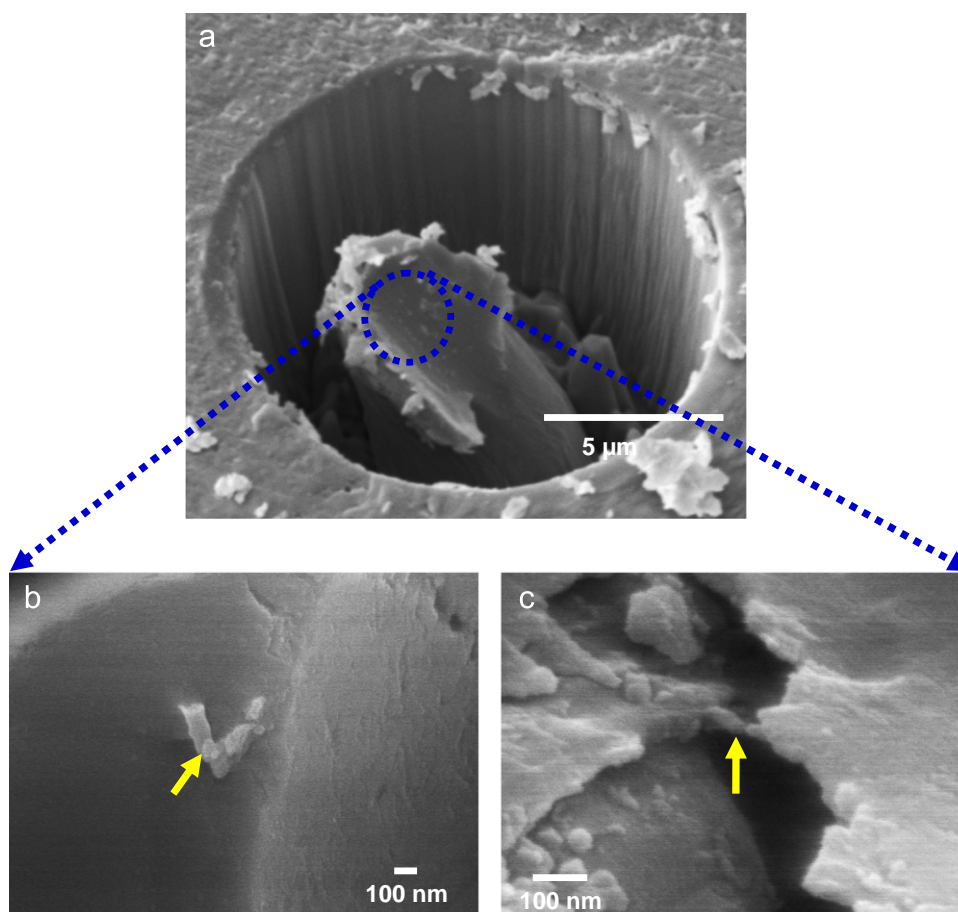


Fig. 6. (a) SEM micrograph of the broken micro-pillar of Al-5BNNT. High magnification SEM images of fracture surface of broken Al-5BNNT micro-pillar revealing (b) protruding BNNT from Al matrix and (c) BNNT bridge across the crack.

attributed to high inertness of BNNT [4–6]; lower mass of reaction product formation and lower thermodynamic probability of reaction with Al as compared to CNT [21]. Yamaguchi et al. have also reported absence of any interfacial reaction product in their sputter synthesized Al–BNNT nano-composites [27]. Singhal et al. have reported formation of a very thin (4–6 nm) AlB_2 layer in cold pressed and sintered Al–BNNT composite by HRTEM analysis, which is supportive of the observations in the present study [28].

SEM micrographs from both Al and Al–5BNNT pellets reveal signs of ductile fracture domination (Fig. 4a and b). The thin high ridges on the fracture surfaces are formed due to high amount of localized necking leading to fracture. Fracture surface also reveals the dense structure with minimal porosity for both the compositions, supporting the density data reported earlier. A closer look at the Al–5BNNT fracture surface reveals tubular shape of protruded BNNT (Fig. 4c), indicating their role in strengthening the composite, which is discussed in next section.

3.2. Micro-pillar compressive strength

Micro-pillar compression testing was carried out to evaluate the strengthening role of BNNT. Fig. 5a shows the SEM image of a representative Al–5BNNT micro-pillar prepared by FIB. Prior to compression tests, surface of the sample with micro-pillars was scanned in SPM mode with a minimal applied load of $2\ \mu\text{N}$ (to prevent damage to the pillars) to locate the positioning of the probe accurately at the center of the pillar. Fig. 5b presents a SPM image of a micro-pillar prior to testing. At least 5 micro-pillar compression tests were carried out for each of Al and Al–5BNNT. A representative stress–strain curve for Al and Al–5BNNT, calculated from the load–displacement plot obtained during compression test, is presented in Fig. 5c. The stress–strain curve clearly reveals higher stress absorbance with similar strain values for Al and Al–5BNNT, indicating higher yield strength (YS) and compressive strength (CS) as compared to Al. The higher slope in the initial linear part of the stress–strain curve also indicates higher elastic modulus for Al–5BNNT. But, elastic modulus values are not reported as minor slipping during these tests can significantly alter the strain values, considering the small scale of deformation in micro-pillar testing. However, YS and CS are obtained from the load data and do not depend on the strain (Table 1). Yield strength of 88 MPa is observed for Al–5BNNT, which is 54% improvement over Al. The similar percentage increase in compressive strength is also noted, with the values being 142 MPa and 216 MPa, for Al and Al–5BNNT, respectively. Increase in the yield strength can be attributed to the elastic deformation of the material, whereas the compressive strength also bears the contribution from plastic deformation and can be related to strengthening phenomenon. Thus, BNNT reinforcement is found to influence both elastic and plastic deformation of sintered Al–5BNNT structure.

Fig. 6a presents the SEM image of a micro-pillar after compression tensing. The fracture surface makes an angle of $\sim 45^\circ$ with the loading direction. The pillars are polycrystalline and sintering is not expected to impose any crystallographic texture in these pellets. As a result, slipping is evitable in the maximum shear stress direction, which is at 45° to the compressive load direction. Thus, the observation in Fig. 6a indicates the deformation taking place by slipping under shear stress. It is quite justified considering the ductile behavior of both Al and Al–5BNNT, shown in Fig. 4. The high magnification images of fracture surface of Al–5BNNT micro-pillar are shown in Fig. 6b and c. Fig. 6b shows a protruded BNNT from Al matrix, where Fig. 6c reveals a BNNT bridge across a crack. These microstructural features are indicator of strengthening of Al matrix by load bearing ability of BNNT before the failure occurs. Further evidence of strengthening mechanisms is visible from the fracture surface of Al–5BNNT sintered pellet shown in

Fig. 7. Presence of BNNT bridge (Fig. 7a) on the fracture surface is the evidence of resistance to failure, which contributes towards the compressive strength. The ‘sword in sheathe’ structure of BNNT is observed in Fig. 7b, which further augments the load transfer from the matrix to reinforcement. A similar structural feature of BNNT has also been observed in aluminum, alumina, silicon nitride and hydroxyapatite matrix composites [13,14,27]. This telescopic structure of BNNT is formed due to transfer of load from the matrix to reinforcement and then gradual failure of outer layers of the multiwall nanotube in a sequence, when stress is transferred to the inner layer. The key of strengthening in any metal matrix composite lies in effective load transfer from matrix to reinforcement phase, which is detected in Al–5BNNT structure. Effective sharing of load by the reinforcement restricts both elastic and plastic deformation of matrix, leading to improvement in YS and compressive strength. The reaction products at Al–BNNT interface are also important for interfacial bonding and effective load transfer from matrix to reinforcement. Al–BNNT interface is reported to have higher mass fraction of AlN with greater spatial distribution across interface than AlB_2 [21]. In addition, AlN forms on the Al side with a crystallographically coherent interface, facilitating strong bonding at Al–BNNT interface [21]. Thus, the excellent elastic modulus and tensile strength of BNNT in synergy with strong bonding at the interface results in improvement in mechanical properties of Al–5BNNT composite. Our future efforts

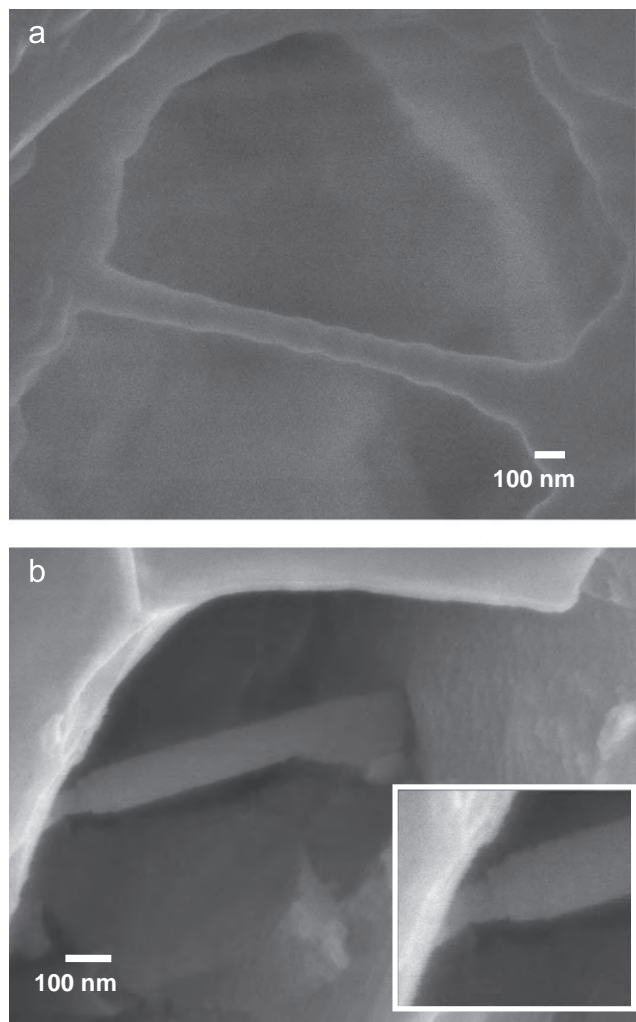


Fig. 7. Fracture surface of Al–5BNNT pellet revealing strengthening mechanism: (a) crack bridging by BNNT and (b) ‘sword-in-sheath’ structure of BNNT resulting in efficient load transfer from Al–matrix to BNNT.

are directed to synthesize large Al–BNNT pellets to machine tensile samples for large scale tensile testing.

3.3. Heavy deformation by rolling: evaluation of formability

Al and Al–5BNNT pellets were subjected to heavy deformation via cold rolling to understand the effect of BNNT addition on the formability of the composite. Fig. 8a presents Al–5BNNT SPS pellet and the thin cold-rolled strips. The pellet was cut in strips of 0.6 mm thickness and then rolled upto $\sim 150\ \mu\text{m}$. A 75% reduction in thickness in a single pass of cold rolling did not introduce any major crack or disintegration of the structure. Fig. 8b and c presents the SEM micrograph of fracture surfaces of Al and Al–5BNNT rolled strips, respectively. The fracture was made perpendicular to the rolling direction. Both the surfaces show highly dense structure and ductile failure. The retention of ductility even after 75% deformation in Al–5BNNT makes them suitable for fabrication. High magnification SEM image of fracture surface of rolled Al–5BNNT shows undamaged tubular BNNT protruding from the matrix (Fig. 8d). BNNT survives severe deformation during rolling, which was possible due to high flexibility and fracture strain of BNNT [4,22]. The survival of undamaged BNNT in the rolled structure ensures strengthening capability of the composite in the final fabricated shape.

Microhardness was evaluated for Al and Al–5BNNT in sintered and rolled strips (Table 2). Hardness is similar for Al and Al–5BNNT in SPS pellet and increases after rolling in both samples, due to strain hardening. However the rolling induced hardness improvement in Al is only 21%, as compared to 59% in Al–5BNNT structure. Moreover the microhardness of rolled Al is 647 MPa, which is 25% lower than that of Al–5BNNT being 807 MPa. Rolling potentially improves the densification and bonding of BNNT with Al matrix. Thus, after rolling, the BNNT can cause further strain hardening and an increase in the hardness.

4. Summary

This study presents the potential of BNNT as reinforcement in strengthening bulk scale aluminum matrix composites. Spark

Table 2
Microhardness of Al and Al–5BNNT pellets before and after rolling.

Sample	Hardness (MPa)	
	SPS	SPS + Rolled
Al	499 ± 28	647 ± 10
Al–5BNNT	506 ± 12	807 ± 34

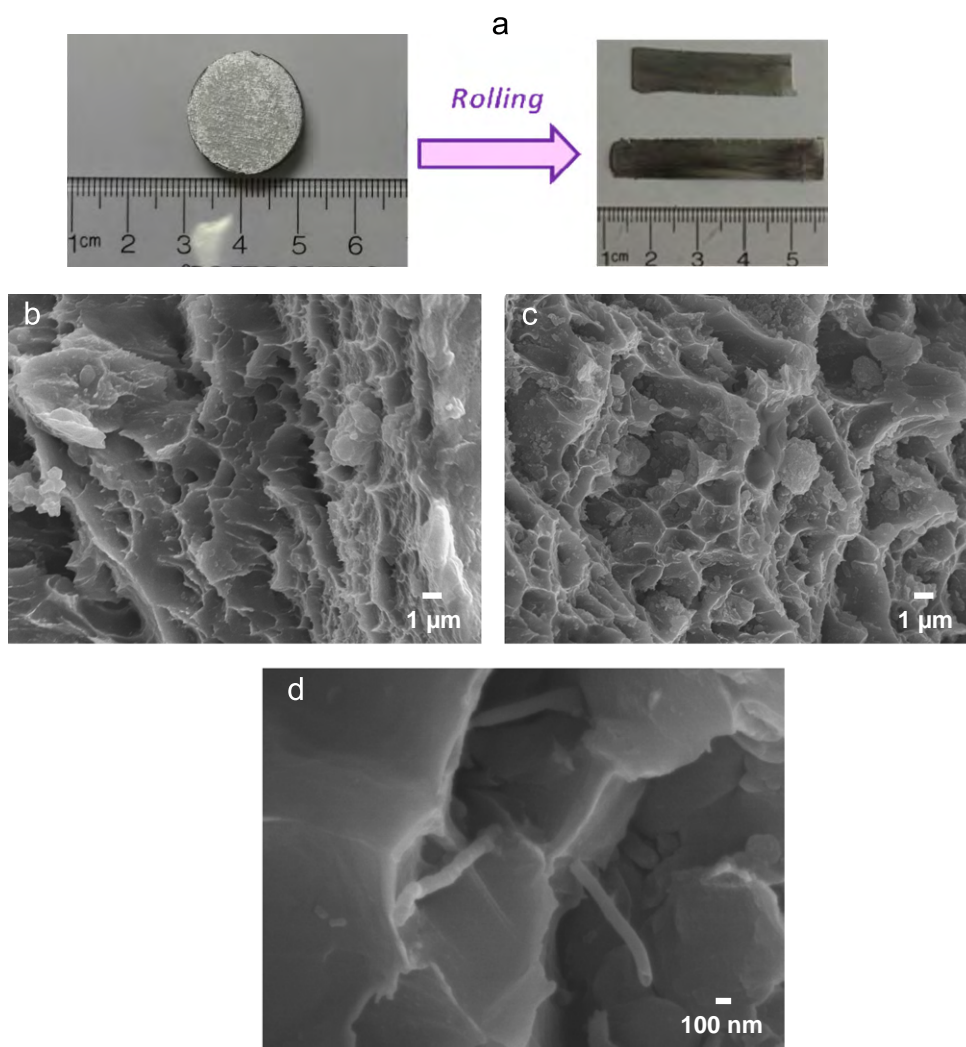


Fig. 8. (a) SPS Al–5BNNT pellet and thin strips after cold rolling. SEM micrographs of fracture surfaces from the rolled strips of (b) Al and (c, d) Al–5BNNT. The high magnification micrograph of Al–5BNNT fracture surface reveals survival of BNNT after heavy deformation.

plasma sintering is an effective method for consolidating Al–BNNT composites with excellent densification of 98–99% TD. BNNT survives the high pressure and temperature application for prolonged time in SPS and do not form significant amount of reaction products at the interface. Micro-pillar compressive tests shows > 50% improvement in both yield and compressive strength with 5 vol% BNNT addition in Al matrix. Microstructural analysis reveals ‘sword in sheathe’ and crack bridging as major strengthening mechanism for effective load transfer from the matrix to reinforcement. Al–5BNNT exhibits high deformability as it undergoes 75% thickness reduction in a single pass of cold rolling without cracking or disintegration.

Acknowledgments

AA would like to acknowledge support from US Air Force Office of Scientific Research through DURIP (FA9550-11-1-0334) Grant. The overall support of AMERI at FIU, in maintaining the research facilities are greatly acknowledged.

References

- [1] A.P. Suryavanshi, M.F. Yu, J. Wen, C. Tang, Y. Bando, *Appl. Phys. Lett.* 84 (2004) 2527–2529.
- [2] N.G. Chopra, A. Zettl, *Solid State Commun.* 105 (1998) 297–300.
- [3] R. Arenal, M.-S. Wang, Z. Xu, A. Loiseau, D. Golberg, *Nanotechnology* 22 (2011) 265704.
- [4] D. Golberg, Y. Bando, C. Tang, C. Zhi, *Adv. Mater.* 19 (2007) 2413–2432.
- [5] Y. Chen, J. Zou, S.J. Campbell, G. Le, *Appl. Phys. Lett.* 84 (13) (2004) 2430–2432.
- [6] D. Golberg, Y. Bando, K. Kurashima, T. Sato, *Scr. Mater.* 44 (2001) 1561–1565.
- [7] C. Zhi, Y. Bando, C. Tang, S. Honda, K. Sato, H. Kuwahara, D. Golberg, *Angew. Chem.* 44 (2005) 7929–7932.
- [8] C. Zhi, Y. Bando, C. Tang, *J. Mater. Res.* 21 (2006) 2794–2800.
- [9] C. Zhi, Y. Bando, T. Terao, C. Tang, H. Kuwahara, D. Golberg, *Adv. Funct. Mater.* 19 (2009) 1857–1862.
- [10] T. Terao, C. Zhi, Y. Bando, M. Mitome, C. Tang, D. Golberg, *J. Phys. Chem.* 114 (2010) 4340–4344.
- [11] J. Ravichandran, A.G. Manoj, J. Liu, I. Manna, D.L. Carroll, *Nanotechnology* 19 (2008) 085712.
- [12] D. Lahiri, F. Rouzaud, T. Richard, A.K. Keshri, S.R. Bakshi, L. Kos, A. Agarwal, *Acta Biomater.* 6 (2010) 3524–3533.
- [13] Q. Huang, Y. Bando, X. Xu, T. Nishimura, C. Zhang, C. Tang, F. Xu, L. Gao, D. Golberg, *Nanotechnology* 18 (2007) 485706.
- [14] D. Lahiri, V. Singh, A.P. Benaduce, S. Seal, L. Kos, A. Agarwal, *J. Mech. Behav. Biomed. Mater.* 4 (2011) 44–56.
- [15] M. Du, J.-Q. Bi, W.-L. Eang, X.-L. Sun, N.-N. Long, *J. Alloys Compd.* 509 (2011) 9996–10002.
- [16] W.-L. Wang, J.-Q. Bi, K.-N. Sun, M. Du, N.-N. Long, Y.-J. Ba, *J. Am. Ceram. Soc.* 94 (2011) 3636–3640.
- [17] W.-L. Wang, J.-Q. Bi, K.-N. Sun, M. Du, N.-N. Long, Y.-J. Bai, *J. Am. Ceram. Soc.* 94 (2011) 2304–2307.
- [18] W.-L. Wang, J.-Q. Bi, S.-R. Wang, K.-N. Sun, M. Du, N.-N. Long, Y.-J. Bai, *J. Eur. Ceram. Soc.* 31 (2011) 2277–2284.
- [19] M. Du, J.-Q. Bi, W.-L. Wang, X.-L. Sun, N.-N. Long, Y.-J. Bai, *Mater. Sci. Eng. A* 530 (2011) 669–674.
- [20] A. Agarwal, S.R. Bakshi, D. Lahiri, *Carbon Nanotubes: Reinforced metal Matrix Composites*, CRC Press, Boca Raton, ISBN 9781439811498, 2010.
- [21] D. Lahiri, V. Singh, L.H. Li, T. Xing, S. Seal, Y. Chen, A. Agarwal, *J. Mater. Res.* 27 (2012) 2760–2770.
- [22] H.M. Ghassemi, C.H. Lee, Y.K. Yap, R.S. Yassar, *Nanotechnology* 22 (2011) 115702.
- [23] M. Yamaguchi, D.-M. Tang, C. Zhi, Y. Bando, D. Sntansky, D. Golberg, *Acta Mater.* 60 (2012) 6213–6222.
- [24] S.K. Singhal, A.K. Srivastava, R. Pasricha, R.B. Mathur, *J. Nanosci. Nanotechnol.* 11 (2011) 5179–5186.
- [25] L.H. Li, Y. Chen, A.M. Glushenkov, *Nanotechnology* 21 (2010) 105601.
- [26] E.J. Lavernia, B.Q. Han, J.M. Schoenung, *Mater. Sci. Eng. A* 493 (2008) 207–214.
- [27] B.Q. Han, Z. Lee, D. Witkin, S.R. Nutt, E.J. Lavernia, *Metall. Mater. Trans. A* 36 (2005) 957–965.
- [28] V.L. Tellkamp, A. Melmed, E.J. Lavernia, *Metall. Mater. Trans. A* 32 (2001) 2335–2343.
- [29] S.Y. Chang, J.G. Lee, K.T. Park, D.H. Shin, *Mater. Trans.* 42 (2001) 1074–1080.
- [30] M. Kubota, B.P. Wynne, *Scr. Mater.* 57 (2007) 719–722.
- [31] M. Kubota, M. Sugamata, *Rev. Adv. Mater. Sci.* 18 (2008) 269–275.
- [32] C. Zhi, Y. Bando, C. Tang, S. Honda, K. Sato, H. Kuwahara, D. Golberg, *J. Phys. Chem. B* 110 (2006) 1525–1528.
- [33] L. Guo, R.N. Singh, *Nanotechnology* 19 (2008) 065601.
- [34] S.K. Singhal, A.K. Srivastava, R.P. Pant, S.K. Halder, B.P. Singh, A.K. Gupta, *J. Mater. Sci.* 43 (2008) 5243–5250.
- [35] S.H. Lim, J. Luo, W. Ji, J. Lin, *Catal. Today* 120 (2007) 346–350.

Ultrahigh-pressure consolidation and deformation of tantalum carbide at ambient and high temperatures

Debrupa Lahiri^a, Virendra Singh^b, Giovani Ritta Rodrigues^c, Tania Maria Haas Costa^c,
Marcia R. Gallas^c, Srinivasa Rao Bakshi^{a,d}, Sudipta Seal^b, Arvind Agarwal^{a,*}

^a Plasma Forming Laboratory, Department of Mechanical and Materials Engineering, Florida International University, Miami, FL 33174, USA

^b AMPAC and Nanoscience Technology Center, University of Central Florida, Orlando, FL 32816, USA

^c Instituto de Física and Instituto de Química, Universidade Federal do Rio Grande do Sul, Porto Alegre RS, Brazil

^d Department of Metallurgical and Materials Engineering, Indian Institute of Technology, Madras, Chennai 600 036, India

Received 4 December 2012; received in revised form 13 March 2013; accepted 14 March 2013

Available online 26 April 2013

Abstract

The deformation mechanism of the ultrahigh-temperature ceramic, tantalum carbide (TaC), consolidated at room temperature at a very high hydrostatic pressure of 7.7 GPa is investigated using high-resolution transmission electron microscopy. The deformation behavior of TaC at room temperature is also compared with that consolidated at high temperature (1830 °C) at a similar pressure. TaC could be consolidated to a bulk structure (90% theoretical density) at room temperature. The deformation mechanisms operating at room temperature and 1830 °C are found to be significantly different. The room-temperature deformation is dominated by the short-range movement of dislocations in multiple orientations, along with nanotwinning, grain rotation, crystallite misorientation with low-angle grain boundary formation and lattice structure destruction at interfaces. In contrast, at high temperature, the strain is accommodated mostly by a single slip system, forming a parallel array of dislocations. The consolidation at room temperature occurs by heavy deformation with the support from short range diffusion, whereas the consolidation at high temperature is mostly diffusion dominated, indicating a classic sintering mechanism. The improved degree of consolidation with fewer defects results in significantly improved elastic modulus and hardness in the case of high-temperature consolidate.

© 2013 Acta Materialia Inc. Published by Elsevier Ltd. All rights reserved.

Keywords: Tantalum carbide; Ultrahigh pressure; Room-temperature consolidation; Deformation mechanism

1. Introduction

Tantalum carbide is an important transition metal monocarbide with an extremely high melting point of 3880 °C [1]. TaC has shown great promise as the next-generation aerospace material for throat and nozzle inserts due to its excellent refractory nature that can withstand the combustion flame temperature for most propellants [2]. However, the high melting point of TaC has made its consolidation into useful engineering shapes a major challenge. Achieving a fair degree of consolidation requires high-

temperature exposure, as sintering occurs typically at temperatures $>0.6T_m$. The temperature required for consolidation is usually >2200 °C in pressureless conditions, whereas in pressure-assisted sintering (spark plasma sintering or hot isostatic pressing) it is >1200 °C [3–7]. Consolidation of TaC has been performed using different techniques, e.g. pressureless sintering, hot pressing, hot isostatic processing, high frequency induction heating, vacuum plasma spraying, spark plasma sintering and dynamic consolidation [8–21]. Additives like boron carbide, hafnium carbide, niobium carbide etc., have effectively reduced the sintering temperature to as low as 1400 °C, but at the expense of structural fineness and loss of mechanical performance [5,7]. Thus, there is a need for a suitable consolidation

* Corresponding author. Tel.: +1 305 348 1701.
E-mail address: agarwala@fiu.edu (A. Agarwal).

technique for TaC which can effectively decrease the consolidation temperature and retain the fine grain structure simultaneously.

The application of high pressure aids in consolidation through the powder metallurgy technique. Gallas and co-workers' method of consolidating nanosized ceramic particles through the application of high pressure has shown great promise [22–24]. The application of high pressure (several GPa) can effectively consolidate ceramics such as alumina, silica and ferroelectrics, even at room temperature with a density >90%. In addition, these consolidates retained their nanosize grain structure and were free from secondary phase(s) from sintering additives. These studies inspired the present authors to explore the potential of a high-pressure compression technique in consolidating ultrahigh-temperature ceramics (UHTC), like TaC.

High-pressure consolidation of TaC at room temperature is expected to be deformation-dominated, considering the negligible chance of atomic diffusion. Thus, the high-pressure consolidation of TaC can possibly give new insight into the deformation mechanism leading to the manufacturing of an engineering component. The deformation behavior of TaC becomes different from other ceramics, due to the presence of a majority of Ta–Ta metallic bonds, unlike other ceramics, which have a majority of ionic and covalent bonds. The presence of a good amount of metallic bonds in TaC activates favorable slip planes and produces plastic deformation in a significant amount as compared to similar high-temperature ceramics, even at low temperatures [1,25–27]. However, these studies on room-temperature deformation of TaC are carried out using indentation based deformation and are limited to a very small volume [1,25–27]. The application of high hydrostatic compression over the entire volume of the body is expected to activate all possible deformation mechanisms to accommodate the severe plastic strain generated. Thus, it is possible to observe several possible low temperature deformation mechanisms in TaC over the large volume of high-pressure consolidate as compared to confined small volume beneath the indent.

In the context of the above discussion, the present study investigates an ultrahigh-pressure compression technique as a tool for room-temperature consolidation of TaC. The deformation mechanisms operating at room temperature and high hydrostatic pressure are analyzed with the help of high-resolution transmission electron microscopy (HR-TEM). Efforts are made to understand the consolidation mechanism of TaC at room temperature in terms of the structural changes taking place as a result of active deformation phenomena. A similar study was performed to consolidate TaC at high temperature (1830 °C) and ultrahigh pressure to understand and compare the deformation mechanisms operating at room and high temperature. The mechanical properties (elastic modulus and hardness) of TaC consolidated at RT and 1830 °C are also reported.

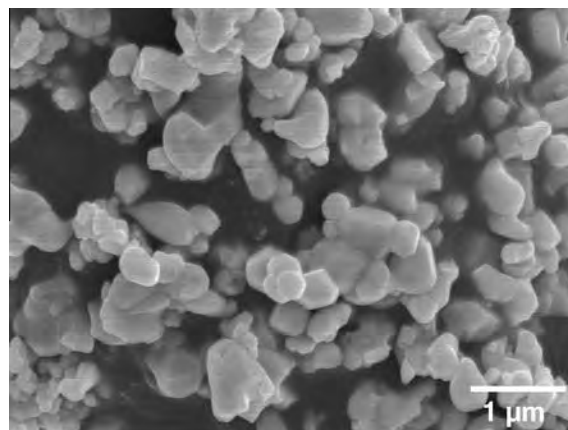


Fig. 1. SEM micrograph of the as-received TaC powder. The average particle size is $0.36 \pm 0.13 \mu\text{m}$.

2. Materials and methods

Fine tantalum carbide powder, with an average particle size of $0.36 \pm 0.13 \mu\text{m}$, was obtained from Inframat advanced Materials LLC (CT, USA). The TaC powder has a purity of 99.7% with the total carbon content $\geq 6.2 \text{ wt.}\%$, free carbon $\leq 0.15 \text{ wt.}\%$, Nb $< 0.3 \text{ wt.}\%$ and O in the range of 0.13–0.3 wt.%. Fig. 1 shows an SEM micrograph of as-received fine TaC powders. The high-pressure (HP) consolidation of TaC was performed at 7.7 GPa at room temperature (RT) and high temperature (HT; 1830 °C). The experiments were carried out using a toroidal-type chamber (a detailed description of this high-pressure method is given elsewhere [28,29]) assembled in a 1000 t hydraulic press. The precursor powder was initially pre-compacted in a piston cylinder type up to 0.2 GPa. For the HP-RT experiments, the pre-compacted samples were placed into a lead container, which acts as a quasi-hydrostatic pressure-transmitting medium. The external diameter of the lead pressure cell is 12.0 mm, with an internal diameter of 8.0 mm and height of 12.0 mm [22]. This container was then put into a ceramic gasket that works as a sealing between the two parts of the toroidal-type chamber, to achieve the desired pressure. For the HP-HT experiments, the pressure cell consisted of a graphite heater (height of 12.0 mm, external diameter of 12.0 mm, internal diameter of 8.0 mm and wall thickness of 2.0 mm), two small discs of fired pyrophyllite and two h-BN discs (diameter of 8.0 mm). A capsule of h-BN (6.0 mm internal diameter) is placed between these discs, with the sample inside. A schematic of this container is shown in Fig. 2a. In this experimental set-up, h-BN acts as a nearly hydrostatic pressure-transmitting medium. The temperature was measured with a chromel–alumel type K thermocouple encapsulated in an Al_2O_3 sleeve. In both experiments (RT and HT), the pressure calibration was performed by the “fixed points” technique [28]. The pressure is accurate to $\pm 0.5 \text{ GPa}$. A small piece of Bi was put on top of the sample in order to check the applied

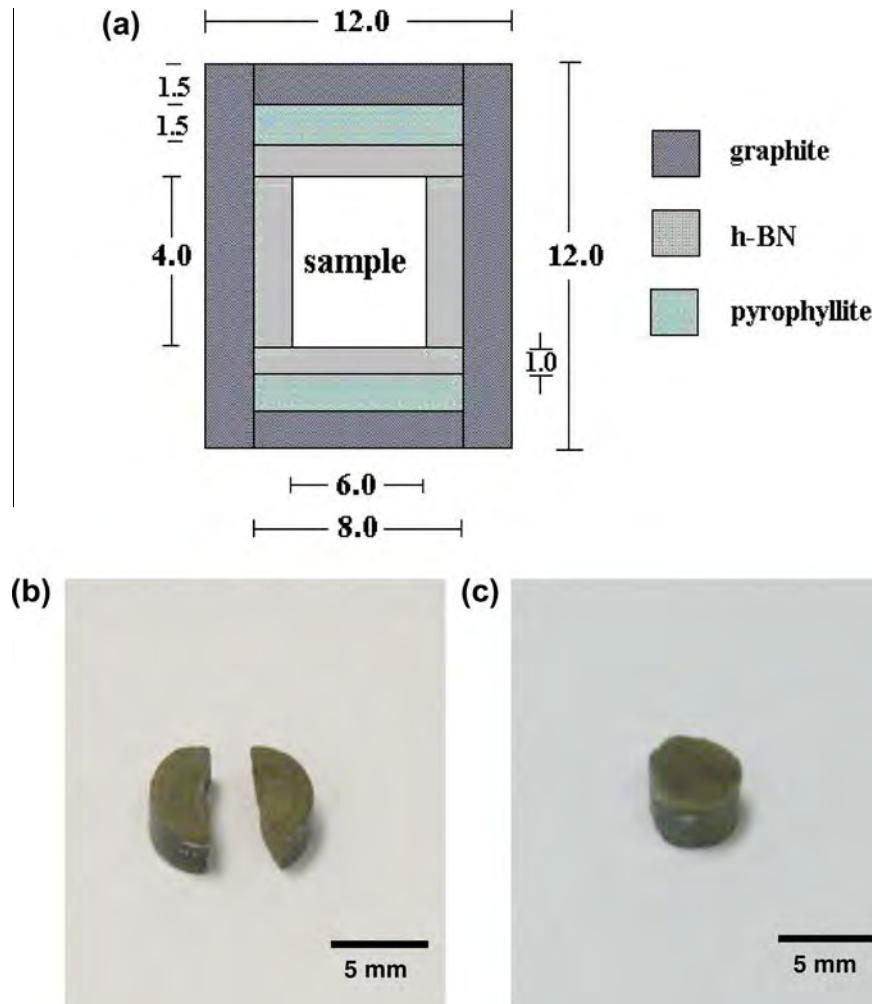


Fig. 2. (a) Schematic of the high-pressure consolidation system. Digital images of (b) TaC-RT and (c) TaC-HT pellets. The pellets were 1.5–1.9 mm in thickness and 4.5 mm in diameter.

pressure. After pressure stabilization, the sample was maintained at this pressure for 5 min. In the HP-HT experiment, after pressure stabilization, the sample (without Bi gauge) was heated to 1830 °C for 10 min. Quenching was performed by turning off the power and, after 20–25 min, pressure was released. Both the samples used in this study were subjected to a similar hydrostatic pressure of 7.7 GPa, but at ambient and 1830 °C, which will be referred as TaC-RT and TaC-HT, respectively.

The density of the pellets was measured using helium gas pycnometry (Accupyc 1340, Micromeritics Instrument Corporation, Norcross, GA, USA) and expressed in terms of relative density considering the true density of TaC as 14.67 g cm^{-3} . The microstructural characterization was carried out using a JEOL JSM-6330F field emission scanning electron microscope operating at 15 kV. A Philips/FEI Tecnai F30 high-resolution transmission electron microscope, operating at an accelerating voltage of 300 kV, was used to analyze the lattice structure of the consolidated TaC. Forward and inverse Fourier transform analysis, using Gatan, Inc. Digital Micrograph software,

was used for the accurate calculation of the lattice spacing. ImageJ [30] software was used for quantitative analysis from micrographs. Nanoindentation studies on both the compacts were carried out using a Hysitron Triboindenter TI-900 in quasistatic mode with a 100 nm radius diamond Berkovich probe. A peak load of 4500 μN was used for indenting, with a constant loading/unloading rate of $450 \mu\text{N s}^{-1}$ and a dwell of 3 s at peak load. Load vs. displacement plots were obtained for more than 50 indentation tests on each sample over three randomly chosen areas. The indents in each area were placed 9 μm apart to cover a representative sample area for reporting the properties of consolidates. The Oliver–Pharr method [31] was used to calculate the reduced elastic modulus (E_r) from the unloading part of the load–displacement plot. The elastic modulus (E_s) was calculated from the measured reduced modulus by introducing the correction factor for tip deformation using the following relationship:

$$\frac{1}{E_r} = \frac{(1 - \nu_s^2)}{E_s} + \frac{(1 - \nu_i^2)}{E_i} \quad (1)$$

Table 1
Effect of processing conditions on density, grain size, elastic modulus and nano-hardness of TaC consolidates.

Sample ID	Processing conditions	Relative density (%)	Grain size (μm)	Elastic modulus (GPa)	Nano-hardness (GPa)
TaC-RT	Ambient Temp., 7.7 GPa	89.8	0.42 ± 0.06	204 ± 22	8.8 ± 1.8
TaC-HT	1830 °C, 7.7 GPa	94.3	0.50 ± 0.10	524 ± 30	21.7 ± 1.5

E and ν are the elastic modulus and Poisson's ratio, respectively. The subscripts i and s denote properties of indenter and sample, respectively. The Poisson's ratio for TaC is 0.24 [32] and the elastic modulus and Poisson's ratio for the diamond probe are 1140 GPa and 0.07, respectively [33].

3. Results and discussion

Fig. 2b and c presents a digital image of TaC-RT and TaC-HT pellets, respectively. It is interesting to observe that ultrahigh-temperature ceramic, like TaC, can be consolidated even at room temperature to a large, free-standing body, as observed in Fig. 2b. However, the pellet had broken into two parts during handling after the consolidation at room temperature. Table 1 summarizes the relative density, grain size and mechanical properties of TaC consolidated at room and high temperatures. The relative density of TaC-RT is $\sim 90\%$ without any sintering additive or second phase. The average grain size of TaC-RT is $0.42 \mu\text{m}$, which is slightly higher than starting particle size of $0.36 \pm 0.13 \mu\text{m}$. Thus, the room-temperature high-pressure consolidation of TaC is found to be successful in suppressing the grain growth. TaC-HT shows a higher relative density of $\sim 94\%$ with an average grain size of 0.50 ± 0.10 . A 39% increase in grain size over the starting powder is obtained for TaC consolidated at high temperature.

The SEM micrographs of TaC-RT and TaC-HT (Fig. 3) reveal the difference in the consolidated structures. Fig. 3a shows a lower degree of consolidation with aggregate of TaC particles and the presence of porosity. TaC-RT does not show any sign of extended diffusion and neck formation as observed in SEM micrograph of TaC-HT (Fig. 3b). TaC-HT also shows a lower porosity, indicating higher degree of consolidation. The difference in degree of consolidation observed from microstructure is consistent with the density measurement by helium pycnometer.

Table 1 also presents elastic modulus (E) and hardness (H) values obtained from the nanoindentation experiments. The elastic modulus value shows a 150% improvement in TaC-HT (524 GPa) over TaC-RT (204 GPa). The nano-hardnesses of TaC-HT and TaC-RT are found to be 21.7 and 8.8 GPa, respectively, showing similar improvement again. The major contribution in improvement in E and H in TaC-HT comes from the degree of consolidation.

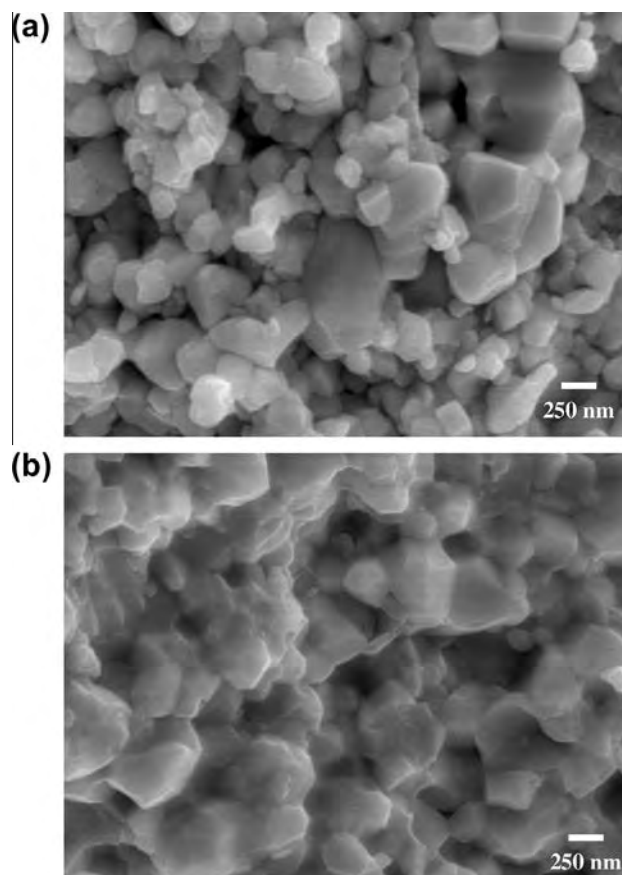


Fig. 3. SEM micrographs of (a) TaC-RT and (b) TaC-HT revealing the difference in degree of consolidation.

However, only a 5% increase in degree of consolidation may not be solely responsible for such an impressive improvement in modulus and hardness of TaC-HT. It is envisaged that crystalline structure of TaC-HT with significantly less density of defects may be responsible for its impressive improvement in the mechanical properties. High-resolution transmission electron microscopic (HR-TEM) observations are made on TaC-RT and TaC-HT to understand the substructure (defects, nanocracks) and correlate with the operating deformation and consolidation mechanisms.

3.1. Deformation and consolidation mechanisms in TaC-RT

Ideally, ceramics with a majority of covalent and ionic bonds do not show any room-temperature slip or plastic deformation. However, ultrahigh-temperature carbides of group IV and V elements show some metallic behavior, due to the metallic bond between atoms, which is also reflected in their electrical conductivity [26–27,34]. In fact, transition metal carbides have a majority of metallic bonds due to their atomic arrangement in cubic-rocksalt type crystal structure [27]. The existence of metallic bonds in the slip systems makes plastic deformation easy. Researchers have concluded $\{111\}\langle 110 \rangle$ to be the preferred slip

system for TaC at low temperature deformation produced by indentation [1,25,27,35]. These studies have proven the significant dislocation activity in TaC at low and ambient temperature. The TEM image in Fig. 4a reveals a high density of dislocations in multiple orientations in TaC consolidated at room temperature. Such arrangement of dislocations in different orientations in a small region suggests slip on multiple planes [34].

High dislocation density results from the accommodation of high strain created by an extremely high hydrostatic pressure of 7.7 GPa over the entire volume. Other sources of dislocation in the structure could be the nanocracks and nanovoids created during high-temperature application. Fig. 4b presents a nanocrack emanating from the surface of the compact at an angle of 40° to the (111) plane. The ICDD PDF No. 03-065-0282 is used for information on the lattice spacing of TaC. Cracks are reported to nucleate in TaC due to dislocation pile-ups and interactions at

intersecting slip bands, under compressive stress at room temperature [25,36]. Crack tips, again, act as a good source of further dislocation activities and nanoscale deformation. Grain boundary rotation, sliding and nanotwin formation can also take place at the crack tip to relax the stress [36]. Local stress concentration near a propagating crack can initiate intergrain sliding and immobile dislocations [36]. Thus, the presence of nanocracks in TaC-RT is a rich source of high dislocation density. However, the structure does not get totally disintegrated due to crack suppression under hydrostatic stress condition [26]. The hydrostatic compressive force does now allow the crack to open up and propagate by suppressing the necessary tensile stresses normal to the plane of the cracks nucleation.

Apart from high dislocation density, amorphous regions and disturbed lattice structure is another significant feature of TaC-RT compacts. Fig. 5a presents severely disturbed lattice layers on the edge. The interior structure also contains multiple amorphous regions surrounding nanocrystallites as marked by arrows (Fig. 5a). Disturbance in the lattice structure is created by the application of high

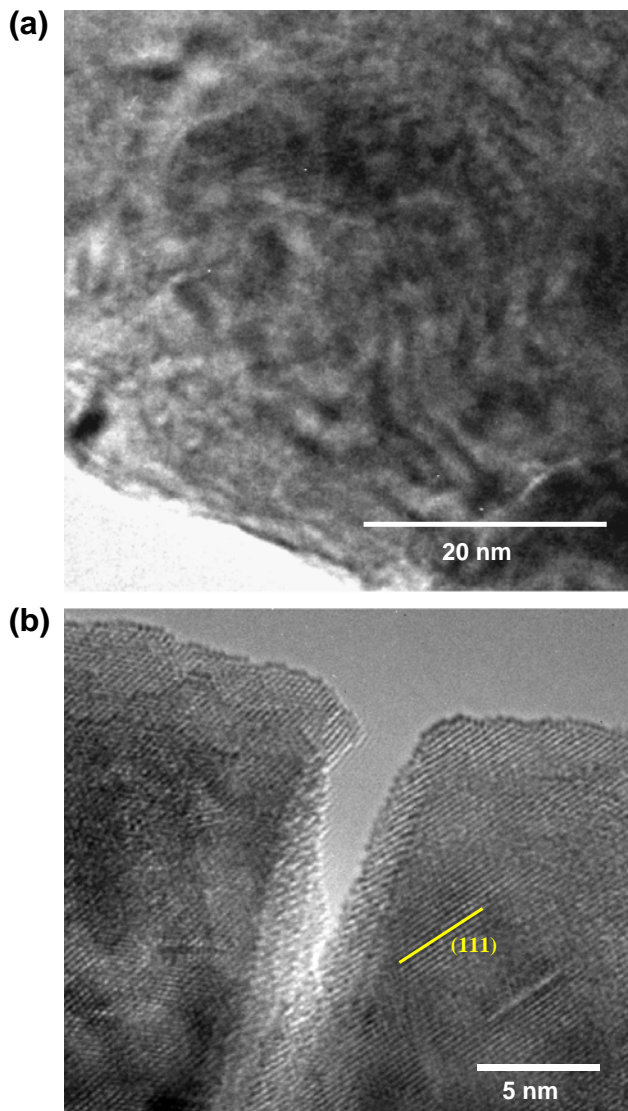


Fig. 4. HRTEM images of TaC-RT showing (a) the high density of dislocations in multiple orientations and (b) a propagating nanocrack.

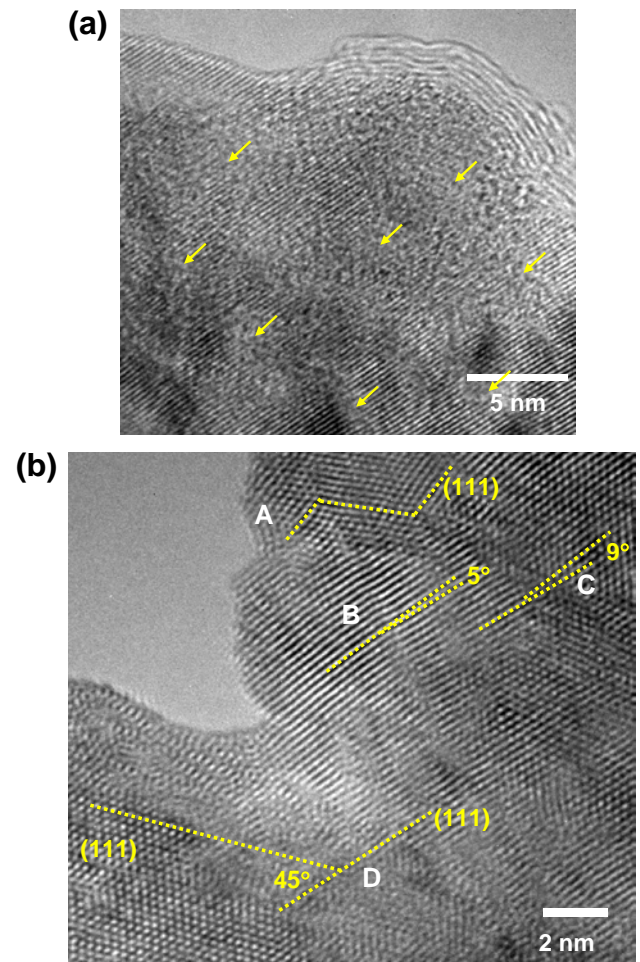


Fig. 5. HRTEM images of TaC-RT revealing (a) the disturbed surface layer and the amorphous region surrounding nanocrystallites and (b) nanotwins, low-angle grain boundaries and high-angle grain boundaries with amorphous layer.

pressure that causes maxima of localized stress at the surface of compressed particles leading to fracture [37].

Other modes of deformation and the results of high dislocation activity in TaC-RT are also observed in high-resolution lattice images. Region A in Fig. 5b evidences the presence of a nanotwin in the TaC-RT structure. The twinning occurs on the (111) set of planes and the twin angle is 65° , whereas the twin band is ~ 3 nm wide. Such nanotwins have been observed by other researchers as a result of deformation in nanocrystalline metallic materials [38–40]. However, Li et al. have noted a similar feature in metal–ceramic composite multiscale structures, which they consider as not a typical twin structure; rather, it is due to the presence of stacking faults or dislocation cores [37]. Other than twinning, the high-density dislocations can also align and form low-angle grain boundaries to divide the structure into nanocrystalline regions. Regions B and C in Fig. 5b present two such grain boundaries with the angle of mismatch in (111) lattice being 5° and 9° , respectively. The same micrograph also shows the presence of a high-angle grain boundary with (111) lattice mismatch of 45° . The high-angle grain boundary consists of a ~ 2 nm wide amorphous/disturbed region.

Fig. 6 presents some wedge-like features in the lattice image of TaC-RT, which are produced due to grain boundary twisting [37]. It is possible to find out the intergrain twisting angles from the Moiré fringes that are created due to the angular mismatch of lattice orientation. The twist angle θ is related to the spacing of Moiré fringes D and lattice spacing of the twist plane d with the following relationship:

$$D = \frac{d}{2 \sin \frac{\theta}{2}} \quad (2)$$

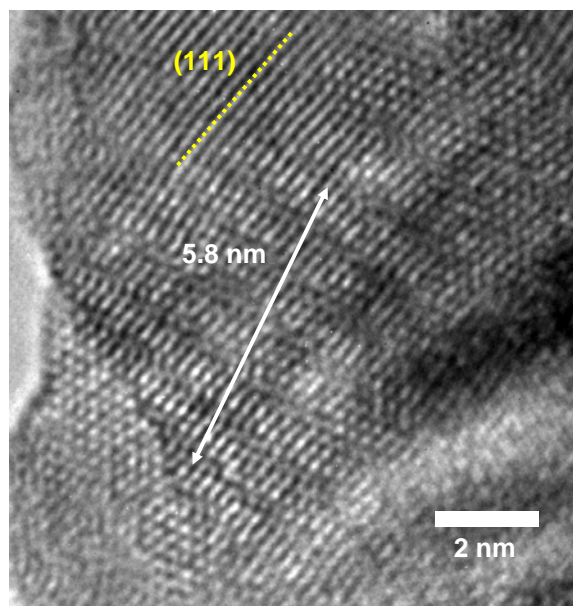


Fig. 6. Moiré fringes observed in lattice images of TaC-RT indicating twisted grain boundary due to grain rotation.

where $D = 5.8/6 \text{ nm} = 0.97 \text{ nm}$; $d_{(111)} = 0.256 \text{ nm}$, thus the twist angle calculated is 15° . This twisting in grain boundary is possible due to rotation of grains with respect to each other. The application of compressive stress, even at room temperature, leads to material flow by grain reorientation and relative sliding along intergranular grain boundaries in ceramics [41]. Nanograin rotation can take place in extreme conditions, i.e. high value of applied stress and plastic strain rate, which generates a high density of dislocation. The shear strain generated inside a small grain forms a dipole, which causes the grain to rotate in order to accommodate the plastic deformation through crystal lattice rotation [42,43]. Thus, the grain rotation in TaC-RT seems to succeed in forming nanocrystallites due to segregation of dislocations at low-angle grain boundaries. Grain boundary sliding and rotation can orient the grains in positions favorable for slip [44].

Hence, the room-temperature consolidation of an ultra-high melting ceramic like TaC under an extremely high pressure of 7.7 GPa can be explained in terms of multiple mechanisms postulated based on the deformation behavior observed in HRTEM micrographs (Figs. 4–6).

- (i) The presence of numerous entangled dislocation networks (Fig. 4a) in TaC-RT indicates plastic deformation in the structure. During plastic deformation, crystallographic planes slip against each other and new surfaces are created on powder particles with numerous broken bonds. The adjacent particles going through plastic deformation together would take advantage of dangling broken bonds at the surface and due to pressure such surfaces come very close to forming new bonds. Especially, the structure of TaC comprises many Ta–Ta metallic bonds, which are easier to form. Such bonding would help in the consolidation of TaC-RT.
- (ii) Consolidation can also be caused by short range diffusion at interparticle surfaces. The amorphous/glassy structure created at particle surfaces due to high-pressure application (Fig. 5a) causes easier diffusion through already disturbed lattices with high internal energy. Disturbed amorphous or glassy structures at the particle–particle interface or grain boundary of ceramic structure may allow rapid diffusion through the glassy layer [45]. This is more evident from the presence of an amorphous layer at the high-angle grain boundaries only (Fig. 5a), which is possibly created by coalescence of particles. On the other hand, the low-angle grain boundaries are created within one particle due to high deformation and thus do not have a thick amorphous layer at the boundary (Fig. 5a). In addition, diffusion can also be caused by a temperature rise at the interface due to friction generated heat on colliding surfaces at high pressure. A simple calculation is carried out on temperature rise at the interface based on conversion of pressure to heat energy, which is absorbed at a very

thin layer (1 nm) at particle interface. The calculations reveal a 350 K temperature rise at the interparticle surface at 7.7 GPa pressure, the specific heat for TaC at room temperature being $45.75 \text{ cal g}^{-1} \text{ K}^{-1}$ [46]. A temperature of $\sim 375^\circ \text{C}$ may not be sufficient for significant diffusion in high-temperature ceramics like TaC. But simultaneous application of very high pressure can introduce some amount of short range diffusion in TaC, even with a small increase in the temperature.

- (iii) The third possible mechanism of consolidation in TaC-RT is the mechanical interlock at particle surfaces. High pressure assisted collision at particle surfaces can very well create partial breakage and increased roughness at the particle surfaces. These rough surfaces with hills and ditches can provide some degree of mechanical interlocking when they fall in exact fitting. The importance of topological interlock in the strength of ceramic structures is also reported by Krause et al. in free gelation processed compacts [47]. The debris generated by breakage at particle surfaces can also fill the interparticle voids, thus increasing the contact area and improving the degree of consolidation in the TaC-RT composite.

A surprising $\sim 90\%$ TD density of TaC processed at RT is a result of these consolidation mechanisms acting simultaneously.

3.2. Deformation and consolidation mechanisms in TaC-HT

As compared to TaC-RT, the deformation and consolidation mechanisms observed in TaC-HT are significantly different. Fig. 7a presents the traces of dislocations, which are all aligned in a similar direction as compared to random orientation of the same in TaC-RT. TaC-HT is consolidated at 1830°C . It is easy for TaC to deform in its most favorable $\{111\}\langle 110 \rangle$ slip system. A significant plastic strain in TaC above 720°C has been reported [25]. Thus $\{111\}\langle 110 \rangle$ dominated slip in TaC-HT results in parallel orientation of dislocations.

A qualitative comparison reveals much lower dislocation density in TaC-HT (Fig. 7a) as compared to TaC-RT (Fig. 4a). This observation can be justified in terms of stress relaxation that may take place in TaC-HT. Annealing at $T_m/2$ for 1 h (1940°C) can cause strongly recovered and partially recrystallized structure in TaC [1]. In the present study the temperature is slightly lower (1830°C) than $T_m/2$ and time is much shorter. But the presence of extremely high hydrostatic stress (7.7 GPa) can significantly reduce the requirement for recovery and recrystallization in terms of temperature and time by accelerating the diffusion. A clear evidence of recovery and recrystallization is recorded in lattice images of TaC-HT, viz. decreased dislocation density (Fig. 7a) and perfect lattice structure with no sign of amorphous region at the edges (Fig. 7b). The absence of any amorphous region on

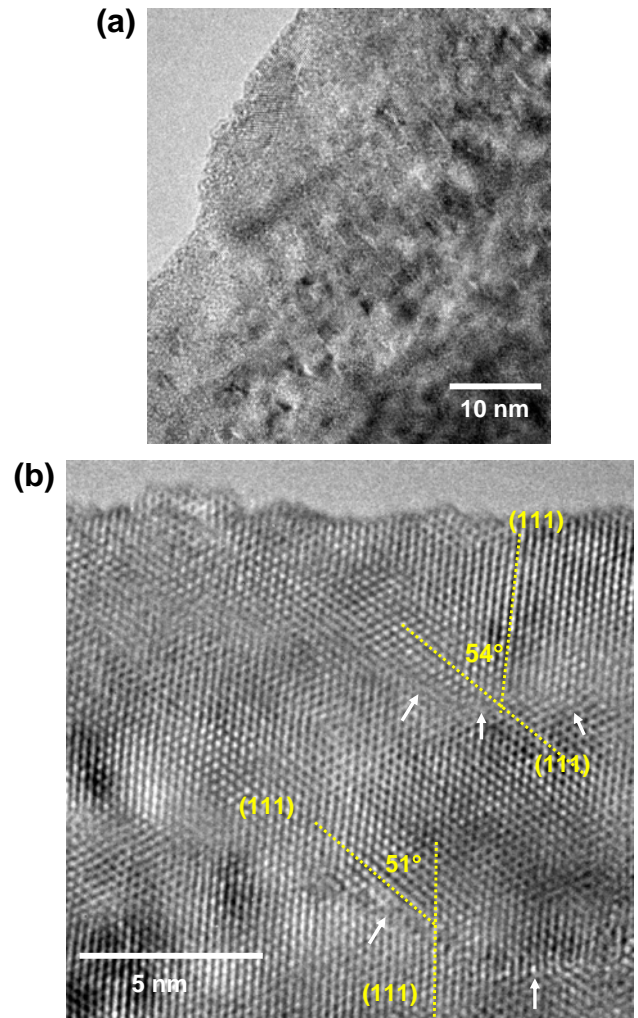


Fig. 7. HRTEM micrograph of TaC-HT consolidate displaying (a) dislocation lines in one direction; (b) lattice fringes with high-angle grain boundaries and the absence of amorphous region.

the surface and interior of the TaC-HT structure (Fig. 7b) is possible due to accelerated diffusion in TaC-HT, which causes perfect crystal lattice formation. In addition, the high-angle grain boundaries in TaC-HT also contain a thin disturbed lattice layer (marked by arrows in Fig. 7b) as compared to the thick amorphous region in TaC-RT (Fig. 5b). This is possible due to the coalescence of particles in TaC-HT in classical sintering mechanism due to the high rate of diffusion at the interface. No traces of nanocracks or nanovoids are observed in TaC-HT. Nanocrack generation is suppressed at high temperature due to accelerated diffusion along the grain boundary [36]. Thus it is concluded that the formation of nanocracks is partially suppressed in TaC-HT, which also suppresses the nucleation of dislocation and nanotwin formation. However, in addition to low density parallel dislocations, high stress in TaC-HT structure introduces another kind of deformation mechanism, which is grain boundary twisting. Fig. 8a presents the sign of Moiré fringes in the TaC-HT structure. And calculations according to the procedure

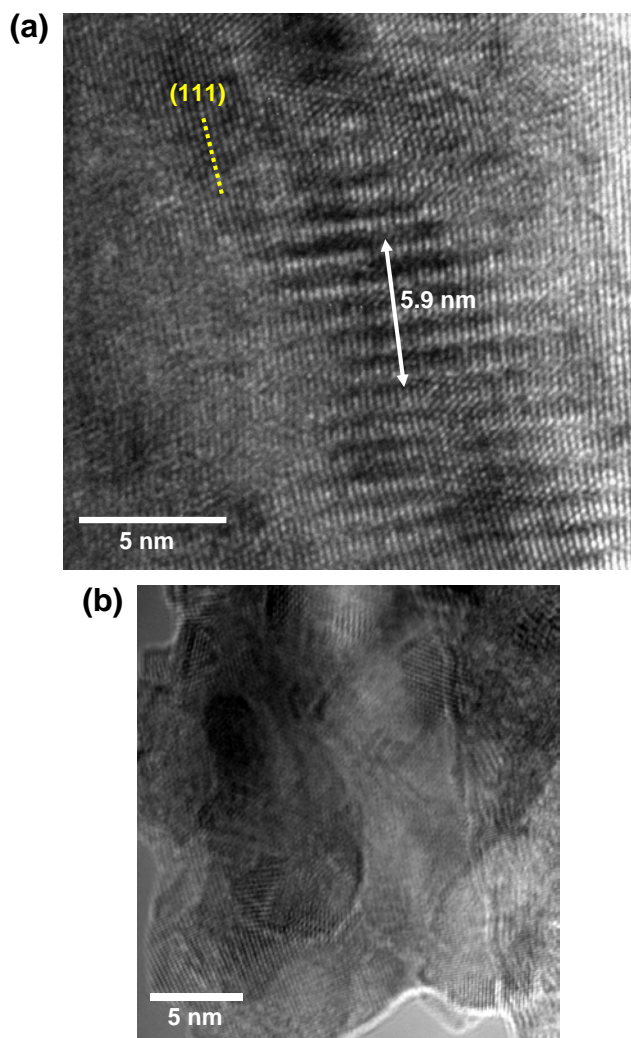


Fig. 8. HRTEM micrographs of TaC-HT consolidate revealing signs of (a) grain boundary twisting and (b) grain rounding due to diffusion driven sintering.

described earlier, following Eq. (2) ($D = 5.9/5 \text{ nm} = 1.18 \text{ nm}$; $d_{(111)} = 0.256 \text{ nm}$ in this case) reveals a grain boundary twisting of $\sim 3^\circ$ in case of TaC-HT, which is five times lower than that in TaC-RT. This observation is justified due to a much lower density of dislocation in TaC-HT, which can cause grain rotation. However, due to the parallel nature of dislocations in TaC-HT, it is generally unexpected to form a dipole inside a grain that can cause grain rotation. Some localized defects might be the cause of stress concentration and grain rotation in TaC-HT. The increased grain size is another inhibitor of grain rotation in TaC-HT. The grain rotation rate is found to have an inverse relationship with grain size [48]. However, this phenomenon needs further observation.

The evidence from SEM micrographs clearly indicates that classical sintering mechanism has taken place in TaC-HT with accelerated diffusion at particle surfaces, neck formation and closure of porosity. The TEM micrograph of TaC-HT (Fig. 8b) also shows grain rounding,

which is an indication of sintering at high temperature. The grain size of TaC-HT is also 24% higher than that of TaC-RT (Table 1), which indicates sintering and grain growth in the former.

4. Conclusions

This study substantiates the application of high pressure (7.7 GPa) as an efficient technique for consolidating ultra-high-temperature ceramics like TaC, even at room temperature. The deformation of TaC under high pressure follows different mechanisms at room temperature and high temperature of 1830 °C. At room temperature, multiple orientation of the dense dislocation network indicates activation of several slip systems apart from the most favorable $\{111\}\langle 110 \rangle$ for TaC. In addition, nanotwin formation, grain boundary twisting and disturbance of lattice layers at interfaces are other signs of deformation at room temperature. The consolidation in TaC at room temperature is governed by high-pressure-generated physical and chemical bonding at the interface and limited diffusion through disturbed/amorphous interface lattice structure. In contrast, the consolidation at high temperature is achieved through diffusion across particle interfaces, leading to neck formation inside the particles. The deformation at high temperature is dominated by a favorable slip system, generating parallel dislocations. The structure remains crystalline except high-angle narrow grain boundaries. TaC consolidate at high temperature shows $\sim 150\%$ higher elastic modulus and hardness than the room-temperature one, which is attributed to the high degree of densification and absence of nanocracks, and other defects in the TaC-HT structure.

Acknowledgements

A.A. acknowledges support from the US Air Force Office of Scientific Research (FA9550-12-1-0263) through the High Temperature Materials Program managed by Dr Ali Sayir. The support from AMERI at FIU in providing the research facilities is also greatly acknowledged.

References

- [1] Kim C, Gottstein G, Grummon DS. *Acta Metall Mater* 1994;42:2291.
- [2] Upadhyaya K, Yang JM, Hoffman WP. *Am Ceram Soc Bull* 1997;58:51.
- [3] Samonov GV, Petrikina RY. *Phys Sintering* 1970;2:1.
- [4] Liu JX, Kan YM, Zhang GJ. *J Am Ceram Soc* 2010;93:370.
- [5] Khalegi E, Lin YS, Meyers MA, Olevsky EA. *Scripta Mater* 2010;63:577.
- [6] Yohe WC, Ruoff AL. *J Am Ceram Soc Bull* 1978;57:647.
- [7] Zhang XH, Hilmas GE, Fahrenholtz WG, Deason DM. *J Am Ceram Soc* 2007;90:393.
- [8] Bakshi SR, Musaramthota V, Virzi DA, Keshri AK, Lahiri D, Singh V, et al. *Mater Sci Eng A* 2011;528:2538.
- [9] Talmy IG, Zaykoski JA, Opeka MM. *J Eu Ceram Soc* 2010;30:2253.
- [10] Hackett K, Verhoef S, Cutler RA, Shetty DK. *J Am Ceram Soc* 2009;92:2404.

- [11] Zhang X, Hilmas GE, Fahrenholtz WG. *J Am Ceram Soc* 2008;91:4129.
- [12] Zhang XH, Hilmas GE, Fahrenholtz WG. *Mater Sci Eng A* 2009;501:37.
- [13] Desmaison Brut M, Alexandre N, Desmaison J. *J Eu Ceram Soc* 1997;17:1325.
- [14] Kim BR, Woo KD, Doh JM, Yoon JK, Shon IJ. *Ceram Int* 2009;35:3395.
- [15] Sciti D, Silvestroni L, Guicciardi S, Fabbri D, Bellosi A. *J Mater Res* 2009;24:2056.
- [16] Balani K, Gonzalez G, Agarwal A, Hickman R, O'Dell JS, Seal S. *J Am Ceram Soc* 2006;89:1419.
- [17] Limeng L, Feng Y, Yu Z, Zhiguo Z. *J Am Ceram Soc* 2010;93:2945.
- [18] Bakshi SR, Musaramthota V, Lahiri D, Singh V, Seal S, Agarwal A. *Mater Sci Eng A* 2011;528:1287.
- [19] Lahiri D, Khalegi E, Bakshi SR, Li W, Olevsky EA, Agarwal A. *Scripta Mater*; 2012. <http://dx.doi.org/10.1016/j.scriptamat.2012.10.043>.
- [20] Balani K, Bakshi SR, Mungole T, Agarwal A. *J Appl Phys* 2012;111:063521.
- [21] Xu L, Marchant D, Matson L, Marchol P, Majumdar BS. *SAMPE Conference* Nov 2006, Long Beach CA.
- [22] Gallas MR, Rosa AR, Costa TMH, Jornada JAH. *J Mater Res* 1997;12:764.
- [23] Mesquita A, Bernardi MIB, Mastelaro VR, Lente MH, Eiras JA, Gallas MR, et al. *J Am Ceram Soc* 2009;92:1679.
- [24] de Andrade MJ, Lima MD, Bergmann CP, Ramming GDO, Balzaretto NM, Costa TMH, et al. *Nanotechnology* 2008;19:265607.
- [25] Rowcliffe DJ, Hollox GE. *J Mater Sci* 1971;6:1261.
- [26] Rowcliffe DJ, Hollox GE. *J Mater Sci* 1971;6:1270.
- [27] Rowcliffe DJ, Warren WJ. *J Mater Sci* 1970;5:345.
- [28] Sherman WF, Stadtmuller A. *Experimental techniques in high-pressure research*. London: Wiley; 1987.
- [29] Khvostantsev LG, Slesarev VN, Brazhkin VV. *High Pressure Res* 2004;3:371.
- [30] Abramoff MD, Magelhaes PJ, Ram SJ. *Biophotonics Int* 2004;11:36.
- [31] Oliver WC, Pharr GM. *J Mater Res* 1992;7:1564.
- [32] López-de-la-Torre L, Winkler B, Schreuer J, Knorr K, Avalos-Borja M. *Solid State Commun* 2005;134:245.
- [33] Park K, Mishra S, Lewis G, Losby J, Fan Z, Park JB. *Biomaterials* 2004;25:2427.
- [34] Ghosh D, Subhash G, Bourne GR. *Scripta Mater* 2009;61:1075.
- [35] Hoffman M, Williams WS. *J Am Ceram Soc* 1986;69:612.
- [36] Ovid'ko IA, Sheinerman AG. In: Li JCM, editor. *Mechanical properties of nanocrystalline materials*. Singapore: Pan Stanford Publishing; 2011.
- [37] Li Y, Zhang Z, Vogt R, Schoenung JM, Lavernia EJ. *Acta Mater* 2011;59:7206.
- [38] Dao M, Lu L, Shen YF, Suresh S. *Acta Mater* 2006;54:5421.
- [39] Lu L, Shen Y, Chen X, Qian L, Lu K. *Science* 2004;304:422.
- [40] Shen YF, Lu L, Lu QH, Jin ZH, Lu K. *Scripta Mater* 2005;52:989.
- [41] Dericioglu AF, Liu YF, Kagawa Y. *J Mater Res* 2009;24:3387.
- [42] Ovid'ko IA, Sheinerman AG. *Appl Phys Lett* 2011;98:181909.
- [43] Gutkin MY, Ovid'ko IA. *Appl Phys Lett* 2005;87:251916.
- [44] Dokko PC, Pask JA. *Mater Sci Eng* 1976;25:77.
- [45] Suffner J, Scherer T, Wang D, Fasel C, Jaeorska L, Hahn H. *Acta Mater* 2011;59:7592.
- [46] Turchanin AG, Guseva EA, Fesenko VV. *Powder Metall Metal Ceram* 1971;10:823.
- [47] Krause T, Molotnikov A, Carlesso M, Rente J, Rezwan K, Estrin Y, et al. *Adv Eng Mater* 2012;14:335.
- [48] Chaim R. *Scripta Mater* 2012;66:269.

Photocatalytic activity of spark plasma sintered TiO₂–graphene nanoplatelet composite

Cheng Zhang,^a Ujwal Chaudhary,^b Debrupa Lahiri,^a
Anuradha Godavarty^b and Arvind Agarwal^{a,*}

^aPlasma Forming Laboratory, Advanced Materials Engineering Research Institute (AMERI),
Department of Mechanical and Materials Engineering, 10555 West Flagler Street, EC 3464, Miami, FL 33174, USA

^bDepartment of Biomedical Engineering, Florida International University, 10555 West Flagler Street,
EC 2675, Miami, FL 33174, USA

Received 19 November 2012; accepted 8 January 2013

Available online 17 January 2013

This study reports on the photocatalytic activity of TiO₂–1 vol.% graphene nanoplatelet (GNP) composite synthesized by spark plasma sintering. Graphene platelets form a strong interface with sub-micron TiO₂ grains providing increased pathways for improved electron transport. The photocatalytic activity of TiO₂–GNP was measured by methylene blue solution decomposition under UV light exposure. The addition of 1 vol.% GNP to TiO₂ improved its photocatalytic property by 25% by enhancing the electron mobility and reducing the photoexcited electron–hole recombination rate.

© 2013 Acta Materialia Inc. Published by Elsevier Ltd. All rights reserved.

Keywords: TiO₂; Rutile; Graphene nanoplatelet; Spark plasma sintering; Photocatalytic activity

TiO₂, an oxide semiconductor, is widely used for photocatalytic applications because it is environmental friendly, relatively inexpensive and a chemically stable material [1]. TiO₂ has two common phases: anatase and rutile. However, the large band gap of TiO₂ (anatase: 3.2 eV, rutile: 3.0 eV) limits its application to the ultraviolet region of the solar spectrum [2]. The high electron–hole recombination rate also restricts its application. Graphene as a two-dimensional nanomaterial has outstanding electrical and mechanical properties, high surface area and high chemical stability [3]. Due to these promising properties, TiO₂–graphene composites have recently been investigated for photocatalytic activity [4–7]. It is proposed that addition of graphene can narrow the band gap of TiO₂, lower the electron–hole recombination rate, and enhance electron transport between TiO₂ and the graphene [4].

Lee et al. synthesized graphene-wrapped anatase nanoparticles by graphene oxide reduction and hydrothermal treatment [4]. The photocatalytic activity of the graphene-wrapped anatase was significantly enhanced under visible light, which was attributed to

lowering of the TiO₂ band gap to 2.8 eV. Yang et al. synthesized granum-like stacking structures of TiO₂–graphene nanosheets using a layer-by-layer assembly technique [5]. Such a structure separated the charge and transported electrons more easily, increasing the photoelectric conversion [5]. An electro-spun TiO₂–graphene composite also exhibited improved photocatalytic activity [6]. TiO₂–reduced graphene oxide composite exhibited a 90% improvement in photocurrent, which was attributed to the excellent electron collection and transport capabilities of reduced graphene oxide [7]. Although these studies [4–7] demonstrated improved photocatalytic properties of TiO₂ by graphene addition, the synthesis techniques are relatively time consuming and complex, involving multiple processing steps. Motivated by this scenario, we report the synthesis of TiO₂–graphene nanoplatelet (GNP) composite by spark plasma sintering (SPS). SPS is a rapid consolidation technique that retains nanostructured features in a bulk composite [8,9]. The process utilizes DC current, and heats the powder internally to reduce the sintering time from hours to few minutes. TiO₂–GNP composite is characterized for microstructure, phases and photocatalytic activity by methylene blue solution decomposition experiments. The novelty of this work is twofold: (i) evaluating a rapid synthesis SPS technique

* Corresponding author. Tel.: +1 305 348 1701; fax: +1 305 348 1932; e-mail: agarwala@fiu.edu

for TiO_2 -GNP; and (ii) use of exfoliated GNPs, which are very inexpensive and readily available in comparison to graphene and/or graphene oxide.

Nano TiO_2 powder (20–50 nm, purity 99.9%, anatase) was obtained from Inframat[®] Corporation, Manchester, CT, USA. GNPs (xGNP-M-5) were obtained from XG Sciences, Lansing, MI, USA. The GNPs have an average thickness of 6–8 nm and comprise about 20 sheets of graphene as each pair of graphene layers is ~ 0.35 nm thick [10]. GNP particles have an average diameter of 15 μm , giving the platelets a relative surface area of 120–150 $\text{m}^2 \text{g}^{-1}$ [11]. A physical mixture of TiO_2 and GNP powder was prepared by a wet chemistry method to give TiO_2 -1 vol.% GNP powder (referred to as TiO_2 -GNP hereafter). 5.7 g GNP was added to 100 ml acetone in a glass beaker. The mixture was ultrasonicated for 90 min. Subsequently 7.6 g TiO_2 was added into the same beaker and ultrasonicated for another 30 min. The final mixture was dried in a vacuum oven at 80 $^\circ\text{C}$, and crushed to obtain blended TiO_2 and GNP powder. A scanning electron microscopy (SEM) image of mixed powder after ultrasonication, drying and crushing is shown in Figure 1. Nano- TiO_2 particles are well dispersed and reside over the surface of GNP sheets.

The TiO_2 -GNP powder mixture was placed in a 20 mm graphite die in an SPS Furnace, SPS Nano Ceramics (Chicago, IL, USA). The sintering was performed in vacuum at 800 $^\circ\text{C}$ with a hold time of 5 min at 70 MPa. A heating rate of 100 $^\circ\text{C}$ was used. TiO_2 powder without GNPs was also consolidated under identical conditions and used as a reference sample. X-ray diffraction was carried out using a Bruker D5000 X-ray diffractometer with $\text{Cu } K_\alpha$ X-rays at a scan rate of 2°min^{-1} . A JEOL JSM 6330 F field emission scanning electron microscope was used to observe the powder morphology and microstructure of the sintered pellets.

Methylene blue (MB) solution with a concentration of $5 \times 10^{-5} \text{mol l}^{-1}$ was prepared from MB powder (M9140, Sigma Aldrich, USA) for evaluation of the photocatalytic property. Sintered pellets were sectioned into $1 \times 1 \times 0.1$ cm samples using a low-speed precision diamond saw. These samples were then immersed in MB solution, which were exposed to UV light. The light source is a XX-15s shortwave UV bench lamp (UVP

Llc., Upland, CA) with a wavelength of 254 nm. MB solution (3 ml) was collected from the bath after 0, 30, 120 and 240 min of exposure to the UV light in order to measure the concentration. The absorption peak of the collected MB solution after UV light exposure was determined using a UV–visible spectrophotometer (Cary 100 Bio, Varian, Inc.). The spectrophotometer employs the Beer–Lambert law which describes the linear relationship between the absorbance and the concentration of absorbing species. The output was recorded as a plot of the absorbance vs. wavelength, from which the peak absorption wavelength was determined. The change in the concentration of MB solution is plotted as a function of exposure time to obtain a measure of the photocatalytic activity of TiO_2 and TiO_2 -GNP composite.

Figure 2a shows a high-magnification SEM image of the fracture surface of TiO_2 . Figure 2b and c show low- and high-magnification images of TiO_2 -GNP, respectively. The average grain size of TiO_2 and TiO_2 -GNP is 297 ± 72 and 299 ± 99 nm, respectively. The higher standard deviation in TiO_2 -GNP is attributed to the presence of GNPs in the matrix. Since the GNPs have a higher thermal conductivity than TiO_2 , they act as a lo-

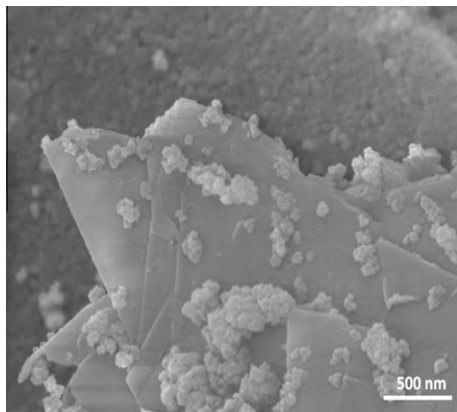


Figure 1. SEM micrograph showing nano- TiO_2 powder particles dispersed over the GNP surface.

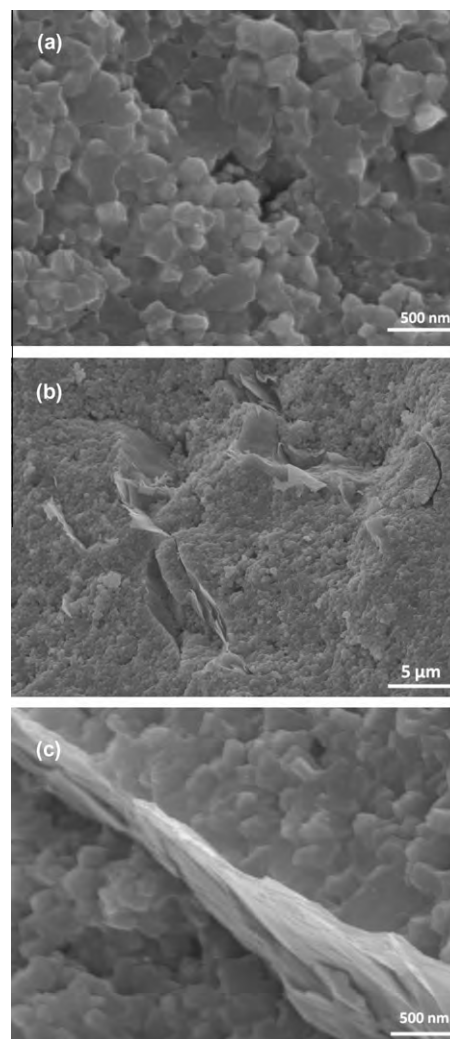


Figure 2. SEM images: (a) high magnification of TiO_2 ; (b) low magnification of TiO_2 -GNP; (c) high magnification of TiO_2 -GNP.

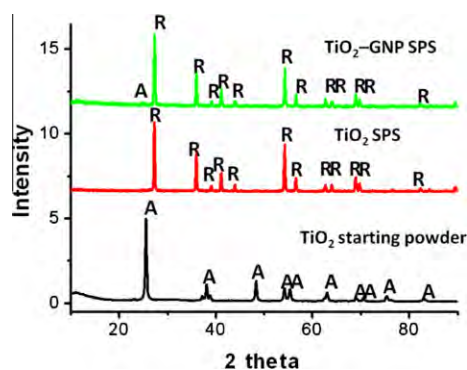


Figure 3. X-ray diffraction pattern of starting TiO_2 powder, sintered TiO_2 and sintered TiO_2 -GNP.

cal heating source, leading to a wider distribution in the grain size. It is also observed that GNPs inside the TiO_2 matrix are largely parallel and sandwiched between TiO_2 grains (Fig. 2b). A high-magnification image (Fig. 2c) shows intimate contact between GNPs and TiO_2 grains, which is expected to provide high current pathways for electron transport [7]. Such a microstructure is also expected to provide higher fracture toughness due to the energy-dissipating mechanisms in GNPs, which include bending, sheet pull out, sliding and grain wrapping [12,13]. In our recent study, Raman spectra of spark plasma sintered pure GNPs (without any matrix material) revealed that GNPs retain their original structure after the harsh processing conditions experienced during SPS [12]. The undamaged GNPs are also observed in SPS TiO_2 -GNP as seen in Figure 2b and c.

X-ray diffraction patterns of starting TiO_2 powder, SPS TiO_2 and SPS TiO_2 -GNP pellets are shown in Figure 3. The starting TiO_2 powder was pure anatase which transforms into rutile after SPS processing. Anatase to rutile transformation is attributed to the rapid heating rates associated with SPS processing. Rutile has been sparingly used for photocatalytic applications due to its high electron-hole recombination rate [14]. However, Sun et al. have demonstrated that calcined rutile powders possess a relatively higher photocatalytic property than anatase powder due to the presence of hydroxyl groups and more active sites for the degradation reaction [15]. In this study, we have demonstrated that addition of GNP improves the photocatalytic activity of rutile.

The absorption spectra of the MB solution collected after UV light exposure of SPS TiO_2 and TiO_2 -GNP pellets is shown in Figure 4a. The spectra for the longest and shortest exposure durations are included. The maximum absorption is observed at the wavelength of 664 nm. The change in the concentration of MB solution is indicated by the C/C_0 ratio, which is plotted as a function of exposure time (Fig. 4b), to obtain a measure of the photocatalytic activity of SPS TiO_2 and TiO_2 -GNP composite. The degradation in concentration of MB solution is comparable for both TiO_2 and TiO_2 -GNP for the first 50 min of exposure. Thereafter, TiO_2 -GNP shows significantly higher photocatalytic activity. After 4 h of UV exposure, TiO_2 -GNP shows a 35% degradation in concentration, whereas TiO_2 shows 10% degradation.

These results clearly indicate that GNPs play a significant role in improving the photocatalytic activity of TiO_2 .

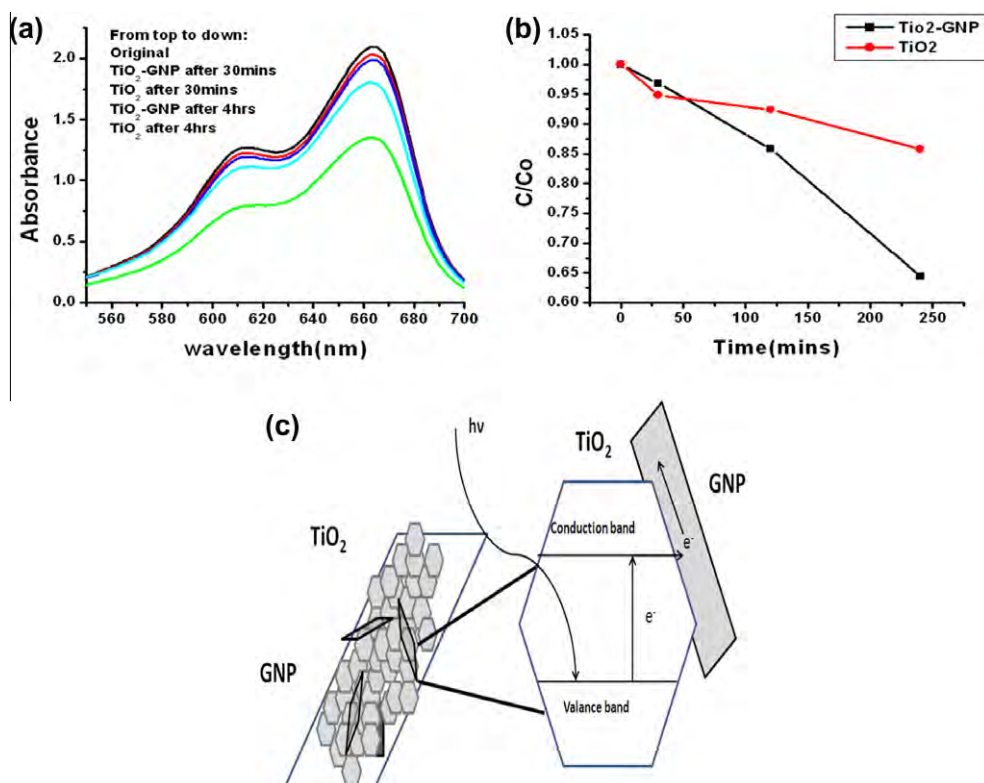


Figure 4. (a) MB solution decomposition absorption curves, (b) normalized MB solution composition as a function of UV exposure time and (c) schematic of TiO_2 -GNP-enhanced photodecomposition.

(rutile). The improved photocatalytic property (25%) is attributed to the addition of GNPs, which increases the electron mobility in TiO_2 . Instead of going back to the holes, the photon-excited electrons are transported through the GNPs into the solution and convert oxygen into singlet oxygen to decompose the dye (MB). Hence GNPs reduce the electron–hole recombination rate [4,7]. As stated earlier, GNPs also act as a localized heating source during the SPS process and enable excellent bonding with TiO_2 grains (Fig. 2c). The excellent interface between GNPs and TiO_2 grains results in improved electron mobility across the grain boundaries. This also helps its photocatalytic behavior. Figure 4c displays these mechanisms schematically. In summary, we have synthesized TiO_2 –GNP composite by a SPS technique, and achieved a 25% improvement in photocatalytic activity.

A.A. acknowledges support from US Air Force Office of Scientific Research (FA9550-12-1-0263). The support of Neal Ricks and AMERI at FIU, in providing the research facilities, is greatly acknowledged.

[1] S.G. Kumar, L.G.J. Devi, *Phys. Chem. A* 115 (2011) 13211.

- [2] G. Liu, Y. Zhao, C. Sun, F. Li, G.Q. Lu, H.M. Cheng, *Angew. Chem. Int. Ed.* 47 (2008) 4516.
- [3] A.K. Geim, *Science* 324 (2009) 1530.
- [4] J.S. Lee, K.H. You, C.B. Park, *Adv. Mater.* 1084 (2012) 24.
- [5] N. Yang, Y. Zhang, J.E. Halpert, J. Zhai, D. Wang, L. Jiang, *Small* 8 (11) (2012) 1762.
- [6] P. Zhu, A.S. Nair, S. Peng, S. Yang, S. Ramakrishna, *ACS Appl. Mater. Interfaces* 4 (2012) 581.
- [7] Y.N. Ng, I.V. Lightcap, K. Goodwin, M. Matsumara, P.V.J. Kamat, *Phys. Chem. Lett.* 1 (2010) 2222.
- [8] D. Lahiri, V. Singh, A.K. Keshri, S. Seal, A. Agarwal, *Carbon* 48 (2010) 3103.
- [9] S.R. Bakshi, V. Musaramthota, D. Lahiri, V. Singh, S. Seal, A. Agarwal, *Mater. Sci. Eng. A* 528 (3) (2011) 1287.
- [10] W. Choi, I. Lahiri, R. Seelaboyina, Y.S. Kang, *Crit. Rev. Solid State Mater. Sci.* 35 (2010) 52.
- [11] XG Science, xGNP[®] graphene nanoplatelets carbon nanoparticles with multifunctional capability, XG Sciences Documentation, 2009.
- [12] A. Nieto, D. Lahiri, A. Agarwal, *Carbon* 50 (2012) 4068.
- [13] L.S. Walker, V.R. Marotto, M.A. Rafiee, N. Koratkar, E.L. Corral, *ACS Nano* 5 (4) (2010) 3182.
- [14] J.M.J. Herrmann, *Catal. Today* 53 (1999) 115.
- [15] J. Sun, L. Gao, Q.J. Zhang, *Am. Ceram. Soc.* 86 (10) (2003) 1677.

Unfolding the Damping Behavior of Multilayer Graphene Membrane in the Low-Frequency Regime

Debrupa Lahiri,[†] Santanu Das,[‡] Wonbong Choi,[‡] and Arvind Agarwal^{†,*}

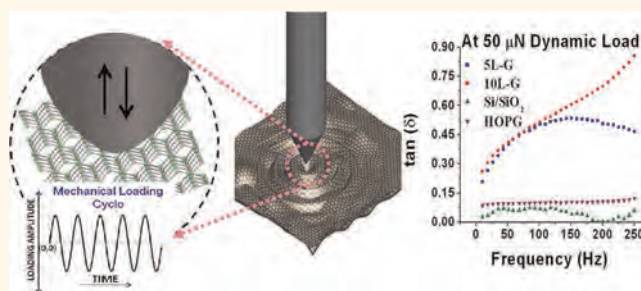
[†]Nanomechanics and Nanotribology Laboratory and [‡]Nanomaterials and Device Laboratory, Department of Mechanical and Materials Engineering, Florida International University, Miami, Florida 33174, United States

Damping characteristics of graphene are of paramount interest considering its numerous fields of applications such as nanomechanical resonators,^{1–6} transparent electrodes,^{7,8} heat spreaders,⁹ nonvolatile memory,¹⁰ thin film speakers,¹¹ acoustic emission devices,¹² and many more. The damping potential of graphene could also be very effective in macroscale dynamic systems, *e.g.*, tracking and pointing weapon systems in aircraft and suspension and steering in automotive and turbomachinery mountings, which need damping from shock vibrations.^{13,14}

The experimental^{1–6} and theoretical^{15–17} studies performed on the damping/vibrational behavior of graphene, to date, are at a higher frequency range (>MHz), through electrostatic actuation. The theoretical studies on high-frequency regime vibrational behavior of single and multilayer suspended graphene have used molecular dynamics and continuum models to derive the vibration mode shapes, natural frequencies, and the influence of van der Waals interactions.^{15–17} Bunch *et al.* established the application of graphene for nanomechanical resonators, in synergy with its excellent charge sensitivity.¹ Further experimental studies have explored the stress distribution on the graphene resonators,² their response to mass and temperature,³ and the nonlinear damping behavior.⁴ Low-frequency damping of graphene has a significant contribution toward graphene-based micro/nanoscale devices and macroscale dynamic systems for absorbing shock-generated energies.¹³ *But the damping behavior of graphene in the low-frequency regime is not reported to date.*

In contrast to the available high-frequency damping studies, we have experimentally investigated the damping behavior of graphene at a much lower frequency

ABSTRACT



The damping behavior of few-layered graphene membrane in the *low-frequency regime* of mechanical loading is investigated in the present study. Damping of graphene has significant applications in micro/nanoscale devices and macroscale dynamic systems for absorbing shock-generated energies. Damping behavior of graphene is experimentally evaluated, for the first time, by dynamic mechanical analysis at the nanoscale with cyclic mechanical loading in the range 0.1–50 μN applied at a frequency range of 10–250 Hz. This study reveals 260% higher damping on graphene membranes than a silicon surface. The damping shows excellent reproducibility and remains steady even after 100 000 cycles. The damping of multilayer graphene membrane, supported on a Si/SiO₂ substrate, shows a strong dependence on the frequency of cyclic loading. The mechanism governing impressive damping of a graphene membrane is elucidated by structural changes such as ripple formation, ripple wave propagation, and z-axis compression. Damping behavior of a graphene membrane in this low-frequency regime is also found to depend on the number of graphene layers and is explained as the interplay between in-plane sp^2 and out-of-plane van der Waals forces. These findings are important for establishing the potential of graphene for applications in macro- to nanoscale structures that require continuous absorption of shock waves without destruction/failure.

KEYWORDS: multilayer graphene · damping · dynamic ripple · nano-DMA · shock absorption · frequency · cyclic loading

(10–250 Hz) by application of cyclic mechanical load (0.1–50 μN). The aim of the present study is to comprehend the *low-frequency* damping behavior of graphene in light of the interplay between out-of-plane van der Waals and in-plane sp^2 bonds, which would govern the elastic and viscoelastic behavior of graphene in this regime. The role of cycling loading-assisted dynamics of ripples in the energy absorption

* Address correspondence to agarwala@fiu.edu.

Received for review January 18, 2012 and accepted April 21, 2012.

Published online
10.1021/nn3014257

© XXXX American Chemical Society

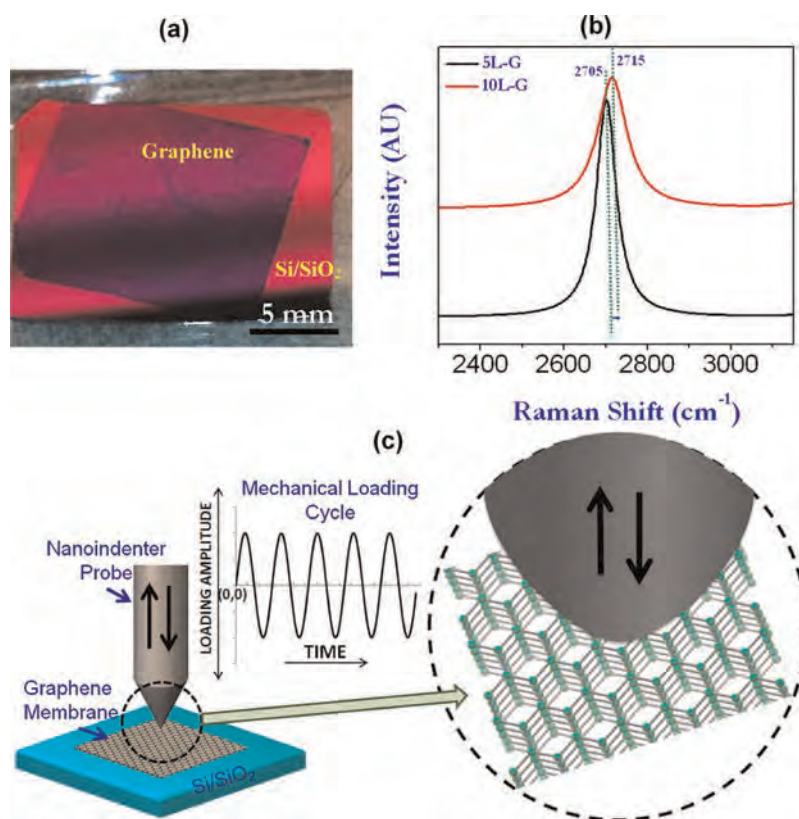


Figure 1. (a) Digital image of 5L-G on a Si/SiO₂ substrate. (b) Comparative Raman spectra of various layers of graphene on Si/SiO₂ substrates exhibiting the characteristic 2D band of graphene. (c) Schematic showing nano-DMA of the graphene membrane on a Si/SiO₂ substrate.

and its contribution toward the damping behavior of graphene membranes is also analyzed. This is the first experimental study on low-frequency damping behavior of graphene.

RESULTS AND DISCUSSION

The present study uses chemical vapor deposition (CVD)-grown graphene, which was transferred on a Si/SiO₂ substrate for studying the damping behavior. The transferred membrane consists of about 4 or 5 layers of graphene sheets, as observed in HRTEM (Figure S1, Supporting Information¹⁸), and is referred to as 5L-G, hereafter. Another sample was prepared by transferring a second membrane on top of another, thus consisting of 8–10 layers of graphene and is referred to as 10L-G. It is expected that the second transferred layer of graphene could have some crystallographic misalignment with the first layer of graphene. The double transferred graphene membrane was annealed to reduce the interfacial mismatch and induce bonding between the two transferred membranes. Sample 5L-G was also given a similar annealing treatment after transferring onto the substrate.

The peak related to the 2D band in the Raman spectra for 5L-G and 10L-G provides additional support for relative graphene layer content in the two membranes (Figure 1b). The 2D peak in 5L-G is located at

~2705 cm⁻¹, which corresponds to ~4 or 5 layers of graphene in the membrane.^{19,20} A blue shift in the same peak to ~2715 cm⁻¹ indicates the presence of 8–10 layers in the 10L-G membrane.^{19,20} A similar graphene membrane was also transferred on a Si/SiO₂ surface with a matrix of 50 μm diameter holes to study the existence of micrometer size dirt at the interface and top of the membrane. Transparent graphene membranes on a Si/SiO₂ substrate with comparable optical micrographs reveal a dirt-free surface of the membrane from micrometer-level impurities (Figure S2, Supporting Information). However, some atomic-scale impurities may be present at the interface of the wet transferred graphene membrane and the Si/SiO₂ substrate.

Damping behavior was evaluated through nanodynamic mechanical analysis (nano-DMA) in a frequency range of 10–250 Hz and dynamic (cyclic) load range of 0.1–50 μN (Figure 1c). Damping characteristics of the bare Si/SiO₂ surface is also determined to study the substrate effect. The damping of graphene is expressed as “tan (δ)”, where δ is the phase lag between force applied and displacement obtained (see Supporting Information and Figure S3 for the measurement principle). Higher damping causes higher phase lag.

Both 5L-G and 10L-G show significant changes in the damping behavior with the frequency (Figure 2a and b).

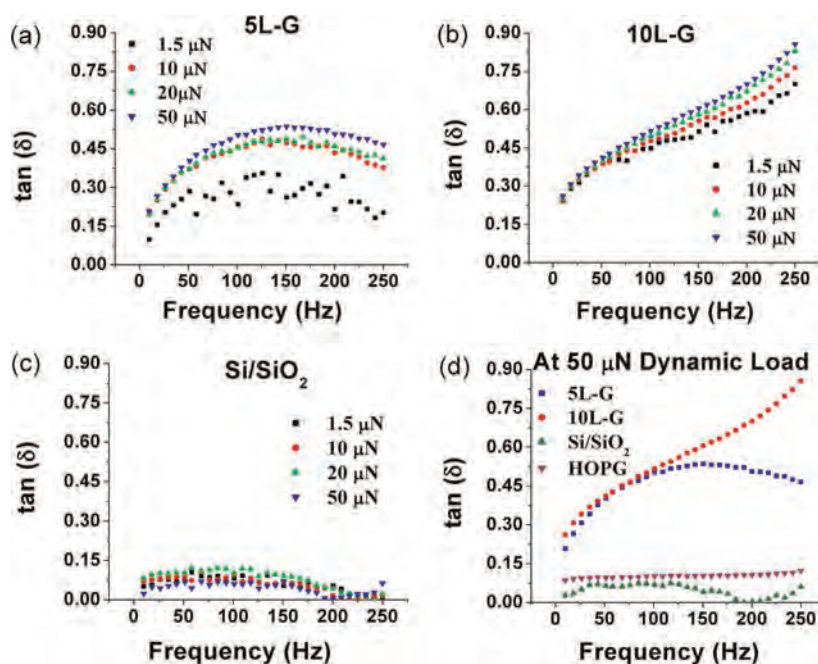


Figure 2. Damping behavior in the frequency range 10–250 Hz for (a) 5 L-graphene (b) 10 L-graphene, and (c) bare Si/SiO₂ at different dynamic load amplitudes. Si/SiO₂ substrate shows very low damping (<0.1) and almost no change with the frequency. (d) Comparative dynamic behavior of 5L-G, 10L-G, bare Si/SiO₂ substrate, and highly ordered pyrolytic graphite (HOPG) at a dynamic load of 50 μN and varying frequency.

Damping ($\tan \delta$) reaches a peak in 5L-G at ~ 150 Hz and then decreases for loads between 1.5 and 50 μN (Figure 2a). On the contrary, damping continues to increase with the frequency for 10L-G up to 250 Hz (Figure 2b). Damping is similar in 5L-G and 10L-G up to ~ 150 Hz (Figure 2d). The Si/SiO₂ substrate shows much lower $\tan \delta$ (Figure 2c and d) and thus eliminates the possibility of contributing toward the damping response of both graphene membranes. Also, damping increases slightly at higher dynamic load (Figure 2a and b). These observations indicate a dominating influence of the frequency on the damping behavior. Similar observations are made in Figure 3, where increasing the dynamic load causes a slight increase in the damping for both graphene membranes at fixed frequencies of 100 and 200 Hz. Further, damping of 10L-G remains similar to 5L-G at 100 Hz, but increases by almost two times at 200 Hz for the entire range of dynamic load, which corroborates earlier observations in Figure 2d. Thus, graphene membranes are found to show similar trends in damping behavior irrespective of the testing conditions, *i.e.*, changing frequency or changing dynamic loads (Figure S4, Supporting Information, provides a graphical representation of additional results). Figures 3c and S4c show damping behavior of 5L-G, 10L-G, and the substrate after 100,000 loading cycles. $\tan \delta$ is consistent with small error bars, implying the steadiness of the damping during the long life-span. Damping is almost zero in the Si/SiO₂ substrate, whereas 5L-G and 10L-G show very high values of $\tan \delta$. Small error bars in Figure 3c also indicate no significant damage to graphene layers and

bonds in the membranes. These observations indicate that the damping behavior of graphene membranes is governed by fundamental structural and morphological aspects, which are discussed below.

The nature of dynamic mechanical loading is more suitably defined by the impact- and indentation-based deformation behavior of graphene^{13,21–26} as compared to high-frequency resonance through electrical actuation.^{1–6} Hence, the deformation mode of graphene during nano-DMA is a combination of impact and indentation loadings.

Graphene possess a very high in-plane Young's modulus of ~ 1 TPa²¹ due to strong sp^2 bonds. However, the layers of the graphene membrane are held together by weak van der Waals forces, which strongly influences its mechanical behavior.²⁷ Strong sp^2 bonding increases the probability of the elastic response due to in-plane mechanical loading. Thus the initial energy absorption in multilayer graphene membranes takes place in the out-of-plane direction, mainly through the following two mechanisms: (i) dynamic ripple formation in individual graphene layers and (ii) energy absorption through van der Waals bonds, working as nonlinear springs, and gradual reduction in interlayer spacing.

Role of Ripples in Damping. During dynamic loading, ripple formation becomes inevitable in the graphene layers,¹³ some part of which could be recovered during unloading. However, the unrecovered part causes absorption of the energy and damping. He *et al.* have studied dynamic ripple formation in monolayer graphene due to impact and predicted energy absorption with the ripple wave propagation.¹³ The decay in the

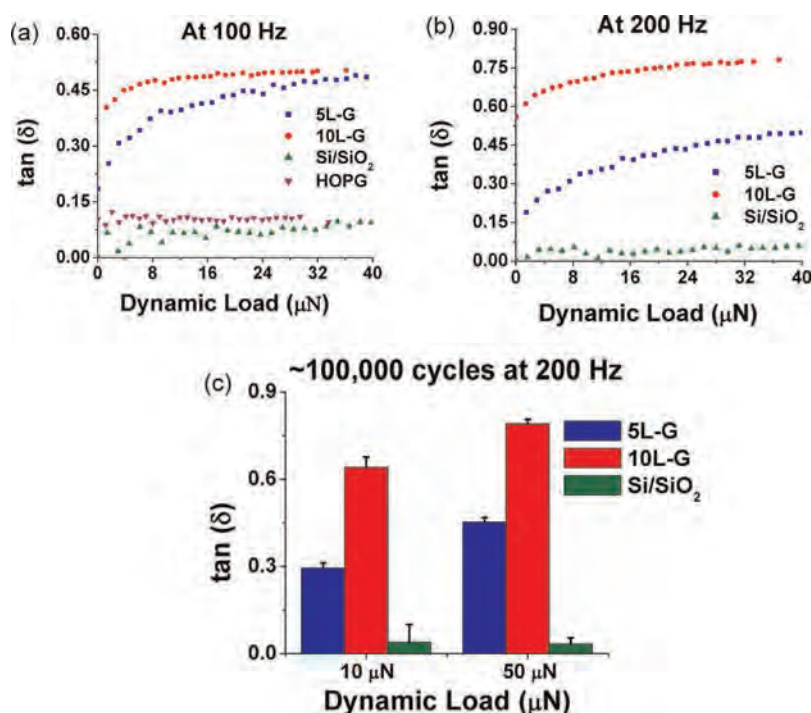


Figure 3. Comparative damping behavior of 5L-G, 10L-G, and Si/SiO₂ substrate at a dynamic load range of 0.1–40 μN with a frequency of loading of (a) 100 Hz and (b) 200 Hz. (c) Long cycle damping study for 5L-G, 10L-G, and Si/SiO₂ substrate at a frequency of 200 Hz and loads of 10 and 50 μN , showing the stability of the damping behavior of graphene membrane over 100,000 cycles of loading. 10L-G shows much higher damping than 5L-G, with almost negligible damping in Si/SiO₂.

amplitude of the ripple waves has been defined using the following relationship:

$$\text{amplitude}(x) = 2.59943e^{(-|x|/7.33993)} - 0.01351 \quad (1)$$

where x is the horizontal distance of a ripple from the point of impact.¹³ This relationship shows that ripple height is higher near the point of contact and decreases at a farther distance. It is emphasized that ripples that are intrinsic to graphene sheets²⁸ may lead to complex interactions with new ripples formed during loading. The ripples associated with the graphene membranes in this study are both intrinsic and originated from the transfer of graphene. These ripples might disturb the propagation of new ripple waves generated by the loading. However, theoretical study suggests that impacting ripple waves propagate forward and do not fade away completely.¹³ Thus, dynamic wave formation due to the cyclic loading remains as one of the causes for the energy absorption in graphene membranes. Ripples can also play an active role in energy absorption during compressive loading. The flattening out of intrinsic ripples in the neighborhood of the stress/loading point²² during nanoindentation of monolayer graphene is a potential cause for the damping. The force required for the flattening of ripples is much lower than in-plane stretching of graphene, which makes flattening more inevitable during loading of graphene layers with intrinsic ripples.²² The schematic diagram in Figure 4 presents a graphical explanation of these two ripple-related energy absorption mechanisms.

van der Waals Contribution to Damping. Compressive deformation in graphene is initially dominated by out-of-plane weak van der Waals bonding, compared to strong in-plane sp^2 bonding. However, compression is restricted due to an increase in van der Waals force with decreasing interlayer distance. The van der Waals energy of interaction between two atoms 1 and 2 separated by distance H is defined as²⁹

$$E = -\frac{\lambda_{1,2}}{H^6} \quad (2)$$

where $\lambda_{1,2}$ is London's constant, whose value depends on the atomic number. Hamaker modified the concept to quantify the van der Waals force between two spherical particles as³⁰

$$F_{\text{VDW}} = \frac{AR}{12H^2} \quad (3)$$

where R is the reduced radius and A is Hamaker's coefficient, expressed as

$$R = \frac{2R_1R_2}{R_1 + R_2} \text{ and } A = \pi q_1 q_2 \lambda_{1,2}$$

R_1 and R_2 are the radii of two particles; q_1 and q_2 are the atoms/ cm^3 in the particles. The expression can be further modified for van der Waals force/unit area between two smooth plane surfaces (similar to graphene) as²⁹

$$P_{\text{VDW}} = \frac{A}{6\pi H^3} \quad (4)$$

Equation 4 shows an increase in the van der Waals force between two planes with a decrease in interplanar

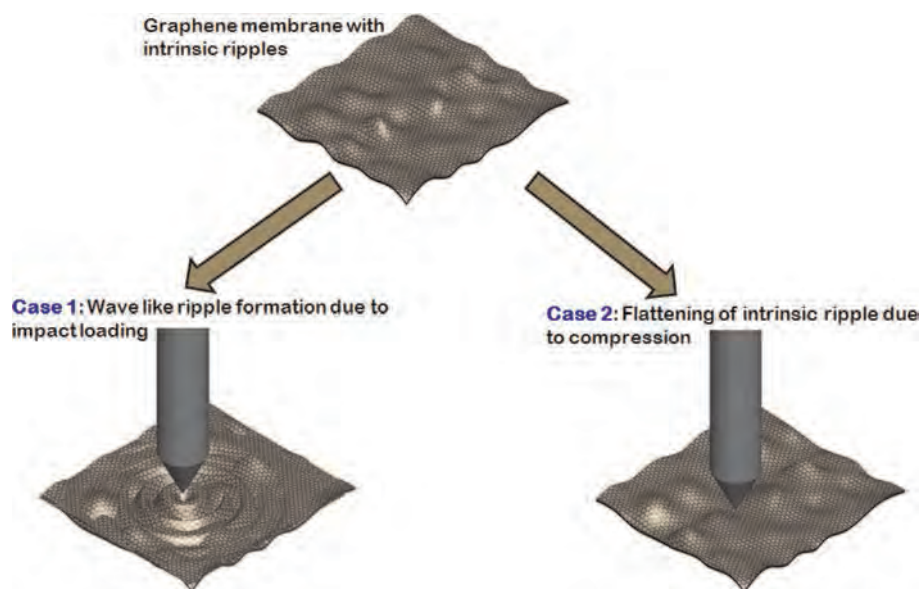


Figure 4. Schematic showing the ripples in CVD-grown and transferred graphene and change in ripple structure with dynamic mechanical loading. The figure at the top shows a graphene membrane with ripples. Case 1 presents ripple wave propagation due to impact loading. The final ripple profile of the graphene membrane is the combined effect of the impacting waves and existing ripples, which are the primary cause of energy absorption. In case 2, the existing ripples are flattened due to the compressive loading. The flattening causes reduction in the amplitude of the existing ripples in the neighborhood of the indent in case 2, resulting in damping of the response to dynamic mechanical loading.

distance. This is the condition of graphene layers in a membrane during initial stages of compression. As the bonding between two layers becomes stronger with decreasing bond length (eq 4), it takes more energy to bring the two planes or particles closer or move them apart. In this process, the compressed membrane reaches a point when the force required to further compress the out-of-plane van der Waals bonds becomes higher than that for stretching the in-plane sp^2 bonds. From this point onward the deformation is dominated by sp^2 bonds. The energy absorption due to a decrease in interlayer distance of a multilayer graphene membrane is possible until the van der Waals force becomes very high and in-plane deformation (sp^2 dominated) starts taking place. During weak van der Waals domination, the nature of deformation remains viscoelastic with more damping. As sp^2 is a stronger bond, the associated deformation after transition is more elastic in nature, leading to a decrease in damping.

The damping increases with frequency up to ~ 150 Hz for both 5L-G and 10L-G (Figure 2). Increasing the frequency of loading causes more ripple formation and interlayer compression, because the graphene layers have less time to recover the ripples or deformation in the z -direction. This causes more absorption of energy and more damping. If the previous hypothesis holds true, then damping should continue to increase with the frequency. That is what we observe in the case of 10L-G in our experimental range of 10–250 Hz (Figure 2). However, for 5L-G, the damping decreases after ~ 150 Hz (Figure 2). The reason lies in the number

of graphene layers in the membrane. As postulated in eq 1, the ripple waves fade out in the x -direction along the propagation front. This means both 5L-G and 10L-G would have a similar spatial spread of the ripple propagation zone, but, due to more layer content in 10L-G, it can accommodate more ripple formation. Similarly, 10L-G has more space available along the z -axis to accommodate extra compression than 5L-G. At a frequency of loading higher than ~ 150 Hz, due to very fast ripple formation with less propagation time, the wavefront becomes saturated in the case of 5L-G. The situation is aggravated by less recovery in the z -direction due to faster loading cycles. So, the z distance between graphene layers is decreased enough to reach a transition point from van der Waals to sp^2 domination. Thus, the in-plane deformation starts to accommodate the cyclic load applied beyond 150 Hz. This leads to more elastic recovery and less damping in 5L-G above 150 Hz. In the case of 10L-G, more layers accommodate more ripple formation and more z -compression before reaching the transition, leaving less chance of in-plane C–C bond stretching. Thus, the damping increases beyond 150 Hz. It is possible that damping in 10L-G will start dying down at even higher frequency, when the critical z distance between graphene layers, corresponding to the deformation transition, is reached. However, it is also possible that at a very high frequency the damping behavior would be governed by some other phenomenon. Nano-DMA tests could not be carried out beyond 250 Hz due to limitation in machine capability. In addition to more ripple formation and z -axis compression, the possible

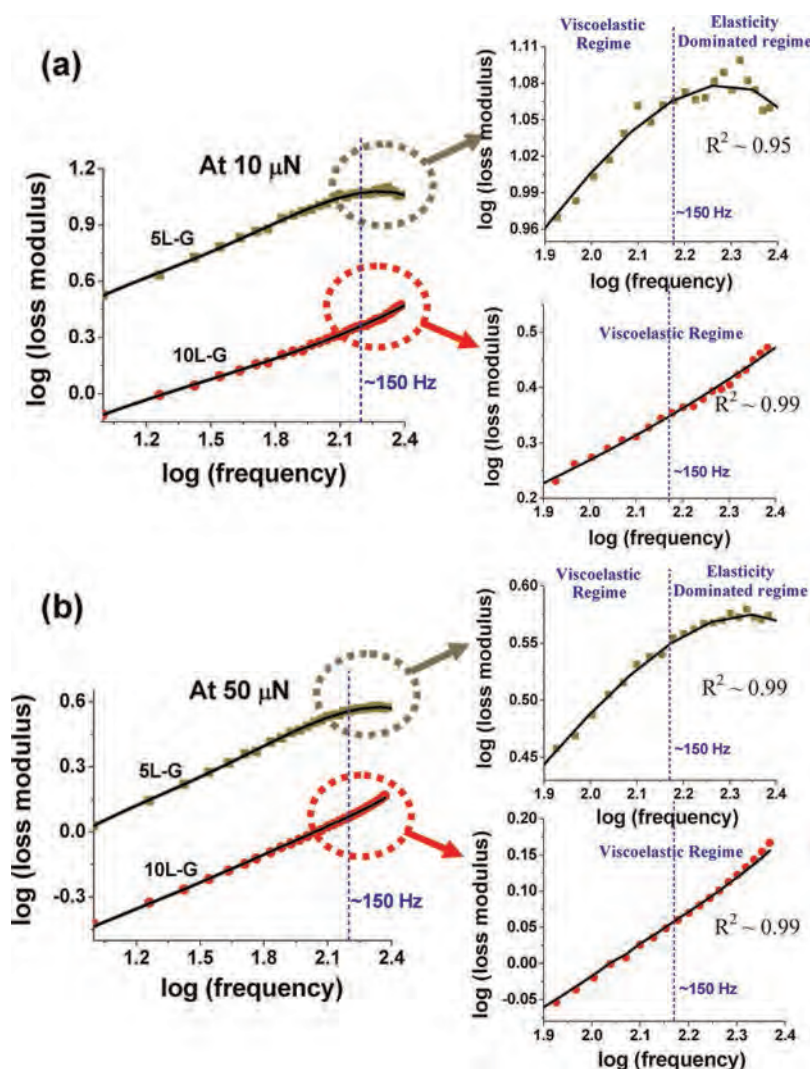


Figure 5. Log–log plot of frequency vs loss modulus for 5L-G and 10L-G at (a) 10 μ N and (b) 50 μ N dynamic loads. Polynomial fit is applied for a better visualization of the transition point. The polynomial fit shows a change in the slope for 5L-G at ~ 150 Hz, denoting a viscoelastic to elastic transition in the deformation behavior. The absence of such slope change in 10L-G indicates no change in the damping mechanism in the experimental frequency range of 10–250 Hz.

interlayer crystallographic mismatch, caused during transfer, could assist in increased damping for 10L-G.

To ascertain the change in the deformation mechanism of 5L-G at ~ 150 Hz, a log–log plot of loss modulus and frequency is obtained (Figure 5). This type of plot is commonly utilized for defining phase transformation in viscoelastic materials.³¹ The sudden change in the slope for 5L-G at ~ 150 Hz is similar in nature to the transition from rubbery to glassy regime in the case of polymers. At higher frequency, the dynamic deformation is supposed to be dominated by in-plane covalent bonding, making it more elastic (or less viscoelastic) in nature, which is similar to rubbery to glassy transition. On the contrary, 10L-G does not show any change in slope (and deformation behavior) throughout the frequency range.

Higher damping in 10L-G as compared to 5L-G raises the question of whether the damping on such structures would increase infinitely with the number of

graphene layers. To answer this query, a 1 mm thick highly oriented pyrolytic graphite (HOPG) sample was tested under some of the mechanical loading conditions used for graphene membranes. The results show much lower damping ($\tan \delta \approx 0.1$) in HOPG than either of the graphene membranes ($\tan \delta \approx 0.5$ and higher, Figures 2d and 3b). The reason for this behavior lies in the energy absorption by ripples in graphene membranes. HOPG, being a rigid 3D structure (no longer a complying membrane), does not have intrinsic ripples and is not prone to ripple formation. Thus, the energy absorption in HOPG is only through z-axis compression, and it exhibits lower damping than graphene membranes. In addition, the graphene layers of HOPG are stacked in perfect crystallographic alignment, unlike the crystallographic mismatch in transfer layers of 10L-G, as mentioned before. The perfect stacking of graphene layers in HOPG would also restrict the disturbance in structure by ripple formation to some

extent. This aspect has potential to contribute toward the difference in damping behavior between HOPG and 10L-G.

It is observed that dynamic load at fixed frequencies (Figure 3a and b) causes a smaller increase in the damping, compared to significant changes with an increasing frequency (Figure 2a and b) for both graphene membranes. The change in the load influences the z-axis compression, whereas change in the frequency is mainly accommodated through ripple formation. This understanding leads to the conclusion that the damping in graphene is more dominated by rippling than z-axis compression.

Long-cycle dynamic behavior also shows more damping for 10L-G than 5L-G at higher frequency (200 Hz), due to extended viscoelastic behavior of the former. SPM images of 5L-G after a long-cycle test reveals no residual impression of mechanical loading, indicating retention of the damage-free graphene structure (Figure S5, Supporting Information). Similar SPM images of Si/SiO₂ substrate after a long-cycle test indicate permanent deformation. This set of results provides encouraging input toward practical applications of graphene as a shock-resistant membrane for extended periods.

A brief nano-DMA study of a similar 5L-G graphene layer transferred on a single-crystal mica surface is also carried out to understand the universality of the damping behavior of graphene membranes. Mica is not the best substrate to reveal the full damping potential of graphene membranes because mica itself is known and used as a good vibration dampener.^{32,33} The results, presented in Figure S6 (Supporting Information), show mica generating much higher damping (up to $\tan \delta \approx 0.4$) than the Si/SiO₂ substrate ($\tan \delta \approx 0.1$). However, it is more interesting to find out that graphene membranes can even enhance the damping capability (up to $\sim 40\%$) of a surface like mica, which itself is known for its damping capabilities. However, the damping capability ($\tan \delta$) is found to decrease, both at higher frequency and at higher dynamic load, which is attributed to the damage of the mica substrate beneath the graphene membrane, causing permanent damage in the graphene membrane also. The signs of such

damage can be observed in the SPM images in Figure S7, Supporting Information. The nano-DMA tests carried out on a graphene membrane over a mica substrate at 200 Hz frequency and 10 μ N dynamic load for only 5000 cycles show signs of permanent damage, whereas no such features are observed on a graphene membrane over Si/SiO₂ even after 100,000 cycles of loading in similar conditions. The nature of change in $\tan \delta$ with frequency for a graphene–mica surface (Figure S6, Supporting Information) does not exactly match that for a graphene–Si/SiO₂ surface (Figure 2). The damping behavior of a graphene membrane on a mica surface is more influenced by the dampening from the substrate as compared to the rigid Si/SiO₂ substrate. Thus, damping behavior of a graphene membrane on a Si/SiO₂ substrate is more representative of the true behavior of graphene, whereas the different behavior on graphene–mica surface is attributed to the composite effect of substrate and membrane.

Excellent repeatability of the damping behavior of a graphene membrane on a Si/SiO₂ substrate, presented in Figure S8(a–c), Supporting Information, proves its intrinsic nature of origin. Atomic level impurities, if present at the graphene–Si/SiO₂ interface, do not show any significant contribution to the damping behavior. Otherwise, the damping behavior would be influenced in a localized manner and deviate from reproducibility, checked by a minimum of 50 tests in each membrane at a randomly selected spot with macroscale spatial distribution.

CONCLUSIONS

In summary, this study reveals excellent damping capability of few-nanometer graphene membranes in the low-frequency cyclic loading regime. The damping mechanism of the micrometer-level dirt-free graphene membrane is governed by structural changes such as ripple formation, ripple wave propagation, and z-axis compression. These results multiply the advantages of using graphene membranes in electronics and other nanoscale devices, as graphene membranes resist structural damage by mechanical impacts/shocks. This study paves the way for using graphene membranes as a nanoscale shock reservoir for impact-sensitive structures.

METHODS

Graphene Growth by CVD and Transfer to Si/SiO₂ Substrate. A copper foil of 54 μ m thickness (NIMROD Hall, USA) was annealed at 1000 °C for 1 h in an argon atmosphere followed by surface cleaning with acetic acid at 70 °C. The preannealed metal foils were placed inside a 2 in. diameter quartz tube of a low-pressure thermal CVD system (Atomate, USA). Furnace temperature was raised to 1000 °C at a heating rate of 120 °C/min in an argon atmosphere. Graphene precipitation occurred on the Cu foil using the reaction of the precursor gas mixture of CH₄/H₂ (1:5) for 10 min. After the CVD process, the graphene film was transferred to a 300 nm SiO₂ coated Si substrate (Si/SiO₂) using

a chemical process. The chemical process for graphene transfer consists of the etching of Cu foil and then transferring the floating graphene onto a Si/SiO₂ substrate, followed by washing with water, acetone, and isopropyl alcohol as described elsewhere.¹⁸ Furthermore, the rapid thermal annealing was carried out for graphene on the Si/SiO₂ substrate at 400 °C under a N₂ atmosphere for 30–40 s. Similarly, the second graphene membrane was transferred onto the graphene–Si/SiO₂ substrate followed by annealing.

Raman spectroscopy of the graphene membranes was performed using a Spectra Physics (model 177G02) system with a spectral resolution of 4 cm^{−1} with an argon ion (Ar⁺) laser

having a wavelength of 514.5 nm. The Raman spectra were collected using a high-throughput holographic imaging spectrograph (model HoloSpec f/1.8i, Kaiser Optical Systems) inbuilt with a volume transmission grating, a holographic notch filter, and a thermoelectrically cooled CCD detector (Andor Technology). Raman spectra were collected at room temperature and 1 atm.

Damping Characterization through nano-DMA Testing. Damping behavior of 5L-G, 10L-G, Si/SiO₂, and HOPG was characterized using the nano-DMA module of the Hysitron Triboindenter TI-900. For all the measurements, a 100 nm Berkovich diamond tip was used. The working principle of the nano-DMA module with the relevant equations is provided in the Supporting Information. The tests were performed with three different modes: (1) varying frequency with fixed load cycle; (2) varying load cycles with fixed frequency; (3) fixed load cycle and frequency with ~100 000 cycles of loading. During the tests, a cyclic dynamic load of 10% was applied over a fixed static load, with the indenter tip sitting on the sample surface. A minimum of 50 tests were carried out in each sample at macrolevel spatial distances randomly chosen on a >100 mm² surface area (Figure 1a) of each graphene membrane. Figure S8(a–c), Supporting Information, show the very high repeatability of the tests performed in some of these conditions.

Conflict of Interest: The authors declare no competing financial interest.

Acknowledgment. A.A. acknowledges support from the U.S. Air Force Office of Scientific Research (FA9550-09-1-0297) through High Temperature Materials Program managed by Dr. Ali Sayir. DURIP (N00014-06-0675) support from the Office of Naval Research is also greatly acknowledged. The authors thank Mr. Samarth Thomas, an undergraduate research assistant in the Nanomechanics and Nanotribology Laboratory, for drawing schematics. W.C. acknowledges support from the National Science Foundation (CMMI-0900583), U.S. Air Force Office of Science Research (FA9550-09-1-0544), and S.D. acknowledges the Dissertation Year Fellowship from University Graduate School, Florida International University. The overall support of Mr. Neal Ricks and AMERI at FIU, in maintaining the research facilities, is greatly acknowledged.

Supporting Information Available: HRTEM image of 5L-G, transfer procedure of free-standing graphene membrane on Si/SiO₂ with holes, optical images to evaluate cleanliness, calculation details for $\tan \delta$ in the nano-DMA study, comparative damping behavior plots of 5L-G, 10L-G, and Si/SiO₂ (additional to those presented in the main text), scanning probe images of 5L-G and Si/SiO₂ surfaces after nano-DMA testing, damping behavior of mica and 5L-G on mica, comparative scanning probe images of graphene membrane on Si/SiO₂ and mica after long-cycle tests, three test data plots on graphene membranes in each condition to show the repeatability of the damping behavior. This material is available free of charge via the Internet at <http://pubs.acs.org>.

REFERENCES AND NOTES

- Bunch, J. S.; van der Zande, A. M.; Verbridge, S. S.; Frank, I. W.; Tanenbaum, D. M.; Parpia, J. M.; Craighead, H. G.; McEuen, P. L. Electrochemical Resonators from Graphene Sheets. *Science* **2007**, *315*, 490–493.
- García-Sánchez, D.; van der Zande, A. M.; San Paulo, A.; Lassagne, B.; McEuen, P. L.; Bachtold, A. Imaging Mechanical Vibrations in Suspended Graphene Sheets. *Nano Lett.* **2008**, *8*, 1399–1403.
- Chen, C.; Rosenbalt, S.; Bolotin, K. I.; Kalb, W.; Kim, P.; Kymissis, I.; Stormer, H. L.; Heinz, T. F.; Hone, J. Performance of Monolayer Graphene Nanomechanical Resonators with Electrical Readout. *Nat. Nanotechnol.* **2009**, *4*, 861–867.
- Eichler, A.; Moser, J.; Chaste, J.; Zdrojek, M.; Wilson-Rae, I.; Bachtold, A. Nonlinear Damping in Mechanical Resonators Made from Carbon Nanotubes and Graphene. *Nat. Nanotechnol.* **2011**, *6*, 339–342.
- van der Zande, A. M.; Barton, A.; Alden, J. S.; Ruis-Vargas, C. S.; Whitney, W. S.; Pham, P. H. Q.; Parpia, J. M.; Craighead, H. G.; McEuen, P. L. Large-Scale Array of Single-Layer Graphene Resonators. *Nano Lett.* **2010**, *10*, 4869–4873.
- Barton, R. A.; Ilic, B.; van der Zande, A. M.; Whitney, W. S.; McEuen, P. L.; Parpia, J. M.; Craighead, H. G. High, Size-Dependant Quality Factor in an Array of Graphene Mechanical Resonators. *Nano Lett.* **2011**, *11*, 1232–1236.
- Lii, X. S.; Zhu, Y. W.; Cai, W. W.; Borysiak, M.; Han, B. Y.; Chen, D.; Piner, R. D.; Colombo, L.; Rouff, R. S. Transfer of Large-Area Graphene Film for High-Performance Transparent Conductive Electrodes. *Nano Lett.* **2009**, *9*, 4359–4363.
- Lahiri, I.; Verma, V. P.; Choi, W. An All-Graphene Based Transparent and Flexible Field Emission Device. *Carbon* **2011**, *49*, 1614–1619.
- Prasher, R. Graphene Spreads the Heat. *Science* **2010**, *328*, 185–186.
- Zheng, Y.; Ni, G. X.; Toh, C. T.; Zheng, M. G.; Chen, S. T.; Yao, K. Gate-Controlled Nonvolatile Graphene-Ferro-Electric Memory. *Appl. Phys. Lett.* **2009**, *94*, 163505.
- Shin, K. Y.; Hong, J. Y.; Jang, J. Flexible and Transparent Graphene Films as Acoustic Actuator Electrodes Using Inkjet Printing. *Chem. Commun.* **2011**, *47*, 8527–8529.
- Tian, H.; Ren, T.-L.; Xie, D.; Wang, Y.-F.; Zhou, C.-J.; Feng, T.-T.; Fu, D.; Yang, Y.; Peng, P.-G.; Wang, L.-G.; *et al.* Graphene-on-Paper Sound Source Devices. *ACS Nano* **2011**, *5*, 4878–4885.
- He, Y. Z.; Li, H.; Si, P. C.; Li, Y. F.; Yu, H. Q.; Zhang, X. Q.; Ding, F.; Liew, K. M.; Liu, X. F. Dynamic Ripples in Single Layer Graphene. *Appl. Phys. Lett.* **2011**, *98*, 063101.
- Korathkar, N.; Wei, B.; Ajayan, P. M. Carbon Nanotube Films for Damping Applications. *Adv. Mater.* **2002**, *14*, 997–1000.
- He, X. Q.; Kitipornchai, S.; Liew, K. M. Resonance Analysis of Multilayer Graphene Sheets Used as Nanoscale Resonator. *Nanotechnology* **2005**, *16*, 2086–2091.
- Kitipornchai, S.; He, X. Q.; Liew, K. M. Continuum Model for Vibration of Multilayered Graphene Sheets. *Phys. Rev. B* **2005**, *72*, 075443.
- Iyakutti, K.; Surya, V. J.; Emelda, K.; Kawazoe, Y. Simulation of Single Layer Graphene Sheets and Study of Their Vibrational and Elastic Properties. *Comput. Mater. Sci.* **2012**, *51*, 96–102.
- Das, S.; Sudhagar, P.; Verma, V.; Song, D.; Ito, E.; Lee, S. Y.; Kang, Y. S.; Choi, W. Charge-Transfer Characteristics of Graphene for Triiodide Reduction in Dye-Sensitized Solar Cells. *Adv. Func. Mater.* **2011**, *2*, 3729–3736.
- Rafiee, J.; Mi, X.; Gullapalli, H.; Thomas, A. V.; Yavari, F.; Shi, Y.; Ajayan, P. M.; Korathkar, N. A. Wetting Transparency of Graphene. *Nat. Mater.* **2012**, *11*, 217–222.
- Ferrari, A. C.; Meyer, J. C.; Scardaci, V.; Casiraghi, C.; Lazzeri, M.; Mauri, F.; Piscanec, S.; Jiang, D.; Novoselov, K. S.; Roth, S.; *et al.* Raman Spectrum of Graphene and Graphene Layers. *Phys. Rev. Lett.* **2006**, *97*, 187401.
- Lee, C.; Wei, X.; Kysar, J. W.; Hone, J. Measurement of the Elastic Properties and Intrinsic Strength of Monolayer Graphene. *Science* **2008**, *321*, 385–388.
- Ruiz-Vargas, C. S.; Zhuang, H. L.; Huang, P. Y.; van der Zande, A. M.; Garg, S.; McEuen, P. L.; Muller, D. A.; Henning, R. G.; Park, J. Softened Elastic Response and Unzipping in Chemical Vapor Deposition Graphene Membranes. *Nano Lett.* **2011**, *11*, 2259–2263.
- Huang, M.; Pascal, T. A.; Kim, H.; Goddard, W. A., III; Greer, J. R. Electronic-Mechanical Coupling in Graphene from *in-Situ* Indentation Experiments and Multiscale Simulations. *Nano Lett.* **2011**, *11*, 1241–1246.
- Wang, C. Y.; Mylvaganam, K.; Zhang, L. C. Wrinkling of Monolayer Graphene: A Study by Molecular Dynamics and Continuum Plate Theory. *Phys. Rev. B* **2009**, *80*, 155445.
- Frank, I. W.; Tanenbaum, D. M.; van der Zande, A. M.; McEuen, P. L. Mechanical Properties of Suspended Graphene Sheets. *J. Vac. Sci. Technol. B* **2007**, *25*, 2558–2561.
- Poot, M.; van der Zant, H. S. J. Nanomechanical Properties of Few-Layer Graphene Membranes. *Appl. Phys. Lett.* **2008**, *92*, 063111.
- Koenig, S. P.; Boddeti, N. G.; Dunn, M. L.; Bunch, J. S. Ultrastrong Adhesion of Graphene Membranes. *Nat. Nanotechnol.* **2011**, *6*, 543–546.

28. Fasolino, A.; Los, J. H.; Katsnelson, M. I. Intrinsic Ripples in Graphene. *Nat. Mater.* **2007**, *6*, 858–861.
29. London, F. The General Theory of Molecular Forces. *Trans. Faraday Soc.* **1937**, *33*, 8–26.
30. Hamaker, H. C. The London—van der Waals Attraction between Spherical Particles. *Physica* **1937**, *4*, 1058–1072.
31. Schoff, C. K. Molecular Organization and Dynamics: Rheological Measurements. In *Characterization and Analysis of Polymers*; John Wiley & Sons: Hoboken, NJ, 2008 (ISBN: 978-0-470-23300-9).
32. Basu, S.; Zhou, A.; Barsoum, M. W. On Spherical Nanoindentations, Kinking Nonlinear Elasticity of Mica Single Crystals and Their Geological Implications. *J. Struct. Geol.* **2009**, *31*, 791–801.
33. Deonath; Narayan, R.; Rohatgi, P. K. Damping Capacity, Resistivity, Thermal Expansion and Machinability of Aluminum Alloy-Mica Composites. *J. Mater. Sci.* **1981**, *16*, 3025–3032.

Available at www.sciencedirect.com

SciVerse ScienceDirect

journal homepage: www.elsevier.com/locate/carbon

Synthesis and properties of bulk graphene nanoplatelets consolidated by spark plasma sintering

Andy Nieto, Debrupa Lahiri, Arvind Agarwal *

Plasma Forming Laboratory, Nanomechanics and Nanotribology Laboratory, Mechanical and Materials Engineering, Florida International University, 10555 West Flagler Street, EC 3464, Miami, FL 33174, USA

ARTICLE INFO

Article history:

Received 21 January 2012

Accepted 19 April 2012

Available online xxxx

ABSTRACT

Graphene nanoplatelets (GNPs) are consolidated as a bulk structure by spark plasma sintering (SPS) to study the feasibility of its structure retention at extreme processing conditions. Structural characterization of the sintered GNP pellet is performed using Raman spectroscopy and scanning electron microscopy. Mechanical and tribological properties are evaluated through nanoindentation and ball-on-disk tribometer. GNPs survived the SPS processing at an extreme temperature of 1850 °C and a pressure of 80 MPa with minimal damage to the structure. Energy dissipation mechanisms are observed in the form of multiple bending at sharp angles and sliding of the platelets, which could provide effective toughening mechanisms to ceramic matrices. Tribological studies suggest that GNP shear off and weld at higher load and provides a lubricating effect. Our study shows the potential for GNPs to be successfully used as a reinforcing and lubricating phase in ceramic matrix composites synthesized by SPS.

© 2012 Elsevier Ltd. All rights reserved.

1. Introduction

Graphene is an allotrope of carbon consisting of a single layer of sp^2 bonded carbon atoms. Graphene has generated a great interest as the reinforcement for composite materials because of its impressive mechanical, thermal, and electrical properties. Properties such as high tensile strength (130 GPa) [1] and high Young's modulus (0.5–1 TPa) [2] make graphene an ideal reinforcement. Much of the work on graphene composites has been focused on polymer matrix composites. The addition of graphene has resulted in the improvement of mechanical and electrical properties of the polymer matrix composites [3–6]. Recently, focus is emerging on graphene reinforced metal and ceramic composites [7–15]. Early studies have shown that presence of graphene results in hindering of grain growth [7], improved electrical conductivity [11,12], new toughening mechanisms [13], and improved thermal conductivity [14] in ceramic matrix composites.

Graphene nanoplatelets (GNPs) are multi-layer particles consisting of 10–30 sheets of graphene with much retention of single layer properties [16,17]. The use of GNP is desirable as they are cheaper and easier to produce than single layer graphene or carbon nanotubes [18]. One of the major challenges in composite synthesis is the uniform dispersion and efficient use of the secondary phase. GNPs are easier to disperse than both single layer graphene and carbon nanotubes (CNT). Single layer graphene has a tendency to curl during dispersion and CNT has a tendency to become entangled. Graphene is particularly promising for strong interfacial bonding with the matrix because it has a very high surface energy due to the high surface area intrinsic to its geometry. GNPs have a slightly lower relative surface area; however it is still much higher than those of CNT.

One of the consolidation methods recently used for nanostructured ceramics and CNT reinforced composites is spark plasma sintering (SPS). SPS is a sintering method that

* Corresponding author. Fax: +1 305 348 1932.

E-mail address: agarwala@fiu.edu (A. Agarwal).

0008-6223/\$ - see front matter © 2012 Elsevier Ltd. All rights reserved.

<http://dx.doi.org/10.1016/j.carbon.2012.04.054>

employs high pressure, high temperature, along with a pulsing current through the material during sintering [19]. The current is believed to lead to the formation of plasma in the form of micro-discharge originating from impurities on the particle surfaces. The plasma has the effect of cleansing the particles of impurities and providing an enhanced heat transfer effect that produces better bonding. This process has been shown to have many advantageous effects such as quick sintering times, grain growth inhibition, high densification, and improved bonding between composite phases [20,21]. SPS has been used to consolidate graphene reinforced composites in aluminum oxide [7,11,12] and silicon nitride [13] matrices utilizing pressures of 35–60 MPa and temperatures of 1000–1650 °C. The graphene sheets or platelets used in these studies did not reveal adverse effects from the SPS processing. The resulting composites had dense structures with nearly defect free graphene sheets or platelets.

In this study we have synthesized a bulk sample of GNPs using SPS technique at an extreme temperature of 1850 °C and a pressure of 80 MPa. We have shown that GNPs are capable of surviving the extreme sintering conditions while retaining their structure. GNP is less vulnerable to being damaged by SPS as compared with CNT because of its structure. GNPs are nearly 2-dimensional unlike the CNT whose tubular structure makes it vulnerable to buckling and collapse during the high pressure processing. By synthesizing bulk GNP, we are able to definitively attribute observed phenomena and mechanisms to the GNP and not to the matrix phase. Knowledge of GNP mechanisms allows for a better prediction of the effects that GNP will have as secondary phases in composites.

2. Materials and methods

2.1. Graphene nanoplatelet powder

Graphene Nanoplatelets (xGNP-M-5) were obtained from XG Sciences, Lansing, MI, USA. The GNP has a thickness of 6–8 nm [16]. This indicates that the average GNP particle has about 20 sheets of graphene as each pair of graphene layers has a thickness of ~0.35 nm [17]. GNP particles have an average diameter of 15 µm, giving the platelets a relative surface area of 120–150 m²/g. [16]. GNPs have some functional groups at the edges, consisting of approximately 0.075% ether, 0.035% carboxyl, and 0.03% hydroxyl groups [16]. Fig. 1a shows the SEM micrographs of the GNPs with wrinkles and folds in the individual GNP. Fig. 1b shows a stack of few GNPs in the

cross-section. As-received GNPs were used for the synthesis of the bulk GNP structure.

2.2. Spark plasma sintering processing

The GNP powder was consolidated at Thermal Technologies LLC (Santa Rosa, California, USA) using their spark plasma sintering facility. The consolidation was carried out in a 20 mm diameter graphite die using a holding pressure of 80 MPa, a holding temperature of 1850 °C, and a hold time of 10 min. The environment in the die consisted of Argon gas at a pressure of 3–6.5 Pa. GNP powder was wrapped in a graphite foil for improved current flow. The current was held at approximately 2500 A during the 10 min hold at 1850 °C. The current at the 3 min hold at 1100 °C was approximately 1110 A. The heating rate used was 200 °C/min.

2.3. Structural characterization

The bulk GNP pellet obtained through SPS processing was polished in order to remove the graphite foil from the surface. This thin layer of graphite originates from the graphite die used during the SPS. A Helium gas pycnometer (Accupyc 1340, Micrometrics Instrument Corporation, Norcross, GA, USA) was used to measure the true density of the bulk GNP pellet as well as the starting GNP powder. The starting GNP powder and the bulk GNP pellet were also characterized using micro-Raman spectroscopy in order to study the effects of the SPS processing on the GNP structure. The equipment used was a Spectra Physics (Model 3900S, California, USA) with Ti-sapphire crystal as the target (514 nm), a laser power of 18 mW and a detector with 4 cm⁻¹ spectral resolution from Kaiser Optical Systems, Inc. (Michigan, USA). Scanning electron microscopy of the GNP powder and the bulk GNP pellet were done using a JEOL JSM-6330F field emission scanning electron microscope (FE-SEM) with an operating voltage of 15 kV.

2.4. Mechanical and tribological characterization

The bulk GNP pellet was fractured in order to study the transverse surface. Both the top and transverse surfaces were mounted and grinded using 600 grit silicon carbide paper followed by polishing using an alumina slurry of 0.3 µm particles. Nano-indentation experiments were carried out using a Hysitron Triboindenter (Hysitron Inc., Minneapolis, MN, USA) with

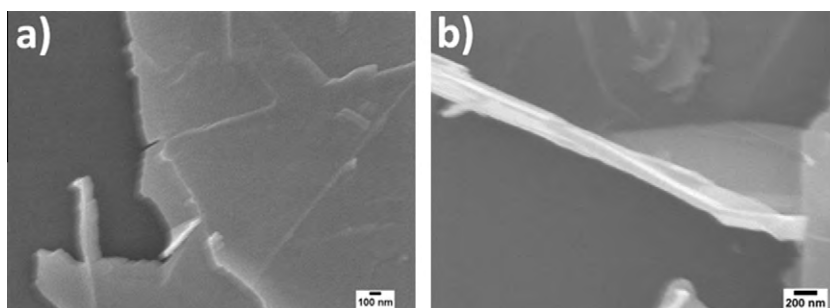


Fig. 1 – SEM images of starting GNP powder (a) top view at and (b) stack of few GNPs in cross-section.

a 100 nm Berkovich tip. The tip-area calibration was done using a standard fused quartz substrate of known modulus (69.6 GPa). The triboindenter was used in quasi-static indentation mode in order to measure the elastic modulus and hardness of the transverse and top surfaces of the GNP pellet. The indentation process consisted of a 10 s period to reach a load of 125 μ N, with a holding time of 3 s, followed by a 10 s unloading to 0 N. The elastic modulus was calculated from the load-displacement curves using Oliver–Pharr method [22].

Tribological studies on the GNP pellet were done using a ball-on disk tribometer (Nanovea, Micro Photonics Inc., CA) in order to evaluate the macro-scale wear resistance and to measure the coefficient of friction. An aluminum oxide ball of 3 mm diameter was used as the counter surface on a track of 6 mm diameter. The tests were performed using a speed of 65 RPM for 30 min which gave a total linear traverse distance of 36.7 m. The use of these parameters was based on a previous tribological study done by Kumar et al. [23] on the graphite. The lateral force between the aluminum oxide ball and the GNP pellet surface was measured by the linear variable differential transformer (LVDT) sensor. The coefficient of friction data was acquired at a frequency of 16.67 Hz. The depth and volume of the wear tracks was measured by obtaining the topographical profile of the wear tracks using an Optical Profilometer (Nanovea PS50, Irvine, California, USA). Wear tracks were examined using SEM to understand the wear mechanism.

3. Results and discussion

3.1. Bulk GNP structure

3.1.1. Bulk structure consolidation

Fig. 2 shows the variation of temperature, applied pressure, and the punch displacement during SPS processing. The temperature was gradually increased up to 1100 °C before increasing the pressure. The pressure is then ramped up to 80 MPa, the temperature is held steady during the increase in pressure.

It can be seen from the punch displacement, that the powder in the die is compressed significantly (over 2 mm), when the pressure was ramped up. Once the desired pressure was reached, the temperature was further increased to the maximum required temperature of 1850 °C. During this increase in temperature, there is a positive change in the punch displacement, due to expansion of the graphite die stack assembly. However, at the tail end of the heating period (1650–1850 °C), there is a substantial negative change in the punch displacement, indicating that the majority of the powder compression occurs at this time. The powder is then sintered at the desired holding pressure and temperature for ~10 min. During this sintering period, the powder steadily continues to densify until the sintering process is complete; at which point the pressure is released and the temperature gradually ramped down. The resulting bulk GNP pellet is shown in Fig. 3, along with the actual dimensions. The density of the starting GNP powder was measured using a Helium Pycnometer, and found to be 1.82 g/cm³. The true density of the bulk GNP pellet was found to be 2.11 g/cm³. The increase in the density is largely attributed to the consolidation of powder. The formation of high density phases of carbon was not observed as discussed in the next section.

3.1.2. Bulk GNP microstructure

Fig. 4a and b show low magnification SEM images of the fracture surface of SPS consolidated GNPs. The pellet shows dense structure at the top and bottom surfaces with stacks of GNPs in the intermediate. GNPs are uniformly oriented as layered structure throughout the thickness of the pellet.

Fig. 5a shows the top surface of the consolidated GNP structure. GNPs retain their platelet shape on the top surface with some signs of damage at the edges. A high magnification SEM image of the cross-section of the layered GNP stack shows undamaged and oriented GNPs in Fig. 5b. It can be concluded from Fig. 5 that GNP experience very little damage during the SPS processing.

The structure of the GNPs before and after SPS consolidation is also examined by micro-Raman spectroscopy as shown

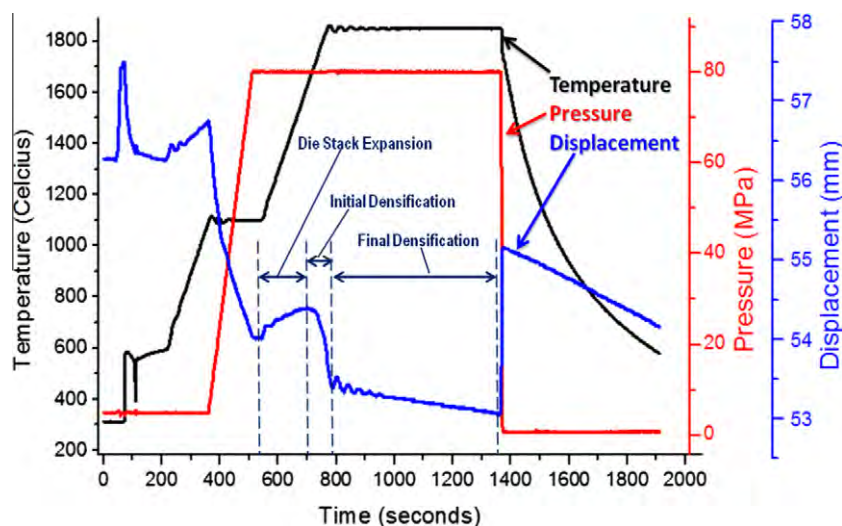


Fig. 2 – GNP SPS processing conditions.

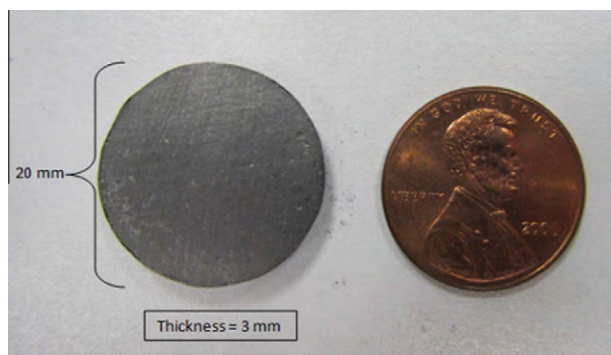


Fig. 3 – Bulk GNP synthesized by SPS processing, penny shown for size comparison.

in Fig. 6. Raman spectra from both GNP powder and SPS-pellet show presence of D, G and 2D peaks (2D peak also known as G) in the positions, which are the signatures of graphite like structure [24–26]. The G and 2D peaks appear from the in-plane C–C bond stretching in graphene, whereas the D peak corresponds to the defects introduced in the structure. A very small intensity D peak as compared to G peak in GNP-powder indicates very small amount of defects present at the powder stage. Slightly higher D peak in the case of the pellet might indicate some amount of defect introduced during SPS process. But the thermal annealing during cooling cycle of SPS might help in releasing pressure induced stress on GNP struc-

ture. In fact, the I_D/I_G ratio for both powder and sintered structure remains similar (0.125) indicating no significant damage to the structure during SPS. This observation along with similar intensity of G peaks (the crystallization peak for graphene) for powder and pellet indicates retention of graphene in the SPS consolidated structure.

Retention of graphene structure is further confirmed by the presence and intensity of 2D peak. Both samples show presence of 2D peak at $\sim 2700\text{ cm}^{-1}$, as reported for graphene Raman spectra at 514 nm [24]. The intensity ratio of 2D/G peak is almost 4 for single layer graphene [24] and decreases with an increase in the number of layers [24–27]. The intensity of 2D band becomes lower than G for bulk graphite [24–27]. Moreover, the 2D peak in single layer graphene is a narrow and sharp one, which gets broadened and shows sign of splitting with increasing number of graphene layers [24–27]. In the present study, both the powder and the pellet show broadened 2D peaks with sign of splitting, indicating presence of multiple graphene layers. But, the intensity ratio of 2D/G is still greater than 1, indicating the retention of graphene structure and not fully transforming to bulk graphite. Hence, it can be concluded from Raman spectroscopy that GNP structure is largely retained after SPS consolidation.

3.1.3. Toughening mechanisms in consolidated GNP structure

Fig. 7 shows SEM images of the fracture surface of GNPs revealing unique bending, folding and curling structure leading to energy dissipation. The bending of the GNPs is observed

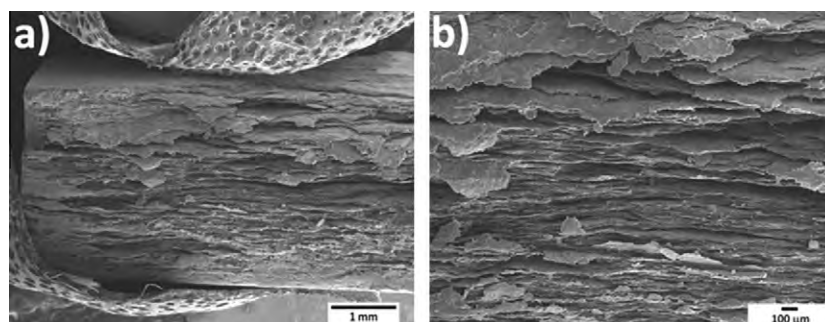


Fig. 4 – SEM images of consolidated GNP structure's fracture surface reveal stacks of uniformly oriented GNP layers at (a) low magnification and (b) higher magnification. Carbon tape used to hold sample for SEM is seen near top and bottom of image in Fig. 4a.

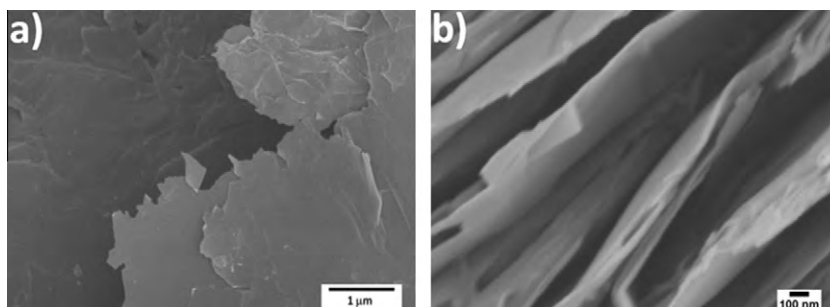


Fig. 5 – SEM images of consolidated GNP structure: (a) Top Surface showing minor damage at edges and (b) transverse surface showing highly oriented structure.

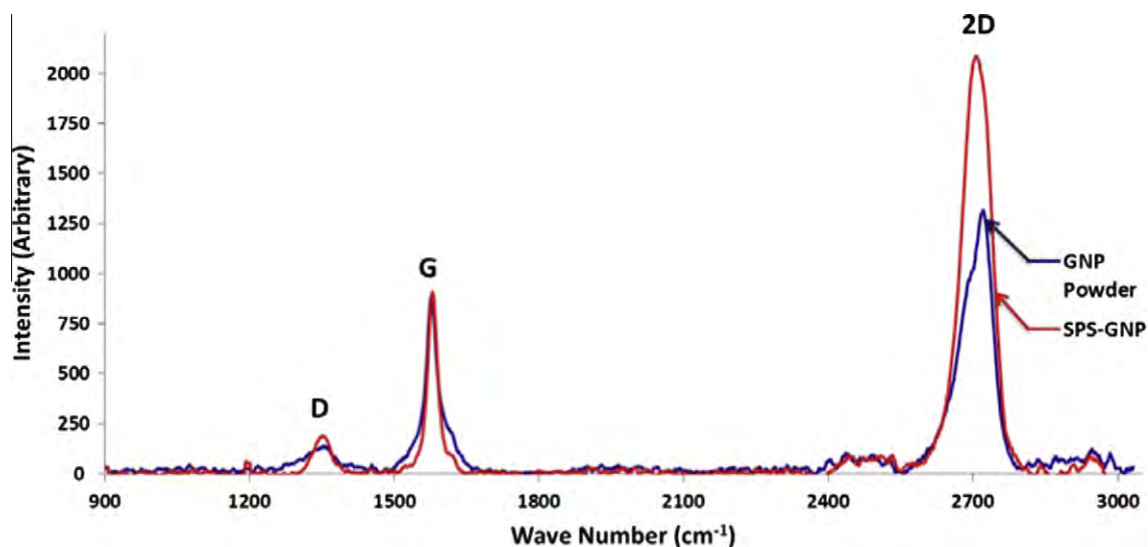


Fig. 6 – Micro-Raman spectroscopy of starting GNP powder and GNP SPS Pellet.

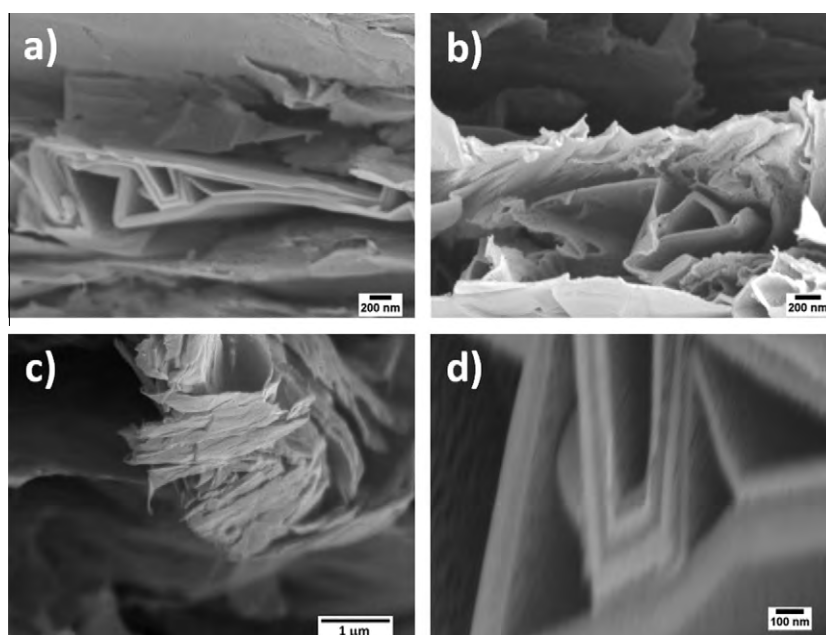


Fig. 7 – (a) Bending at high angles observed across multiple stacks of GNPs, (b) Bending at high angles observed in single stack of GNP, (c) in-plane view of bent GNPs, (d) Bending of multiple GNP stacks, with some stacks becoming offset because of the interlayer sliding. No fracture is observed at high bending angles indicating high strength and flexibility of GNPs.

to occur for a single stack as in Fig. 7b, as well as in multiple stacks as observed in Fig. 7a and d. These bends are the result of the high pressure experienced during the SPS processing. Fig. 7c shows wrapping phenomena of GNPs with minimal damage on the surface. It can be concluded from Fig. 7d that despite bending angles exceeding 90° and in some cases approaching 180° , the GNP does not fracture, giving way to the U-shape structure. GNP layers are concurrently undergoing sliding during the bending, especially between stacks of GNP as in Fig. 7d. Some of the stacks become offset from

the other stacks during the bending. This form of deformation is similar to the pseudo-plastic behavior observed in Ti_3SiC_2 [28–29]. Mechanisms in the Ti_3SiC_2 microstructure include interlayer sliding, grain buckling, and kink band formation. The kink boundaries are believed to enhance mechanical properties by containing damage. The bending observed in the GNP occurs at much larger angles than those in the Ti_3SiC_2 kink band formation and would be expected to have the same toughening effects as the Ti_3SiC_2 . Since these sliding and bending mechanisms are observed in a pure bulk

GNP structure and not a composite, it can be concluded that this is a fundamental energy dissipation mechanism of GNP. Hence, GNPs can offer unique energy dissipating mechanisms when used as reinforcement in ceramic matrix composites, as energy would be absorbed during the bending and sliding of the GNPs. This energy dissipation mechanism would presumably not only occur during processing but also during load bearing. The toughening mechanisms and the ability of the GNP to absorb energy during load bearing make it an excellent candidate for use in brittle ceramic matrices. As is the case with Ti_3SiC_2 , the GNP bends would be expected to contain the spread of damage in a composite. This bending mechanism is likely responsible for the wrapping phenomena observed by Walker et al. [13] where the GNPs bend and wrap themselves around grains thus inhibiting crack propagation and increasing toughness.

3.2. Bulk GNP mechanical properties

3.2.1. Nano-indentation

Nanoindentation experiments were conducted on the top and transverse surfaces of the bulk GNP structure. Representative curves of the load–displacement curves obtained during the indentation process are shown in Fig. 8. For the transverse surface; there are two characteristic curves as the data displays a bi-modal distribution. This bi-modal distribution is believed to be mostly a product of the porous nature of the transverse sample as observed in Fig. 4. The top surface has an elastic modulus of 8.7 ± 1.3 GPa and a hardness of 0.61 ± 0.13 GPa. The lower distribution of the transverse surface has an elastic modulus of 10.3 ± 2.9 GPa and a hardness of 0.284 ± 0.02 GPa. The higher distribution of the transverse surface has an elastic modulus of 15.2 ± 2.2 GPa and a hardness of 0.513 ± 0.07 GPa. Both distributions of elastic modulus values for the transverse surface were higher than the values obtained for the top surface. The elastic modulus is lower in the top surface because the loading occurs mostly out of plane relative to the graphene sheets. The loading on the transverse surface can be both in-plane and out of plane because of the nature of the transverse surface which features

bending deformations of the layered GNP structure. If the transverse structure was a purely dense layered structure then the elastic modulus would be even higher because pure graphene has extremely high in-plane properties ($\sim 0.5\text{--}1$ TPa) [2]. While the transverse loading is more of a mixed-mode loading as compared to the top surface, in-plane loading should dominate because of the layered structure resulting in higher elastic modulus values at the transverse surface.

Both the top surface and the higher distribution of the fracture surface had about 55 nm of recovery, which corresponds to 35% permanent deformation. The lower distribution of the transverse surface has an elastic recovery of 60 nm, which corresponds to 50% permanent deformation. The top surface had a higher hardness than the fracture surface and is consistent with the amount of permanent deformation. Hardness is a measure of resistance to deformation and therefore it is expected that the porous transverse surface would have a lower hardness than the top surface.

3.3. Bulk GNP tribological properties

Ball on disk experiments were used to evaluate tribological properties such as coefficient of friction and wear resistance. All experiments were done on the top surface as a large surface area is needed to perform the macro-scale ball-on-disk wear experiments. Fig. 9 shows the coefficient of friction (COF) at 1 and 3 N loads. The average COF at 1 N is 0.37 which reduces to 0.16 at 3 N. The higher load causes more graphene layers to shear off the bulk consolidated GNPs and provides a lubricating effect.

The wear depth was obtained from the optical profiles of the wear tracks. Fig. 10 shows that the depth of the 1 N wear track is about $8\text{ }\mu\text{m}$ which increases to $22\text{ }\mu\text{m}$ at 3 N. The volume of the wear track was calculated by measuring the cross sectional area of the track and multiplying with the circumference. The average track volume of bulk consolidated GNP structure at 1 and 3 N loads are shown in Fig. 11. It must be emphasized that there was no measurable weight change after the wear experiments at 1 and 3 N loads, even though change in the track volume was observed in Fig. 11.

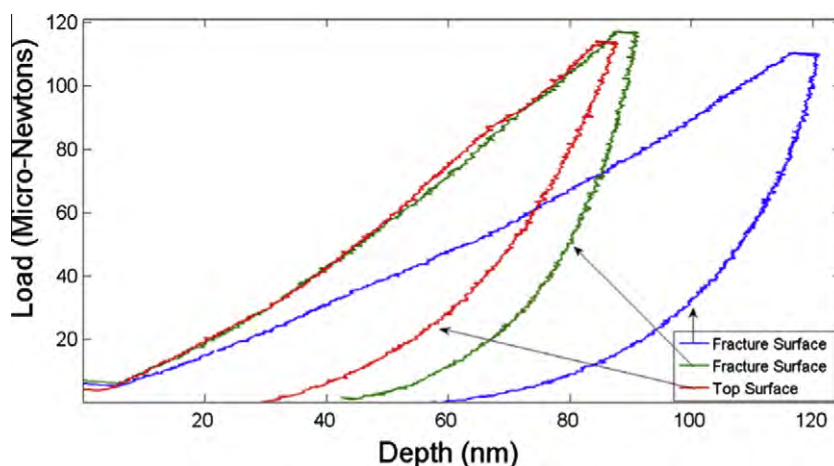


Fig. 8 – Load–displacement curves of nano-indentations performed on fracture surface and top surface. Fracture surface displays a bi-modal distribution.

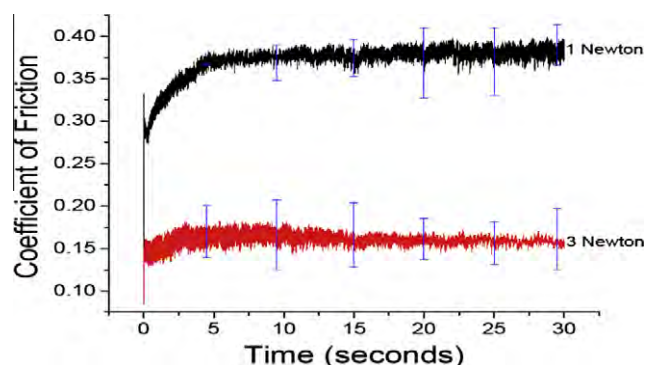


Fig. 9 – Coefficient of friction of top surface using 1 N and 3 N loads.

Wear tracks were examined by SEM to understand the mechanism governing the wear behavior of GNP pellet at different normal loads. Fig. 12 shows portions of the wear tracks at 1 N and 3 N loads with magnified views of different regions. The wear track at 1 N load reveals both worn and un-worn regions on the track (Fig. 12a). The worn regions are characterized by a smooth surface formed due to smearing off graphene layers on the track. The un-worn region, on the other

hand, reveals the rough as-received surface of GNP pellet. The presence of un-worn patches on this wear track suggests that 1 N is a very small load for causing uniform wear. Hence a larger error bar is shown for the wear volume at 1 N in Fig. 11. On the contrary, wear track at 3 N reveals different features at the edge and center of the track, resulting from differential wear mechanism (Fig. 12b). The edge of the track shows tearing of the surface revealing multiple GNP layers underneath. This was a result of the stress concentration along the edge of the track, which is a partition between loaded and unloaded regions on the surface. 3 N load is found to be sufficiently high to cause damage to the pellet surface. The damaged region shifts spatially on the surface with the increasing depth of the track, considering the spherical shape of the probe. As a result, the earlier damaged region will gradually occupy the inner region of track with the progression of time, as new un-worn surface would be exposed at the edge of the track. Thus, the central part of the track should also show the damaged surface. But the surface at the center of the 3 N track is very smooth (Fig. 12b). This is attributed to shear force introduced welding of the loosened graphene sheets, which is also supported by the earlier observation of scanty amount of wear debris (i.e. insignificant weight loss) present in this track.

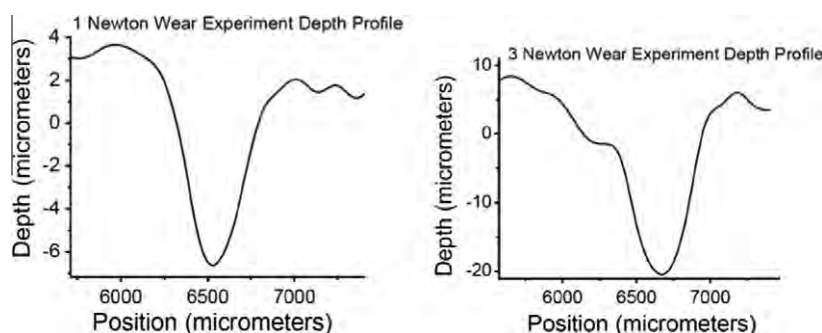


Fig. 10 – Wear track depth profiles at (a) 1 Newton and (b) 3 Newton load.

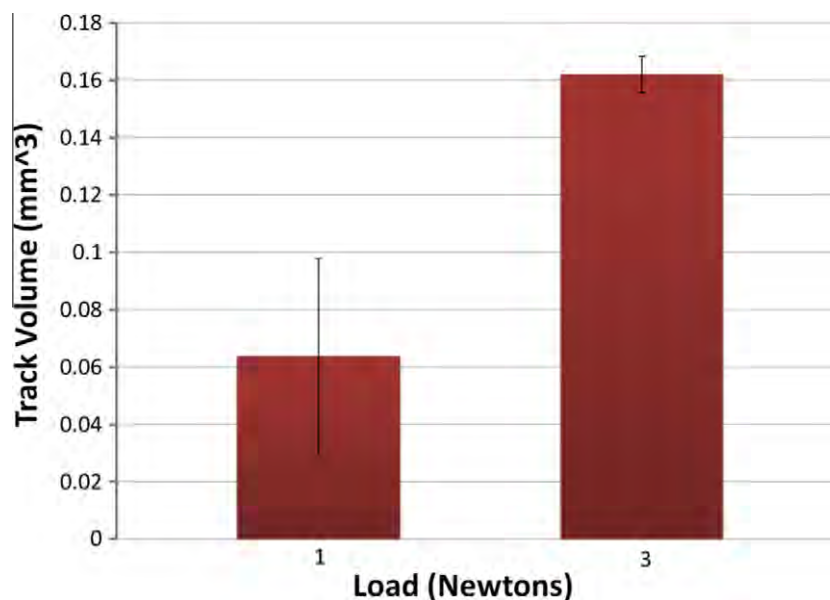


Fig. 11 – Track volume of SPS consolidated GNP at 1 and 3 N normal load.

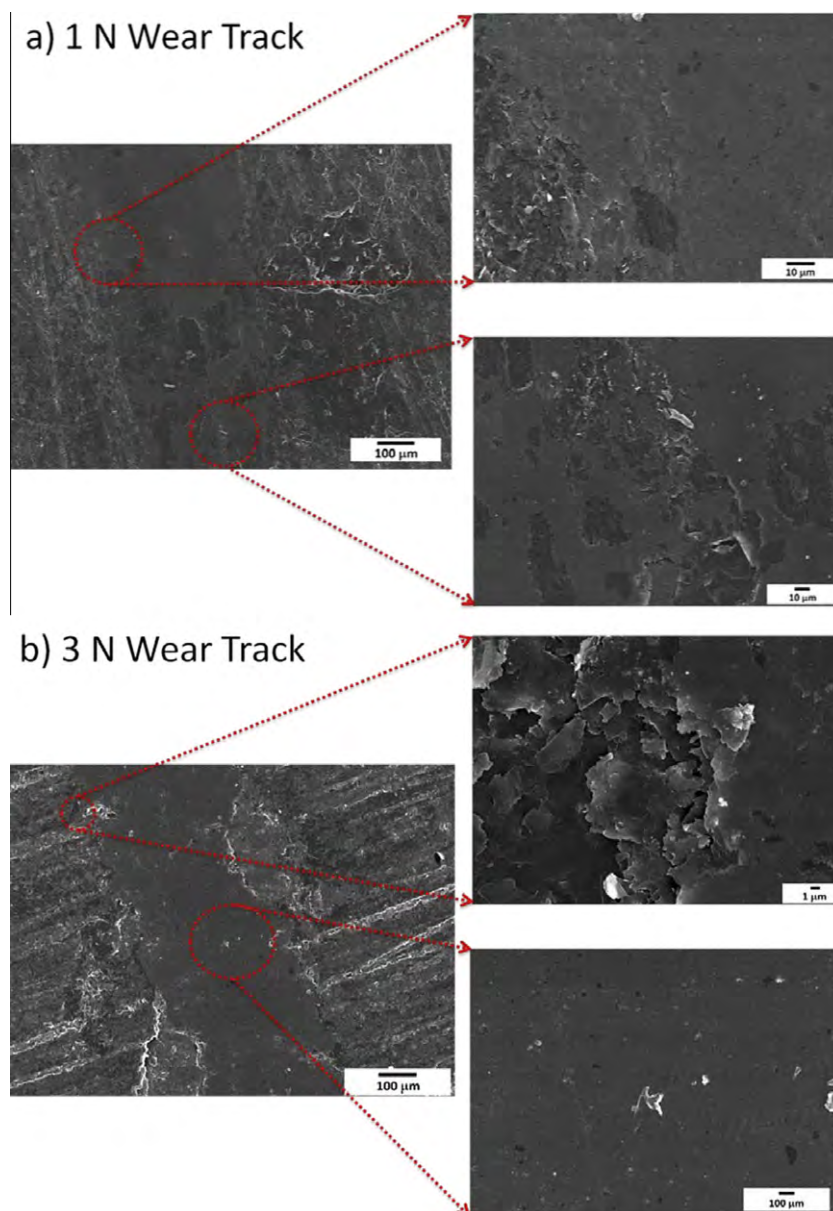


Fig. 12 – Wear tracks on SPS-GNP top surface at (a) 1 N and (b) 3 N load.

As stated before, there was little to no debris observed during the tests, supported by the fact that the weight of the pellet remained the same before and after the wear. Fig. 13 shows SEM images of the cross section of the wear track at 3 N load. The region beneath the surface of the track shows a very dense GNP structure. However, on a region far below the track, the GNPs have the same porous layered structure as observed in Fig. 4. Hence, it can be concluded that volume of the track created is not due to the removal of material; instead it is caused by the local consolidation of GNPs which results in the dense structure just below the wear track surface. The 3 Newton test results in a larger track volume as the load is higher resulting in a stronger local consolidation effect.

The differential wear mechanism observed at 1 and 3 N loads also supports the coefficient of friction shown in Fig. 9. A normal load of 1 N is not large enough to cause

uniform wear on GNP pellet surface and hence, cannot provide uniform lubrication through the track. The lack of lubrication causes higher coefficient of friction for 1 N load. The non-uniform wear along the track also explains larger error bar in the track volume for 1 N. On the other hand, shearing and welding of graphene at 3 N load causes enough lubrication at the probe surface and reduces coefficient of friction. Uniform wear on the track leads to smaller deviation in the track volume for 3 N load.

4. Conclusions

Bulk GNP structure is synthesized by SPS using parameters of 1850 °C and 80 MPa which are extremely harsh conditions; they are the harshest ever used for synthesis of graphene reinforced composites. GNPs are successfully retained with

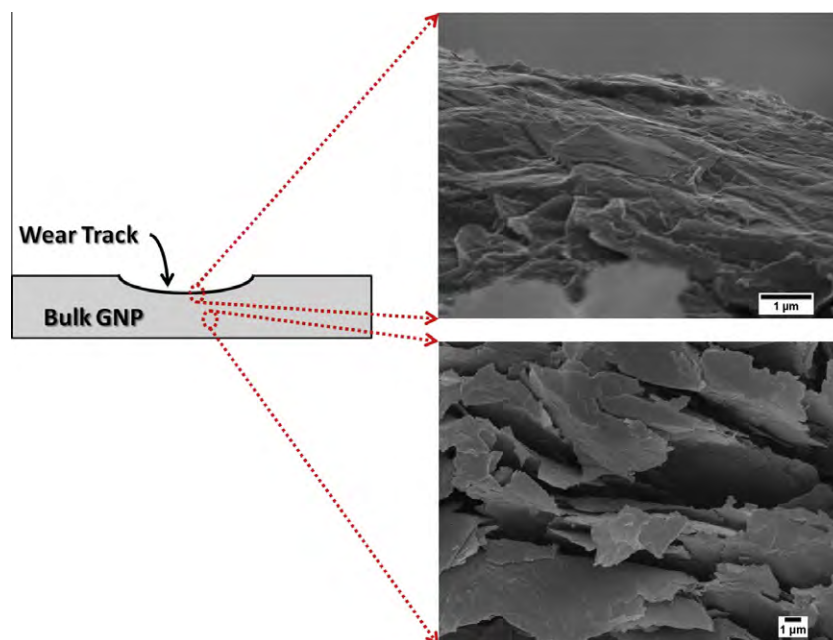


Fig. 13 – Cross sectional SEM images of the region below wear track. Region just below the track region show denser GNP structure due to localized consolidation. Region away from the track surface shows layered and porous GNP structure.

minimal damage during the SPS processing. GNPs undergo sharp bends and turns and form a corrugated-like structure. Such bending provides a source of the energy dissipation mechanisms during load bearing. These bending mechanisms make GNP an ideal candidate for use as reinforcing phase in ceramic composites and also explain some toughening previously observed in graphene reinforced composites. GNP bending is also responsible for the wrapping mechanisms around the grains that have been observed to inhibit crack propagation and to increase toughness in composites. Tribological properties suggest that GNP shear off and weld at a higher load and provides a lubricating effect. It is concluded that GNP reinforced ceramic composites can be effectively synthesized by SPS technique with a dual effect of increasing the toughness and reducing the coefficient of friction.

Acknowledgements

Authors would like to acknowledge Dr. Ali Sayir, Program Manager of High Temperature Aerospace Materials at the Air Force Office of Scientific Research and FA9550-09-1-0297 Grant. Authors also acknowledge support from Mr. Neal Ricks, Advanced Materials Engineering Research Institute (AMERI) and Center for the study of Matter at Extreme Conditions (CeSMEC) at Florida International University.

REFERENCES

- [1] Lee C, Wei X, Kysar JW, Hone J. Measurement of the elastic properties and intrinsic strength of monolayer graphene. *Science* 2008;321(5887):385.
- [2] Frank IW, Tanenbaum DM, Van der Zande AM, McEuen PL. Mechanical properties of suspended graphene sheets. *J Vac Sci Technol* 2007.
- [3] Ramanathan T, Abdala AA, Stankovich S, Dikin DA, Herrera-Alonso M, Piner RD, et al. Functionalized graphene sheets for polymer nanocomposites. *Nat Nanotechnol* 2008;3:327–31.
- [4] Rafiee MA, Rafiee J, Wang Z, Song H, Yu ZZ, Koratkar N. Enhanced mechanical properties of nanocomposites at low graphene content. *ACS Nano* 2009;3:3884–90.
- [5] Kuilla T, Bhadra S, Yao D, Kim NH, Bose S, Lee JH. Recent advances in graphene based polymer composites. *Progress Polym Sci* 2010;35:1350–75.
- [6] Kim H, Abdala AA, Macosko CW. Graphene/polymer nanocomposites. *Macromolecules* 2010;43:6515–30.
- [7] He T, Li J, Wang L, Zhu J, Jiang W. Preparation and consolidation of alumina/graphene composite powders. *Mater Trans* 2009;50(4):749–51.
- [8] Zhang XY, Li HP, Cui XL, Lin Y. Graphene/TiO₂ nanocomposites – synthesis characterization and application in hydrogen evolution from water photocatalytic splitting. *J Mater Chem* 2010;20:2801–6.
- [9] Yang S, Cui G, Pang S, Cao Q, Kolb U, Feng X, et al. Fabrication of cobalt and cobalt oxide/graphene composites: towards high-performance anode materials for lithium ion batteries. *Chem Sus Chem* 2010;3:236–9.
- [10] Ding Y, Jiang Y, Xu F, Yin J, Ren H, Zhou Q, et al. Preparation of nano-structured LiFePO₄/graphene composites by co-precipitation method. *Electrochem Commun* 2010;12:10–3.
- [11] Wang K, Wang Y, Fan Z, Yan J, Wei T. Preparation of graphene nanosheet/alumina composites by spark plasma sintering. *Mater Res Bull* 2010.
- [12] Fan Y, Wang L, Li J, Li J, Sun S, Chen F, et al. Preparation and electrical properties of graphene nanosheet/Al₂O₃ composites. *Carbon* 2010;48:1743–9.
- [13] Walker LS, Marotto VR, Rafiee MA, Koratkar N, Corral EL. Toughening in graphene ceramic composites. *ACS Nano* 2010;5(4):3182–90.
- [14] Raza MA, Westwood A, Brown A, Hondow N, Stirling C. Characterization of graphite nanoplatelets and the physical

- properties of graphite nanoplatelets/silicon composites for thermal interface applications. *Carbon* 2011;49:4269–79.
- [15] Lahiri D, Agarwal A. Graphene reinforced ceramic and metal matrix composites. In: Choi W, Lee J, editors. *Graphene: synthesis and applications*. Boca Raton: CRC Press; 2012. p. 187–232.
- [16] XG Sciences. xGnP® Graphene Nanoplatelets Carbon Nanoparticles with Multifunctional Capability. XG Sciences Documentation 2009.
- [17] Choi W, Lahiri I, Seelaboyina R, Kang YS. Synthesis of graphene and its applications: a review. *Crit Rev Solid State Mater Sci* 2010;35:52–71.
- [18] Kotov NA. Materials science: carbon sheet solutions. *Nature* 2006;442:254–5.
- [19] Lu K. Sintering of nanoceramics. *Int Mater Rev* 2008;53(1):21–38.
- [20] Munir ZA, Anselmi-Tamburini U. The effect of electric field and pressure on the synthesis and consolidation of materials: a review of the spark plasma sintering method. *J Mater Sci* 2006;41:763–77.
- [21] Ragulya AV. Consolidation of ceramic nanopowders. *Adv Appl Ceram* 2008;107(3):118–34.
- [22] Oliver WC, Pharr GM. An improved technique for determining hardness and elastic modulus using load and displacement sensing indentation experiments. *J Mater Res* 1992;7(6):1564–83.
- [23] Kumar N, Dash S, Tyagi AK, Raj B. Super low to high friction of turbostratic graphite under various atmospheric test conditions. *Tribol Int* 2011;44:1969–78.
- [24] Ferrari AC, Meyer JC, Scardaci V, Casiraghi C, Lazzeri M, Piscanec S, et al. Raman spectrum of graphene and graphene layers. *Phys Rev Lett* 2006;97:187–401.
- [25] Dresselhaus MS, Jorio A, Hofmann M, Dresselhaus G, Saito R. Perspectives on carbon nanotubes and graphene Raman spectroscopy. *Nano Lett* 2010;10:751–8.
- [26] Kalbac M, Farhat H, Kong J, Janda P, Kavan L, Dresselhaus MS. Raman spectroscopy and in situ raman spectroelectrochemistry of bilayer 12C/13C graphene. *Nano Lett* 2011;11:1957–63.
- [27] Ni ZH, Wang HM, Ma Y, Kasim J, Wu YH, Shen ZX. Tunable stress and controlled thickness modification in graphene by annealing. *ACS Nano* 2008;2:1033–9.
- [28] Gilbert CJ, Bloyer DR, Barsoum MW, El-Raghy T, Tomsia AP, Ritchie RO. Fatigue-crack growth and fracture properties of coarse and fine-grained Ti_3SiC_2 . *Scripta Materialia* 2000;42:761–7.
- [29] Sun Z-M, Zhang Z-F, Hashimoto H, Abe T. Ternary compound Ti_3SiC_2 : Part II. Deformation and fracture behavior at different temperatures. *Mater Trans* 2002;43(3):432–5.

Graphene-induced strengthening in spark plasma sintered tantalum carbide–nanotube composite

Debrupa Lahiri,^a Evan Khaleghi,^b Srinivasa Rao Bakshi,^{a,c} Wei Li,^b Eugene A. Olevsky^b and Arvind Agarwal^{a,*}

^a*Plasma Forming Laboratory, Department of Mechanical and Materials Engineering,
Florida International University, FL 33174, USA*

^b*Department of Mechanical Engineering, San Diego State University, San Diego, CA 92182, USA*

^c*Department of Metallurgical and Materials Engineering, Indian Institute of
Technology Madras, Chennai 600036, India*

Received 20 September 2012; accepted 27 October 2012

Available online 2 November 2012

Transverse rupture strength of spark plasma sintered tantalum carbide (TaC) composites reinforced with long and short carbon nanotubes (CNTs) is reported. The rupture strength depends on the transformation behavior of the CNTs during spark plasma sintering, which is dependent on their length. The TaC composite with short nanotubes shows the highest specific rupture strength. Shorter CNTs transform into multi-layered graphene sheets between TaC grains, whereas long ones retain the tubular structure. Two-dimensional graphene platelets offer higher resistance to pull-out, resulting in delayed fracture and higher strength.

© 2012 Acta Materialia Inc. Published by Elsevier Ltd. All rights reserved.

Keywords: TaC; Carbon nanotube; Graphene; Spark plasma sintering; Rupture strength

TaC is a group V ultrahigh-temperature carbide and shows great promise as the aerospace material for throat and nozzle inserts due to its very high melting point, which exceeds the combustion flame temperature of most propellants [1]. Consolidation of TaC has been performed using different techniques, e.g. pressure-less sintering, hot pressing, hot isostatic processing, vacuum plasma spraying, high-frequency induction heating and spark plasma sintering (SPS) [2–15]. Sintering aids such as carbon and boron carbide have been added to TaC during hot pressing, which has resulted in finer grains and improved density [6]. Although promising results have been obtained in these studies, consolidation of TaC with improved mechanical properties still remains a challenge due to its extremely high melting point of 3880 °C. SPS has emerged as a promising technique to consolidate fully dense ultrahigh-temperature ceramics such as HfB₂, HfC, ZrB₂, ZrC and TaC in short sintering times [13,16–18]. These ceramics display rupture/flexural strength in the range of 400–700 MPa at room temperature, revealing the potential of SPS in consolidating high-temperature ceramics [13,16–18].

In our recent study [2], fine ($0.36 \pm 13 \mu\text{m}$) TaC powder was consolidated using SPS with carbon nanotubes (CNT) as a sintering aid and reinforcement. Long and short CNTs were added as reinforcement to synthesize TaC–4 wt.% LC and TaC–4 wt.% SC composites, respectively. A wet chemistry method was used to disperse the long CNTs in the TaC powder, whereas a spray drying method was used for the short CNTs. Spray drying led to better dispersion of the shorter CNTs compared to the wet chemistry technique used for the longer CNTs. The SPS was carried out in an argon atmosphere at 1850 °C and 100 MPa [2]. The sintered pellets were 20 mm in diameter and 4–5 mm in thickness. TaC, TaC–4 wt.% long CNT and TaC–4 wt.% short CNT compositions will hereafter be referred as TaC, TaC–LC and TaC–SC, respectively. The addition of CNTs increased the density of the spark plasma sintered TaC from 89% to 95% at 100 MPa pressure and 1850 °C (Table 1). The increase in the density is achieved by better consolidation due to the possible inhibition of the grain growth affecting densification and due to the pore closure by CNTs. Interparticle diffusion is also increased due to the high thermal conductivity and electrical conductivity of the CNTs sitting between the TaC particles [2,19].

* Corresponding author. Tel.: +1 305 348 1701; fax: +1 305 348 1932; e-mail: agarwala@fiu.edu

Table 1. Summary of TaC-based composites: microstructural features and mechanical properties.

Sample	CNT content and size	Relative density (%)	Grain size (μm)	Rupture strength (MPa)	Fracture strain	Specific strength ($\text{MPa g}^{-1} \text{cc}^{-1}$)	Microstructure characteristics
TaC-AR	–	89	0.56 ± 0.12	259 ± 25	0.10	18.1	Fine grains with intergranular porosity
TaC-LC	4 wt.% Diameter: 30–50 nm Length: 10–20 μm	95	0.61 ± 0.27	279 ± 10	0.22	23.9	Fine grains, long pulled out CNTs
TaC-SC	4 wt.% Diameter: 40–70 nm Length: 1–3 μm	94	1.85 ± 0.72	368 ± 22	0.14	28.1	Damaged CNTs as graphene platelets at grain boundaries

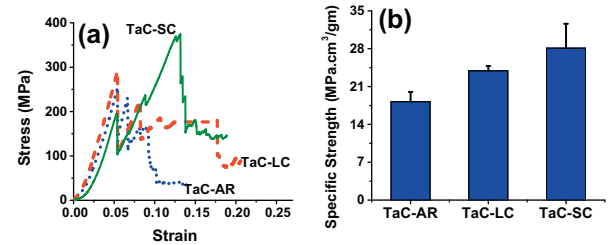
CNTs are also known to act as grain growth inhibitors in ceramics due to grain boundary pinning [20–22]. However, TaC-LC and TaC-SC did not result in grain refining at the relatively lower pressure of 100 MPa. Khalegi et al. [13] also noticed insignificant grain refining with 0.77 wt.% CNT addition during SPS at a low pressure (30–75 MPa). On the other hand, our previous work resulted in significant grain refinement (by 3–4.5 times) in TaC-CNT at a higher pressure of 255–363 MPa during SPS consolidation [2]. These observations indicate the dependence of grain refinement on applied pressure for SPS-processed TaC-CNT composites. Nanoindentation studies revealed higher elastic modulus and hardness for TaC-LC as compared to TaC-SC [2]. However, nanoindentation studies restrict deformation to a limited volume of the material under compressive stress. Since the crack generation and propagation in a heterogeneous composite can be abrupt and discontinuous across the scale length, a macroscale test could provide more insight into the strengthening criterion. Rupture strength represents the highest stress experienced within the material at the failure. Thus, the goal of the present study is to understand the effect of CNT types on the transverse rupture strength (TRS) of spark plasma sintered TaC-based composites. The transformation of CNT structure during SPS and its influence on TRS is also discussed.

The test procedure followed for TRS evaluation is similar to the one developed by Khalegi et al. [13] for SPS-synthesized ceramic matrix composites. This test method is versatile for disk-shaped specimens obtained from SPS. As-received samples can be used for mechanical testing without further machining, which is very difficult for super-hard and brittle materials like TaC. Disk-shaped samples with ~ 20 mm diameter and ~ 3 mm thickness were sintered for TRS evaluation. A minimum of three samples for each condition were tested for this. The test method involves the application of pressure onto the TaC disks through a ball-shaped tungsten carbide indenter to cause fracture. The computation of TRS for a disk-shaped specimen was carried out using the following relationship [13]:

$$\sigma_{\max} = \frac{P}{h^2} \left[(1 + \nu) \left(0.485 \log \frac{a}{h} + 0.52 \right) + 0.48 \right] \quad (1)$$

where P is the measured force, and a and h are the specimen's radius and thickness, respectively. Poisson's ratio, ν , for TaC was taken as 0.21, as reported by Lopez-de-la-Torre et al. [23].

Figure 1a shows the representative stress–strain behavior of the TaC, TaC-LC and TaC-SC samples.

**Figure 1.** (a) Stress–strain plot from transverse rupture tests on TaC, TaC-LC and TaC-SC composites; (b) specific transverse rupture strength of TaC, TaC-LC and TaC-SC.

TaC shows the lowest rupture strength of the three compositions (TaC-SC shows the highest rupture strength and TaC-LC shows the intermediate strength). All samples show peaks and valleys in stress–strain curves, which is indicative of different stages of fracture, such as cascades of crack propagation, energy absorption and generation of new cracks. The fracture strain is highest in TaC-LC, possibly due to the effective bridging of wider cracks by long CNTs. TaC-LC shows a large drop in the stress followed by an increase which is attributed to the load-transfer to the reinforcement in ceramic matrix composites. Several researchers have reported bridging of cracks and toughening in CNT-reinforced ceramic matrix composites [20,24–27].

Figure 1b presents the specific transverse rupture strength for the TaC, TaC-LC and TaC-SC samples. The small error bars indicate the consistency of the results for all compositions. The variation in the density of SPS samples as a function of composition (Table 1) necessitates the calculation of the specific rupture strength, which is determined by dividing the rupture strength by the corresponding density. TaC-LC and TaC-SC show 32% and 55% improvement in the specific rupture strength, respectively, as compared to TaC. The specific rupture strength is an important design criterion for lightweight aerospace materials to improve fuel efficiency without sacrificing strength.

Figure 2 shows the fracture surfaces of the spark plasma sintered TaC, TaC-LC and TaC-SC; these elucidate the different strengthening mechanisms. Partially sintered TaC shows intergranular porosity (Fig. 2a), which leads to the lowest densification (89%). TaC-LC and TaC-SC show denser structures, with faceted grains and reinforcement phases present at the intergranular region (Fig. 2b and c, respectively). The presence of tubular CNTs in TaC-LC (Fig. 2b) indicates the survival of longer CNTs during SPS. However, the fracture surface of TaC-SC lar-

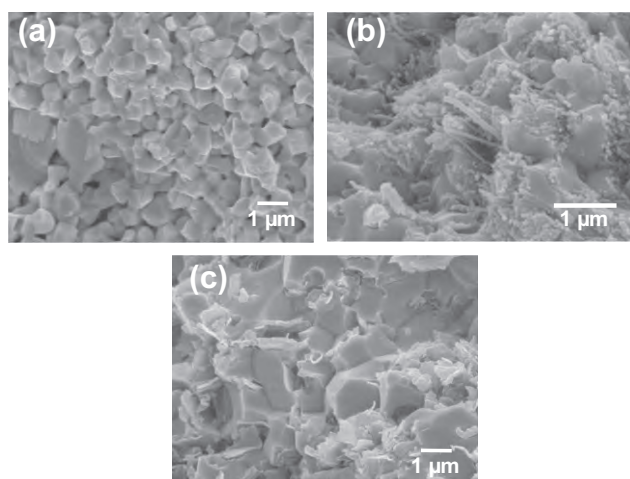


Figure 2. SEM micrograph of fracture surfaces for (a) TaC, (b) TaC-LC and (c) TaC-SC.

gely shows thin platelet-type morphologies, with just traces of tubular shapes (Fig. 2c). This thin platelet morphology is suggestive of the transformation of shorter CNTs to TaC-SC. Lower elastic modulus and lower nanohardness were reported for TaC-SC as compared to TaC-LC [2]. However, TaC-SC exhibited the highest transverse rupture strength in the present study. It is concluded that the evolution of thin platelet-type reinforcement may play a dominating role in improving the rupture strength of TaC-SC as compared to TaC-LC.

Figure 3a presents high-magnification scanning electron microscopy (SEM) images of the fracture surface for TaC-SC, showing the layered graphene platelet structure. These platelets are formed via transformation of short tubular CNTs into two-dimensional (2-D) platelets. Graphene platelets are largely found at the intergranular region, sandwiched between individual TaC grains (Fig. 3b). Due to its 2-D nature, graphene covers more intergranular area than CNTs do. As a result, during fracture, when a crack is arrested in the presence of a graphene platelet, it needs to propagate across a much larger distance than in the vicinity of a CNT [28]. Graphene platelets in the SPS structure are found to bend to more than 90° without getting damaged and thus leading to high energy dissipation [29]. The presence of graphene platelets at the intergranular region provides higher resistance to crack propagation during rupture of the TaC-SC, as compared to CNTs in TaC-LC. Moreover, the pulling out of 2-D platelets from any matrix requires higher energy as compared to 1-D tubes, considering the similar interfacial bonding strength in both structures and the higher area in the former. Figure 3c furnishes proof of the strong interfacial bonding at the graphene-TaC interface of a partially pulled-out platelet. Absorption of more fracture energy during the pulling out of the graphene platelet further delays the rupture and increases the strength of the TaC-SC structure. A comparative study on a polymer-based composite has reported graphene to be more effective than CNT in improving the fracture energy and fatigue strength [30].

The transformation of a tubular CNT structure into a 2-D sheet like graphene platelets during SPS can be attributed to the application of high pressure, tempera-

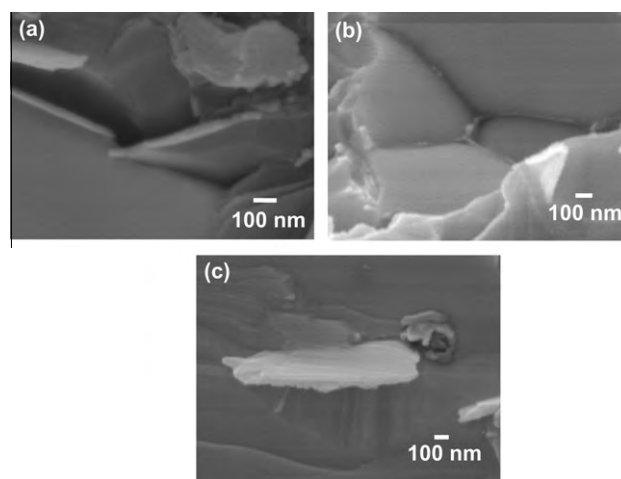


Figure 3. High-magnification SEM micrographs of TaC-SC fracture surface revealing: (a) transformed graphene platelets with straight edges; (b) graphene platelets sandwiched at TaC grain boundaries; (c) pulled-out graphene platelet forming a strong interface with the TaC matrix.

ture and electric current density. Exposure to high temperature and pressure has been reported to damage the tubular structure of CNT [20,31,32]. A high pulse current passing through multi-walled CNTs can break the sp^2 bonds holding the carbon atoms in each wall of a CNT, resulting in unzipping [33]. High axial electrical conductivity of CNTs assists an easy flow of energy through it [34]. The unzipping of tubular CNTs results in the formation of 2-D graphene platelets [33]. The unzipping of CNT to graphene also occurs by oxidation and intercalation. Oxidation opens up end caps and kink sites of planar walls of CNT, through which the intercalation of molecules occur. The intercalation causes the stretching of C–C bonds, resulting in unzipping to graphene [35]. Since SPS of TaC-CNT was performed in an argon atmosphere, the unzipping of CNT should be largely unaffected by oxidation and intercalation. Thus, the transformation of CNT to graphene in TaC-SC is attributed to the high pulse current assisted unzipping.

It may be argued that the SPS parameters were same for both TaC-LC and TaC-SC, hence the two structures should ideally show similar transformation of CNT to graphene. However, most of the CNT content in TaC-SC is transformed to graphene, whereas in TaC-LC a significant amount of CNTs remains. This difference in behavior could be explained in terms of the relative size of the reinforcement. In the case of TaC-SC, the length of the CNTs (1–3 μm) is similar to the size of TaC grains ($1.85 \pm 0.72 \mu\text{m}$). Thus, the short CNTs remain sandwiched between TaC grains, experiencing maximum pressure. In addition, these CNTs are also exposed to high thermal energy due to Joule heating and plasma at the particle interface. Damage due to high temperature and pressure along with electrical energy causes easier unzipping of short CNTs to graphene platelets. Figure 4a presents a high-resolution transmission electron microscopy (HRTEM) image of one such short CNT getting unzipped into graphene platelets. In contrast, long CNTs (10–20 μm) are at least 20 times longer than TaC grains ($0.61 \pm 0.27 \mu\text{m}$) in TaC-LC. Thus, the CNTs do not remain sandwiched in one intergranular

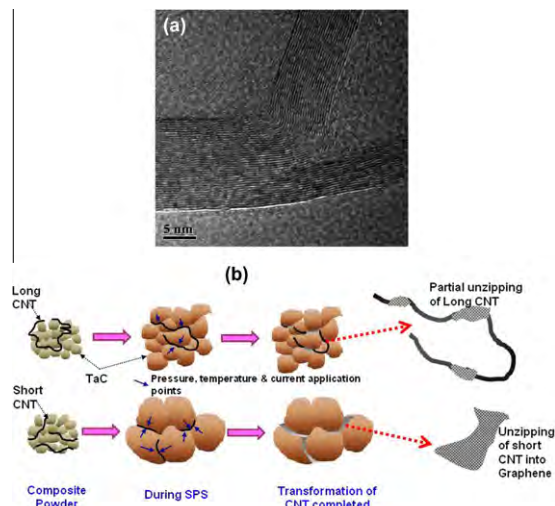


Figure 4. (a) HRTEM image of graphene platelet formed by unzipping of CNT in TaC–SC composite; (b) schematic of the CNT to graphene platelet transformation in TaC–LC and TaC–SC composites.

region, but cover many of the regions and remains curled and twisted. The full length of a long CNT does not experience as much heat and pressure as the short CNTs in TaC–SC do. In addition, there is no straight path along which the electrical energy can travel fast, thus unzipping does not occur. As a result, long CNTs are able to retain their tubular structure in TaC–LC. This retention of their tubular structure is responsible for the effective wide crack bridging and higher rupture strain of TaC–LC. However, partial damage and unzipping of long CNTs is also expected in the parts that remain sandwiched in the intergranular region. The debris-like features in Figure 2b are attributed to such damage in long CNTs.

A schematic of the differential transformation behavior of CNTs in TaC–LC and TaC–SC is presented in Figure 4b for better visualization of the mechanism described above. The confinement of short CNTs in a singular intergranular region also causes better interfacial bonding of the reinforcement with the TaC matrix from all sides during sintering. This leads to the higher pull-out energy of the reinforcement and to the higher transverse rupture strength of the TaC–SC composite.

A.A. acknowledges support from the US Air Force Office of Scientific Research (FA9550-12-1-0263) through the High Temperature Materials Program managed by Dr. Ali Sayir. The support of Neal Ricks and AMERI at FIU in providing the research facilities is greatly acknowledged. The SDSU authors' support by the National Science Foundation Division of Civil and Mechanical Systems and Manufacturing Innovations (NSF Grant CMMI 0758232) and by the Department of Energy Division of Materials Sciences and Engineering (DOE Award DE-SC0008581) is gratefully appreciated.

- [1] K. Upadhyaya, J.M. Yang, W.P. Hoffman, *Am. Ceram. Soc. Bull.* 58 (1997) 51–56.
- [2] S.R. Bakshi, V. Musaramthota, D.A. Virzi, A.K. Keshri, D. Lahiri, V. Singh, S. Seal, A. Agarwal, *Mater. Sci. Eng. A* 528 (2011) 2538–2547.
- [3] J.X. Liu, Y.M. Kan, G.J. Zhang, *J. Am. Ceram. Soc.* 93 (2010).

- [4] I.G. Talmy, J.A. Zaykoski, M.M. Opeka, *J. Eur. Ceram. Soc.* 30 (2010) 2253–2263.
- [5] K. Hackett, S. Verhoef, R.A. Cutler, D.K. Shetty, *J. Am. Ceram. Soc.* 92 (2009) 2404–2407.
- [6] X.H. Zhang, G.E. Hilmas, W.G. Fahrenholtz, D.M. Deason, *J. Am. Ceram. Soc.* 90 (2007) 393–401.
- [7] X. Zhang, G.E. Hilmas, W.G. Fahrenholtz, *J. Am. Ceram. Soc.* 91 (2008) 4129–4132.
- [8] X.H. Zhang, G.E. Hilmas, W.G. Fahrenholtz, *Mater. Sci. Eng. A* 501 (2009) 37–43.
- [9] M. Desmaison Brut, N. Alexandre, J. Desmaison, *J. Eur. Ceram. Soc.* 17 (1997) 1325–1334.
- [10] B.R. Kim, K.D. Woo, J.M. Doh, J.K. Yoon, I.J. Shon, *Ceram. Int.* 35 (2009) 3395–3400.
- [11] D. Sciti, L. Silvestroni, S. Guicciardi, D.D. Fabbriche, A. Bellosi, *J. Mater. Res.* 24 (2009) 2056–2065.
- [12] K. Balani, G. Gonzalez, A. Agarwal, R. Hickman, J.S. O'Dell, S. Seal, *J. Am. Ceram. Soc.* 89 (2006) 1419–1425.
- [13] E. Khalegi, Y.-S. Lin, M.A. Meyers, E.A. Olevsky, *Scr. Mater.* 63 (2010) 577–580.
- [14] L. Limeng, Y. Feng, Z. Yu, Z. Zhiguo, *J. Am. Ceram. Soc.* 93 (2010) 2945–2947.
- [15] S.R. Bakshi, V. Musaramthota, D. Lahiri, V. Singh, S. Seal, A. Agarwal, *Mater. Sci. Eng. A* 528 (2011).
- [16] D. Sciti, S. Guicciardi, M. Nygren, *Scr. Mater.* 59 (2008) 638–641.
- [17] D. Sciti, G. Bonnefont, G. Fantozzi, L. Silvestroni, *J. Eur. Ceram. Soc.* 30 (2010) 3253–3258.
- [18] D. Sciti, F. Monteverde, S. Guicciardi, G. Pezzotti, A. Bellosi, *Mater. Sci. Eng. A* 434 (2006) 303–309.
- [19] R. Sivakumar, S. Guo, T. Nishimura, Y. Kagawa, *Scr. Mater.* 56 (2007) 265–268.
- [20] D. Lahiri, V. Singh, A.K. Keshri, S. Seal, A. Agarwal, *Carbon* 48 (2010) 3103–3120.
- [21] D. Lahiri, V. Singh, A.P. Benaduce, S. Seal, L. Kos, A. Agarwal, *J. Mech. Behav. Biomed. Mater.* 4 (2011) 44–56.
- [22] Q. Huang, Y. Bando, X. Xu, T. Nishimura, C. Zhang, C. Tang, F. Xu, L. Gao, D. Golberg, *Nanotechnology* 18 (2007) 485706.
- [23] L. Lopez-de-la-Torre, B. Winkler, J. Schreuer, K. Knorr, M. Avalos-Borja, *Solid State Commun.* 134 (2005) 245–250.
- [24] Y. Chen, K. Balani, A. Agarwal, *Appl. Phys. Lett.* 92 (2008) 011916.
- [25] D. Lahiri, S. Ghosh, A. Agarwal, *Mater. Sci. Eng. C* (2012), <http://dx.doi.org/10.1016/j.msec.2012.05.010>.
- [26] K. Balani, T. Zhang, A. Karakoti, W.Z. Li, S. Seal, A. Agarwal, *Acta Mater.* 56 (2008) 571–579.
- [27] S.C. Tjong, *Carbon Nanotube Reinforced Composites: Metal and Ceramic Matrices*, Wiley-VCH Verlag, Weinheim, 2009.
- [28] L.S. Walker, V.R. Marotto, M.A. Rafiee, N. Koratkar, E.L. Corral, *ACS Nano* 5 (2011) 3182–3190.
- [29] A. Nieto, D. Lahiri, A. Agarwal, *Carbon* 50 (2012) 4068–4077.
- [30] M.A. Rafiee, J. Rafiee, I. Srivastava, Z. Wang, H. Song, Z.-Z. Yu, N. Koratkar, *Small* 6 (2010) 179–183.
- [31] K. Yang, J. He, J.B. Reppert, M.J. Skove, T.M. Tritt, A.M. Rao, *Carbon* 48 (2010) 756–762.
- [32] S.R. Bakshi, V. Singh, D.G. McCartney, S. Seal, A. Agarwal, *Scr. Mater.* 59 (2008) 499–502.
- [33] W.S. Kim, S.Y. Moon, S.Y. Bang, B.G. Choi, H. Ham, T. Sekino, K.B. Shim, *Appl. Phys. Lett.* 95 (2009) 083103.
- [34] T.W. Ebbesen, H.J. Lezec, H. Hiura, J.W. Bennet, H.F. Ghaemi, T. Thio, *Nature* 382 (1996) 54–56.
- [35] S.R. Dhakate, N. Chauhan, S. Sharma, R.B. Mathur, *Carbon* 49 (2011) 4170–4178.

1.

1. Report Type

Final Report

Primary Contact E-mail**Contact email if there is a problem with the report.**

bboesl@fiu.edu

Primary Contact Phone Number**Contact phone number if there is a problem with the report**

305-348-3028

Organization / Institution name

Florida International University

Grant/Contract Title**The full title of the funded effort.**

Graphene Nanoplatelet Reinforced Tantalum Carbide

Grant/Contract Number**AFOSR assigned control number. It must begin with "FA9550" or "F49620" or "FA2386".**

FA9550-12-1-0263

Principal Investigator Name**The full name of the principal investigator on the grant or contract.**

Benjamin Boesl

Program Manager**The AFOSR Program Manager currently assigned to the award**

Dr. Ali Sayir

Reporting Period Start Date

05/31/2012

Reporting Period End Date

05/30/2015

Abstract

In this study, Graphene nanoplatelet (GNP) reinforced tantalum carbide (TaC) composites were studied for their mechanical and thermal properties as they relate to usage as ultra high temperature materials. Samples were fabricated using Spark Plasma Sintering (SPS) and ultrahigh-pressure consolidation. The results of mechanical property testing showed GNP reinforced composites have improved modulus, hardness, damping, and damage resistance over unreinforced TaC. Results of thermal analysis during plasma oxidation testing showed an increase in thermal conductivity in GNP reinforced composites resulting in a reduction of peak sample surface temperature. This study resulted in the publications listed below and attached to this document for additional detail (the support from this grant was acknowledged in each). This award also supported the research of three graduate students (A. Nieto, C. Zhang, S. Rengifo : 1 female, 2 of Hispanic decent) and one undergraduate student (S. Thomas).

Distribution Statement**This is block 12 on the SF298 form.**

Distribution A - Approved for Public Release

Explanation for Distribution Statement**If this is not approved for public release, please provide a short explanation. E.g., contains proprietary information.**

SF298 Form

Please attach your [SF298](#) form. A blank SF298 can be found [here](#). Please do not password protect or secure the PDF. The maximum file size for an SF298 is 50MB.

[AFD-070820-035.pdf](#)

Upload the Report Document. File must be a PDF. Please do not password protect or secure the PDF. The maximum file size for the Report Document is 50MB.

[AFOSR-BBoesl-FinalReport.pdf](#)

Upload a Report Document, if any. The maximum file size for the Report Document is 50MB.

Archival Publications (published) during reporting period:

1. C Rudolf, et al. In Situ Indentation Behavior of Bulk Graphene Nanoplatelets with Respect to Orientation, Carbon 94 (2015) 872-878
2. Nieto, A. et al. Three Dimensional Graphene Foam - Polymer Hybrid as a High Strength Biocompatible Scaffold, Advanced Functional Materials Volume 25, Issue 25 (2015), pages 3916–3924
3. A Nieto, et al. Multi-scale intrinsic deformation mechanisms of 3D graphene foam, Carbon 85 (2015) 299-308
4. B Boesl, et al. Direct observation of carbon nanotube induced strengthening in aluminum composite via in situ tensile tests, Carbon 69 (2014) 79-85
5. A Nieto, et al. Oxidation behavior of graphene nanoplatelet reinforced tantalum carbide composites in high temperature plasma flow, Carbon 67 (2014) 398-408
6. A Nieto, et. al., Nanodynamic mechanical behavior of graphene nanoplatelet-reinforced tantalum carbide. Scripta Materialia 69-9 (2013) 678-681
7. A Nieto, et. al. Graphene Nanoplatelets reinforced tantalum carbide consolidated by spark plasma sintering. Materials Science and Engineering: A 582 (2013) 338-346
8. D Lahiri, et. al., Boron nitride nanotubes reinforced aluminum composites prepared by spark plasma sintering: Microstructure, mechanical properties and deformation behavior. Materials Science and Engineering: A 574 (2013) 149-156
9. D Lahiri, et. al. Ultrahigh-pressure consolidation and deformation of tantalum carbide at ambient and high temperatures. Acta Materialia 61-11 (2013) 4001-4009
10. C Zhang, et. al. Photocatalytic Activity of Spark Plasma Sintered TiO₂-Graphene Nanoplatelet Composite, Scripta Materialia 68 (2013) 719–722
11. D Lahiri, et. al. Unfolding the Damping Behavior of Multilayer Graphene Membrane in the Low-Frequency Regime. ACS Nano 6-5 (2013), 3992-4000
12. A Nieto, et. al. Synthesis and properties of bulk graphene nanoplatelets consolidated by spark plasma sintering. Carbon 50-11 (2012), 4068-4077
13. D. Lahiri, et al. Graphene-induced strengthening in spark plasma sintered tantalum carbide–nanotube composite. Scripta Materialia 68 (2013) 285–288

Changes in research objectives (if any):

N/A

Change in AFOSR Program Manager, if any:

N/A

Extensions granted or milestones slipped, if any:

N/A

AFOSR LRIR Number**LRIR Title****Reporting Period****Laboratory Task Manager****Program Officer****Research Objectives**

Technical Summary

Funding Summary by Cost Category (by FY, \$K)

	Starting FY	FY+1	FY+2
Salary			
Equipment/Facilities			
Supplies			
Total			

Report Document

Report Document - Text Analysis

Report Document - Text Analysis

Appendix Documents

2. Thank You

E-mail user

Aug 20, 2015 20:56:27 Success: Email Sent to: bboesl@fiu.edu